P-12-07

Temperature Buffer Test

Final THM modelling

Mattias Åkesson, Daniel Malmberg,
Lennart Börgesson, Jan Hernelind,
Clay Technology AB

Alberto Ledesma, Abel Jacinto
UPC

January 2012

Svensk Kärnbränslehantering AB
Swedish Nuclear Fuel
and Waste Management Co

Box 250, SE-101 24 Stockholm
Phone +46 8 459 84 00

ISSN 1651-4416
SKB P-12-07
ID 1327618

Temperature Buffer Test

Final THM modelling

Mattias Åkesson, Daniel Malmberg,
Lennart Börgesson, Jan Hernelind,
Clay Technology AB

Alberto Ledesma, Abel Jacinto
UPC

January 2012

Keywords: Field test, Buffer, Bentonite, Temperature, Relative humidity, Displacement, Swelling pressure, Water retention curve, Thermo-hydro-mechanical processes, Numerical modelling.

Abstract

The Temperature Buffer Test (TBT) is a joint project between SKB/ANDRA and supported by ENRESA (modelling) and DBE (instrumentation), which aims at improving the understanding and to model the thermo-hydro-mechanical behavior of buffers made of swelling clay submitted to high temperatures (over 100°C) during the water saturation process. The test has been carried out in a KBS-3 deposition hole at Äspö HRL. It was installed during the spring of 2003. Two heaters (3 m long, 0.6 m diameter) and two buffer arrangements have been investigated: the lower heater was surrounded by bentonite only, whereas the upper heater was surrounded by a composite barrier, with a sand shield between the heater and the bentonite. The test was dismantled and sampled during the winter of 2009/2010.

This report presents the final THM modelling which was resumed subsequent to the dismantling operation. The main part of this work has been numerical modelling of the field test. Three different modelling teams have presented several model cases for different geometries and different degree of process complexity. Two different numerical codes, CODE_BRIGHT and ABAQUS, have been used.

The modelling performed by *UPC-Cimne using CODE_BRIGHT,* has been divided in three subtasks: i) analysis of the response observed in the lower part of the test, by inclusion of a number of considerations: (a) the use of the Barcelona Expansive Model for MX-80 bentonite; (b) updated parameters in the vapour diffusive flow term; (c) the use of a non-conventional water retention curve for MX-80 at high temperature; ii) assessment of a possible relation between the cracks observed in the bentonite blocks in the upper part of TBT, and the cycles of suction and stresses registered in that zone at the start of the experiment; and iii) analysis of the performance, observations and interpretation of the entire test. It was however not possible to carry out a full THM analysis until the end of the test due to convergence problems, and therefore a model limited to the TH processes was analysed.

The modelling performed by *Clay Technology's team using CODE_BRIGHT* has been divided into four sub-tasks: i) analysis of the evolution around the lower heater at the height of Ring 3 and 4. Several model versions were solved the thermal, hydraulic and mechanical problems. Due to the high temperatures in the bentonite it was also necessary to solve the mass balance of air; ii) analysis of the evolution around the upper heater at the height of Ring 9 and 10; iii) attempt to reproduce the shearing which appears to have occurred in Cylinder 3 in the beginning of the test. The model was run for 200 days and only solved the hydraulic and mechanical problems (temperature was kept constant at 60°C); iv) in the last task, results from a axisymmetric model of the full field experiment were presented. The model solves the Thermal and Hydraulic problem, as well as for the gas pressure. However, due to computational problems with such models, the mechanical problem was not solved. The motivation for this model was to understand how a lower gas pressure may influence the overall hydration in the experiment.

The modelling performed by *Clay Technology's team using ABAQUS* has been focused on a large-scale axisymmetric geometry which included the deposition hole as well as a substantial portion of the surrounding rock. The model solved the THM problem with a staggered solution technique facilitated by ABAQUS.

The work has also included different *evaluations of experimental results* with the aim to validate a number of data sets, and to assess the conditions in the tests prior to the dismantling operation. The evaluation was made in five different tasks with the following goals: i) to demonstrate consistency between the void ratio profiles at compaction and dismantling; the initial block heights; and the results from the leveling at installation and dismantling; ii) to demonstrate consistency between the void ratio profiles at dismantling; the final total pressure readings; and swelling pressure curves; iii) to test the assumption that the bentonite was totally water saturated before the termination of the heaters, and that the observed saturation profile was caused be the thermal "contraction" of water when the bentonite was cooled; iv) to obtain a correction factor for evaluated thermal conductivity values due to a radial displacement field; v) to characterize the final saturation state, before the termination of the heaters, and the progress of saturation around Heater I.

Finally, the *validity of the material models has been assessed*. This task has been a test of the different parts, or constitutive equations, of the material models, especially for the bentonite, for their ability to reproduce the experimental data. The following parts have been evaluated: i) the thermal model, i.e. the thermal conductivity; ii) the TH model, i.e. the two flow coefficients and the retention properties; iii) the mechanical model, and especially the plastic model; iv) the thermal expansion of water, which currently is a constant in the used codes; v) the gas transport and the significance of its inclusion; vi) the sand compressibility; and vii) the friction along the rock wall. This evaluation shows that the material models could satisfactory reproduces some of the experimental results: the thermal evolution; the hydration process around the upper heater; the swelling pressures (i.e. the relation between the void ratio and net mean stress during the final state) and the cable forces. Other aspects were less well reproduced: the dehydration around the lower heater which was generally exaggerated; the early evolution of relative humidity and the occurrence of pore pressures, especially around the lower heater, were generally not reproduced; the calculated von Mises stresses were in some cases significantly lower than the experimental data.

Contents

1 Introduction

1.1 TBT experiment

The Temperature Buffer Test (TBT) is a joint project between SKB/ANDRA and supported by ENRESA (modelling) and DBE (instrumentation). The test aims at improving the understanding of the thermo-hydro-mechanical (THM) behaviour of clay buffers at temperatures around and above 100°C during the water saturation transient, in order to be able to model this behaviour.

The experiment was installed during the spring of 2003 and was dismantled during the winter of 2009/2010. The test has been carried out at the –420 m level in Äspö HRL in a 8 meters deep and 1.76 m diameter deposition hole, with two steel heaters (3 m long, 0.6 m diameter), surrounded by four cylinders and 12 rings of compacted MX-80 bentonite. On the top, there was a confining concrete plug and a steel lid anchored with 9 rods (Figure 1-1). Two buffer arrangements have been investigated. The lower heater was surrounded by bentonite only, whereas the upper heater was surrounded by a composite barrier, with a sand shield between the heater and the bentonite. The latter has acted as a thermal protection for the bentonite, and as an important component for the retrievability. The installation of the experiment was reported by Johannesson et al. (2010). A time-line of major events in the operational conditions is shown in Figure 1-2.

The experiment has resulted in major sets of data:

- Sensors data, i.e. the evolution of temperature, relative humidity, total pressure (in axial, radial and tangential direction) and pore pressure in different locations, as well as cable forces and lid displacements (Goudarzi et al. 2010). In general, there is an assumption of axis symmetry, and these variables are thus largely functions of height, radius and time.
- Dismantling data, i.e. results form the core sampling and base characterization program, i.e distributions of the void ratio and the degree of saturation (Johannesson 2010); and results from the dismantling operation, i.e. levelling and interface measurements, which together with the initial geometry can be interpreted as displacements (Åkesson 2010). These variables are thus largely functions of height and radius.

1.2 Final THM modelling task

The evaluation of THM processes in TBT has previously been made through analysis of sensors data, through numerical modelling of the field test and through evaluation and numerical modelling of parallel lab-scale mock-up tests.The final THM modelling of TBT was resumed after the completion of the dismantling when the data from this operation became available.

Four different sub-tasks were proposed for this modelling task:

i. 1D axisymmetric THM model of the lower heater mid section.

ii. 1D axisymmetric THM model of the upper heater mid section.

iii. 2D axisymmetric HM model of the upper package mimicking the early shearing of R12/C3.

iv. 2D axisymmetric THM model of the entire test.

The reason for dividing the program in minor sub-tasks was to enhance the prospects to get relevant result, and to enable parameter studies without the substantial time requirements implied by the fourth sub-task. By this reason, it could also be useful to study variants of subtask i, ii and iv, without the mechanical process.

Apart from these proposals, the emphases of the actual contributions were left to the modelling teams to decide upon. All relevant information such as geometries, initial conditions, sensors data, and data from the dismantling were made available to the teams, without the preparation of any special program. In contrast, the selection of material models and parameter values were left to the modelling teams to motivate and decide upon.

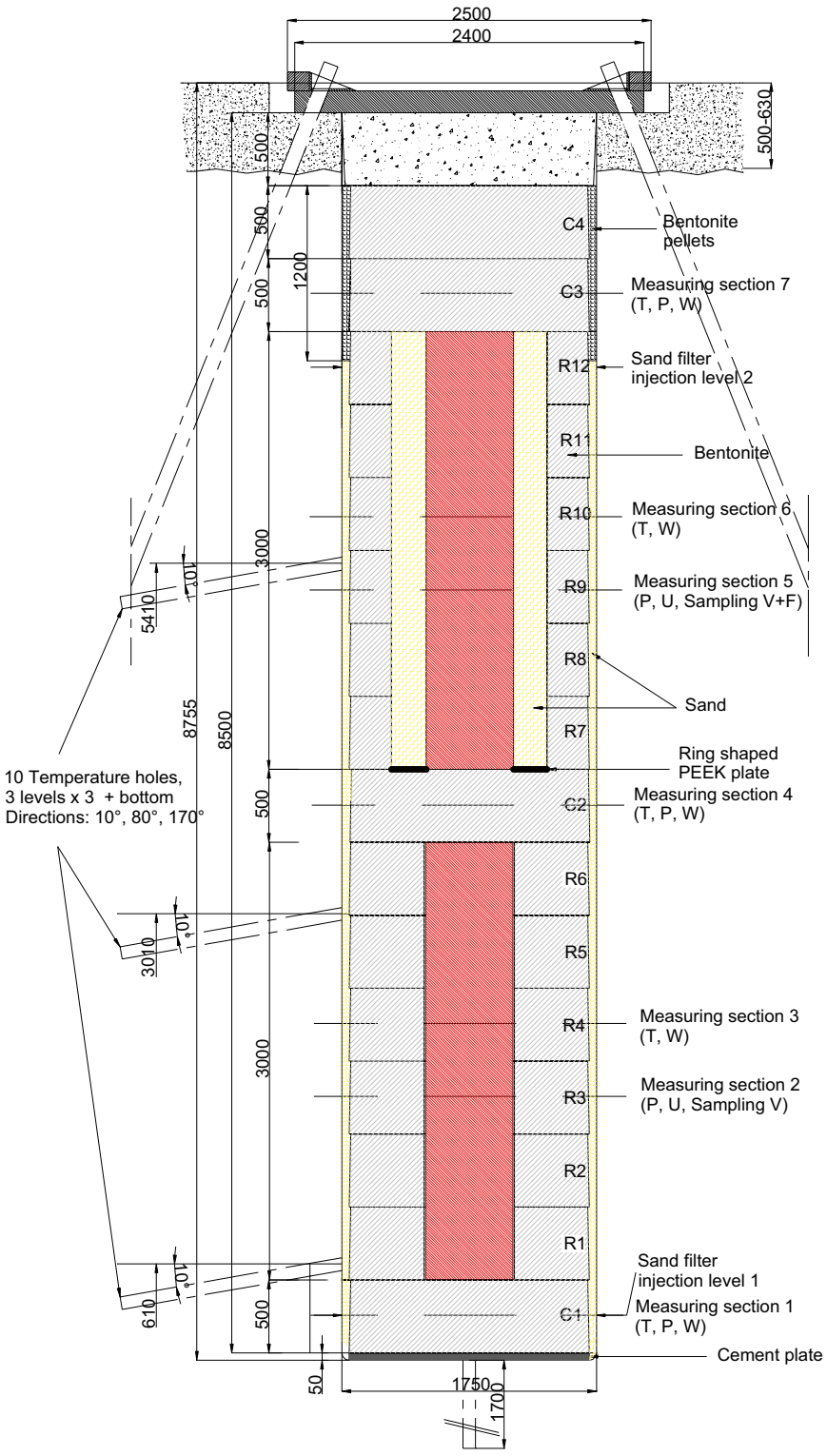

Figure 1-1. *Design of the TBT experiment.*

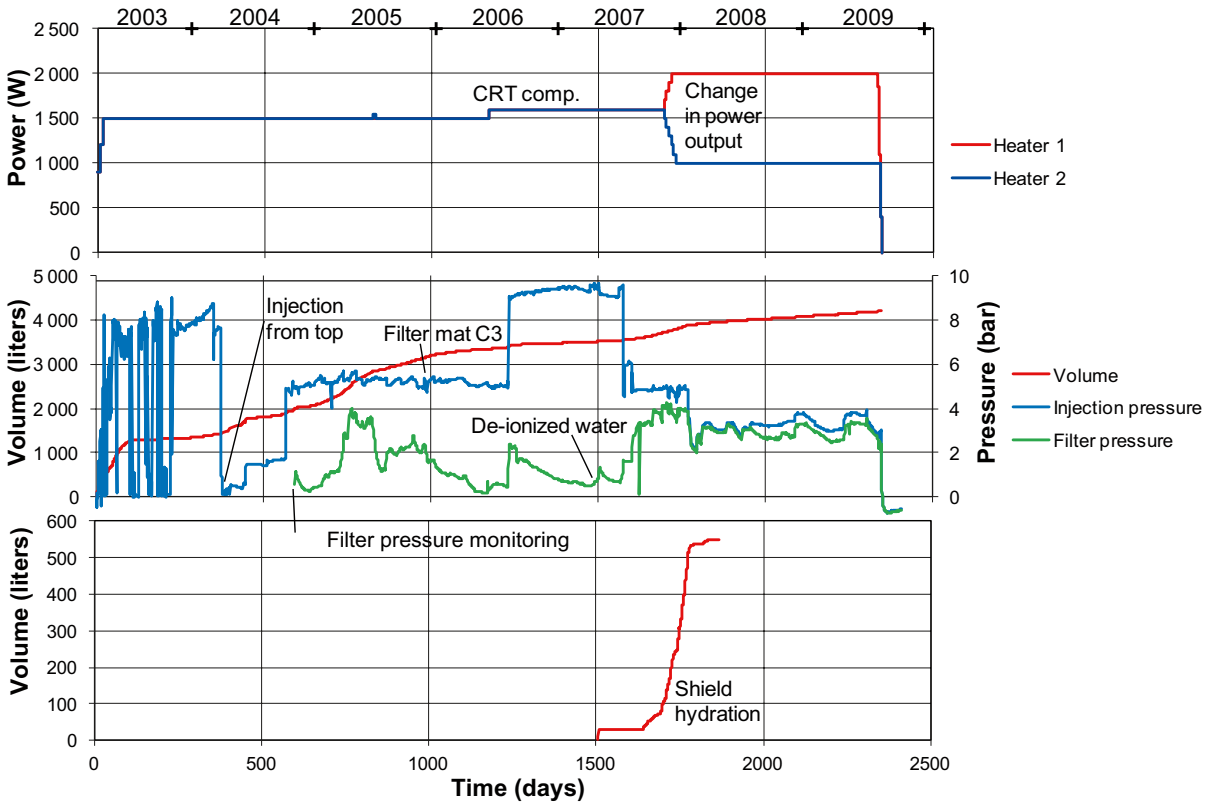

Figure 1-2. *Timeline of major events regarding power output (upper), filter injection system (middle); and shield hydration (lower).*

Three modelling groups have contributed to this final modelling effort: from UPC using CODE_BRIGHT and from Clay Technology, using CODE_BRIGHT and ABAQUS. The modelling groups have chosen different scopes and geometries based on their interest of processes, code capabilities, and other resources. A compilation of presented models is shown in Table 1-1. These contributions are reported in separate chapters in the current report.

The two final chapters focus on the discussion of the validity of experimental data and the material models. This also includes different evaluations and interpretations of the experimental data.

Table 1-1. Compilation of presented models. Number of models with different geometries and mechanical constitutive law.

Modelling team/code	Section	Time (yr)	Geometry				Processes[1]	Mechanical constitutive law			
			Ring 3/4	Ring 9/10	Upper part	All blocks		BBM	BBM mod[2]	BExM	PE/ DP[3]
UPC/ CODE BRIGHT	2.2	7	3	–	–	–	3 THMg	–	–	3	–
	2.3	2	–	–	–	1	1 THMg	1	–	–	–
	2.4	4/7	–	–	–	2	1 THMg; 1 THg	1	–	–	–
ClayTech/ CODE BRIGHT	3.2	7	14	–	–	–	10 THg; 4 THMg	–	4	–	–
	3.3	7	–	7	–	–	6 THMg; 1 THM	–	7	–	–
	3.4	0.5	–	–	4	–	4 HM	–	4	–	–
	3.5	7	–	–	–	1	1 THg	–	–	–	–
ClayTech/ ABAQUS	4	7	–	–	–	1	1 THM	–	–	–	1

1) THMg = Termo-Hydro-Mechanical with gas.

2) Modified BBM according to Åkesson et al. (2010b).

3) Porous-elastic with Drucker Prager.

2 Cimne-UPC contribution

2.1 Introduction

This chapter presents the modelling work performed by the Cimne-UPC team regarding the simulation of the field experiment Temperature Buffer Test defined by ANDRA (France) and conducted at Äspö Hard Rock Laboratory (Sweden). The modelling groups involved in the analysis of the TBT agreed to consider 3 main "tasks" for this final report, as proposed by the coordinator: analysis of the lower heater, analysis of the upper heater and, if possible, analysis of the whole experiment. All this 3 cases were considered by the CIMNE-UPC team, assuming different geometries and conditions, and they are briefly described here.

The first part of this chapter (section 2.2) presents the simulation of the behaviour of the bentonite barrier at the mid-height of the lower heater. The calculations were carried out using a reduced 2D axisymmetric geometry that only considers that section at the mid-height of the lower heater. As the geometry is small, it is possible to use more complex constitutive models than when analyzing the whole geometry and computing time remains reasonable. In this case, the mechanical response of the bentonite was simulated using a model specially developed to represent the behaviour of high expansive materials.

The second part of the chapter (section 2.3) presents a simulation attempting to explain the final state observed in the bentonite blocks at the upper part of the field experiment. Some preferential planes for cracking were observed in the bentonite when dismantling this part and a possible explanation is suggested. In this case a 2D axisymmetric geometry that does not include the rock mass was used in the analysis.

The third part of the chapter (section 2.4) presents an analysis of the entire test using a 2D axisymmetric geometry that includes an important part of the rock mass. In this case the geometry is more complex than in the previous analyses, but simpler constitutive laws have been employed.

The chapter ends up with the conclusions obtained from the different analyses. Each approach has advantages and drawbacks as it is usually very difficult to cope with all the features of a complex experiment like TBT in a single modelling effort. Finally, the chapter ends up with section 2.5, presenting some general conclusions from the three analyses described. An appendix including details of the models and the parameters involved has been included as section 2.6.

The finite element program CODE_BRIGHT has been used in all simulations. In this code, balance equations that govern the non-isothermal multiphase flow through deformable porous media are formulated following the compositional approach. That is, mass balance is performed for each species in the medium (solid, water and air). In addition to that, an equation for energy balance is established for the medium as a whole and the equation of momentum balance reduces to the conventional stress equilibrium equation. The details of the coupled THM formulation are described elsewhere (Olivella et al. 1994, 1996).

2.2 THM analysis of the lower part

2.2.1 Preface

One of the distinctive aspects of the TBT field experiment was that temperatures of about 150°C were reached at some particular points of the compacted bentonite blocks in correspondence with the mid height of the lower heater. This aspect represents a challenging problem, as most of the previous studies involved temperatures well below 100°C (Gens et al. 1998, Chen and Ledesma 2009). As a consequence, a detailed analysis of that zone of the experiment was proposed as a modelling task. The general guideline to carry out this work was to consider a reduced geometry that represents the zone in correspondence with the mid section of the lower heater.

The section describes the analyses and interpretation of the results at the lower part of the *in situ* test. In the first part, the geometry and boundary conditions as well as the parameters associated to specific constitutive laws are presented. Then, some selected observations together with the associated predictions of the numerical analyses are presented. It is important to highlight that different simulations were carried out in order to test the influence of some parameters in the obtained results; some of these simulations are also included at the end of this section.

2.2.2 Geometry and boundary conditions

The geometry and boundary conditions used in the analyses are shown in Figure 2-1. As it can be observed, an initial gap of 0.01 m between the heater and the bentonite block was considered in the numerical model. A temperature of 20°C and a liquid pressure of 0.1 MPa were applied as boundary condition at the rock end.

Initial temperature and gas pressure were assumed equal to 20°C and 0.1 MPa respectively. It was considered that the rock was saturated at the start of the test and an initial suction of 50 MPa was assigned to the other materials. An initial isotropic stress state of 0.2 MPa was considered and displacements were restricted in the perpendicular directions to the model edges.

A water flux was applied as hydraulic boundary condition at the outer sand. However, as a reduced geometry was adopted in the simulation it was not possible to define that flux using the experimental inflow values. Therefore, a trial and error process was applied to define the net water inflow. Although this aspect represents an approximation of the actual situation, the procedure is still valid to reproduce the main aspects of thermo-hydro-mechanical processes that define this kind of problems.

At the inner radius a thermal boundary condition was applied. The temperature evolution was assumed equal to that registered on the external surface and at the mid height of the lower heater (Figure 2-2). By using this 1D geometry, an infinite long heater is assumed implicitly and that may lead to overprediction of temperatures, away from the heater (in the rock) at large times.

2.2.3 Constitutive laws

Some constitutive laws used to simulate the behaviour of the bentonite blocks were updated taking into account the experience obtained from the TBT_3 mock-up experiment (Åkesson et al. 2009).

Soil water retention curve

Figure 2-3(a) presents the relation between degrees of saturation and suction obtained at steady-state conditions in the TBT_3 experiment. Note that under the experimental conditions, suction can apparently be zero – that is, the vapour is saturated – even though the bentonite is not water saturated. In the

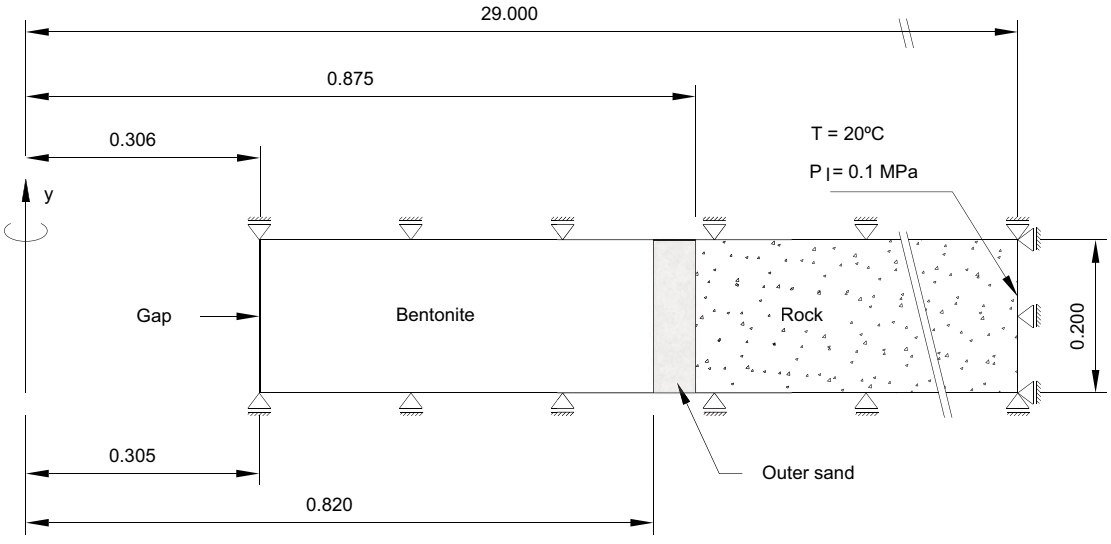

Figure 2-1. *Reduced 2D-axisymmetric geometry considered in the analysis.*

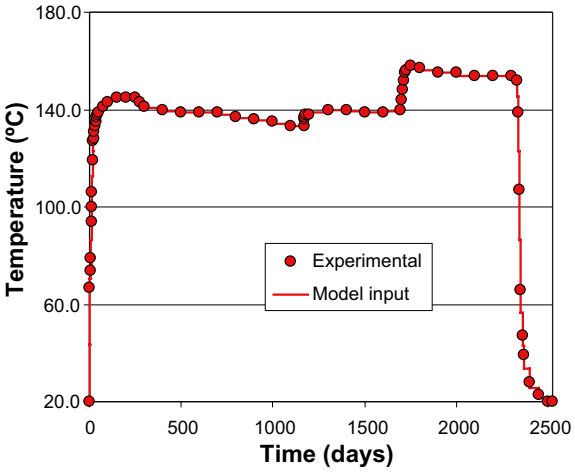

Figure 2-2. *Thermal boundary condition applied at the inner radius.*

figure the final dry densities measured after dismantling (in Mg/m^3) and the temperatures measured in steady-state conditions are also indicated. Retention capacity measurements from Villar et al. (2006), obtained in samples of the same material compacted at dry densities of 1.60 and 1.75 Mg/m^3 and tested at different temperatures, are included in the same figure. It can be observed that the general trend is the same for all the experimental results.

In this simulation, the following expression was adopted for the soil water retention curve

$$S_{le} = \frac{S_l - S_{lr}}{S_{ls} - S_{lr}} = \left[1 + \left(\frac{P_g - P_l}{P_0}\right)^{\frac{1}{1-m}}\right]^{-m} \cdot \left(1 - \frac{P_g - P_l}{P_d}\right)^{d} \qquad (2\text{-}1)$$

where S_{le} is the effective degree of saturation, S_l is the degree of saturation, S_{lr} and S_{ls} are the minimum and maximum degree of saturation respectively, P_g is the gas pressure, P_l is the liquid pressure, and m, P_0, d, and P_d are fitting parameters.

The maximum degree of saturation S_{ls} was defined taking into account the following aspects. On the one hand bentonite blocks in the zone close to the heater were subjected to very high temperatures (higher than in the TBT_3 test). Additionally, the water retention curve is the same for all the bentonite. Because of that a value equal to 0.9 was considered for S_{ls}. Table 2-1 presents the parameters used in equation (2-1) and the curve obtained is shown in Figure 2-3(b).

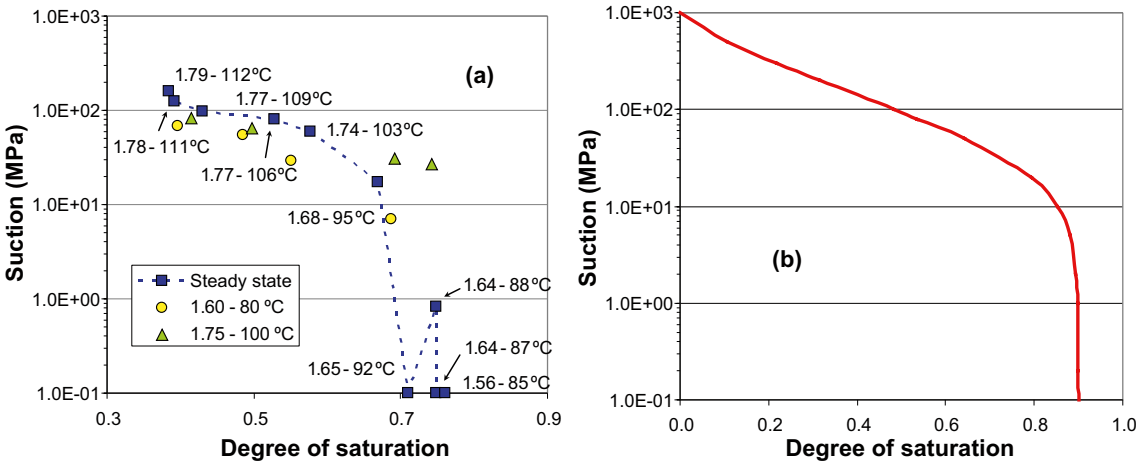

Figure 2-3. *(a) Suction against degree of saturation indicating steady state temperatures and measured dry densities (in Mg/m^3) after dismantling of TBT_3. (b) Water retention curve considered in the numerical analyses.*

Table 2-1. Parameters of the water retention curve used in the analysis.

P_0 (MPa)	m	S_{ls}	S_{lr}	P_d (MPa)	d
40.0	0.3	0.9	0.0	1,000.0	1.5

Nonadvective flux of water in the gas phase

In CODE_BRIGHT the nonadvective flux of water in the gas phase $\mathbf{i}_g^w$ is defined by the Fick´s law. The flux depends on the gradient of the mass fraction of water ω_g^w and on the hydrodynamic dispersion tensor $\mathbf{D}_g^w$

$$\mathbf{i}_g^w = -\mathbf{D}_g^w \cdot \nabla \omega_g^w \qquad (2\text{-}2)$$

The dispersion tensor $\mathbf{D}_g^w$ in that equation is given by the expression (Olivella and Gens 2000)

$$\mathbf{D}_g^w = \tau \phi \rho_g S_g \mathrm{D}_m^w \mathbf{I} \qquad (2\text{-}3)$$

where τ is the tortuosity parameter, ϕ is the porosity of the medium, ρ_g and S_g are the mass density and degree of saturation, respectively, of the gas phase, D_m^w is the molecular diffusion coefficient, and $\mathbf{I}$ is the identity matrix.

One of the parameters to be defined in equation (2-3) is the molecular diffusion coefficient D_m^w. The binary diffusivity is a function of the temperature and pressure, and near standard temperature and pressure conditions it can be expressed as (Massman 1998)

$$D_m^w = D_0 \frac{P_{g,0}}{P_g} \left(\frac{T}{T_0} \right)^n \qquad (2\text{-}4)$$

where D_0 is the diffusivity at $T_0 = 273.15$ K and $P_{g,0} = 101.325$ kPa, T is the absolute temperature, P_g the gas pressure, and n is a coefficient. For the diffusivity of water vapour in air, Massman (1998) proposes a D_0 value of $2.178 \cdot 10^{-5}$ m^2/s and n equal to 1.81. These coefficients are valid in a range of temperatures between –20°C and 100°C. Marrero and Masson (1972, cited in Massman 1998) suggest values of $2.090 \cdot 10^{-5}$ m^2/s and 2.072, respectively, for D_0 and n. These coefficients are also valid for temperatures above 100°C. Values for the coefficient n between 1.5 and 2.3 are also indicated in the literature (Chen and Othmer 1962, Seager et al. 1963, Pollock 1986). A coefficient n equal to 2.2 and a D_0 value of $2.1 \cdot 10^{-5}$ m^2/s were used in the analyses carried out in this work. This results in a variation with the temperature similar to that suggested by other researchers. Figure 2-4 presents the dependence of the molecular diffusion coefficient with the temperature for the coefficient indicated previously.

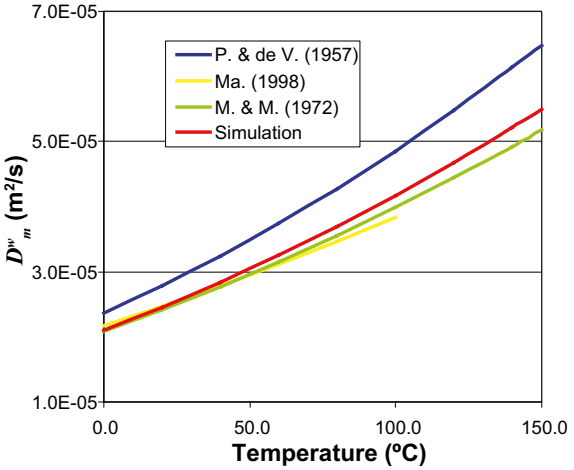

Figure 2-4. *Molecular diffusion coefficient against temperature.*

Philip and de Vries (1957) considered a value of 0.66 for the tortuosity coefficient τ, while Bear (1972) suggested that values varying in the range 0.56–0.8 can be considered. Hökmark (2004) obtained a value of 1.0 by fitting results of temperature gradient tests on MX-80 bentonite samples. A coefficient τ equal to 0.65 was adopted in the calculation.

It is important to emphasise that a combination of different values for the parameters n, D_0 and τ result in a similar variation of the dispersion coefficient [eq.(2-4)] with temperature.

Mechanical model

The Barcelona Expansive Model (BExM) originally proposed by Gens and Alonso (1992) has been used in this work to simulate the mechanical behaviour of the bentonite. The model was implemented in the finite element program CODE_BRIGHT (Sánchez 2004, Sánchez et al. 2005). It assumes that in the material fabric it is possible to define the macrostructural level that is responsible for major structural rearrangements and the microstructural level where swelling of the active minerals takes place (Figure 2-5). A detailed description of the model is presented elsewhere (Gens and Alonso 1992, Alonso et al. 1999, Sánchez 2004, Sánchez et al. 2005).

Mechanical parameters have been obtained from the interpretation of experiments performed on MX-80 bentonite samples and reported in the literature (Villar 2005, Tang et al. 2008). The interaction functions are similar to those adopted in previous analyses to simulate the response of expansive clay (Lloret et al. 2003). Table 2-2 presents the parameters used to define the macrostructural behaviour, and Table 2-3 indicates those corresponding to the microstructural behaviour. An initial value of p_0^* equal to 8.0 MPa was considered. Parameters used are the same as those adopted in the analysis of the TBT_3 mock-up experiment.

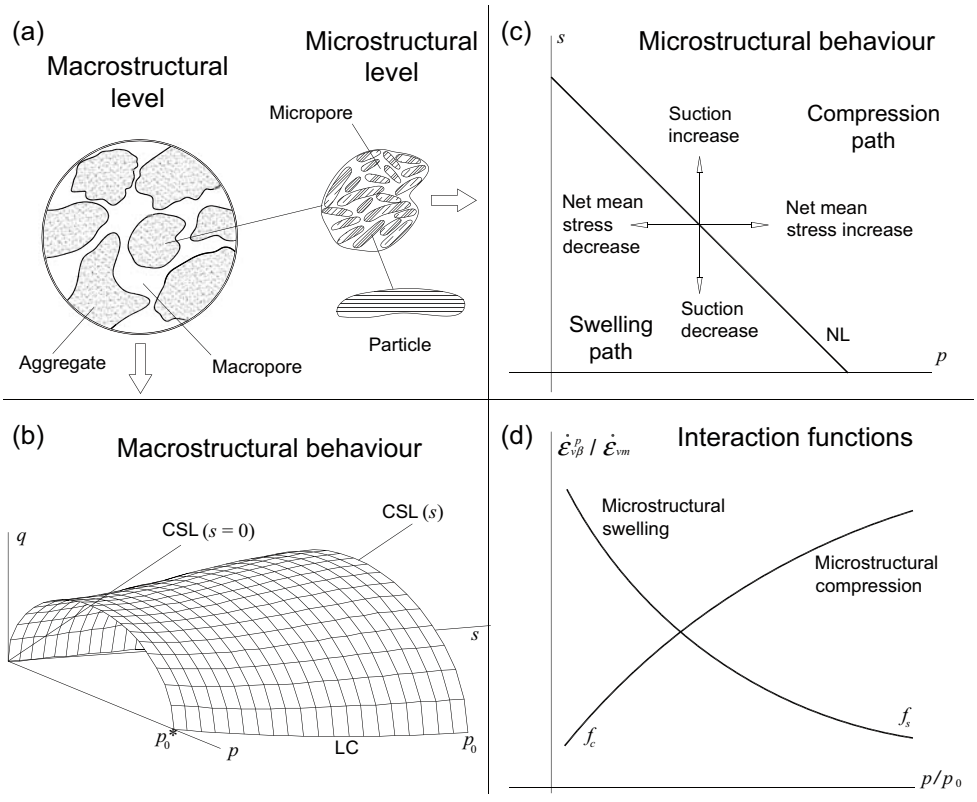

Figure 2-5. *(a) Structural levels in a fabric of a compacted bentonite. (b) Three-dimensional view of the BBM yield surface (macrostructural behaviour). (c) Compression and swelling regions separated by the NL (Neutral Loading) line (microstructural behaviour). (d) Interaction functions (coupling between micro and macrostructure).*

Table 2-2. Parameters for the mechanical model (macrostructural behaviour).

κ_{i0}	0.018	λ_0	0.25
r	0.75	β	0.10
p_r (MPa)	0.5	κ_s	0.001
α_0 ($^oC^{-1}$)	$-1.0\cdot10^{-4}$	α_1 [MPa·(C^o)$^{-1}$]	$-1.0\cdot10^{-4}$

Table 2-3. Parameters for the mechanical model (microstructural behaviour).

α_m (MPa^{-1})	$1.8\cdot10^{-2}$	β_m (MPa^{-1})	$1.8\cdot10^{-3}$
Interaction functions			
$f_c = 1.1+0.9\ \tanh[10(p/p_0-0.45)]$		$f_c = 0.9-1.1\ \tanh[10(p/p_0-0.45)]$	

2.2.4 Test observation and interpretation

Representative test observations concerning the behaviour of the engineered barrier are presented. Predictions of the numerical analysis are plotted alongside the test observations to assess the performance of the model. The analysis reported in this paragraph is assumed as the Base Case (BC).

Experimental data correspond to instrument readings obtained in the field (temperature, relative humidity and total stress) and laboratory values deduced from samples collected during the dismantling operation (dry density and degree of saturation).

Thermal results

Figure 2-6 presents the temperature values at different radial distances from the axis of the hole. As it can be seen, experimental data are well reproduced at the inner part of the engineered barrier. At the outer part, as the water content increases calculated results become higher than the experimental ones. Also, it should be taken into account that the geometry considered replicates an infinite long heater, which may lead to overpredicting temperatures in the rock at large time.

Hydraulic results

In Figure 2-7 experimental values of relative humidity at different radii are shown. In general, numerical results reproduce the main aspects of the observed behaviour. At the start of the test, there is an increase of relative humidity all along the barrier due to an increase of the vapour content. This effect is quite small so it can not be seen in the figure. After that, the increase of temperature originates

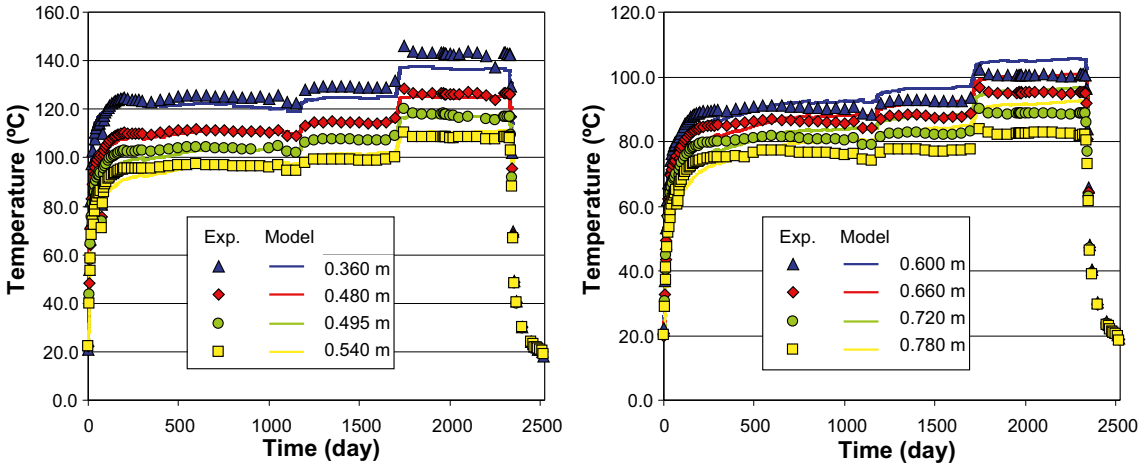

Figure 2-6. Evolution of temperature in bentonite barrier, observations and computed results. Base Case.

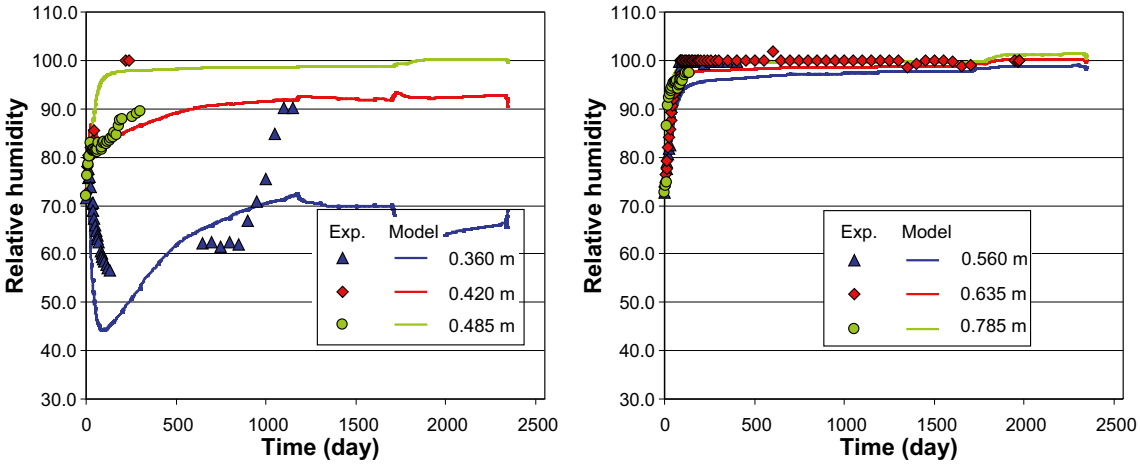

Figure 2-7. *Evolution of relative humidity in bentonite barrier, observations and computed results. Base Case.*

drying of the material closer to the heater and hydration of the middle and outer barrier zones because of the condensation of vapour coming from the inner region. Finally, the water injected to the barrier causes the increase of relative humidity within the barrier.

The experimental distribution of the degree of saturation in the bentonite blocks is shown in Figure 2-8. At the inner region an average value of 0.92 was obtained while in the zone close to the outer sand the material is saturated.

Calculated values of the degree of saturation in correspondence with the external radii are the maximum possible according to the water retention curve considered in the analysis. The differences at the inner zone are also due to the water retention curve used in the analysis as it will be seen later. In fact model degree of saturation and real degree of saturation are different by construction. Nevertheless, in section 2.2.5, additional analyses are presented in order to improve this comparison.

Mechanical results

Figure 2-9 compares results for the total stresses at different radii and in different directions within the engineered barrier.

The slower development of the measured swelling stresses at the inner part in the radial and axial directions may be due, at least in part, to the initial gap between the canister and the bentonite. Also the rigidity of the outer sand influences the deformation (swelling) of the bentonite blocks and consequently the stress level which can be developed within them.

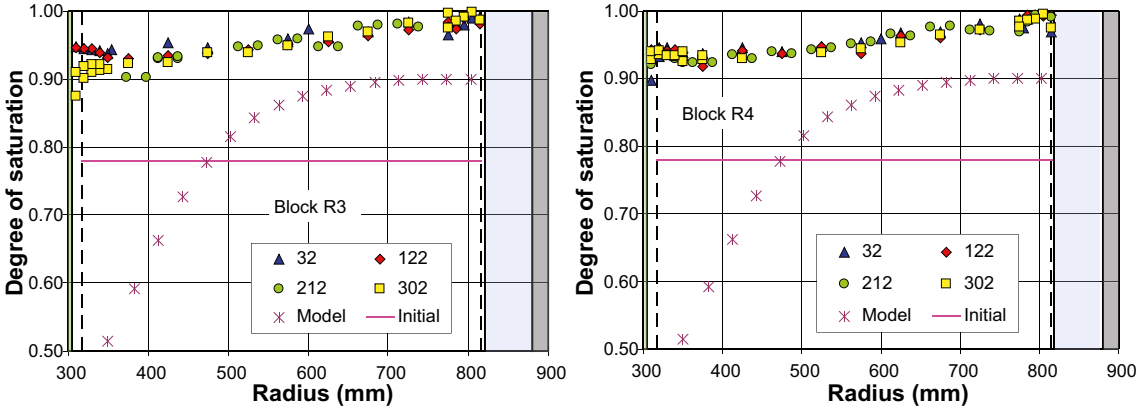

Figure 2-8. *Distribution of degree of saturation in bentonite barrier, observations and computed results. Base Case.*

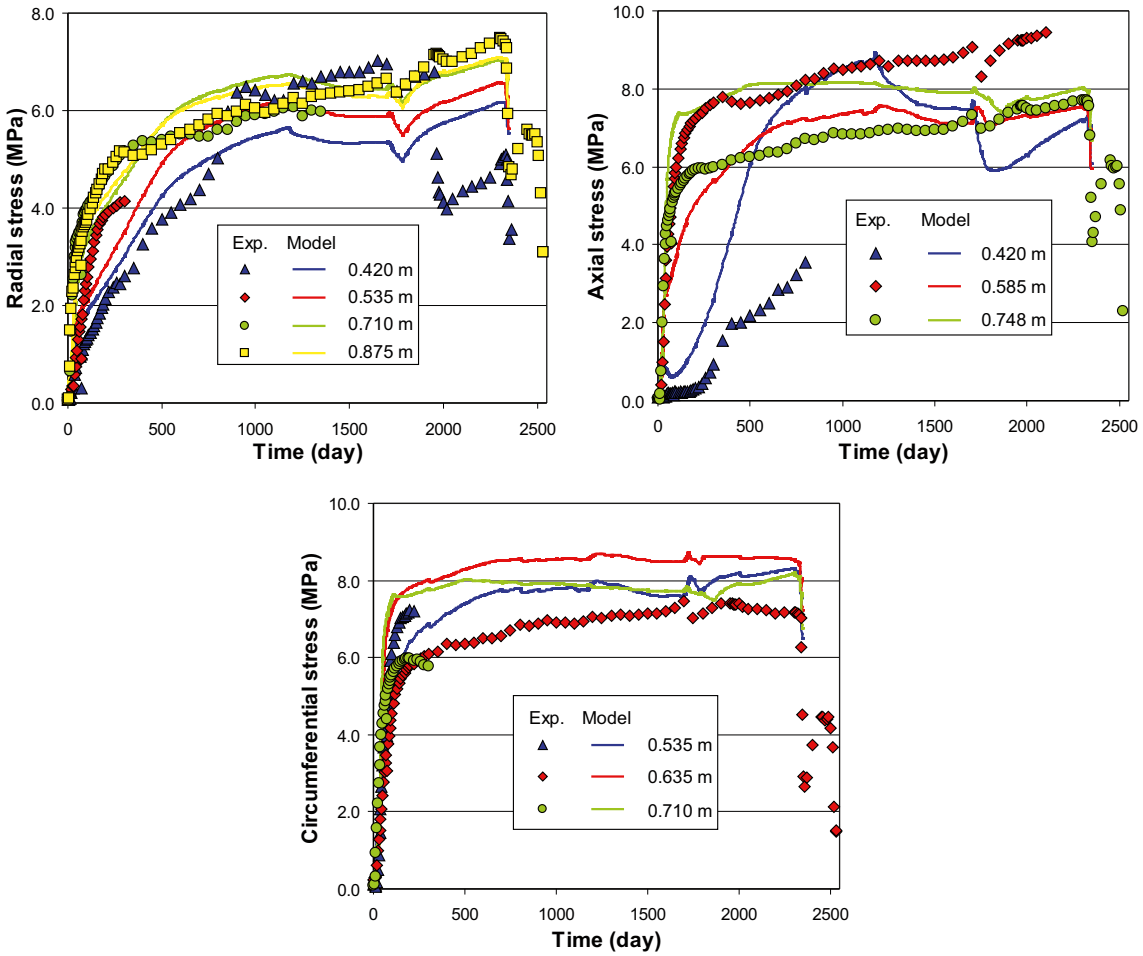

Figure 2-9. *Evolution of stresses in bentonite barrier, observations and computed results. Base Case.*

Figure 2-10 presents values of dry density obtained after the dismantling of the *in situ* test compared with those obtained in the simulation. Although the mechanical model is able to reproduce the swelling of the bentonite blocks at the outer zone, there exist differences between the simulated values and experimental data.

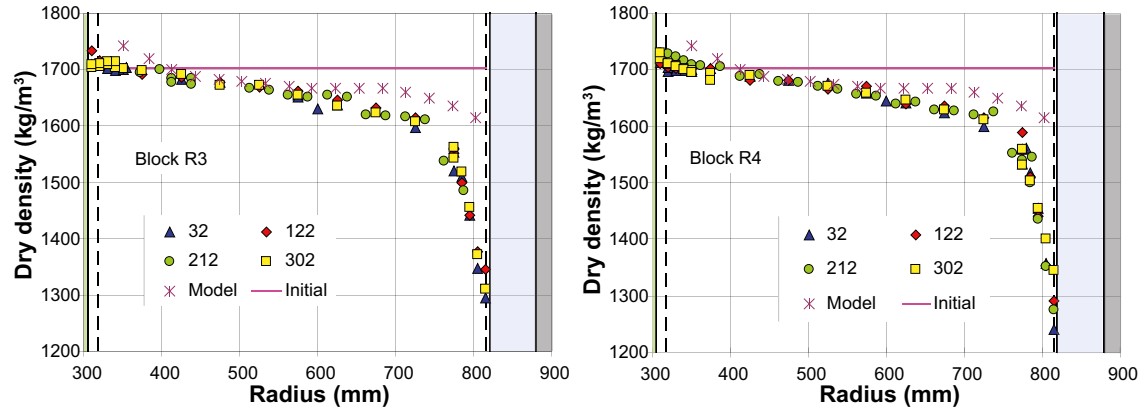

Figure 2-10. *Distribution of dry density in bentonite barrier, observations and computed results. Base Case.*

2.2.5 Additional analyses

As part of this task a series of analyses were conducted to test the influence of some parameters on the final results. Two of them are included in this section and the results are discussed below.

Case 1

The main objective of this analysis was to verify the effect of a change in the water retention curve. It is well known that the simulations are very sensitive to this curve due to the logarithmic dependency on suction. Parameters were adopted in order to obtain a curve similar to that shown in Figure 2-3(b) but using a maximum degree of saturation S_{ls} equal to one. Because of the change in the distribution of the degree of saturation along the barrier the obtained stress resulted excessively high. Therefore, it was necessary to modify the parameter κ_p of the mechanical model; a value of 0.025 instead of 0.018 was adopted. Results obtained are presented below using the same order as in the Base Case.

Thermal results

Figure 2-11 presents the evolution of temperature at different radii within the barrier. During the first part of the test numerical values are lower than the experimental ones. In general, only measured data at the inner radii are well reproduced by the model. As the radial distance from the heater increases the difference between the obtained results and the experimental values of temperature also increases. An explanation to this discrepancy is the use of a 1D geometry for the thermal inner boundary condition, simulating an infinite long heater. That leads to overpredicting temperature away from the heater (i.e. in the rock). However this effect seems to be more important in this case if compared with the Base Case. Then the influence of the water retention curve adopted should be considered. Indeed higher degree of saturation at the inner part may induce a higher heat flux towards the outer parts and a consequent increase of temperature.

Hydraulic results

Figure 2-12 shows numerical and experimental values of relative humidity at different radii. In general, this Case reproduces the measured values corresponding to the inner radii in a better way.

The variation of the degree of saturation along the barrier is better than that obtained in the Base Case (Figure 2-13). The main reason for the improvement is the use of a different water retention curve. In addition to that, the water inflow in the outer sand used in all these 1D analyses was obtained by a trial end error procedure as described in section 2.2.2 and a small error could be expected for that process.

In general, hydraulic results are better reproduced in this Case.

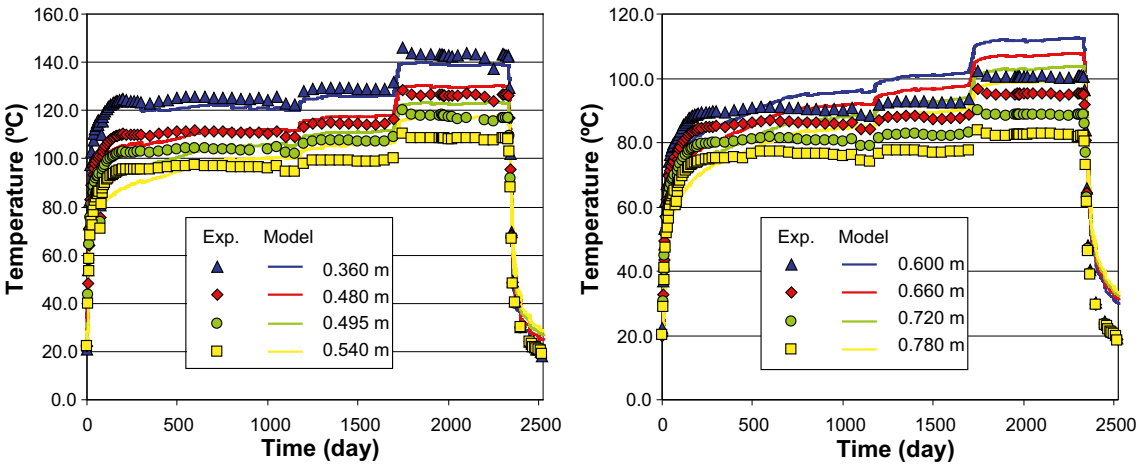

Figure 2-11. *Evolution of temperature in bentonite barrier, observations and computed results. Case 1.*

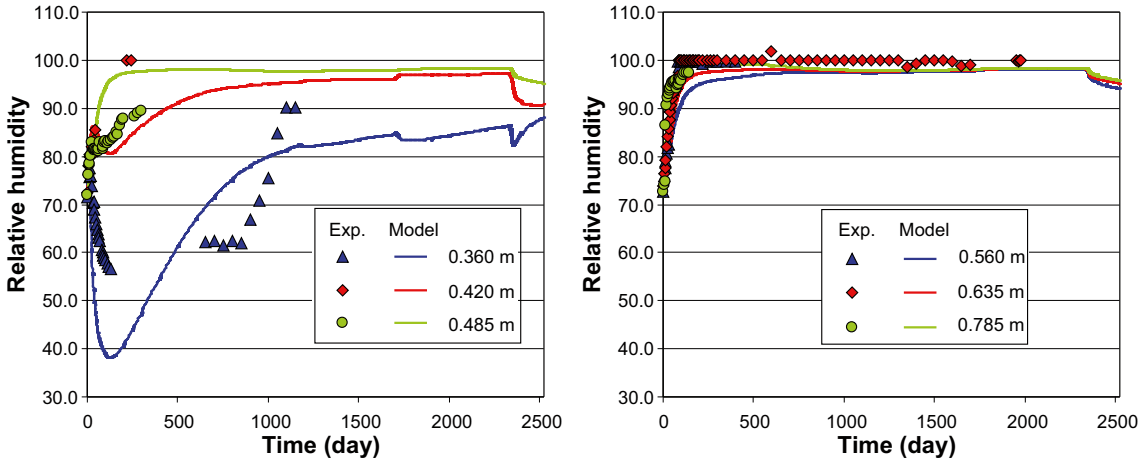

Figure 2-12. *Evolution of relative humidity in bentonite barrier, observations and computed results. Case 1.*

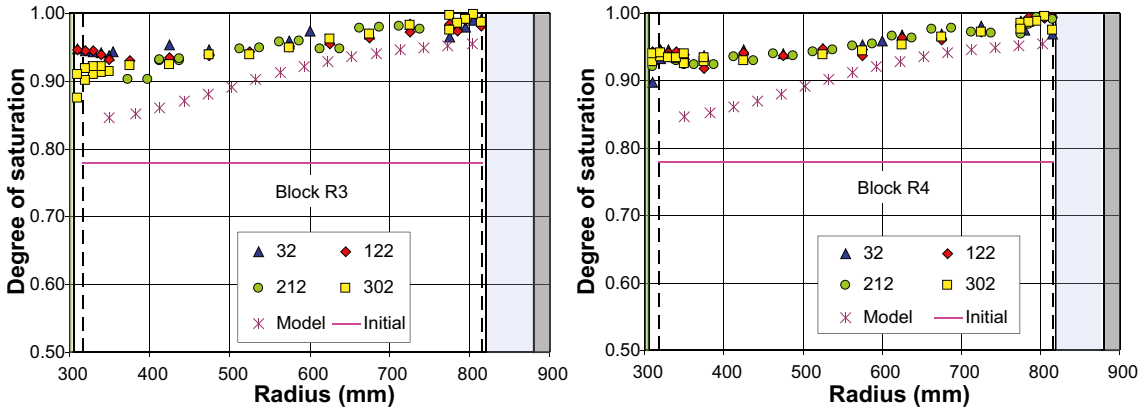

Figure 2-13. *Distribution of degree of saturation in bentonite barrier, observations and computed results. Case 1.*

Mechanical results

Figure 2-14 indicates that numerical values of stresses obtained for all directions are not only lower than the measured data but also than those corresponding to the Base Case. An exception occurs with the axial value of stress obtained at a radius of 0.420 m; it can be explained because as the degree of saturation (suction) in this zone is higher (lower) than in the Base Case the swelling of the bentonite is more important.

Figure 2-15 compares measured and calculated values of dry density along the barrier. As in the Base Case, there exist differences between values from the simulation and experimental data in the zone close to the outer sand.

Case 2

The influence of the stiffness of the outer sand in the obtained results was evaluated in this Case. In the Base Case the elastic modulus of the outer sand was assumed equal to 200 MPa while in this Case a value of 50 MPa was considered.

Thermal results

Numerical values and experimental data of temperature are shown in Figure 2-16. The pattern of the simulated results is similar to that corresponding to the Base Case. It seems therefore that the elastic modulus of the outer sand does not affect the thermal results.

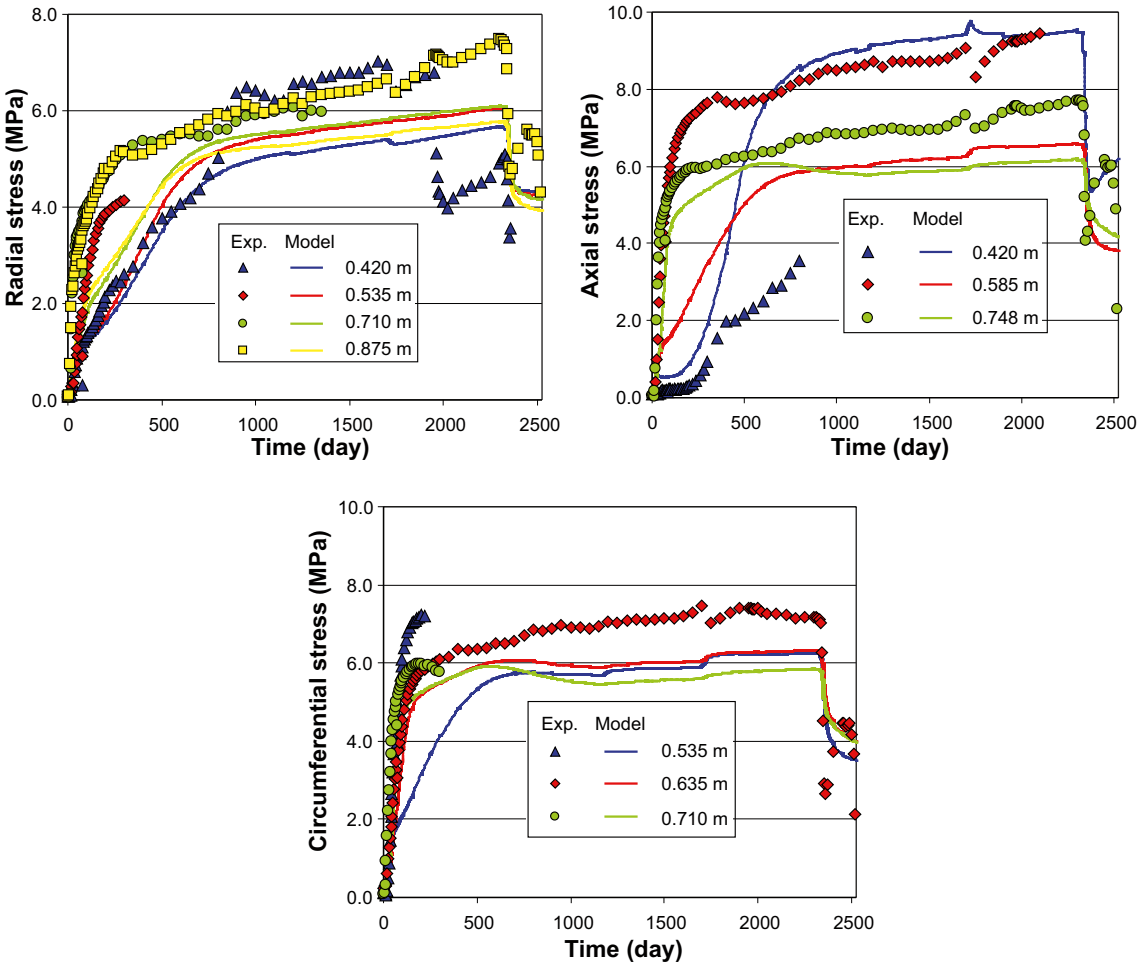

Figure 2-14. *Evolution of stresses in bentonite barrier, observations and computed results. Case 1.*

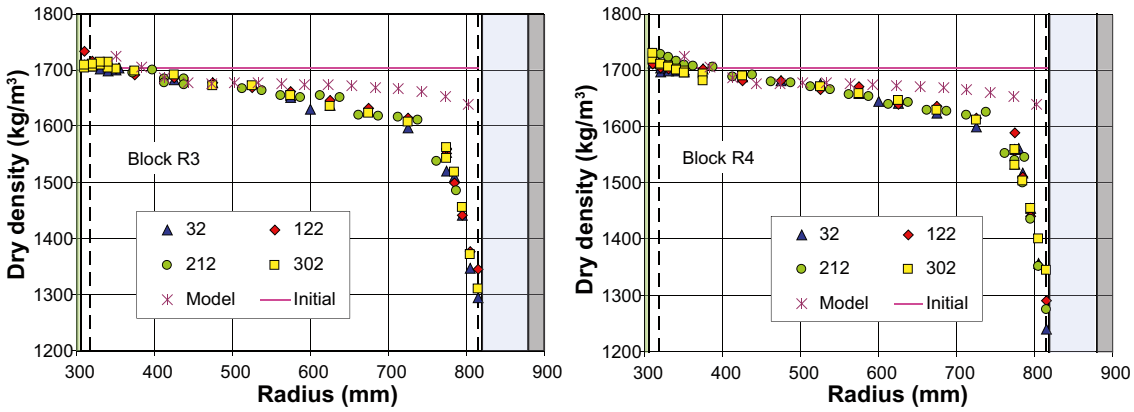

Figure 2-15. *Distribution of dry density in bentonite barrier, observations and computed results. Case 1.*

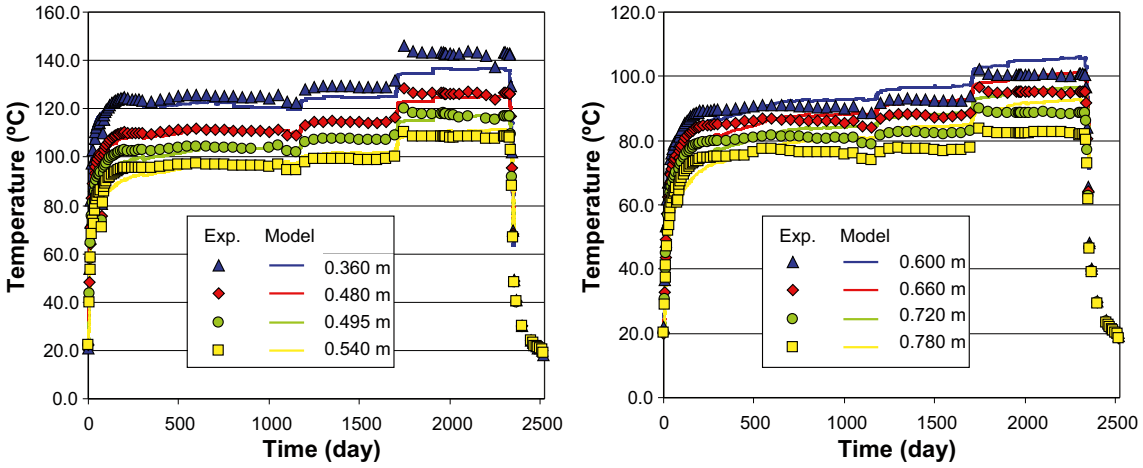

Figure 2-16. *Evolution of temperature in bentonite barrier, observations and computed results. Case 2.*

Hydraulic results

Figure 2-17 suggests that a change in the value of the elastic modulus of the outer sand does not produce appreciable changes in the numerical results of relative humidity when compared to the Base Case.

The final distribution of degree of saturation is similar to that obtained in the Base Case. It is important to highlight that the same water retention curve was adopted in both cases.

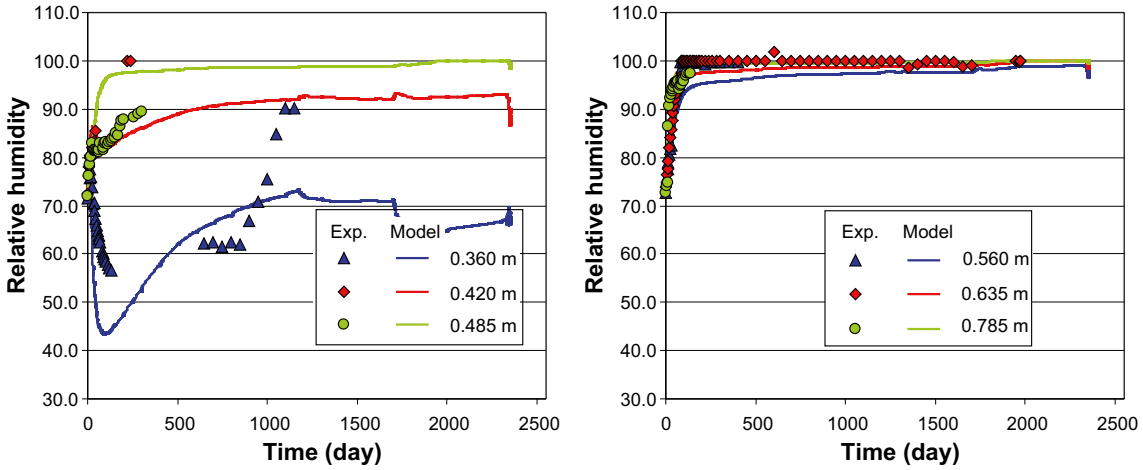

Figure 2-17. *Evolution of relative humidity in bentonite barrier, observations and computed results. Case 2.*

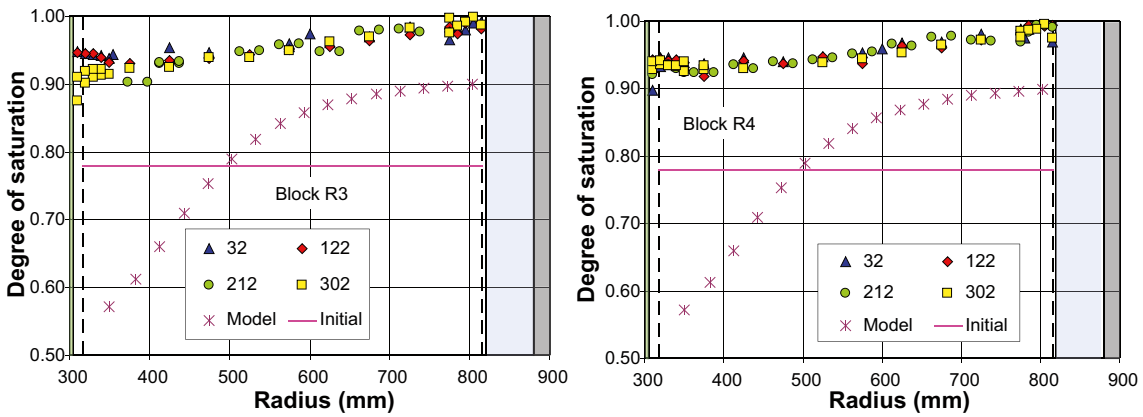

Figure 2-18. *Distribution of degree of saturation in bentonite barrier, observations and computed results. Case 2.*

Mechanical results

Figure 2-19 indicates that the numerical values of the radial and circumferential stresses decrease as the stiffness of the outer sand decreases. This result confirms that the stress evolution within the barrier depends on the level of confinement. This aspect should be carefully considered during the collocation of the sand in this kind of disposal design.

Figure 2-20 indicates that there is not difference between numerical results of dry density for this Case and those obtained in the Base Case.

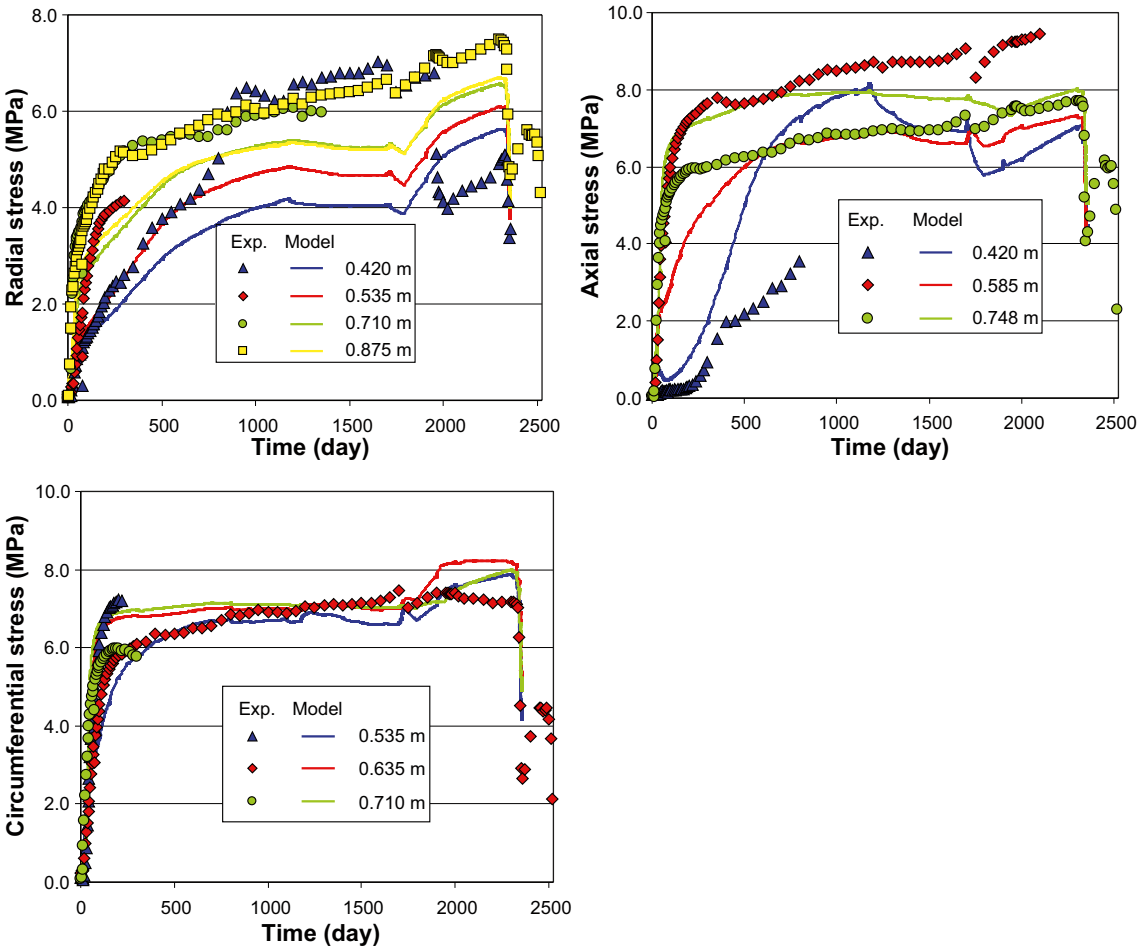

Figure 2-19. *Evolution of stresses in bentonite barrier, observations and computed results. Case 2.*

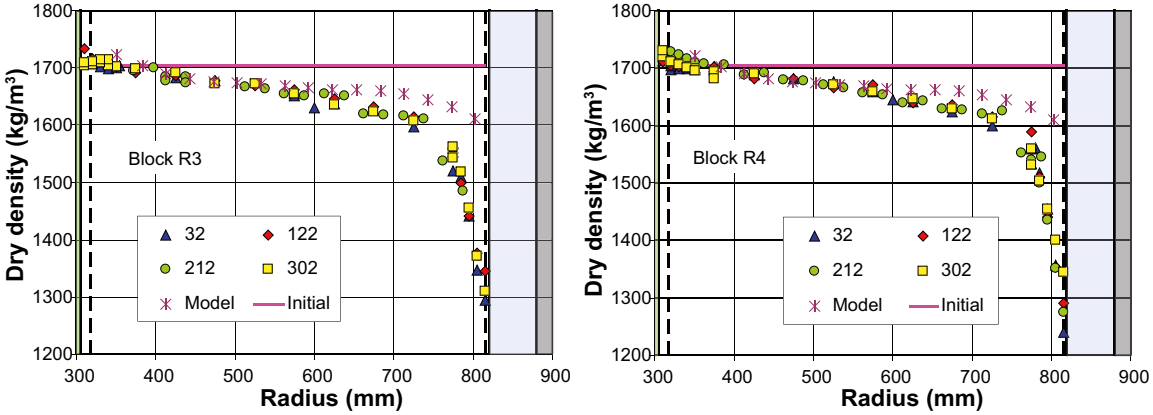

Figure 2-20. *Distribution of dry density in bentonite barrier, observations and computed results. Case 2.*

2.2.6 Concluding remarks

The section describes the numerical simulations carried out to analyse the response observed at the lower part of the *in situ* test. A reduced 2D-axisymmetric geometry was used and specific aspects of some constitutive laws developed in the framework of the Project were included in the analyses. Many simulations were carried out to analyse the influence of some parameters on the final results. Numerical analyses assisted in the interpretation of the observed behaviour.

Numerical simulations were performed using a finite element code that solves the governing equations corresponding to THM coupled problems. In general, temperature and relative humidity results were able to reproduce the tendency of the variables measured during the experiment. Temperatures were overpredicted in the rock at large times due to the 1D geometry and inner thermal boundary condition considered. Also, when a maximum degree of saturation equal to 0.9 was considered for the water retention curve, discrepancies appeared between the distribution of the degree of saturation obtained from the calculation and that resulting after dismantling.

The Barcelona Expansive Model was considered as a constitutive law appropriate for simulation of the mechanical behaviour, because it accounts for the double structure that can be found in compacted samples of bentonite (micro- and macrostructure). Although the geometry adopted introduces some limitations, the model previously implemented in the finite element code allowed reproducing the measured stresses reasonably well. Mechanical parameters were deduced using data from the literature for the MX-80 bentonite and are the same as those used in the TBT_3 simulation.

Major differences between the porosity distribution measured along the barrier at the end of the test and that resulting from the simulation are observed in the zone close to the interface between bentonite blocks and outer sand. It is important to highlight that the porosity evolution is influenced by the compressibility of the outer sand as well as the initial gap existing between the canister and the bentonite blocks.

In general, the good agreement between numerical simulations and measurements indicates that the main THM mechanisms involved in the behaviour of compacted bentonite barrier have been taken into account. In particular, this analysis presents: (a) the use of the Barcelona Expansive Model for MX-80 bentonite; (b) the application in the diffusive flow term of updated parameters to take into account the effect of high temperatures; (c) the use of a non-conventional water retention curve for MX-80 at high temperature.

Results from Case 1 permits to conclude that the major effect due to the water retention curve used in the simulation is on thermo-hydraulic variables. Results suggest that for a water retention curve with a maximum degree of saturation equal to one the values of temperature increase considerably at the outer zone of the bentonite barrier. On the other hand, the evolution of relative humidity improves in correspondence with the inner radii.

Analysis of Case 2 indicates that a change in the elastic modulus of the outer sand mainly affects the numerical values of stress in some directions. This result suggests that the confinement level due to the outer sand influences the stress evolution within the bentonite blocks. On the other hand, it seems that the numerical values of the thermo-hydraulic variables are independent of the stiffness of the outer sand.

2.3 THM analysis of the upper part

2.3.1 Preface

During the dismantling of the field test it was observed that bentonite blocks at the upper part of the barrier presented important cracks. It is believed that the origin of those cracks could be related to the stress and suction cycles that were registered at the mid-high of the lower heater (R9 & R10) between days 200 and 400 (Figure 2-21).

Vertical straight lines in Figure 2-21 correspond to the time when the lower (orange) and higher (violet) values of suction within the cycle were registered. It is evident that at the time when suction started to increase stress values showed a change in their tendency. After a time, suction reached

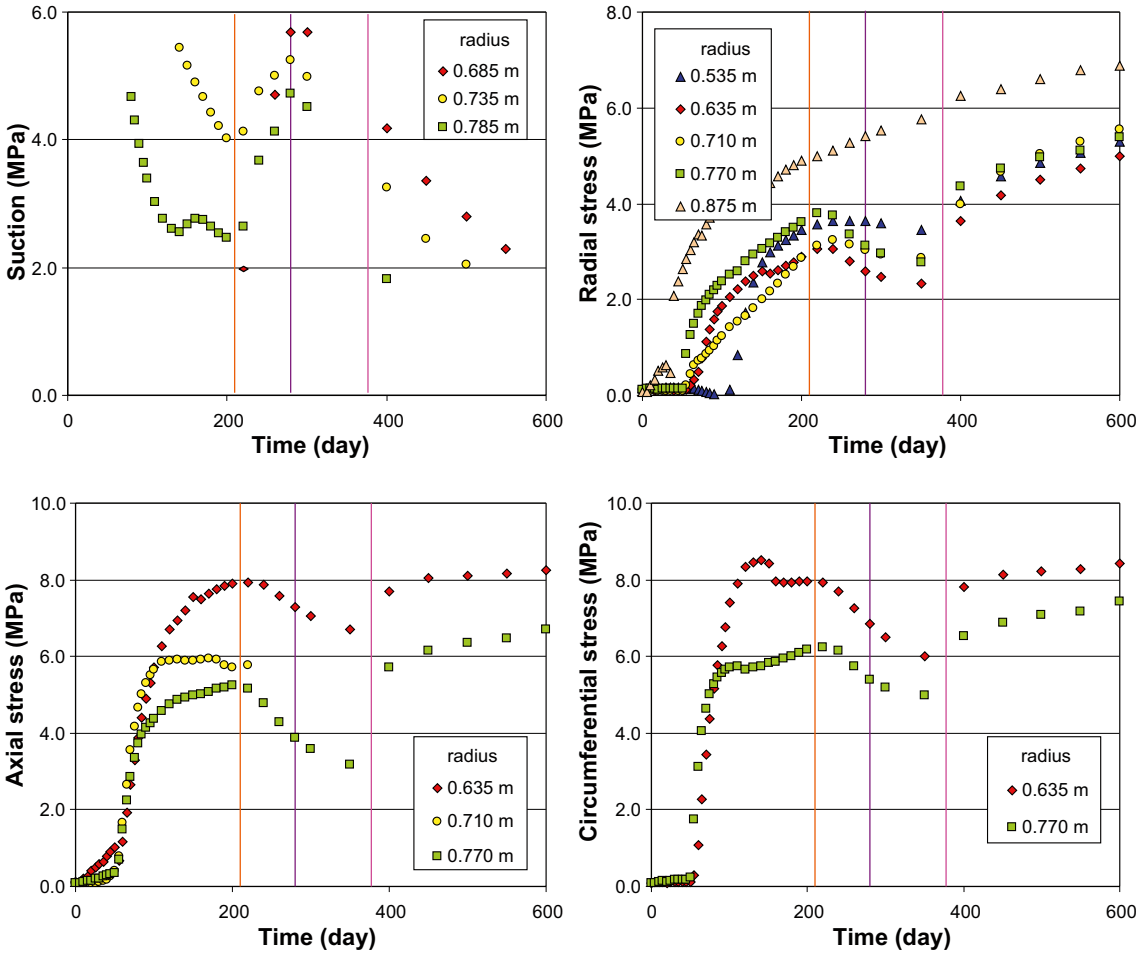

Figure 2-21. *Cycles of suction (R10) and cycles of stresses (R9) measured at the start of the test.*

a maximum and began to decrease again. However, stress sensors at that time did not show any change in the tendency of registered values. Only when water was also injected through the upper pipes (pink vertical lines in Figure 2-21), stress sensors registered an increase in the measured values.

The unexpected behaviour of R9 & R10 deserved special attention. One of the first tasks was to check if under normal conditions that cycle could be due to the normal behaviour of the sand-bentonite system, or to an anomalous application of the hydraulic boundary condition. The following explanations were considered at the beginning of the analyses:

a) The cycles of stresses may be due to a mechanical effect of the sand-bentonite system. Bentonite swells and generates compression everywhere, including the sand filter and the sand shield. A sudden deformation of the sand (i.e., a collapse created by wetting an initial unsaturated state under loading), may release stresses in the bentonite for a period of time. The further hydration of the bentonite would increase again the stresses everywhere. Expanding the bentonite due to a stress release, would increase void ratio and suction for a while, and that would explain the measured suction cycle.

b) The cycle of suction may be due to a lack of water available for hydrating the bentonite. The reason could be of a practical nature (i.e. a problem in the water supplying system, etc). Bentonite stops swelling and even may shrink a bit when water is taken out. That would explain the cycle in stresses as well.

After many analyses, it was concluded that the behaviour of R9 & R10 during that period of the experiment could be explained by a lack of water available in the sand filter (especially after day 100th). The alternative “b” indicated above seems to be more realistic than the explanation “a”, based on the mechanical response of the system sand-bentonite-sand.

However, it was also suggested in the report by UPC (Åkesson 2006), that there is little experience in this combined system including different materials in the context of THM problems. Indeed in most of the *in situ* or mock up experiments the bentonite is confined between a heater and the rock. Stresses usually develop due to swelling of the bentonite, in a quite homogeneous manner, and final state should be mainly isotropic.

At the beginning of the field test, however, axial and circumferential stresses at R9 exhibited a higher value than radial stresses due to the confinement of other rings. From the records of stresses in different directions in R9, it was possible to obtain the stress path followed by some points during the experiment. Figure 2-22 presents those paths, where it becomes evident that deviatoric stresses developed at the beginning of the experiment. The final trend is a decrease in shear, which may indicate eventually a development of isotropic confinement.

Straight dashed lines in Figure 2-22 indicate the critical state lines for internal friction angles of 20º and 25º, and a suction value equal to the lower one registered at the start of the cycle in correspondence with each radius. Crosses in this Figure represent the same instant of time as the straight lines showed in Figure 2-21.

The origin of the behaviour shown in Figure 2-22 could be attributed to the low confinement provided by the sand shield and sand filter. Also another source of this response could be the presence of gaps. In both situations the stress state may be anisotropic because at the beginning the bentonite can swell in one direction whereas in the other directions the confinement is effective.

The first part of the chapter describes the geometry and boundary conditions used in the analysis. A comparison between numerical results and measured values is then carried out. Finally, conclusions obtained from this analysis are presented.

2.3.2 Geometry and boundary conditions

The main objective of this analysis was to study the behaviour at the upper part of the engineered barrier in order to give an explanation about the final state observed at the bentonite blocks located at this zone. Taking into account this aspect, it was decided to adopt a geometry able to reproduce the main characteristics of the global response but with a reasonable computational effort. Because of that, a 2D-axisymmetric geometry which does not include the rock mass was used in the analysis (Figure 2-23).

Because cycles of suction and stresses were registered between days 200 and 400, only 600 days were considered in the analysis.

The thermal boundary applied to the heaters was a power which reproduces the protocol used in the test (Table 2-4). The power per unit length of heater is computed and the used as boundary condition in CODE_BRIGHT. The instant of switching the heaters on is taken as time zero. The steel of the heaters are modelled in the geometry.

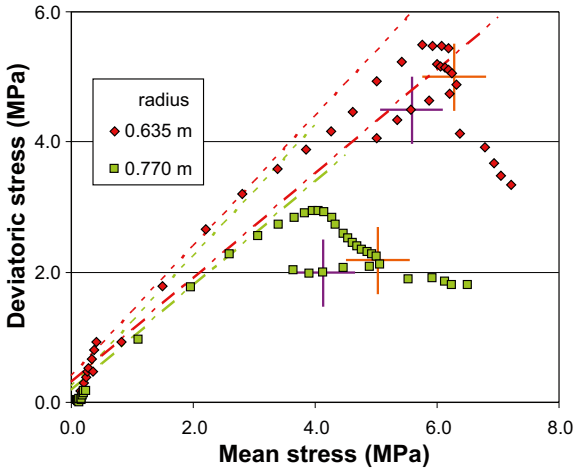

Figure 2-22. *Values of deviatoric stress against mean stress calculated from the measured stresses in different directions.*

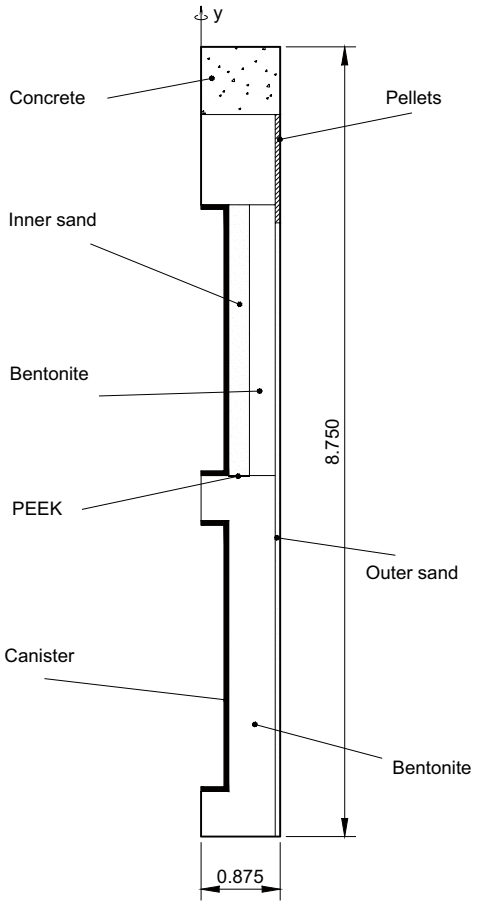

Figure 2-23. *2D-axysimmetic geometry used in the analyses.*

Table 2-4. Power applied on each heater in the field test.

Time (days)	Power (W)
0–8	900
8–15	1,200
15–600	1,500

Hydraulic boundary conditions were defined on the outer sand. It was considered that some nodes at the top of the sand filter were connected to the atmosphere at the beginning, in order to account for the effect of the open pipes as in the field test. A fixed gas pressure of 0.1 MPa was considered until day 377 and, after that, a water flux was applied on them. Also, a water flux was applied at the bottom of the outer sand. As the total water inflow instead of the inflow on each pipe was registered in the field test some assumptions were made to calculate the liquid flux applied to the nodes of the model. During the first 377 days, the water flux to be applied at the lower part of the outer sand can be well defined. Since then, it was assumed that the water flux is the same in the upper and lower pipes. Figure 2-24 shows the distribution of the inflow water between the upper and lower pipes during the period considered in this study.

The thermal and hydraulic boundary conditions at the upper edge of the model were defined by fixing the values of the temperature, and the gas and liquid pressures. Those values were assumed equal to 20°C and 0.1 MPa respectively.

The influence of the rock mass on the thermo-hydraulic response was considered by applying suitable thermal and hydraulic boundary conditions on the right and lower edges of the model. This was

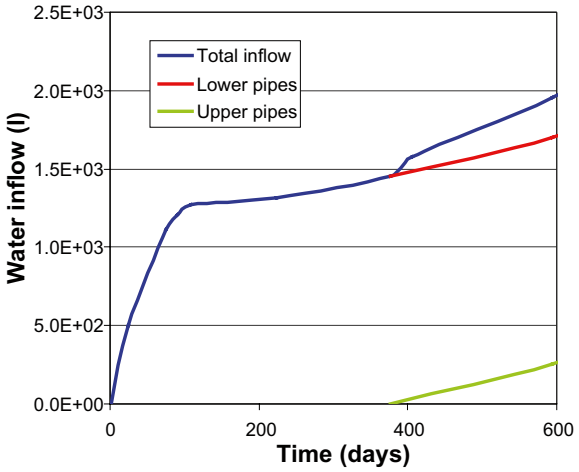

Figure 2-24. *Measured total water inflow and distribution between the upper and lower pipes used in the simulations.*

achieved by using a capability of the CODE_BRIGHT program. In this code, the boundary conditions for mass balance equations are incorporated by adding a flux (Olivella et al. 1996). When the pressure in the β phase is fixed, the mass flux of a species α as a component of this phase is

$$j_\beta^\alpha = \left(\omega_\beta^\alpha\right)^0 \gamma_\beta \left(P_\beta^0 + \Delta P_\beta^0 \frac{dt}{\Delta t} - P_\beta \right) \qquad (2\text{-}5)$$

with P_β the pressure in the β phase, ω_β^α the mass fraction of the species α in the β phase, dt the current time increment, Δt the current time step, and the superscript zero means prescribed values. The terms $(\Delta P_\beta^0 dt/\Delta t)$ allows for imposing a linear variation of the variable P_β^0 during the time step. The coefficient γ_β is a leakage coefficient that allows the prescribed pressure to be applied with more or less strength.

When the temperature is imposed, the boundary condition for the energy balance reduces to

$$j_e = \gamma_e \left(T^0 + \Delta T^0 \frac{dt}{\Delta t} - T \right) \qquad (2\text{-}6)$$

where T is temperature and γ_e is a leakage coefficient.

In the analysis, the rock mass was simulated by considering low leakage coefficients for the hydraulic and also for the thermal problem, obtained by calibration so values close to the rock were reproduced. Prescribed gas and liquid pressure were assumed equal to 0.1 MPa whereas a temperature of 20°C was applied.

Finally, the mechanical boundary conditions were imposed by fixing the displacement along the edges of the model. This assumption can be considered close to the actual situation on the right and bottom edges (rock mass) whereas it is an approximation of the actual boundary conditions at the upper edge (plug and tensors).

An isotropic initial stress state was assumed within the barrier, with a value equal to 0.2 MPa.
A complete list of the thermal and hydraulic initial conditions considered for each material and of the parameters used in the simulation is given in the Appendix in section 2.6.

2.3.3 Test observation and interpretation

Predictions of the numerical analysis are plotted together with the test observations for sensors located in correspondence with R9 & R10.

Thermal results

Figure 2-25 compares results of the temperature evolution at different radii. Some differences are observed between experimental and numerical results at the beginning of the test. However, after about 100 days temperature values within the bentonite are well reproduced.

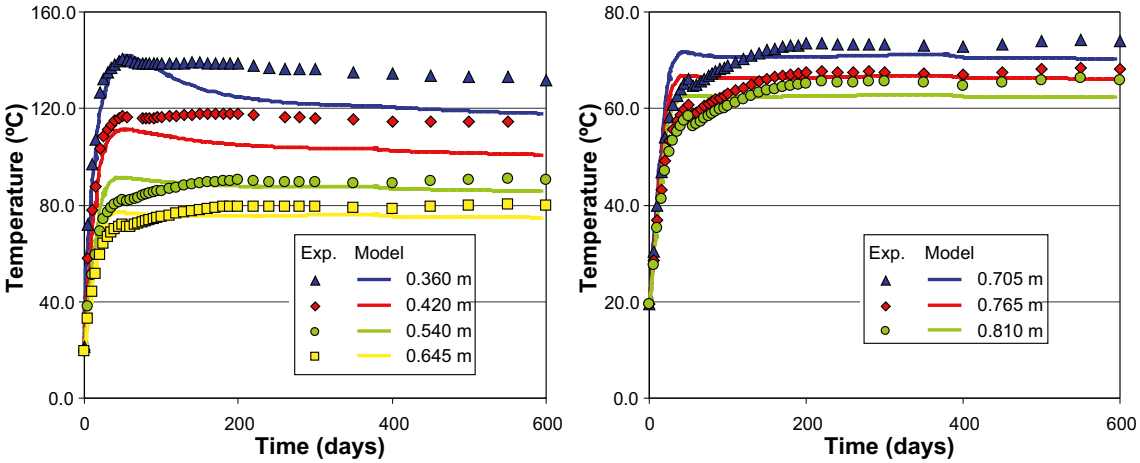

Figure 2-25. Evolution of temperature in the barrier, observations and computed results.

Hydraulic results

Simulated values of relative humidity at different radii are shown in Figure 2-26 together with experimental results. In general, the model captures the evolution of this variable at the different radii considered.

The model is able to reproduce the cycles of suction observed at the beginning of the experiment both qualitatively and quantitatively (Figure 2-27). These results are obtained in a natural way by using the hydraulic boundary condition defined from Figure 2-24.

Mechanical results

Figure 2-28 presents results of deviatoric stress against mean stress at two radii. Appreciable differences between numerical and experimental values are obtained. A possible source of these discrepancies can be attributed to the rigidity considered for the inner and outer sand.

2.3.4 Concluding remarks

The section describes the numerical simulations carried out to find a possible relation between the cracks observed in the bentonite blocks at the upper part of the *in situ* test when dismantling and the cycles of suction and stresses registered in that zone at the beginning of the experiment. A 2D-axisymmetric geometry which does not include the rock mass was considered in the analysis.

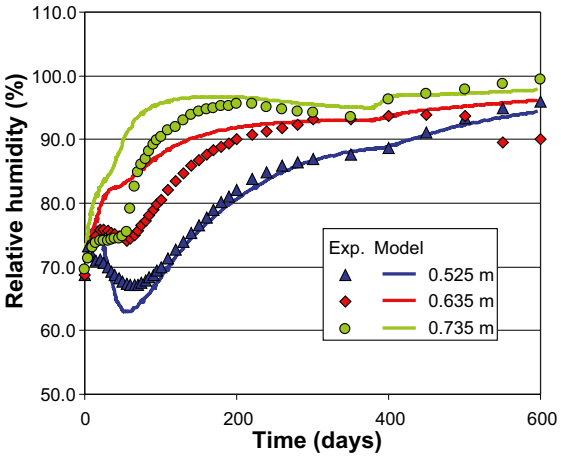

Figure 2-26. Evolution of relative humidity in the barrier, observations and computed results.

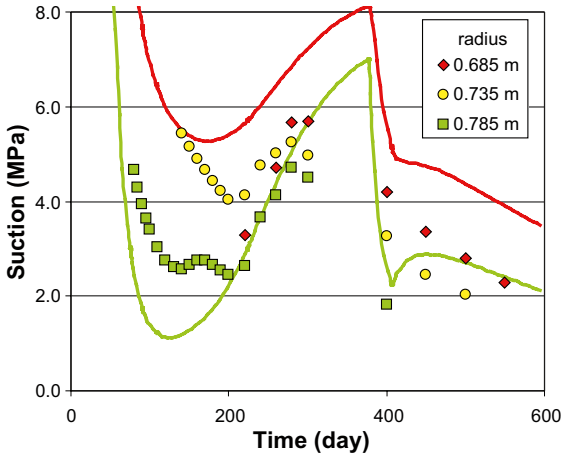

Figure 2-27. *Experimental and simulated suction cycles at the level of R10.*

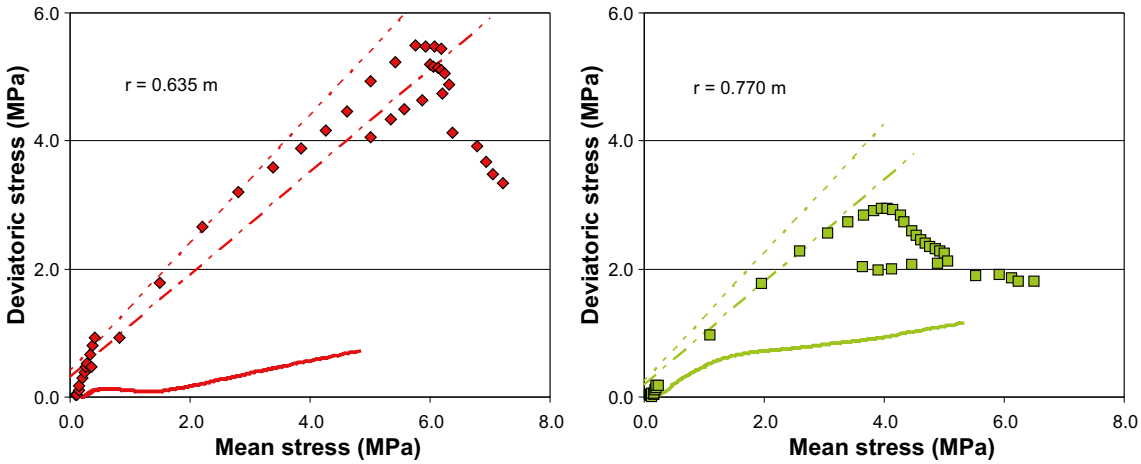

Figure 2-28. *Deviatoric stress against mean stress at the level of R9. Symbols are experimental data and continuous lines are numerical results.*

Results confirm that the cycles of suction and stress measured in the bentonite surrounding the upper heater were mainly due to a lack of water available for saturating the bentonite. Therefore, the reason for that behaviour was mainly hydraulic. This conclusion was also obtained in the analyses carried out in 2004.

Measured values of temperature and relative humidity at different radii were in general well reproduced. Also, the cycles of suction registered at the start of the test could be captured by the numerical results.

The mechanical behaviour of the bentonite blocks was simulated using the Barcelona Basic Model (BBM). Parameters in this model were defined using experimental data from the literature. This set of parameters differs from those used in the simulations carried out in 2004. However, it was not possible to reproduce the unexpected high deviatoric stresses registered at the start of the test on the mid-high of the upper heater. Those stresses may have produced weak surfaces that developed cracks during the dismantling phase.

2.4 THM analysis of the entire experiment

2.4.1 Preface

ANDRA (French National Agency for Radioactive Waste Management) and SKB (Swedish Nuclear Fuel and Waste Management Co) performed the Temperature Buffer Test (TBT) in granitic rock at the Äspö Hard Rock Laboratory, Sweden. The overall objective of the project is to investigate how well the bentonite buffer can endure the high temperatures expected to be found around vitrified waste canisters.

The present section describes the performance, analysis and interpretation of the *in situ* Temperature Buffer Test. In the first part, determination of material parameters and main aspects of the numerical model are presented. The section continues with the simultaneous presentation of some selected observations, and the associated predictions of the numerical analysis. The comparison between predictions and observations provides a firm basis for the interpretation of the test.

2.4.2 Description of the analysis

It is expected that a significant number of coupled THM processes will occur in the near field of a real high level radioactive waste repository. As a consequence, a THM formulation that incorporates the main features of this behaviour will be required to solve this kind of problems. Olivella et al. (1994) describe a formulation which has been discretised in space (finite elements) and time (finite differences) in order to be used for numerical analysis. It constitutes the bases of the computer program CODE_BRIGHT (Olivella et al. 1996), which has been used to perform the analyses reported below.

In the context of the TBT Project, an attempt was made to carry out a gas test in the upper part of the field experiment. Finally, that option was abandoned because the system was not tight. As a necessary and preliminary task, after 1,505 days water started to be injected in the sand shield to guarantee full saturation of the barrier at that level. When that applied protocol was included in the THM analysis of the test, many convergence problems arose. Due to this situation and because the main objective of this section is to validate the applied formulation and the constitutive laws adopted for the materials, only 1,500 days from the instant of switching the heaters on were considered in the numerical simulation.

Material parameters

Many materials take part in TBT and to perform analyses of the coupled processes that develop in this kind of problem, it is necessary to adopt specific constitutive laws that define the thermal, hydraulic and mechanical behaviour of those materials. As a consequence, a large number of parameters have to be determined. In this section a compilation of the experimental information used to define most of the material parameters is given.

Rock

Äspö diorite, Småland granite, greenstone and fine-grained granite make up most of the rock mass in Äspö Hard Rock Laboratory (Andersson and Johansson 2002). The hole used to implement TBT was bored at a depth of 420 m and it has been bored in Äspö diorite with veins of fine-grained granite and minor veins of greenstone. After boring no water inflow into the deposition hole was measured. The magnitude of the major horizontal stress is approximately 25 MPa at 450 m depth. The magnitudes of the minor horizontal stress and the vertical stress at this level are 10 and 12 MPa, respectively. Young's modulus and Poisson's ratio for Äspö diorite are around 50 GPa and 0.27 respectively (Andersson and Johansson 2002).

The rock heat conductivity specified in the predictive modelling program (Åkesson 2006) was 2.6 W/(m·K) while the heat capacity was 800.0 J/(kg·K).

Johansson et al. (1998) present results about the porosity distribution of rock samples from Äspö. The Äspö diorite shows heterogeneous and mineral specific porosity distribution. The measured total porosity varies between 0.003 and 0.005, but porosities of 0.03 were observed near large quartz and feldspar mineral crystals. The porosity pattern of fine-grained granite was uniformly distributed

although a slight foliation could be observed. The global porosity was low, between 0.002 and 0.003, but values as higher as 0.01 were determined in some points. Autio et al. (2003) determined porosity values of 0.003 and 0.008 for undamaged and damaged Äspö diorite, respectively. The corresponding intrinsic permeability values were 8.4×10^{-20} and 1.0×10^{-18} m^2. Measured hydraulic conductivity was three orders of magnitude higher than the corresponding one to the undisturbed rock in a depth of 3 mm from the wall of a tunnel bored in Äspö granite (Pusch and Liedtke 2003).

The retention behaviour has not been measured for the host rock, but values previously used by Börgesson and Hernelind (1999) were considered to determine the parameters of the water retention curve adopted in the calculations.

Bentonite

Table 2-5 indicates the water content and bulk density obtained after compaction for the different bentonite blocks used in TBT (Åkesson 2006). According to the data it was decided to define two kinds of bentonite with different properties; one representing blocks C1 to C4 and R1 to R6, while the other one includes blocks R7 to R12.

The water retention capacity of compacted samples of MX-80 bentonite has been extensively investigated by CIEMAT (Villar 2005, Villar et al. 2005, 2006, Villar and Gómez-Espina 2007). Figure 2-29 presents experimental results of water retention capacity obtained on samples compacted at different densities and tested using different methodologies. Parameters that define the water retention curve adopted in the simulations have been determined using these experimental data.

Figure 2-30 shows experimental values of intrinsic permeability as a function of the sample porosity (Börgesson and Hernelind 1999, Villar 2005). As it can be seen there is some scatter between the reported data.

Table 2-5. Water content and bulk density of bentonite blocks used in the field test.

Block	Inner diameter (mm)	Outer diameter (mm)	Bulk density (Mg/m^3)	Water content
C1–C4	–	1,580	1.996	0.175
R1–R6	630	1,640	1.994	0.175
R7–R12	1,070	1,637	2.064	0.175

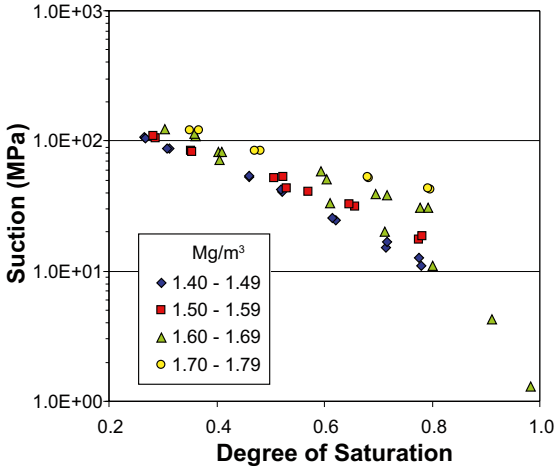

Figure 2-29. *Suction as a function of degree of saturation for samples of MX-80 bentonite compacted at different densities.*

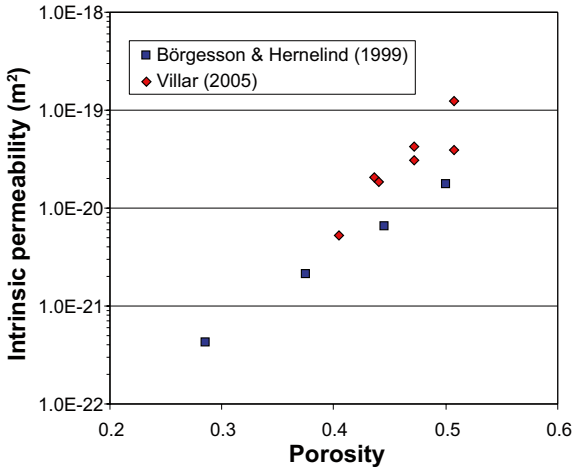

Figure 2-30. *Intrinsic permeability as a function of sample porosity.*

A compilation of experimental values of thermal conductivity for compacted samples of MX-80 bentonite is given in Figure 2-31 (Börgesson et al. 1994, Tang 2005). Results by Börgesson et al. (1994) have been obtained on saturated MX-80 bentonite samples with different void ratios and in samples with the same void ratio but variable degree of saturation. Knutsson (1983) concluded that heat capacity of compacted samples increases with water content and applied pressure, and reported values between 800.0 and 1,050.0 J/(kg·K).

Figure 2-32 presents results of swelling pressure tests of MX-80 bentonite samples compacted at different dry densities (Pusch 1980, Villar 2005). As it can be seen the swelling pressure increases as the dry density increases, and values between 6.0 and 10.0 MPa are obtained in the dry density range that is expected to be found in the final state of TBT.

Villar (2005) has done suction controlled oedometer tests on MX-80 bentonite samples compacted at nominal dry densities of 1.69 and 1.79 Mg/m^3. In one case the suction was imposed using the axis translation method while in the other case the relative humidity of the atmosphere in contact with the sample was controlled. Samples were hydrated at a very low constant vertical load (0.1 MPa), and then this external load was increased by steps. Tang (2005) and Tang et al. (2008) evaluated the effect of changes in suction and temperature on the mechanical response of compacted samples of MX-80 bentonite. Using those experimental results, parameters of the mechanical model used in the simulations were determined as indicated in Jacinto (2010) and summarized in the Appendix in section 2.6.

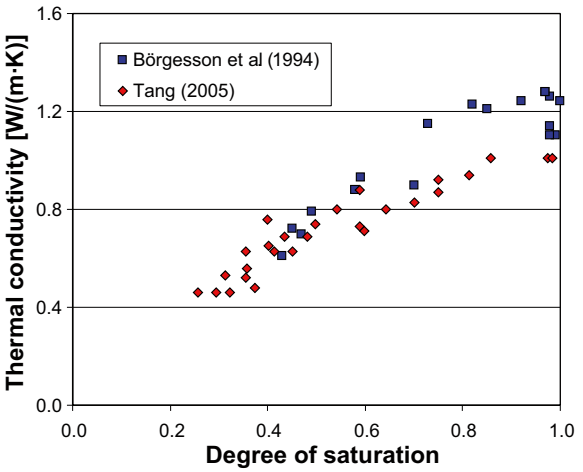

Figure 2-31. *Thermal conductivity at different degrees of saturation. Sample void ratio varies between 0.55 and 1.50.*

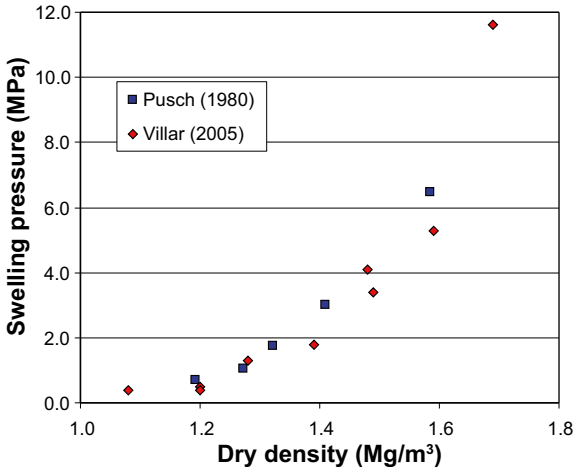

Figure 2-32. *Swelling pressure for MX-80 bentonite samples compacted at different dry densities.*

Sand

Initial water content of the sand was 0.03, while initial target bulk densities were 1.85 and 1.70 Mg/m^3 respectively, for the sand shield and sand filter (Åkesson 2006).

There is small experimental information about the sand behaviour. As a consequence, values suggested in Åkesson (2006) for different parameters were adopted. The thermal conductivity varies between 0.4 W/(m·K) for the dry state to 1.7 W/(m·K) at saturated state, while a heat capacity of 900.0 J/(kg·K) was assumed.

Pellets

The bentonite pellet filling the upper part of the slot between the bentonite blocks and the rock has an initial water content of 0.1 and a bulk density of 1.20 Mg/m^3 (Åkesson 2006).

Pusch et al. (2003) present some experimental results about the behaviour of pellets made up of MX-80 bentonite. The swelling pressure of samples prepared using pellets is higher than that corresponding to samples of the same density but prepared from powder clay. The order of magnitude of hydraulic conductivity informed by these authors is 1.0×10^{-12} m/s. Because of that, a value of intrinsic permeability equal to 2.0×10^{-18} m^2 was adopted in the numerical simulations of the TBT.

To the author's knowledge, there is not information related to the water retention capacity of compacted samples of MX-80 bentonite pellets. Hoffmann et al. (2007) have determined the water retention capacity of pellet mixtures of FEBEX bentonite compacted at three dry densities. There are also experimental data about the retention capacity of compacted powder samples of the same material (ENRESA 2000). The comparison of results permits to obtain a relation between the values of the parameters used to define the water retentiton curve for each case. Using a similar relation to that obtained for the FEBEX material, an estimation of the parameters used to define the water retention curve of the pellet mixture of MX-80 bentonite was obtained.

Thermal parameters were assumed equal to those adopted for the bentonite blocks.

Geometry and boundary conditions

Figure 2-33 presents the axisymmetric geometry used in the analyses. Boundaries were defined far enough to guarantee that they do not influence the obtained results. All materials used in the experiment have been represented. Although there was a gap between the bentonite and the heater in the lower part of the barrier, the analysis has assumed that, initially, there was contact in that interface.

For the thermal problem, a constant temperature of 20°C was assumed throughout. Regarding the hydraulic problem, constant liquid pressures of 4.0 and 4.4 MPa were applied on the upper and lower boundaries of the model respectively, while on the right one a lineal variation between those values was assumed. Additionally, the gas equation was always taken into account, considering that

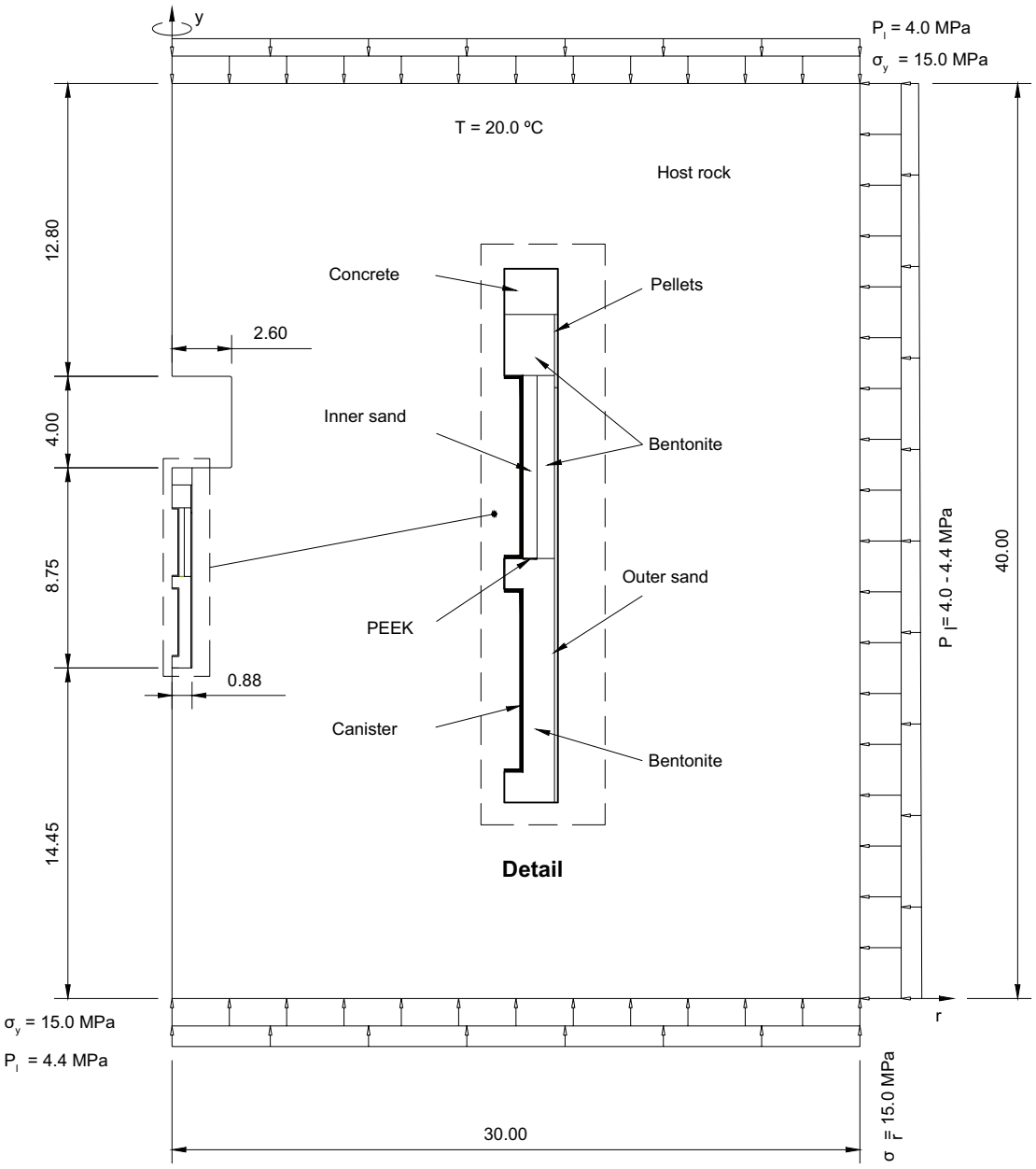

Figure 2-33. *Axisymmetric geometry for the analysis of the in situ heating test (dimensions are in meters).*

some nodes at the top of the sand filter were connected to the atmosphere at the beginning, in order to account for the effect of the open pipes. A fixed gas pressure of 0.1 MPa was considered until day 377 and, after that, a water flux was applied on them. The initial stress field within the rock was assumed uniform and isotropic with a value of 15.0 MPa.

The analysis started simulating the excavation followed by the construction of the bentonite barrier and the insertion of the heater. To represent the bentonite two materials were considered because of the different initial conditions between the block used in the field test. Thus, a dry density of 1.70 Mg/m^3 has been assumed for the clay barrier in correspondence with the upper heater (R7 to R12). For the rest of bentonite a dry density equal to 1.65 Mg/m^3 was used (C1 to C4 and R1 to R6). In accordance with the measurements performed during installation, an average initial water content of 0.15 and a suction of 50 MPa have been assumed for the clay barrier. The water content is lower than that used for block compaction, probably because of some drying during storage and installation. Initial stress in the barrier is assumed isotropic and equal to 0.2 MPa.

Power was applied to the heaters in accordance with the actual test protocol (Table 2-6). The instant of switching the heaters on is taken as time zero.

Table 2-6. Power applied on each heater in the field test.

Time (days)	Power (W)
0–8	900
8–15	1,200
15–1,175	1,500
1,175–1,500	1,600

On the outer sand, a water flux was applied as boundary condition. As the total water inflow instead of the inflow on each pipe was registered in the field test some assumptions were made to calculate the liquid flux applied to the nodes of the model. During the first 377 days, the water flux to be applied at the lower part of the outer sand can be well defined. Since then, it was assumed that the water flux is the same in the upper and lower pipes. After 1,000 days, the total inflow was divided by the total number of injection pipes and then the water flux was applied in the upper and lower nodes of the outer sand and some nodes between C3 and C4. It is noted that the actual water inflow distribution can be different from the distribution assumed in the analyses. Figure 2-34 shows the total volume of water injected into the system and the curves of water inflow adopted in the simulation as input data in the nodes at the bottom and top of the sand filter as well as that applied in the zone between C3 and C4 (mats).

A complete list of the initial conditions and material parameters used in the simulation is given in the Appendix in section 2.6.

2.4.3 Test observations and interpretations

Representative test observations concerning the behaviour of the engineered barrier are presented. Predictions of the numerical analysis are plotted alongside the test observations to assess the performance of the model. In the caption of the figures, z indicates the vertical distance measured from the bottom of the borehole.

Thermal results

Figure 2-35 shows the evolution of the temperature in various sections of the engineered barrier. In each section, temperatures at different radial distances from the axis of the hole are plotted.

It can be noted that, after the initial stage, temperatures generally are constant throughout the barrier. The small increase in temperature about 1,100 days after the heating started is due to the power increase applied to both heaters. The analysis reproduces the observations quite well at the level of the upper heater [Figure 2-35(c)-(d)]. On the other hand, some differences are observed in correspondence with the sensors located at the level of the lower heater.

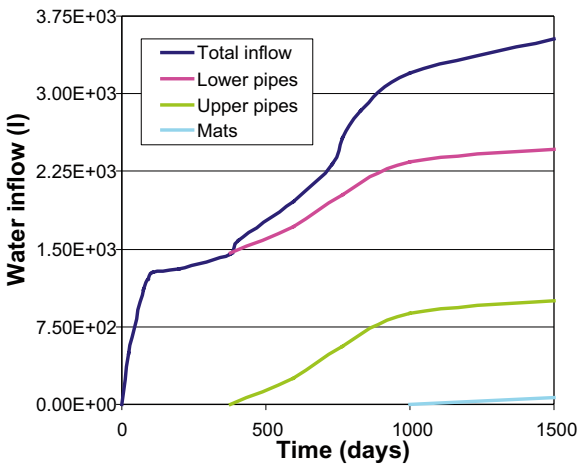

Figure 2-34. *Total water injected into the engineered barrier and distribution adopted in the numerical simulation.*

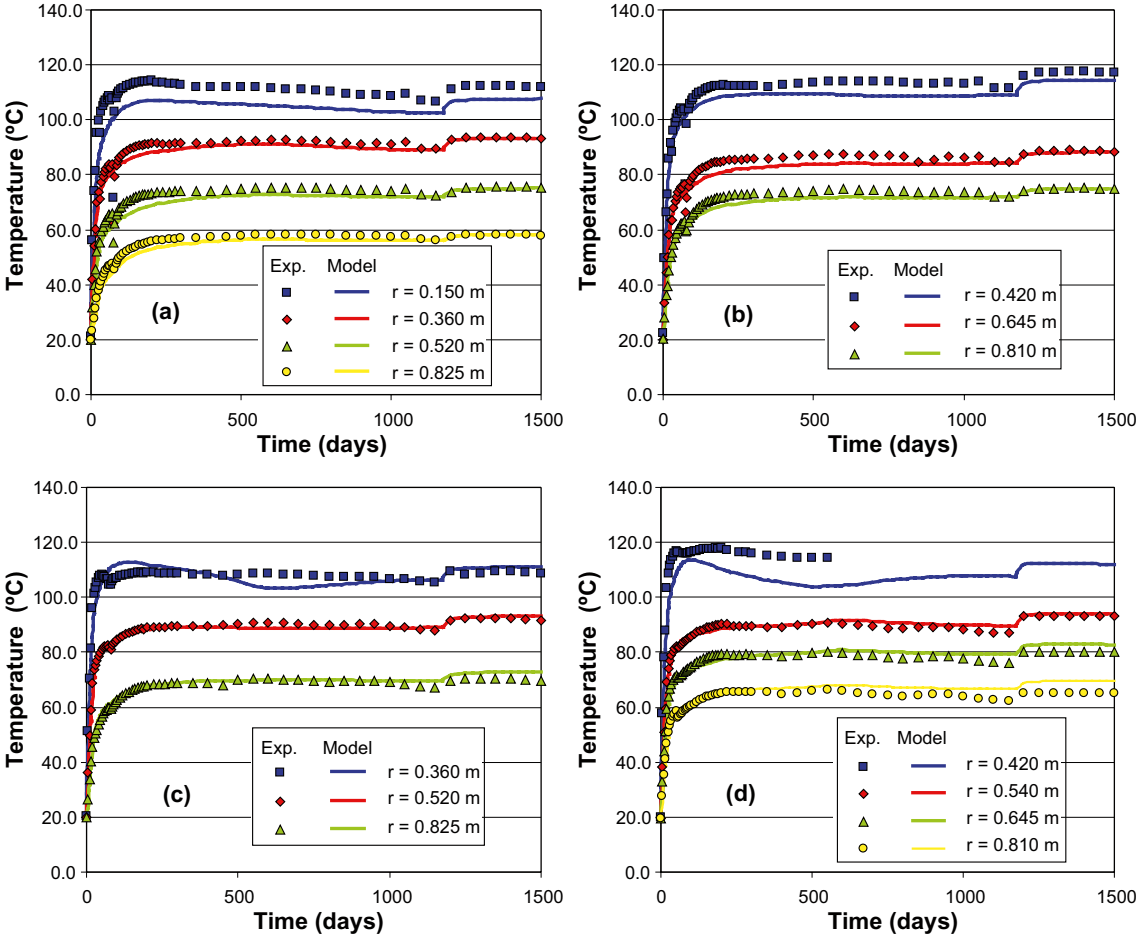

Figure 2-35. *Evolution of temperature in bentonite barrier, observations and computed results. (a) z = 0.45 m; (b) z = 2.45 m; (c) z = 3.95 m; (d) z = 5.95 m. (z is height from the hole base).*

To get a complete picture of the near-field behaviour it is interesting to examine the response of the host rock (granite). It is subjected to a lower heat loading and therefore the observed effects are more limited. Figure 2-36 presents the evolution of temperature measured in several sensors installed at different distances form the periphery of the deposition hole and at different heights from the bottom of the borehole.

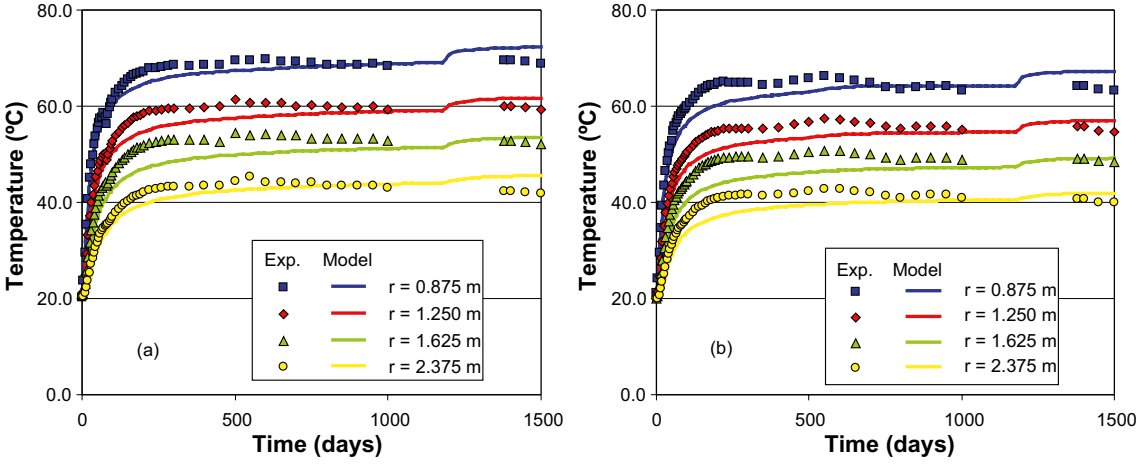

Figure 2-36. *Evolution of temperature in host rock, observations and computed results. (a) z = 3.01 m; (b) z = 5.41 m.*

Observed temperature at the level of the lower heater are higher than those corresponding to the level of the upper heater. The values and evolution of the temperatures are well predicted although the model is not able to reproduce the rapid increase of temperature observed at the start of the test.

It is important to note that the Canister Retrieval Test (CRT) was running in the same gallery that TBT at the time when the latter was mounted. The CRT was a heating experiment running at 6.0 m distance from the TBT deposition hole. Temperature in the rock around of the TBT hole was monitored in four positions using instruments installed in vertical holes drilled at 0.3 m from the periphery of the TBT hole. Before TBT started, registered temperature was 27°C in the sensor facing CRT and about 23°C in the others ones. The influence of the CRT was not included in the simulation and therefore, it is though that part of the discrepancies between measured and simulated results can be associated to this simplification.

Hydraulic results

Figure 2-37 shows the variation with time of relative humidity, measured with capacitive sensors, in four sections.

In the zone near the rock, and in the middle of the barrier, there is a monotonic increase of relative humidity, reflecting the process of hydration induced principally by the injection of water through the outer sand and in minor extent by water drawn from the host rock. However, in the region closer to the hole axis it can be observed that there is first an increase of relative humidity followed immediately by drying; finally, a new increase of relative humidity occurs.

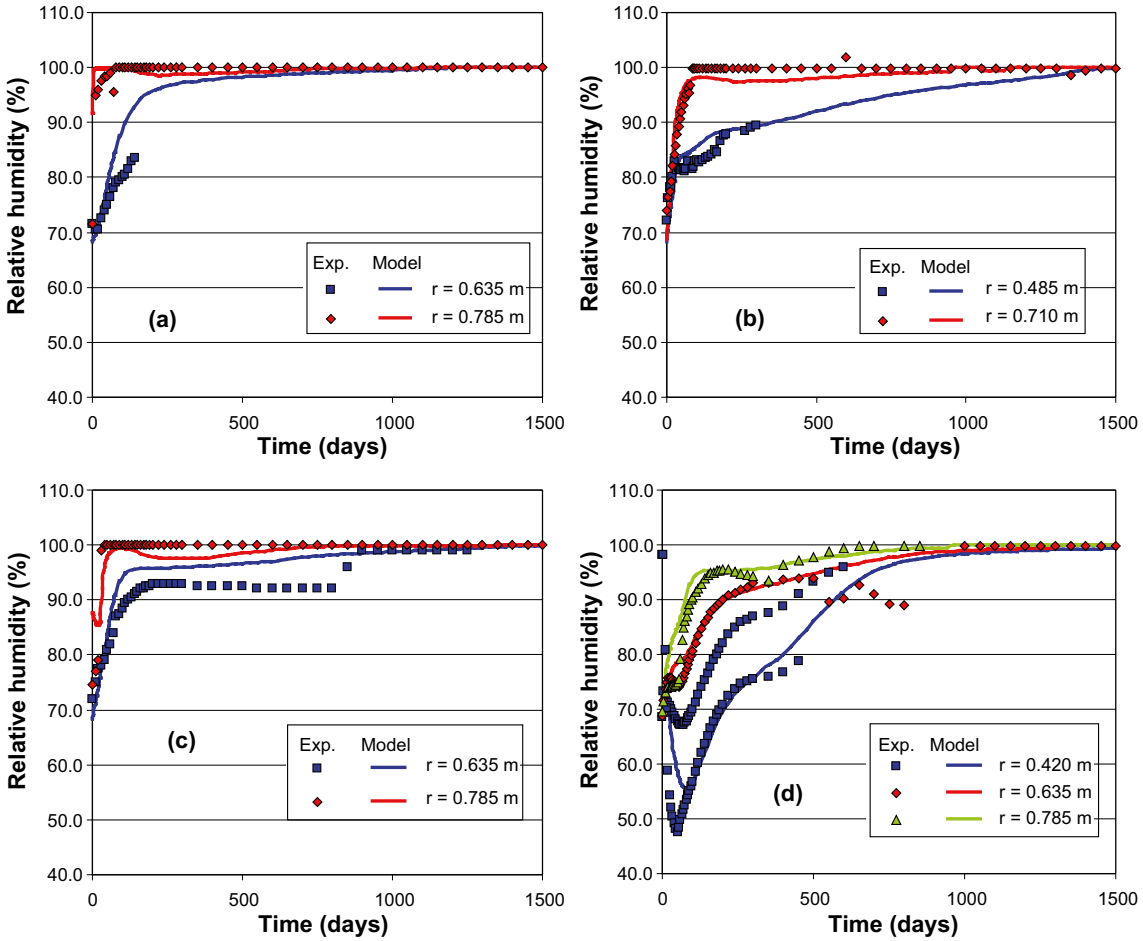

Figure 2-37. *Evolution of relative humidity in bentonite barrier, observations and computed results. (a) z = 0.25 m; (b) z = 2.25 m; (c) z = 3.75 m; (d) z = 5.25 m and 5.75 m.*

By examination of the numerical analysis results it is possible to identify the processes underlying this behaviour. The first relative humidity increase is due to a vapour front (driven by heating) passing through the observation point. After that, a temperature increase causes evaporation and, therefore, drying of the material. After approximately 100 days general hydration takes over, causing the final gradual increase of relative humidity. A significant part of the early hydration of the middle and outer barrier zones is due to the condensation of vapour coming from the inner region.

Figure 2-38 presents the evolution of degree of saturation at different radii within the bentonite buffer in correspondence with the mid-height of the lower and upper heater.

As in the case of the relative humidity, in the region closer to the hole axis it can be observed that there is first a small increase of degree of saturation followed immediately by a decrease of this variable; finally, as the hydration proceeds a new increase of degree of saturation occurs. On the contrary, in the zone near the rock and in the middle of the barrier, there is a monotonic increase of the degree of saturation. Results suggest that the bentontie blocks are close to full saturation after 1,500 days of heating.

Mechanical results

As Figure 2-39 shows stresses in the barrier increase very significantly during hydration because of the high swelling of the compacted bentonite blocks. At the end of the test, values of the total stresses close to 6–8 MPa were reached.

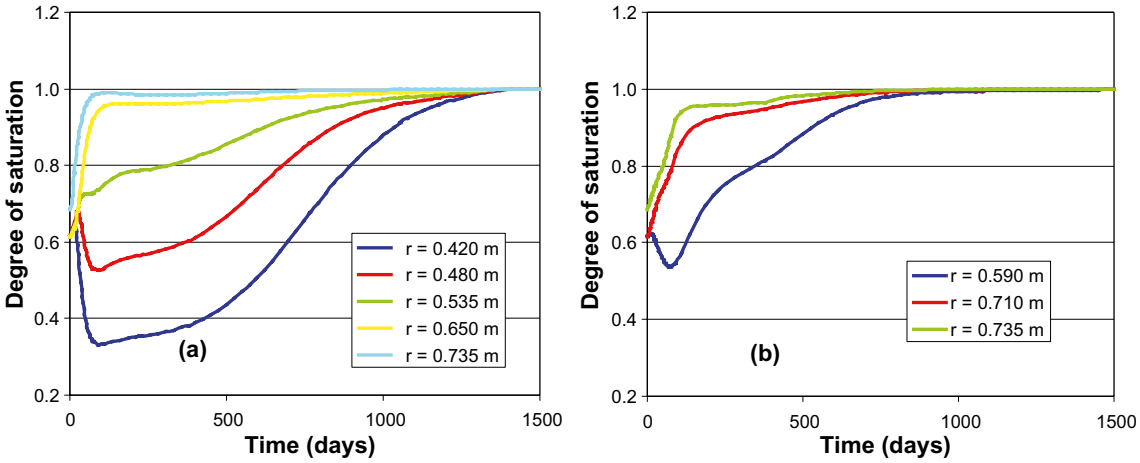

Figure 2-38. *Evolution of degree of saturation in bentonite barrier, computed results. (a) z = 2.25 m; (b) z = 5.75 m.*

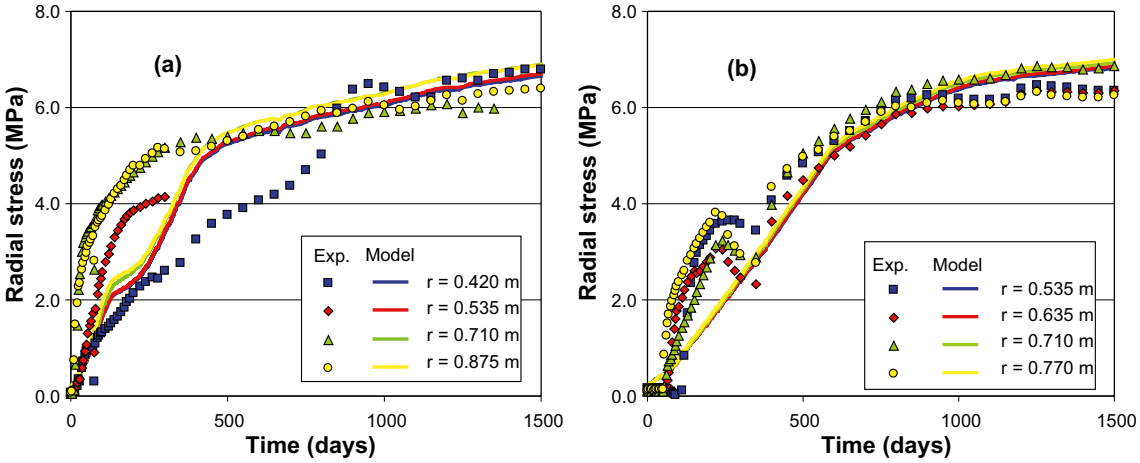

Figure 2-39. *Evolution of stresses in bentonite barrier, observations and computed results. (a) z = 2.25 m; (b) z = 5.75 m.*

It is possible that the slower development of the measured swelling stresses, as compared with the predictions from the analysis, may be due, at least in part, to the initial liner/barrier and rock/barrier gaps, not accounted for in the modelling. In any case, the predicted final total stress in the barrier is similar to that measured in several of total stress cells.

2.4.4 TH analysis until the end of the test

Although it was not possible to carry out a THM analysis of the whole test after the inundation of the upper sand was started because of the convergence problems, it was decided to perform a TH analysis using the geometry shown in Figure 2-33. This analysis is designed as the Thermo-Hydraulical Case.

Thermal results

Figure 2-40 compares experimental and numerical values of temperature at the same locations than those considered in Figure 2-35.

In general, the model is able to reproduce the cooling period at the end of the test. Discrepancies between measured and numerical results are obtained at the zone between the two heaters.

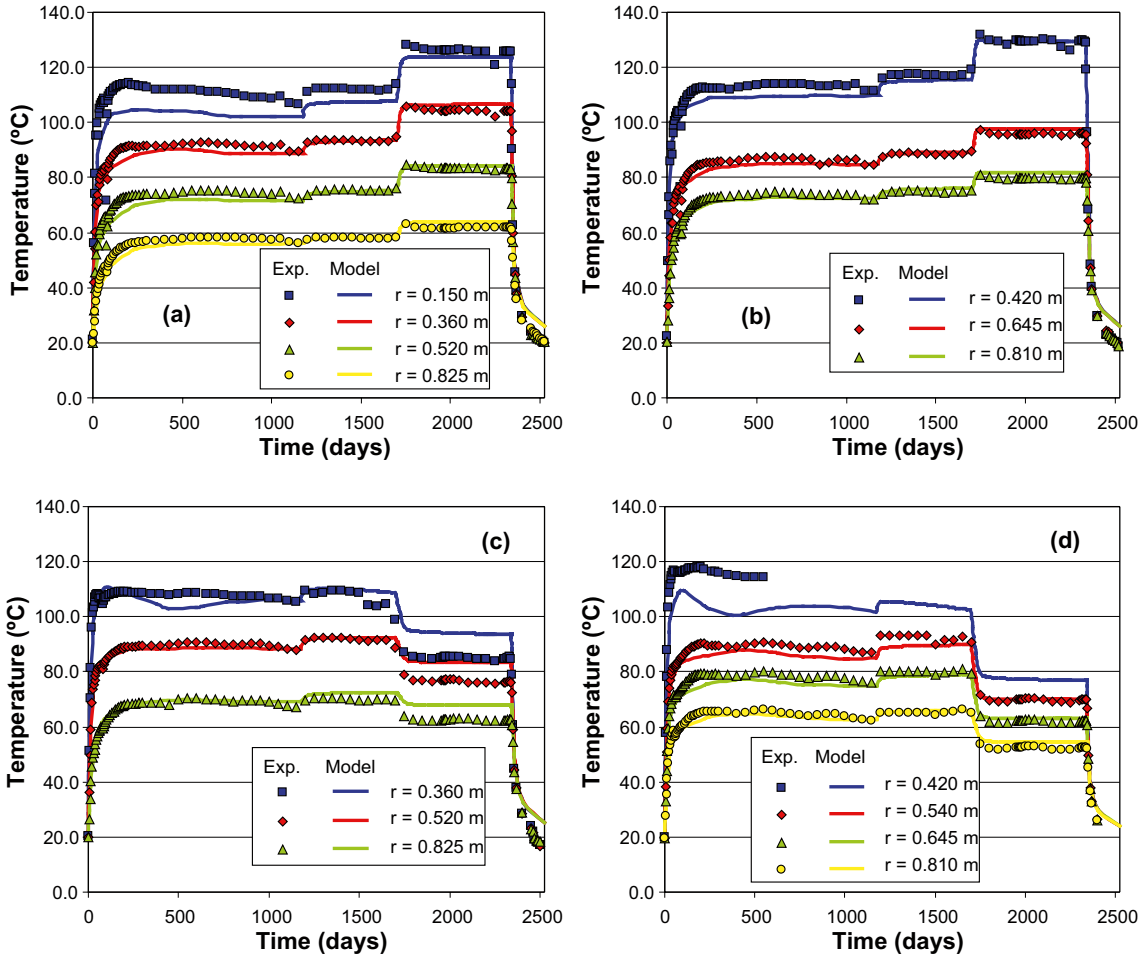

Figure 2-40. *Evolution of temperature in bentonite barrier, observations and computed results. TH Case. (a) z = 0.45 m; (b) z = 2.45 m; (c) z = 3.95 m; (d) z = 5.95 m.*

Hydraulic results

Figure 2-41 corresponds to the evolution with time of relative humidity in four sections of the experiment. A small decrease in the value of the relative humidity is observed at the end of the test at the inner part of the barrier in correspondence with the mid high of the lower heater. This change can be related to the decrease of the degree of saturation because of the changes in water volume as temperature decreases.

2.4.5 Concluding remarks

The Temperature Buffer Test was a large-scale *in situ* heating test performed to simulate the conditions of vitrified high-level radioactive waste disposal in a deep geological repository excavated in granite. Two possibilities for the disposal of vitrified waste are evaluated in the experiment by using heaters that mimic the thermal effects of nuclear waste. In the upper part a composite barrier with a sand shield between the heater and the bentonite buffer is considered, while in the lower part an engineered barrier made up of compacted swelling clay between the heater and the rock is evaluated. The test has provided a large amount of information concerning the thermo-hydro-mechanical behaviour of the bentonite barrier and of the adjacent rock. The progress of hydration, the effects of heating, vapour transport and development of swelling pressures have been identified as the major interacting phenomena underlying the observed patterns of behaviour.

An adequate interpretation of the test could be carried out using an appropriate coupled THM formulation which incorporates the relevant processes involved in the problem under consideration. The general balance equations are complemented by constitutive laws and equilibrium restrictions. Several parameters are required to define the numerical problem and it has been possible to determine them on the basis of an extensive programme of laboratory tests.

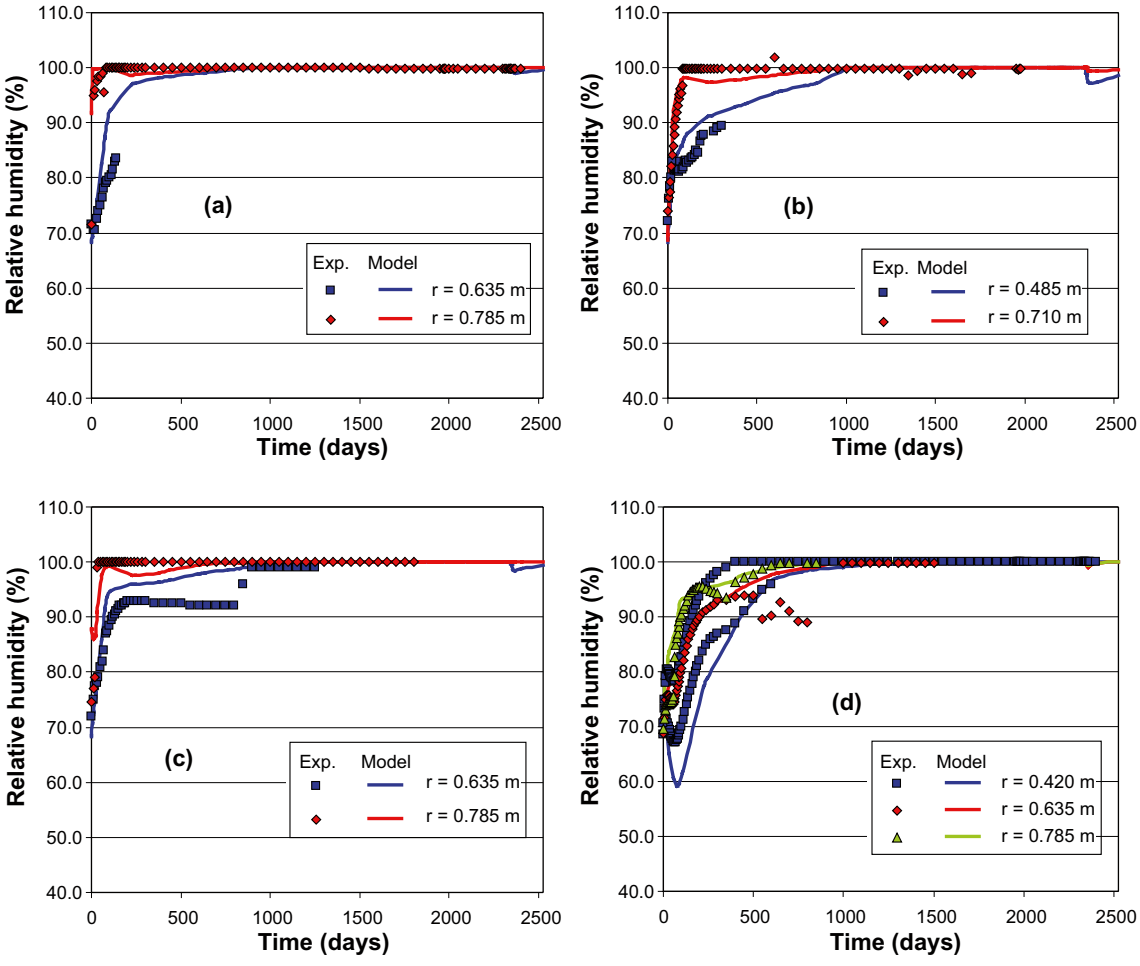

Figure 2-41. *Evolution of relative humidity in bentonite barrier, observations and computed results. TH Case. (a) z = 0.25 m; (b) z = 2.25 m; (c) z = 3.75 m; (d) z = 5.25 m and 5.75 m.*

The comparison between the results of the numerical analysis and the field observations suggests that the formulation and associated computer code are able to reproduce well the main observed features of the THM behaviour of the test. Indeed, quantitative agreement is very satisfactory for a large number of variables. A good representation of the test was achieved without introducing additional complexities like the explicit consideration of the gaps between blocks and the blocks and the heaters.

2.5 General conclusions

This chapter has been organized in such a way that the main conclusions are presented in detail at the end of each section. Because of that, in this section only some remarks and general conclusions are included.

The TBT Project included a full-scale field experiment that simulated repository conditions for high level radioactive waste. Deep geological disposal is by far the most likely possibility to be implemented for the safe disposal of high level radioactive waste. The repository is built placing several barriers, both natural and artificial, between the potentially harmful radionuclides and the biosphere.

This Report describes different analyses of the full-scale *in situ* heating test. The TBT was performed to simulate the conditions of vitrified high-level radioactive waste disposal in a deep geological repository excavated in granite. Two possibilities for the disposal of vitrified waste were evaluated in the experiment by using heaters that mimic the thermal effects of nuclear waste. In the upper part a composite barrier with a sand shield between the heater and the bentonite buffer was considered, while in the lower part an engineered barrier made up of compacted swelling clay between the heater and the rock was evaluated. The test has provided a large amount of information concerning the thermo-hydro-mechanical behaviour of the bentonite barrier and of the adjacent rock. The progress of hydration, the effects of heating, vapour transport and development of swelling pressures have been identified as the major interacting phenomena underlying the observed patterns of behaviour. Numerical simulations were performed using a finite element code that solves the governing equations corresponding to THM coupled problems. The analyses confirm the capabilities of the coupled formulation used in this Project. Several parameters are required to define the numerical problem and it has been possible to determine them on the basis of an extensive programme of laboratory tests.

In section 2.2 the response observed at the lower part of the *in situ* test was analysed. A reduced 2D-axisymmetric geometry was used and changes in some constitutive laws were introduced in this analysis. In particular: a) the use of the Barcelona Expansive Model for MX-80 bentonite; b) updated parameters in the diffusive flow term to take into account the effect of high temperatures; c) the use of a non-conventional water retention curve for MX-80 at high temperature. In general, the good agreement between numerical simulations and measurements indicates that the main THM mechanisms involved in the behaviour of compacted bentonite barrier have been taken into account.

The objective of the section 2.3 was to found a possible relation between the cracks observed in the bentonite blocks at the upper part of the *in situ* test and the cycles of suction and stresses registered in that zone at the start of the experiment. A 2D-axisymmetric geometry which does not include the rock mass was considered in the analysis. Results confirm that the cycles of suction and stress measured in the bentonite surrounding the upper heater was mainly due to a lack of water available for saturating the bentonite. Therefore the reason for that behaviour was mainly hydraulic. Measured values of thermal and hydraulic variables were in general well reproduced. The mechanical behaviour of the bentonite blocks was simulated using the BBM. Parameters in this model were defined using experimental data from the literature. This set of parameters differs from those used in the simulations carried out in 2004. However, it was not possible to reproduce the unexpected high deviatoric stresses registered at the start of the test at the mid-high of the upper heater.

Section 2.4 describes the performance, observations and interpretation of the full-scale *in situ* heating test (TBT). Because convergence problems arose when changes in the boundary conditions were applied in the field test, it was not possible to carry out an analysis until the end of the test. The comparison between the results of the numerical analysis and the field observations suggests that the formulation and associated computer code are able to reproduce well the main observed features of the THM behaviour of the test. Indeed, quantitative agreement is very satisfactory for a large number of variables.

The TBT project has been an opportunity to improve our knowledge on several aspects of THM processes on compacted bentonite. In particular, two important features were: i) the effect of high temperatures on a long term experiment and ii) the effect of another material as the sand shield interacting with the bentonite. The simulation of the test showed that the basic formulation used in the analyses is appropriate. The improvements required by the challenges posed by the test were carried out keeping the same basic formulation used to simulate other previous experiments. However, those improvements have been fundamental in the simulation of TBT and they constitute a significant advance in the analysis of THM processes in the context of radioactive waste confinement.

2.6 Appendix

2.6.1 Preface

This Appendix summarizes the complementary work carried out in the context of the analysis and simulation of the TBT field experiment. The constitutive model used to simulate the mechanical response of bentonite blocks is briefly described. Experimental data of the mechanical response of MX-80 bentonite samples under thermal and hydraulic actions were obtained from a literature review. Finally, parameters used to characterize the thermo-hydro-mechanical behaviour of the different materials used in the simulations of the TBT *in situ* experiment are given.

2.6.2 Mechanical constitutive model of bentonite blocks

In the numerical analysis of the TBT, the mechanical behaviour of bentonite blocks was simulated using a constitutive model based on the Barcelona Basic Model (BBM). The BBM was initially developed to represent the hydro-mechanical response of low and moderate expansive soils in unsaturated state (Alonso et al. 1990). Gens (1995) extended the original version of this model to include the effect of temperature in the mechanical response of unsaturated soils. The model described below has been also applied in the simulation of other heating field tests (Chen and Ledesma 2009, Gens et al. 2009).

In the adopted model, the yield surface depends on stresses, suction and temperature

$$f = f(p, J, \theta, \varepsilon_v^p, s, \Delta T) \tag{2-7}$$

where p is the net mean stress, J is the square root of the second invariant of deviatoric stress tensor, θ is the angle of Lode, ε_v^p is the plastic volumetric strain, s is the suction, and ΔT is the difference between the current temperature T and a reference temperature T_0.

The elastic volumetric strain increment is given by

$$\dot{\varepsilon}_v^e = \left(\frac{\kappa_p}{1+e} + \alpha_{pT} \Delta T \right) \frac{\dot{p}}{p} + \frac{\kappa_s}{1+e} \frac{\dot{s}}{s+0.1} + \alpha_T \dot{T} \tag{2-8}$$

where κ_p is the elastic stiffness parameter for changes in net mean stress, κ_s is the elastic stiffness parameter for changes in suction, e is the void ratio, and α_{pT} and α_T are isotropic thermal expansion coefficients of the solid skeleton.

The elastic deviatoric strain increment is defined as

$$\dot{\varepsilon}_s^e = \frac{\dot{J}}{G} \tag{2-9}$$

with G the shear modulus.

To take into account experimental evidences about the behaviour of highly expansive materials some modifications were introduced in the elastic stiffness parameters with respect to the original version of the BBM. Thus, the elastic stiffness parameter for changes in net mean stress depends on suction through the law

$$\kappa_p = \kappa_{p0}\,(1+\alpha_{ps}s) \tag{2-10}$$

where κ_{p0} is the elastic stiffness parameter in saturated conditions and α_{ps} is a material parameter. The elastic stiffness coefficient for changes in suction depends on net mean stress according to the expression

$$\kappa_s = \kappa_{s0}\left(1+\alpha_{sp}\ln\frac{p}{p_{ref}}\right) \tag{2-11}$$

where κ_{s0} and α_{sp} are material parameters.

The variation of the compressibility coefficient with suction is given by the law (Alonso et al. 1990)

$$\lambda_s=\lambda_0[(1-r)\exp(-\beta s)+ r] \tag{2-12}$$

where r and β are material parameters.

The pre-consolidation pressure p_0 is assumed a function of suction and temperature. The dependence on temperature is adopted equal to that proposed by Hueckel and Borsetto (1990)

$$p_c = p_0^*+\gamma_T\Delta T \tag{2-13}$$

where p_0^* is the pre-consolidation stress for saturated state at the reference temperature, and γ_T is a material parameter that govern the evolution of the yield surface with temperature. For the dependence on suction the same relationship as postulated by Alonso et al. (1990) is considered

$$p_0 = p_r\left(\frac{p_c}{p_r}\right)^{\frac{\lambda_0-\kappa_{p0}}{\lambda_s-\kappa_{p0}}} \tag{2-14}$$

where p_r is a reference stress, and λ_0 is the slope of the virgin consolidation line at saturated state.

Some experimental results indicate that coefficient α_T depends on temperature and, slightly, on pressure (Baldi et al. 1988, Hueckel and Baldi 1990, Cekerevac and Laloui 2004). Hueckel and Borsetto (1990) have suggested the following expression

$$\alpha_T = \alpha_0 + 2\alpha_2\Delta T + (\alpha_1 + 2\alpha_3\Delta T)\ln\frac{p}{p_0} \tag{2-15}$$

where α_i are coefficients related to the thermal expansion of the soil skeleton.

For the coefficient γ_T the expression suggested by Hueckel and Borsetto (1990) was adopted

$$\gamma_T = 2(a_1+a_2|\Delta T|) \tag{2-16}$$

where a_1 and a_2 are parameters (usually negative).

The hardening law depends on plastic volumetric strain according to the following expression

$$\dot{p}_0^* = \frac{1+e}{\lambda_0-\kappa}p_0^*\dot{\varepsilon}_v^p \tag{2-17}$$

with κ defined as

$$\kappa = \left(\frac{\kappa_p}{1+e}+\alpha_{pT}\Delta T\right)(1+e) \tag{2-18}$$

and α_{pT} given by

$$\alpha_{pT} = \alpha_1 + \alpha_3\Delta T \tag{2-19}$$

Table 2-7 summarizes the parameters of the constitutive model adopted to simulate the mechanical behaviour of the bentonite blocks used in the engineered barrier of the TBT field experiment. Those parameters were deduced from experimental data of the thermo-hydro-mechanical response obtained on compacted samples of MX-80 bentonite (Villar 2005, Tang et al. 2008).

Table 2-7. Parameters of the mechanical constitutive model adopted for bentonite blocks.

κ_{p0}	α_{ps} (MPa^{-1})	κ_{s0}	α_{sp}	p_{ref} (MPa)
0.045	–0.007	0.15	0.0	–
α_0 (ºC^{-1})	α_1 (ºC^{-1})	α_2 (ºC^{-2})	α_3 (ºC^{-2})	α_1 [MPa·(Cº)$^{-1}$]
–1.0×10^{-4}	7.0×10^{-5}	4.0×10^{-6}	0.0	–1.0×10^{-4}
α_2 [MPa·(Cº)$^{-2}$]	λ_0	β (MPa^{-1})	r	p_r (MPa)
0.0	0.25	0.05	0.35	0.05

2.6.3 Parameters, boundary and initial conditions used in the analysis of TBT

Parameters presented below (Table 2-8 – Table 2-12) describe the thermo-hydro-mechanical behaviour of the different materials used in the Base Case of the numerical analysis of the TBT *in situ* experiment. Most of these parameters were determined using experimental data reported in section 2.4.

Parameters of the mechanical constitutive model adopted for the bentonite blocks are given in Table 2-7. The other materials were assumed elastic and parameters defining their behaviour are indicated in Table 2-12.

Table 2-8. Thermal conductivity for different materials.

Material	Law	λ_{dry} [W/(m·K)]	λ_{sat} [W/(m·K)]
Rock	$\lambda_T = \lambda_{sat}\sqrt{S_l} + \lambda_{dry}\left(1-\sqrt{S_l}\right)$	2.6	2.6
Steel		50.2	50.2
PEEK		0.25	0.25
Concrete		1.7	1.7
Pellets		0.3	1.3
Sand		0.4	1.7
Bentonite		0.3	1.3

Table 2-9. Specific heat for different materials.

Material	Rock	Steel	PEEK	Concrete	Pellets	Sand	Bentonite
c [J/(kg·K)]	800.0	460.0	2,000.0	750.0	950.0	900.0	950.0

Table 2-10. Retention curves for different materials.

Material	Law	P_0 (MPa)	m	P_d (MPa)	d
Rock	$S_e = \frac{S_l - S_{lr}}{S_{ls} - S_{lr}} = \left[1+\left(\frac{P_g - P_l}{P_0}\right)^{\frac{1}{1-m}}\right]^{-m}$	10.0	0.55	–	–
Steel		1.0×10^{-4}	0.50	–	–
PEEK		1.0×10^{-4}	0.50	–	–
Concrete		10.0	0.55	–	–
Pellets	$S_e = \frac{S_l - S_{lr}}{S_{ls} - S_{lr}} = \left[1+\left(\frac{P_g - P_l}{P_0}\right)^{\frac{1}{1-m}}\right]^{-m} f_{rc}$	0.50	0.19	1,000.0	1.5
Inner sand		0.20	0.39	700.0	1.1
Outer sand		0.15	0.39	700.0	1.1
Bentonite 1†	$f_{rc} = \left(1-\frac{P_g - P_l}{P_d}\right)^d$	35.0	0.42	1,000.0	1.0
Bentonite 2‡		35.0	0.42	1,000.0	1.0

† Bentonite for blocks C1 to C4 and R1 to R6.

‡ Bentonite for blocks R7 to R12.

Boundary conditions were defined according to guidelines given in Åkesson (2006). For the heat flux, the same protocol as that applied in the test field was used (Table 2-6).Water fluxes indicated in Table 2-13 were calculated following the assumptions described in paragraph Geometry and boundary conditions.

Initial conditions (Table 2-14) were determined using experimental data of the different variables measured in the test at the time when the heating was started.

Table 2-11. Intrinsic permeability for different materials.

Material	Law	k_0 (m^2)	ϕ_0
Rock	$\mathbf{k} = \mathbf{k}_0 \frac{\phi^3}{(1-\phi)^2} \frac{(1-\phi_0)^2}{\phi_0^3}$	1.0×10^{-19}	0.015
Steel		1.0×10^{-22}	0.010
PEEK		1.0×10^{-22}	0.010
Concrete		1.0×10^{-19}	0.015
Pellets		1.0×10^{-19}	0.61
Sand		1.0×10^{-15}	0.25
Bentonite		3.0×10^{-21}	0.35

Table 2-12. Elastic parameters for different materials.

Material	E (MPa)	ν
Rock	5.0×10^4	0.25
Steel	2.1×10^5	0.20
PEEK	20.0	0.25
Concrete	3.0×10^4	0.20
Pellets	20.0	0.25
Inner sand	55.0	0.25
Outer sand	25.0	0.25

Table 2-13. Water fluxes through different boundaries.

Time interval (days)	Water flux (kg/s)		
	Lower pipes	Upper pipes	Mats
1 ~ 25	2.411×10^{-4}	–	–
25 ~ 75	1.424×10^{-4}		
75 ~ 90	7.176×10^{-5}		
90 ~ 108	4.308×10^{-5}		
108 ~ 223	3.724×10^{-6}		
223 ~ 377	1.037×10^{-5}		
377 ~ 594	1.349×10^{-5}	1.349×10^{-5}	
594 ~ 766	2.062×10^{-5}	2.062×10^{-5}	
766 ~ 1,000	1.561×10^{-5}	1.561×10^{-5}	
1,000 ~ 1,500	1.505×10^{-6}	1.505×10^{-6}	1.505×10^{-6}

Table 2-14. Initial conditions for different materials.

Material	P_l (MPa)	P_g (MPa)	T (ºC)	ϕ
Rock	Figure 2-33			0.010
Steel	–49.9	0.1	20.0	0.010
PEEK				0.010
Concrete				0.010
Pellets				0.613
Inner sand				0.302
Outer sand				0.358
Bentonite 1				0.415
Bentonite 2				0.397

3 Clay Technology contribution – CODE_BRIGHT

3.1 Introduction

This chapter details the results of modelling the TBT field experiment using CODE_BRIGHT at Clay Technology. The modelling has been divided into four sub-tasks, with the first three focusing on separate parts of the full geometry, and the fourth being a model of the full field experiment.

An important aspect of the TBT experiment is the inclusion of a two decimetre thick sand shield around the upper heater, which effectively shields the bentonite from the high temperatures of the central canister. Furthermore, a thin sand filter was used to artificially hydrate the bentonite from the outside of the geometry. Before any modelling could be done, the parameters describing the sand and target void ratios for bentonite had to be determined. This is done in section 3.2.

The first two modelling tasks are 1D axisymmetric models of the expected evolution at mid-height of both heaters. Task 1 concerns the evolution around the lower heater, at the height of rings 3 and 4 (hereafter R3/4). The model solves the thermal, hydraulic and mechanical problems. Due to the high temperatures in the bentonite (T>150°C) it is also necessary to solve the mass balance of air, including water vapour transport. The models done within this task are presented in section 3.3.

The conditions around the upper heater are modelled in task 2. The materials and boundary conditions are chosen so as to represent the evolution around mid height of the heater, at the location of rings 9 and 10 (hereafter R9/10). The results of this modelling are presented in section 3.4.

In the third modelling task, which is presented in section 3.5, an attempt was made to reproduce the shearing which appears to have occurred in cylinder 3 (hereafter C3). The evidence for this event comes from 1) a spike in the axial stress measured in C3 at day 70, and 2) the displacements which was seen in C3 during dismantling. As this event occurred early on, the model was run for 200 days. It solves the hydraulic and mechanical problems only. The temperature during this period was approximately 60°C in the upper package in the field experiment, and for simplicity it was kept constant in the model at this value.

Finally, in section 3.6, we present the results from a 2D axisymmetric model of the full field experiment. The model solves the Thermal and Hydraulic problem, as well as for the gas pressure. However, due to computational problems with such models, the mechanical problem was not solved. The motivation for this model is to understand how a lower gas pressure may influence the overall hydration in the experiment.

3.2 1D-analytical model of the field experiment – sand parameters

The mechanical model of choice for modelling bentonite using CODE_BRIGHT is the Basic Barcelona Model (BBM), which in most respects provide an accurate description of its mechanical properties. However, one rather important feature of bentonite, the void-ratio dependence of the yield surface, is not included in BBM. As suggested in Åkesson et al. (2010b) the recommended way to handle this problem, is to estimate the homogenized void ratio of the bentonite in the problem at hand. This approach works well if the bentonite does not undergo significant plastic deformation before the homogenized void ratio has been reached. As we shall see later, this assumption is incorrect during the early evolution in TBT, particularly in the upper package. For now, however, the homogenized void ratio will be used to determine the plastic parameters to use, and when needed, a more detailed description will be provided.

The upper and lower packages in TBT differ significantly from each other in terms of the geometrical and material setup. In the lower package, the bentonite is placed directly adjacent to the heater (with only a small gap separating the two), while in the upper package, the bentonite and the heater are separated by a sand shield, about 0.2 m in thickness. Furthermore, the initial dry density of the bentonite used in the lower package ($\rho_{0,lp}$ = 1,705 kg/m^3) is lower than that of the bentonite used in the upper package ($\rho_{0,up}$ = 1,767 kg/m^3). An illustration of the different geometries can be seen in Figure 3-1 below.

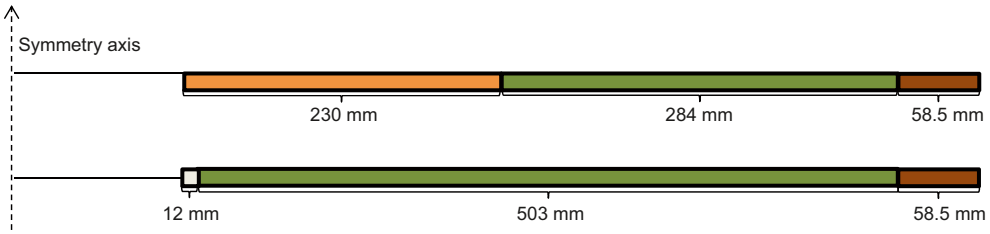

Figure 3-1. *Schematic overview of the geometries in the upper package (top) and lower package (bottom). The green colour corresponds to bentonite, orange to the sand shield, brown to the sand filter and finally white corresponds to air.*

The homogenized (or target) void ratio is here determined using a simple, one-dimensional, analytical model. The underlying assumption is that the final state (and hence the target void ratio) is reached when the radial stress in the sand and bentonite are in equilibrium. Given the different geometrical setup in the lower and upper packages respectively, the target void ratio in the two can be expected to differ.

3.2.1 Mechanical properties of the sand material

To estimate the target void ratio, and to correctly model the mechanical behaviour of the sand, we need to understand how it behaves under an applied load. The sand used is of type "Dalby sand", its behaviour under an applied load was measured as part of the preparation for TBT using oedometer tests. In Figure 3-2, the relationship between density and vertical stress, as determined in these experiments, is shown.

In the numerical models presented in this report, the sand is treated as a linear elastic material. To determine suitable values of the parameters for the sand, we use the oedometer module, M, defined as:

$$M = \frac{\sigma_v}{\varepsilon_v} \tag{3-1}$$

where σ_v is the vertical stress and ε_v the vertical strain. The oedometer module can be written in terms of the Young modulus, E, and Poisson's ratio, ν, as:

$$M = \frac{E(1-\nu)}{(1+\nu)(1-2\nu)} \tag{3-2}$$

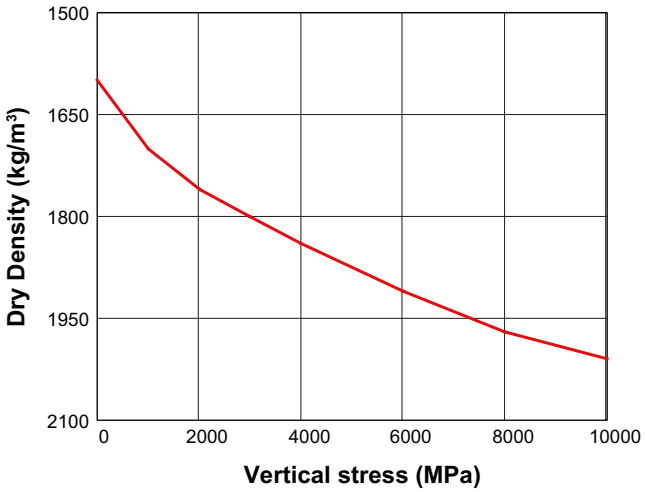

Figure 3-2. *Dry density as function of vertical stress, as measured with an odometer, for the sand used in TBT.*

The change in density with applied vertical strain is:

$$\rho_1 = \frac{\rho_0}{1 - \varepsilon_v} \tag{3-3}$$

For the purposes here, it is more convenient to write out the change in void ratio with vertical strain by combining equation (3-1) and (3-3) with the expression $e = \rho_s/\rho_d - 1$ (where ρ_s is the solid density):

$$e_1 = e_0 - (1 + e_0)\frac{\sigma_v}{M} \tag{3-4}$$

Equations (3-2) and (3-4) together now allow us to find a suitable pair of linear elastic parameters (E and v) which reproduce the experimentally measured vertical stress-strain relationship for the sand. In Figure 3-3 we plot the void ratio of the sand as a function of the applied vertical stress. The red line is the measured relationship, while the blue and green lines are derived from the set of linear elastic parameters chosen for the sand filter and shield respectively.

The difference between these two materials is the initial density (and hence initial void ratio). The sand in the filter is packed to an average density of $\rho_{0,filter} = 1{,}729$ kg/m^3 ($e = 0.533$), while the sand in the shield has an initial density of $\rho_{0,shield} = 1{,}820$ kg/m^3 ($e = 0.456$). We use $v = 0.2$ for both materials, setting $E_{filter} = 60$ MPa and $E_{shield} = 95$ MPa respectively.

However, the results from our 1D models presented below, suggest these parameters do not well reproduce the mechanical behaviour of the sand. One possible cause of this may be axial swelling of the bentonite, which would allow the sand to also move axially, effectively making it softer in the radial direction. A second set of parameters for the sand has therefore been used, with $E_{filter} = 25$ MPa and $E_{shield} = 55$ MPa respectively and $v = 0.25$ for both materials.

3.2.2 Determining the final stress-strain state at different heights in TBT

As the bentonite saturates, it starts to swell, giving rise to a swelling pressure. This pressure applies a radial load onto the sand, compressing the latter. An equilibrium state is reached when the bentonite cannot compress the sand further. The sand is initially rather loose, which has the effect that the bentonite will compress the sand quite significantly before equilibrium is reached. The final (target) void ratio of the bentonite, which sets the final swelling pressure, is thus quite different from the initial void ratio.

The swelling pressure of bentonite can be parameterized as a function of the dry density:

$$\log(p_{swell}) = c_2 \cdot \rho_d^2 + c_1 \cdot \rho_d + c_0 \tag{3-5}$$

Different suggested values for the constants c_0, c_1 and c_2 are given in Åkesson et al. (2010b), here we adopt the following set: $c_0 = -1.74$, $c_1 = 4.12\times10^{-3}$ and $c_2 = -3.94\times10^{-7}$.

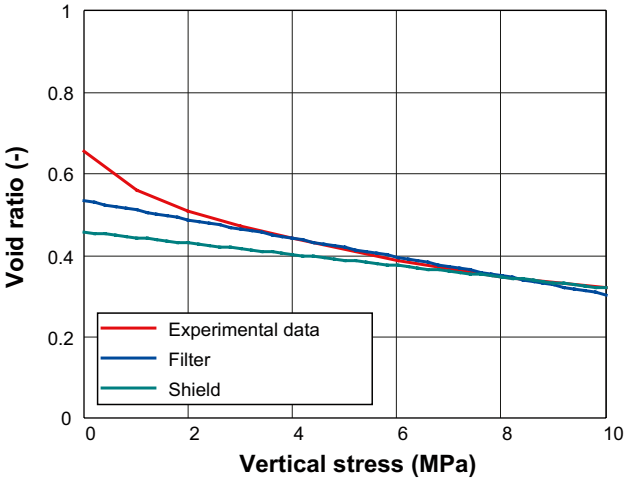

Figure 3-3. *Void ratio as function of vertical stress, as measured with an odometer, for the sand used in TBT (red line). Also included are the same relation when treating the material as linear elastic, with $v = 0.2$ for both materials, and $E_{filter} = 60$ MPa and $E_{shield} = 95$ MPa respectively.*

The radial stress produced by the bentonite does, however, not equal the swelling pressure. In order to calculate the former one should include the shear strength of bentonite. As reported in Åkesson et al. (2010b), the relation between the deviatoric stress, q, and the mean stress, p, can be written as:

$$q = a \cdot p'^{b} \tag{3-6}$$

Suitable parameters here are a = 0.5 and b = 0.77, if the stresses are given in MPa. By assuming that the axial stress equals the tangential stress, and that the latter two are larger than the radial stress, we find that the radial stress produced by the bentonite, $\sigma_{rr,B}$, is:

$$\sigma_{rr,B} = \frac{3p_{swell} - 2q(p_{swell})}{3} \tag{3-7}$$

Here we have assumed that $p' = p_{swell}$.

The density of the bentonite and sand in a thin slice of the experiment only depends on the inner and outer radii, and the transition radius between sand and bentonite. The final inner radius in both the lower and the upper package is equal to the radius of the heater (r_h = 0.305 m), which is considered to be immovable. Similarly, the outer radius equals the radius of deposition hole, of r_r = 0.8785 m.

Lower package

Initially, there is a small gap between the heater and the bentonite. At R3/4 this gap is approximately 12 mm wide, hence, initially the bentonite's inner radius is r_{ii} = 0.317 m.

The outer radius of the bentonite is initially situated at r_{oi} = 0.820 m. However, as the bentonite swells, this radius will increase to its final value. The density of the sand, ρ_F, and bentonite, ρ_{Bl}, respectively, as a function of the contact radius between the sand filter and the bentonite, r_{fb}, is:

$$\rho_F(r_{fb}) = \frac{\rho_{0,F}(r_r^2 - r_{oi}^2)}{r_r^2 - r_{fb}^2} \tag{3-8}$$

$$\rho_{Bl}(r_{fb}) = \frac{\rho_{0,Bl}(r_{oi}^2 - r_{ii}^2)}{r_{fb}^2 - r_h^2} \tag{3-9}$$

We have $\rho_{0,F}$ = 1,729 kg/m^3 and $\rho_{0,Bl}$ = 1,704 kg/m^3 and solving the relation that $\sigma_{rr,B}(\rho_{Bl}(r_{fb})) = \sigma_{sand}(\rho_F)$ numerically using MathCAD, we find that the target void ratio is e_T = 0.686.

Upper package

In the upper package, a sand shield has been added to the geometry. This makes it necessary to solve also for the inner radius of the bentonite, r_{bs}. Initially, this inner interface is located at r_{ii} = 0.535 m. The density of the sand shield, ρ_S, and the bentonite, ρ_{Bu}, can be written as:

$$\rho_S(r_{fb}) = \frac{\rho_{0,S}(r_{ii}^2 - r_h^2)}{r_{bs}^2 - r_h^2} \tag{3-10}$$

$$\rho_{Bl}(r_{bs}, r_{fb}) = \frac{\rho_{0,Bu}(r_{oi}^2 - r_{ii}^2)}{r_{fb}^2 - r_{bs}^2} \tag{3-11}$$

In the upper package we have $\rho_{0,F}$ = 1,729 kg/m^3, $\rho_{0,S}$ = 1,820 kg/m^3 and $\rho_{0,Bu}$ = 1,767 kg/m^3. Furthermore, the radius of the interface between the bentonite and the sand filter, is here r_{oi} = 0.819 m. To determine the value of r_{fb} and r_{bs} in the final state, we numerically solve the relations $\sigma_{rr,B}(\rho_{Bu}(r_{fb})) = \sigma_{sand}(\rho_F)$ and $\sigma_{rr,B}(\rho_{Bu}(r_{bs})) = \sigma_{sand}(\rho_F)$ giving a target void ratio of e_T = 0.692.

3.3 TBT – Modelling task 1: Ring 3/4

The lower package in TBT is particularly interesting in terms of the high temperatures reached in the bentonite (T>150°C). To test our ability to correctly reproduce the experimental data, we have analyzed models of a thin slice of the geometry, representing the conditions at about mid-height of the lower heater.

3.3.1 Geometry – Task 1

The geometry consists of a thin slice (1 cm high), with rotational symmetry around the y-axis, representing a thin disk. The heater is not part of the geometry, instead its influence is handled as a boundary condition (heat flux) applied at the innermost radius (r = 0.305 m). The geometry, with assigned materials and mesh, is depicted in Figure 3-4. The air-filled slot is expected to close quickly due to the swelling of the bentonite. In models which do not include this swelling (i.e. models which does not solve the mechanical problem) we have therefore filled the slot with bentonite from the start of the model. The mesh consists of 102 nodes, with 1 quadrilateral (hereafter *qL*) element in the air slot, 44 qL elements in the buffer, and 5 qL elements in the sand filter.

3.3.2 Material properties

The materials included are bentonite, sand and slot material (air, only in THMg simulations). The properties of these materials are, with a few exceptions, taken from Åkesson et al. (2010b).

The constitutive relations, as well as the parameter values used for the different materials when modelling R3/4, can be found in Table 3-1, Table 3-2, Table 3-3, Table 3-4, Table 3-5, Table 3-6 and Table 3-7 respectively. For the bentonite, only the constitutive relations for the conductive heat flux and retention capability differ from those listed in the SR-Site Data report (Åkesson et al. 2010).

Table 3-1. Hydraulic and solid phase properties.

Material	Solid density [kg/m^3]	Spec. heat cap. [J kg^{-1} K^{-1}]	Intr. perm. [m^2]	Liquid rel. perm. ($k_{rl} = S_{rl}^{\delta}$) δ	Gas rel. perm. ($k_{rl} = AS_{rl}^{\delta}$) A	δ	Tortuosity, τ_v
Bentonite	2,780	800	2.0 x 10^{-21}		10^8		
Sand filter	2,650	800	1.0 x 10^{-15}	3	1	4	1
Slot	2,780	800	1.0 x 10^{-30}		1		

S_l denotes liquid saturation.

3.3.3 Conductive heat flux

The bentonite in TBT experiences very high temperatures (T≥150°C in the lower package, Goudarzi et al. 2010), and hence a significant dehydration can be expected to occur. As discussed in Åkesson et al. (2010b), the otherwise recommended constitutive relation for thermal heat flux:

$$\lambda(S_l) = \lambda_{sat}^{S_l^n} \quad \lambda_{dry}^{(1-S_l)^{1/n}} \tag{3-12}$$

, where S_l denotes liquid saturation, and λ_{sat} and λ_{dry} denotes the thermal conductivity at saturated and dry conditions respectively, does not agree well with experimental data at low saturation levels. A more accurate constitutive relation in such a situation is that proposed by Chen and Ledesma (2009):

$$\lambda(S_l) = \lambda_{sat} sin^2\left(\frac{\pi S_l}{2}\right) + \quad \lambda_{dry} cos^2\left(\frac{\pi S_l}{2}\right). \tag{3-13}$$

Equation (3-13) is not included in CODE_BRIGHT v3. However, for this project we have added it to the source code, and it is used for bentonite in all models. We summarize the parameters and constitutive laws used to describe the conductive heat flux in all materials in Table 3-2.

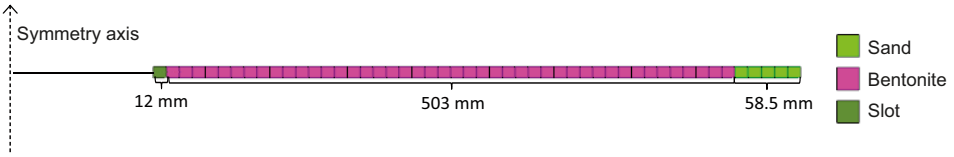

Figure 3-4. *Overview of the geometry used for R3/4, including materials and mesh.*

Table 3-2. Conductive heat flux.

Material	Law	λ_{sat} [W mK^{-1}]	λ_{dry} [W mK^{-1}]
Bentonite	$\lambda(S_l) = \lambda_{sat}\sin^2(\pi S_l/2) + \lambda_{dry}\cos^2(\pi S_l/2)$	0.5	1.3
Sand filter	$\lambda(S_l) = \lambda_{sat}S_l + \lambda_{dry}(1-S_l)$	0.7	1.2
Slot		0.7	1.2

3.3.4 Retention properties

The "standard" retention curve when modelling bentonite (Åkesson et al. 2010b) is the van Genuchten curve:

$$S_l = \left(1 + \left(\frac{\Psi}{P_0}\right)^{\frac{1}{1-\lambda_0}}\right)^{-\lambda_0}. \qquad (3\text{-}14)$$

Here Ψ is the suction, while P_0 and λ_0 are fitting parameters. However, this equation fails to reproduce the experimentally determined data of MX-80 (Dueck 2004) at high suction (see Figure 3-5). An extended version of equation (3-14), with additional fitting parameters P_1 and λ_1, is included in CODE_BRIGHT v3:

$$S_l = \left(1 + \left(\frac{\Psi}{P_0}\right)^{\frac{1}{1-\lambda_0}}\right)^{-\lambda_0}\left(1 - \frac{\Psi}{P_1}\right)^{\lambda_1}. \qquad (3\text{-}15)$$

With equation (3-15) it is possible to reproduce the measured retention properties of MX-80 bentonite fairly well. An example of this can be seen in Figure 3-5 (left panel, green line) where we plot equation (3-15) using the best fit parameters to MX-80 bentonite with void ratio equal to 0.626 (Åkesson et al. 2010b). However, using equation (3-15) in numerical models gives the unwanted behaviour that Ψ can never exceed the value of P_1. Additionally, when $\Psi \rightarrow P_1$ the saturation goes to zero, which is unrealistic. The value of P_1 suggested in Åkesson et al. (2010b) puts a limit on the suction which the bentonite can reach (s_{max} = 280 MPa) which was exceeded in some of our models.

To improve the behaviour of the retention curve at low suction we have implemented an additional retention curve description in CODE_BRIGHT v3 (Fredlund and Xing 1994):

$$S_l = \left[1 - \frac{\ln(1 + \Psi/P_1)}{\ln(1 + 10^6/P_1)}\right]\left\{\ln\left[e + \left(\frac{\Psi}{P_0}\right)^{\lambda_0}\right]\right\}^{-\lambda_1}. \qquad (3\text{-}16)$$

In Figure 3-5 (left panel) we plot the best fit to experimental data (Dueck 2004) using equation (3-16), determined by least-squares minimization. The fit is good both at high and low suction, and has the desired increase in suction for very low saturation. Using equation (3-16) we have also varied the shape of the retention curve at low suction, both increasing and decreasing the steepness of the curve in this range (see right panel of Figure 3-5). The primary purpose of this exercise is to understand how small changes on the wet side of the retention curve can alter the hydration rate of bentonite. All the retention-curve parameters used in the numerical models are summarized Table 3-3.

Table 3-3. Water retention curves used when modelling R3/4. Three different sets of parameters were used for the retention curve of Fredlund and Xing (1994); these will hereafter be referred to as Fr1, Fr2 and Fr3 respectively.

Material	Retention curve	P_0 [MPa]	λ_0 [–]	P_1 [MPa]	λ_1 [–]
Bentonite Fr1	$S_l = C(\Psi, P_1)\left\{\ln\left[e + \left(\frac{\Psi}{P_0}\right)^{\lambda_0}\right]\right\}^{-\lambda_1}$	139.44	1.97	6.7	2.28
Bentonite Fr2		188.548	2.718	2.483	2.451
Bentonite Fr3		69.228	1.811	2.544 x 10^4	1.872
	$C(\Psi, P_1) = 1 - \frac{\ln(1 + \Psi/P_1)}{\ln(1 + 10^6/P_1)}$				

Table 3-3. Continued.

Material	Retention curve	P_0 [MPa]	λ_0 [–]	P_1 [MPa]	λ_1 [–]
Sand filter	$S_l = \left(1 + \left(\frac{\Psi}{P_0}\right)^{\frac{1}{1-\lambda_0}}\right)^{-\lambda_0} \left(1 - \frac{\Psi}{P_1}\right)^{\lambda_1}$	0.005	0.6	700	1.1
Bentonite ext_vG		5.222	0.05	280	0.9
Bentonite vG	$S_l = \left(1 + \left(\frac{\Psi}{P_0}\right)^{\frac{1}{1-\lambda_0}}\right)^{-\lambda_0}$	43.5	0.38		

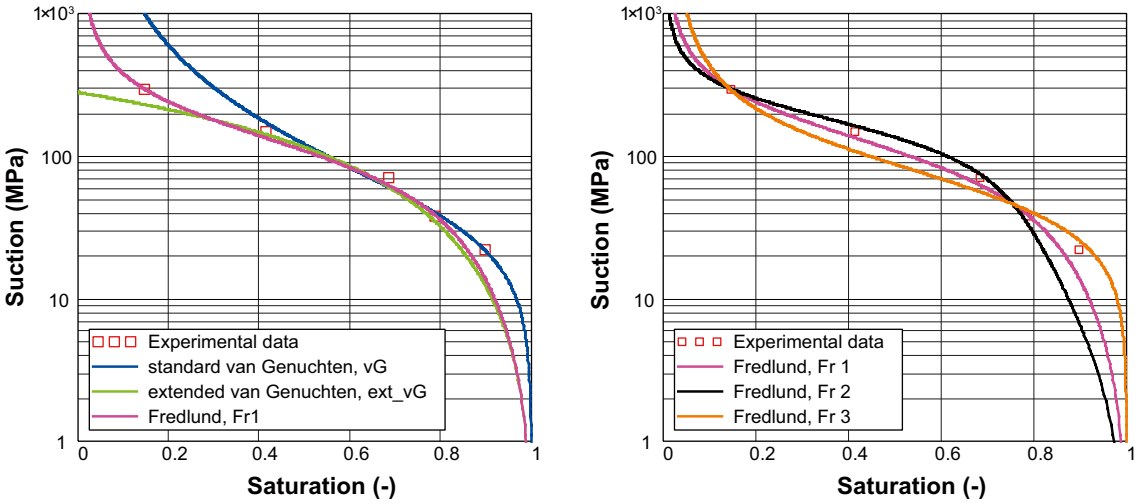

Figure 3-5. Retention curves for bentonite material with e_0 = 0.626. The equations used, with corresponding sets of parameters, can be found in Table 3-3.

3.3.5 Liquid density

The density of water is temperature dependent (Schmidt and Grigull 1982). The unit volume of water increase with temperature, and hence the density decreases. In CODE_BRIGHT v3, this is taken into account, as the water density is a function of temperature (and liquid pressure):

$$\rho_l = \rho_{l,0} \exp[4.5\times10\text{–}4(P_l - 0.1) - \alpha T] \qquad (3\text{-}17)$$

The coefficient α determines the change of ρ_l with temperature; the standard value used in CODE_BRIGHT is $\alpha = 3.4\times10^{-4}$. However, in reality, α = α(T); the value increasing with increasing temperature. Setting $\alpha = 3.4\times10^{-4}$ is reasonable for temperatures below 70°C, but above that temperature, the liquid density given by equation (3-17) differs significantly from the experimentally determined values (see Figure 3-6). Given that the bentonite in R3/4 reaches temperatures of up to 150°C at r = 0.320 m (Goudarzi et al. 2010) choosing a different value of α is motivated. As we want the liquid density to behave realistically only in the temperature interval 20°C to 150°C, it is also motivated to change the value of $\rho_{l,0}$, i.e. the density at T = 0°C in equation (3-17). We find that a suitable choice of parameters is $\rho_{l,0}$ = 1,010.0 kg/m^3 and $\alpha = 6\times10^{-4}$°C^{-1} (see Figure 3-6).

Table 3-4. Liquid density.

Material	Law	$\rho_{l,0}$ [kg/m^3]	α [°C^{-1}]
Bentonite			
Sand filter	$\rho_l = \rho_{l,0} \exp[4.5\times10\text{–}4(P_l - 0.1) - \alpha T]$	1,002.6/1,010.0	3.4/6 10^{-4} **
Slot			

**The alternate values $\rho_{l,0}$ = 1,010.0 kg/m^3 and $\alpha = 6\times10^{-4}$°C^{-1} are used in models TBTR4_THg _A6, and TBTR4_THMg_A2 & A4 (see Table 3-10 and Table 3-11).

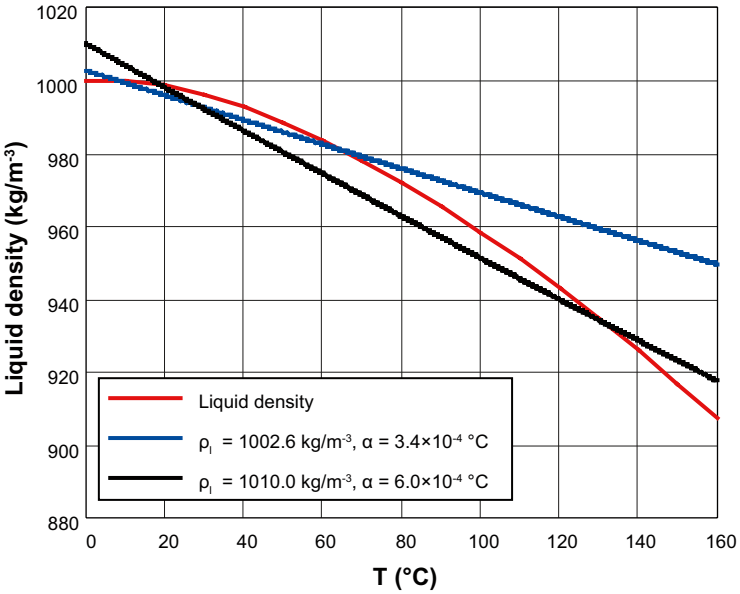

Figure 3-6. *The change in water density with temperature, both the experimentally determined relation (red line (Schmidt and Grigull 1982), and the two relations used in the modelling exercises here (blue and black lines).*

3.3.6 Mechanical parameters

The parameters describing the elastic part of bentonite in BBM are given in (Åkesson et al. 2010b). For convenience, they are summarized here in Table 3-5.

Table 3-5. BBM model – Elastic parameter values.

Material	κ_{i0}	κ_{s0}	K_{min}	v	α_{ss}	α_{sp}	α_i	p_{ref}
Bentonite	0.12	0.3	20	0.2	–0.01	*	–0.021	1

* The α_{sp} parameter is replaced by an in-house development of the code; see Åkesson et al. (2010b).

The value of α_{ss} is not given in the SR-Site Data report, and was here chosen such that the maximum shrinkage of the bentonite during drying, in terms of void ratio ($de \approx 0.2$), corresponds to experimental data (Börgesson 2001).

A strategy for determining the plastic parameters is described in the data report, with only the target void ratio as input. This was calculated in section 3.2.2, for R4 the determined target void ratio is 0.686. The corresponding plastic parameters are summarized in Table 3-6.

Table 3-6. BBM model – Plastic parameter values.

Material	e_0	e_T	λ_0	r	β	ρ	k	p_{s0}	p_c	M	α	p_0*
Bentonite	0.631	0.686	0.158	0	0	0	0	2.7	1	0.23	0.5	21.0

The sand filter was treated as a linear elastic material; the Young modulus and Poisson's ratio were determined so as to correspond with 1) the initial dry density of the sand and 2) the measured vertical stress-strain relationship for the sand. The evaluated parameters were validated in section 3.2.1 and are here listed in Table 3-7.

Table 3-7. Linear elastic materials – Parameter values.

Material	E [MPa]	υ
Sand filter	60	0.2

3.3.7 Initial and boundary conditions

The initial conditions are chosen in accordance with the material data given in the installation report (Johannesson et al. 2010). A suction of 46 MPa corresponds to the initial water content measured in the bentonite before installation. All adopted values are summarized in Table 3-8.

Table 3-8. Initial conditions used when modelling R3/4.

Material	e/n	P_l (MPa)	P_g (MPa)	T (°C)	σ (MPa)
Bentonite	0.631/0.387				
Sand Filter	0.533/0.348	–45.9	0.1	23	–0.11 ***I****
Slot	999/0.999				

*Here ***I*** is the unit matrix.

No horizontal displacement was allowed on the vertical edges of the model, to mimic the effect of the impenetrable surfaces of the heater and rock. Furthermore, as it is a one-dimensional model, no vertical displacement was allowed on the top and bottom surfaces. The mechanical boundary conditions are illustrated in the lower part of Figure 3-7.

To mimic the power output of the heater we apply a heat flux on the "heater surface", (i.e. the left vertical boundary), see Table 3-9.

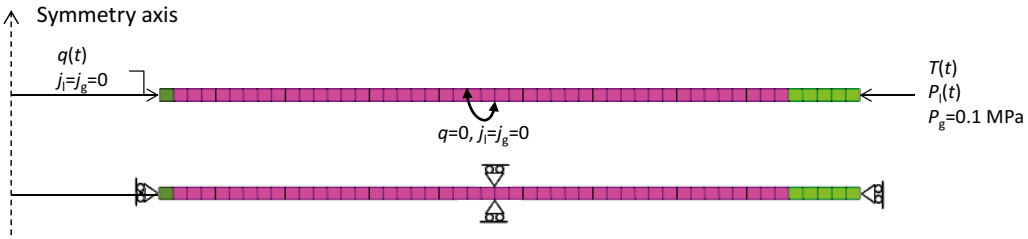

Figure 3-7. *Hydraulic and thermal (upper part), as well as mechanical boundary conditions (lower part), used when modelling R3/4. The time-dependance of the temperature, liquid pressure and heat flux boundary conditions are elaborated on in the text.*

Table 3-9. Heater power (lower package), as well as heat flux boundary condition applied in the 1D model of R3/4, used to mimic the power output of the heater.

Time (days)	Heater Power (W)	q (W/m^2)
0–8	900	156.55
8–15	1,200	208.73
15–1,171	1,500	260.91
1,171–1,695	1,600	278.30
1,695–1,702	1,700	298.70
1,702–1,709	1,800	313.10
1,709–1,716	1,900	330.49
1,716–2,336	2,000	347.88
2,336–2,347	2,000–0	Linearly decreasing: 347.88–0
2,347–2,600	0	0

On the “rock surface”, we apply a temperature boundary condition. It is calculated by assuming three line sources and three mirror sources, thereby taking into account the effect of the nearby CRT heater, the cooling of the surrounding rock and tunnel, as well as heaters in TBT. The method has previously been used in Goudarzi et al. (2005) and is based on the work of Ikonen (2003). The temperature applied on the rock surface, as a function of time, is shown in Figure 3-8.

The liquid pressure in the sand filter was not measured during the first 562 days. Thus, during this time, we have assumed that no overpressure was present, and hence the liquid pressure at the rock surface is kept at 0.1 MPa. However, as of day 562, the actual filter pressure was monitored, and steps were later taken to produce an overpressure in the filter. This variation has been included in the THg models presented below (see Figure 3-9 for an overview), but, for computational reasons, not in the THMg models.

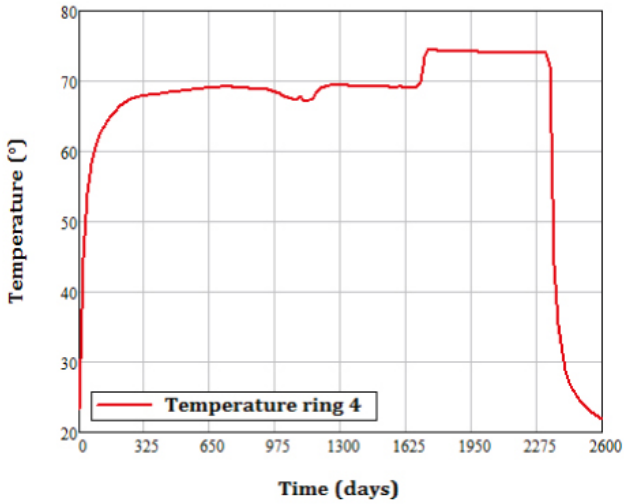

Figure 3-8. *Temperature boundary condition used in the models of R3/4. The temperature was calculated analytically following the model described in Goudarzi et al. (2005).*

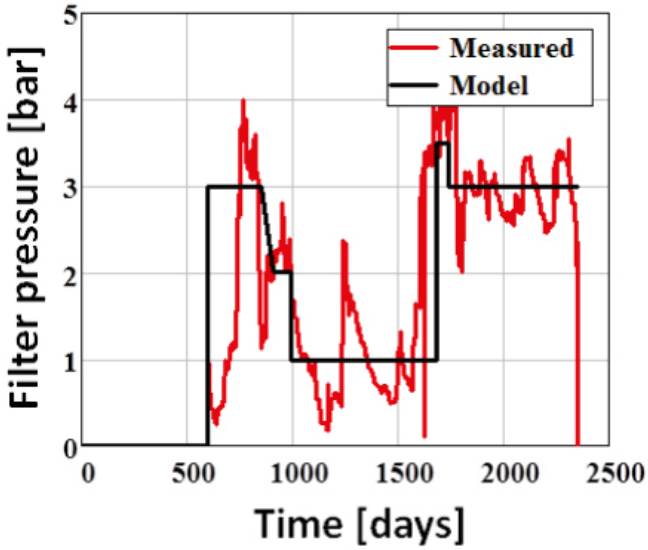

Figure 3-9. *The filter pressure as measured (red line) and that applied in the THg models presented below (red line).*

3.3.8 Interpretation of experimental data

An important question is the reliability of the sensors used in TBT and how to interpret their results. A more detailed discussion of the behaviour of the RH-sensors can be found in section 5.6, but it is worth to point out a few things here. Firstly, the rise in RH at r = 0.360 m, starting on day 860, coincides with the sealing of a leak in a pressure transducer situated just 0.25 m below the RH-sensor. It appears likely that the gas leakage was preventing the buffer from becoming saturated at this radius by keeping p_g close to atmospheric pressure (see also Figure 6-21, right panel). This view is supported by the observation that the RH rose to around 90% in a little less than 300 days once the leak was sealed. We have not included this leakage in our models, and hence we do not expect to reproduce the RH evolution measured at r = 0.360 m in R3/4.

Secondly, in the interval 95% to 100% the accuracy of the RH sensors decrease, and hence the sharp rise from RH = 95% to RH = 100% at, for example, r = 0.710 m close to day 80, does not necessarily represent the actual conditions. Still, if the measured results are accurate, they have important implications for the interpretation of the results (see section 5.6).

Another important consideration is how to interpret the signal from the pore pressure sensors. They indicate that an overpressure built up at all radii in R3/4 shortly after day 1,700, coinciding with the increase in the heater power output. While it may indicate that the buffer was fully saturated at this point, the increase in pore pressure being caused by thermal expansion of the water, the signal could also be caused by an increase in gas pressure.

At the time of dismantling, the saturation of the bentonite was measured. In R3/4, the saturation was measured to be between 0.92 and 1.0, with the driest point closest to the heater. This might indicate that the buffer was never fully saturated. However, another plausible explanation is that the cooling of the buffer led to a decrease in water volume, causing the saturation to decrease. This can in part explain the gradient seen in the saturation levels, as the decrease of water volume would have been most significant at small radii, where the temperature was highest.

3.3.9 Results – TH(g) models

A total of 10 THg models have been analyzed, varying the retention properties and hydraulic conductivity of the bentonite, as well as the behaviour of the water density with temperature. A summary of the variations between the different models can be found in Table 3-10. The motivation for this exercise was to see how sensitive the hydration rate of the buffer material is to changing the hydraulic properties of the material. A further motivation is that the hydration rate is not well reproduced using the standard set of parameters, taken from Åkesson et al. (2010b), and as such it is interesting to see whether a change in the parametric description of bentonite can produce results in better agreement with experimental data.

Table 3-10. Overview of THg models done involving R3/4. For further details on retention curves and parameters, see section 3.3.2.

Model	Bentonite retention curve	Additional parameter variation
TBTR4_THg_A1	van Genuchten, vG	
TBTR4_THg_A2	ext. van Genuchten, ext_vG	
TBTR4_THg_A3	Fredlund, Fr1	
TBTR4_THg_A4	Fredlund, Fr2	
TBTR4_THg_A5	Fredlund, Fr3	
TBTR4_THg_A6	Fredlund, Fr3	$\rho_{l,0}$ = 1,010.0 kg/m^3 and $\alpha = 6\times10^{-4}$°C^{-1}
TBTR4_THg_A7	ext. van Genuchten, ext_vG	$k_{0,Bentonite} = 4.0\times10^{-21}$ m^2
TBTR4_THg_A8	Fredlund, Fr3	$k_{0,Bentonite} = 4.0\times10^{-21}$ m^2
TBTR4_THg_A9	Fredlund, Fr3	$k_{0,Bentonite} = 4.0\times10^{-21}$ m^2, $\tau_{vapour} = 0.5$
TBTR4_THg_A10	Fredlund, Fr3	$p_{l,rock}$ = 0.4 MPa during first 377 d

Temperature profiles

The temperature in R3/4 was measured continuously at 25 radial positions, providing a detailed picture of the radial temperature distribution at any given time. To compare the temperatures in our models with experimental data, we show the radial temperature distribution from TBTR4_THg_A1 (solid lines) together with the measured data (crosses) in Figure 3-10 at five different times. The model reproduces the measured temperatures with very good accuracy, adding confidence in the thermal boundary conditions used, and to some degree also in the thermal conductivity parameterization used. Although small differences in the temperature gradient can be seen between the different models, due to the different saturation evolution, the temperatures in Figure 3-10 are representative of the results, i.e. all models reproduce the measured temperatures well.

Retention properties

In models TBTR4_THg_A1 through TBTR4_THg_A5 we only vary the retention curve used for the bentonite rings. The RH evolution seen in these models are depicted in Figure 3-11, Figure 3-12 and Figure 3-13 (left part only) respectively, which also include the measured data from TBT (dashed lines).

van Genuchten retention curves

The standard van Genuchten retention curve does not agree well with the experimentally determined saturation at high values of suction (e.g. Figure 3-5), and hence it is not well suited to use in this modelling exercise (due to the low saturation reached in the bentonite). Nevertheless, in most modelling tasks it is the standard choice, and as such we include it here for completeness (model TBTR4_THg_A1). The RH-evolution at four different radii in the bentonite is shown in Figure 3-11 (left panel, solid lines), together with data from TBT (dashed lines). The RH in the model, particularly at small radius, reaches very low levels. For example, at r = 0.360 we find values close to 30%, but no evidence of such an extensive dehydration was seen in TBT. The model does, however, recover from this strong dehydration, and reach RH levels of, or close to, 100% at all radii shortly before the heaters are turned off.

As explained above, the extended version of van Genuchten's retention curve can better reproduce the retention properties of MX-80 bentonite at low saturation/high suction. In model TBTR4_THg_A2, this retention curve has been used. We plot the results in Figure 3-11 (right panel, solid lines). However, using the extended van Genuchten curve does not improve the results with respect to the measured evolution; in fact the drying is equally strong, and in addition the later wetting of the buffer is significantly slower in this model.

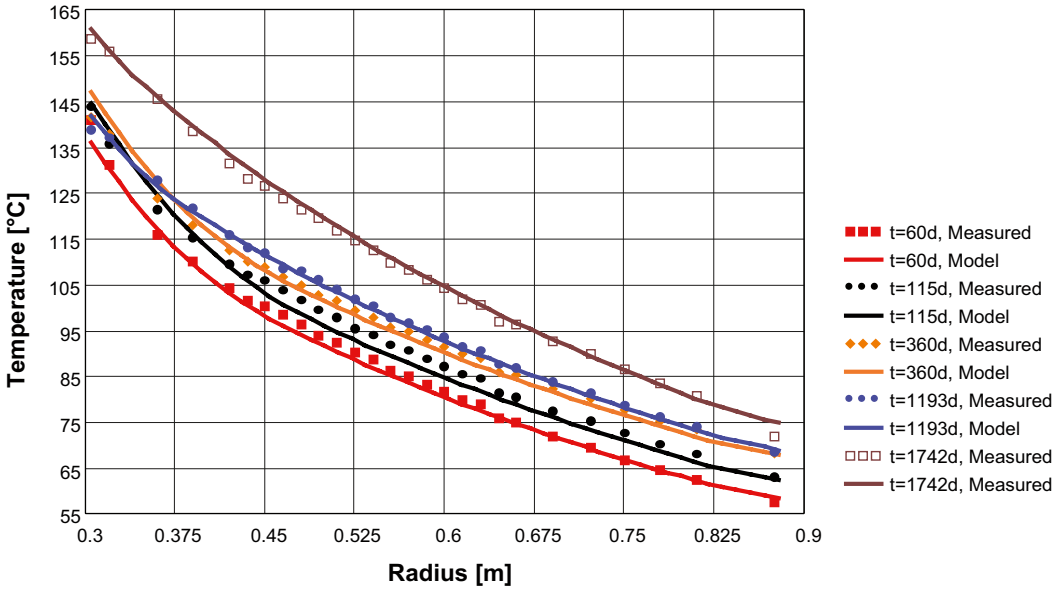

Figure 3-10. *The radial temperature distribution in R3/4 at five different points in time during the experiment. Solid lines are from the model TBT_R4_THg_A1, while the points are the experimentally measured values.*

Fredlund retention curves

The RH evolution from the models with retention curves based on the work of Fredlund is plotted in Figure 3-12 and Figure 3-13 (left panel only). In general they are also too dry, in particular at small radii. However, the retention curve Fr3 (used in model TBTR4_THg_A5) improves the result of the model with respect to the measured RH evolution somewhat, even though also in this case, the drying at small radii is much stronger than what was measured. One important drawback of the Fredlund retention curves used here is that no temperature dependence is included. Hence, the saturation in the bentonite remains almost constant until the sand filter is (artificially) saturated, at t = 15 days for these models, which is inconsistent with experimental data. The van Genuchten relations do include a dependence on temperature, and as such agree better with experimental data during the first 15 days or so (see e.g. Figure 3-11, left panel).

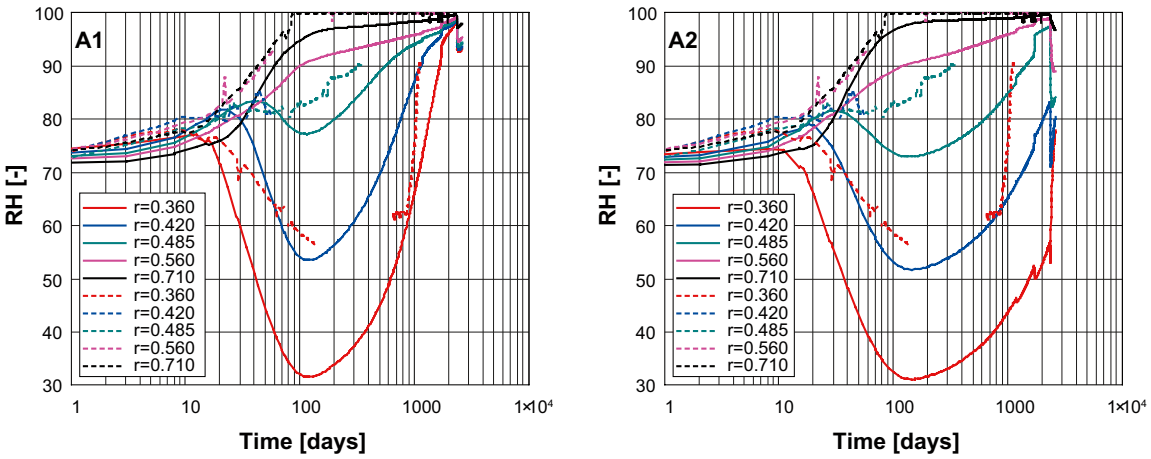

Figure 3-11. RH evolution seen in runs TBTR4_THg_A1 and TBTR4_THg_A2. Model data are in solid lines, while measured TBT data are in dashed lines. In TBTR4_THg_A1 the standard van Genuchten retention curve was used for the bentonite, while TBTR4_THg_A2 uses the extended version (ext_vG).

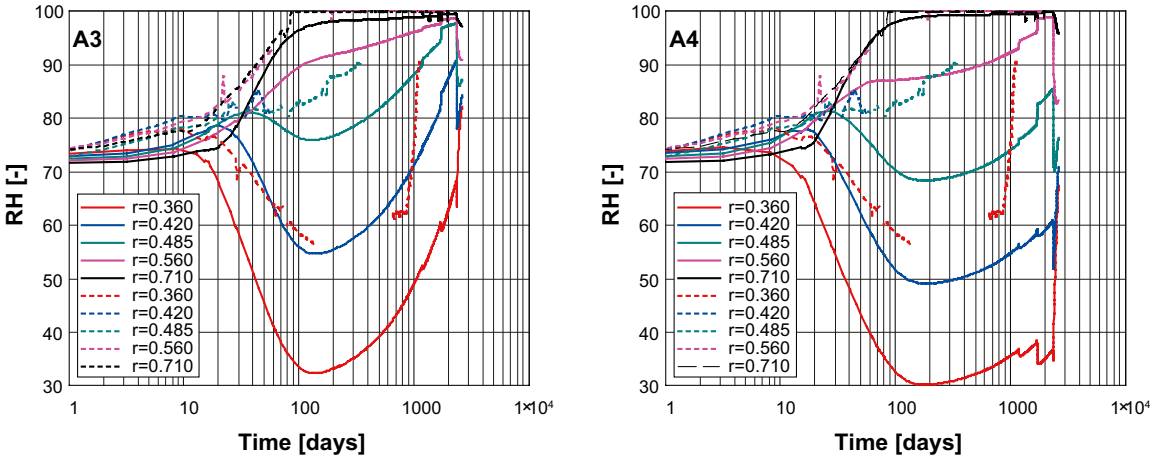

Figure 3-12. RH evolution seen in runs TBTR4_THg_A3 and TBTR4_THg_A4. Model data are in solid lines, while measured TBT data are in dashed lines. Here we have used two variations of the retention curve based on the work of Fredlund for the bentonite. In TBTR4_THg_A3 a curve we use Fr1 and in TBTR4_THg_A4 Fr2 (see Table 3-3 for more on these retention curves).

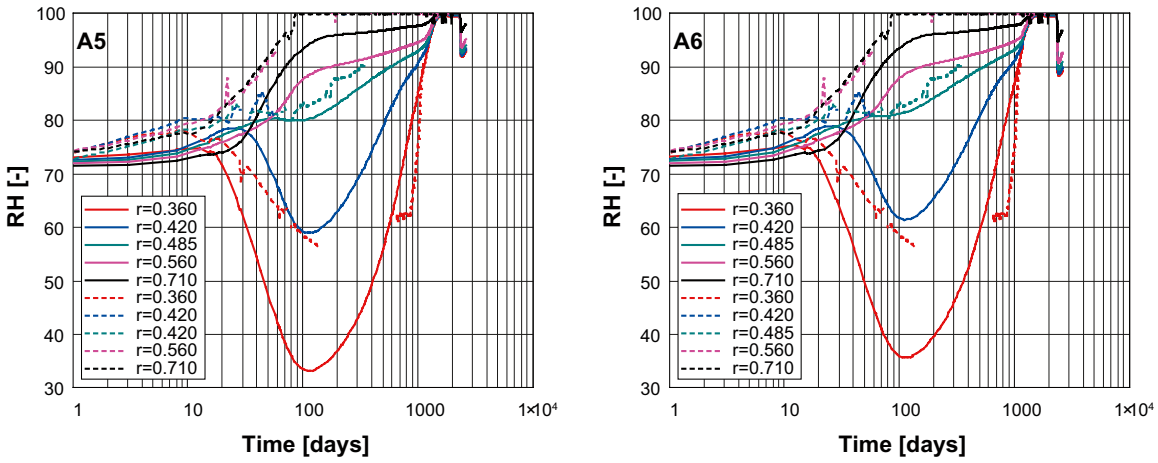

Figure 3-13. *RH evolution seen in runs TBTR4_THg_A5 and TBTR4_THg_A6. Model data are in solid lines, while measured TBT data are in dashed lines. In both models we use the retention curve Fr3 (see Table 3-3). In TBTR4_THg_A6 we have also changed the volumetric expansion coefficient of water (see section 3.1.7). The result of this is a slight increase in the minimum RH-levels reached, as well as a larger RH-gradient at the end of the experiment.*

Volumetric expansion of water

The effects of changing the temperature dependence of the liquid density on the evolution of RH and liquid saturation can, in general, be expected to be rather small. However, it could be very important during the cooling phase of the field experiment, and hence for the final saturation profile. In the model TBTR4_THg_A6 we have increased the volumetric expansion of water with temperature such that it better corresponds with laboratory measurements in the temperature interval in question here (see Figure 3-6 and Table 3-4). The time-evolution from this model is shown in the right panel of Figure 3-13, and should be compared to the reference model in the left panel, in which standard parameters were used for the volumetric expansion of water. The general evolution is rather similar, although the drying in the inner region is somewhat lessened. The gradient in RH at the end of the model is significantly steeper, with the inner regions being dryer than in the reference case. This has important effects on the final saturation profile, as discussed further below.

Intrinsic permeability and vapour tortuosity

The hydration rate of bentonite is strongly dependant on the intrinsic permeability. The value used here comes from several different experimental measurements, summarized in (Åkesson et al. 2010b). However, as discussed there, for void ratios below 0.65 the actual value is uncertain, and a sensitivity analysis, spanning a range of +100% to –40% in intrinsic permeability, is motivated. As the problem in the models presented above is a too slow hydration rate, we here only include one part of this sensitivity analysis, in which we increase the bentonite's intrinsic permeability by 100% (models TBTR4_THg_A7 and A8, see Figure 3-14). These models show a somewhat lesser dehydration, while at the same time becoming fully saturated much more quickly.

The vapour tortuosity coefficient, τ, sets the rate of vapour transport in the model. Typically, one use a value equal to one, but a lower value may also be relevant. As τ sets the rate of vapour diffusion in the material, lowering the value should lessen the dehydration in the high temperature region. In model TBTR4_THg_A9 we use $\tau = 0.5$, but otherwise keep the same material properties is in TBTR4_THg_A8. The result is, as expected, a higher hydration rate, which agrees rather well with experimental data. One remaining discrepancy is the lack of a temperature dependence on the retention curve, which could explain the early increase ($t<20$ days) in RH seen in the field experiment.

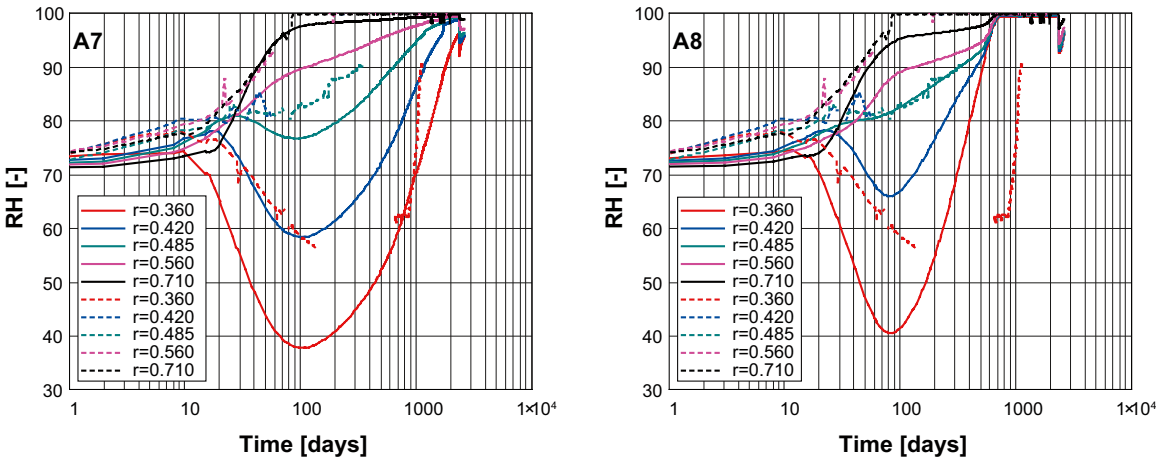

Figure 3-14. *RH evolution seen in runs TBTR4_THg_A7 and TBTR4_THg_A8. Model data are in solid lines, while measured TBT data are in dashed lines. Here we have used two variations of the retention curve based; in TBTR4_THg_A7 ext_vG and in TBTR4_THg_A8 Fr3. Furthermore, in both models we have increased the intrinsic permeability of the bentonite by 100%, to* 4.0×10^{-21} m^2.

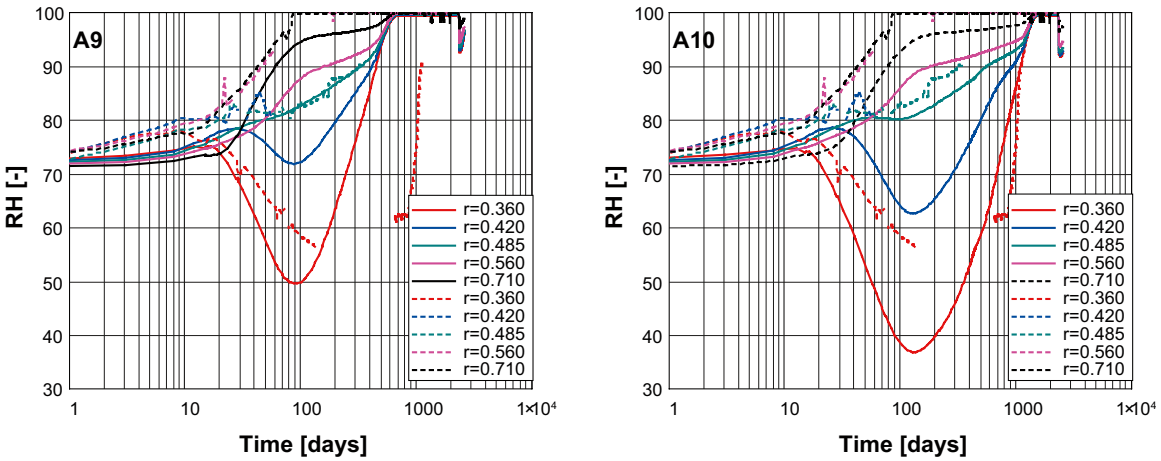

Figure 3-15. *RH evolution seen in runs TBTR4_THg_A9 and TBTR4_THg_A10. Model data are in solid lines, while measured TBT data are in dashed lines. In both models we use the retention curve Fr3 (see section 3.1.6). In TBTR4_THg_A9 we have increased the intrinsic permeability of the bentonite by 100%, to* 4.0×10^{-21} m^2 *and decreased the vapour tortuosity constant to 0.5. In TBTR4_THg_A10 on the other hand, we have increased the liquid pressure at the rock surface to 0.4 MPa during the first 377 days.*

Hydraulic boundary conditions

As no measurements of the liquid pressure in the sand filter were done at the beginning of the field experiment the actual pressure in the filter is unknown during this time. In the previous models the filter pressure was assumed to be atmospheric during this period However, it may be that the liquid pressure during this time was higher than atmospheric, which has been assumed in the previous models. We have therefore done one model in which we prescribed a liquid pressure of 0.4 MPa on the outer filter boundary during the first 448 days (the time of the first hydraulic test). The RH evolution in this model (In TBTR4_THg_A10) can be seen in Figure 3-15. The retention curve Fr3 was used for the bentonite material, and hence, the evolution should be compared to that in TBTR4_THg_A5 (see Figure 3-13). No significant difference can be seen in the outer parts. However at r = 0.420 m, and r = 0.360 m in particular, a slight increase in the hydration rate is observed. The model does not become as dry as TBTR4_THg_A5, suggesting that an initial overpressure in the sand filter might in part explain the difference between the measured data and our models.

Final saturation profile

During the dismantling of the field experiment, the radial saturation profile was determined in R4. We can compare this profile with that in the models at t = 2,600 d. As can be seen in Figure 3-16, most of the models are either significantly drier or wetter than what was measured; only the model TBTR4_THg_A7 reproduces the measured profile. An important feature here is that of the importance of the volumetric expansion of water. Models TBTR4_THg_A5 (standard value) and A6 (increased volumetric expansion) shows significant differences. While A5 is almost fully saturated, the profile in A6 shows a much more significant decrease in saturation in the inner regions, which is consistent with that the temperature was much higher here than in the outer parts. In conclusion, it appears that the radial saturation profile as measured during dismantling may either have arisen because the bentonite was not fully saturated once the heaters were turned off (model A7) or alternatively because of the change in liquid density due to the cooling in the final phase (model A6).

3.3.10 Results – THM(g) models

To do realistic models of TBT, it is necessary to include thermal and hydraulic, as well as mechanical processes. We have completed four such models, varying also here the hydraulic and retention properties of the bentonite, as well as the liquid density's temperature dependence. The models are summarized in Table 3-11 below:

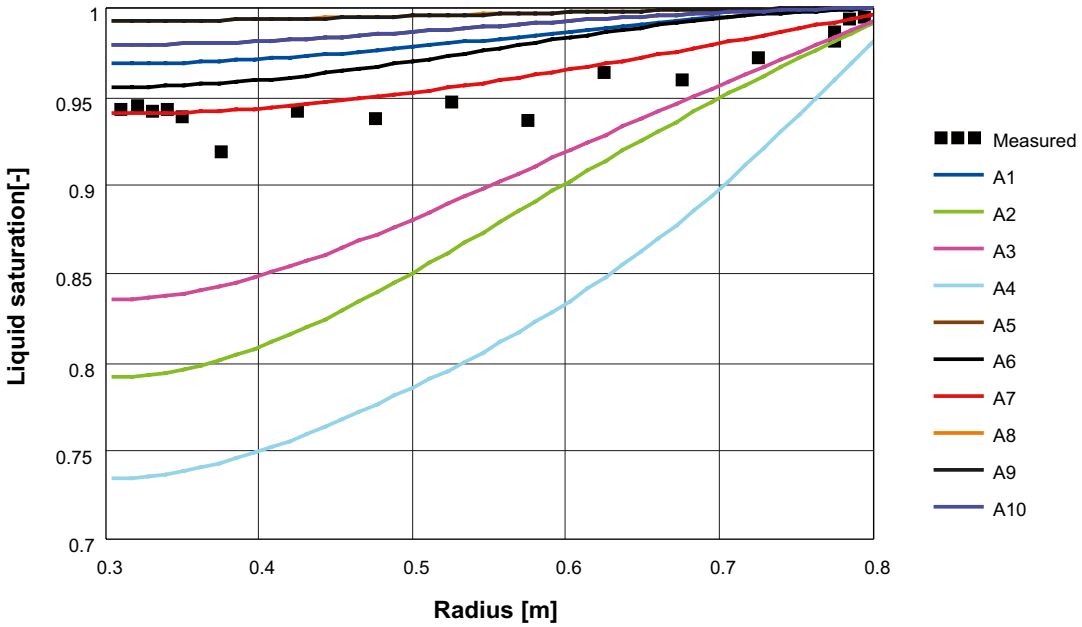

Figure 3-16. *Liquid saturation radial profiles from all THg models of R3/4 presented above. Model TBTR10_THg_A7 does the best job of reproducing the measured data, suggesting that the bentonite may not have been fully saturated when the heaters were turned off. Model TBTR4_THg_A6, in which the bentonite was fully saturated when the heaters were turned off does a reasonable job of reproducing the measured profile in the inner part, but is too wet further out.*

Table 3-11. THM(g) models done to evaluate the behaviour in R3/4.

Model	Bentonite ret. curve	Additional parameter variations
TBTR4_THMg_A1	Fredlund, Fr3	
TBTR4_THMg_A2	Fredlund, Fr3	$\rho_{l,0}$ = 1,010.0 kg/m^3 and $\alpha = 6\times10^{-4}$°C^{-1}
TBTR4_THMg_A3	ext_vG	
TBTR4_THMg_A4	Fredlund, Fr3	$k_{0,Bent.} = 4.0\times10^{-21}$ m^2, $\tau = 0.5$, $\rho_{l,0}$=1,010 kg/m^3 and $\alpha = 6\times10^{-4}$°C^{-1}

RH

One expects that solving the mechanical problem will change the RH evolution in the models slightly, as the porosity will now change with time due to swelling of the buffer. In Figure 3-17 we plot the relative humidity with time in all four models (solid lines) against the values measured in TBT. Some small differences are seen as compared to our earlier THg models, caused by the changing void ratios in models solving the mechanical problem. However, the general results still stand. It is worth to point out that while models TBTR4_THMg_A1–A3 has a directly corresponding model in the set of THg simulations done (TBTR4_THg_A5, A6 & A2 respectively), the model TBTR4_THMg_A4 differs somewhat from its corresponding THg model (TBTR4_THg_A9), since the thermal expansion of water is increased in the former.

The hydration rate in the field experiment is in general higher than in the models, the closest resemblance to the measured data is model TBTR4_THMg_A4, in which the permeability of the bentonite was increased by 100%, the vapour tortuosity was decreased by a factor of two, to $\tau = 0.5$ and the thermal expansion of water was increased, to correspond to experimentally determined data.

One important difference here, however, relates to the thermal expansion of water and how it is handled. In model TBTR4_THMg_A2 the expansion parameters are chosen so as to correspond better to laboratory data (the same as in TBTR4_THg_A6). However, the effects with respect to the reference model (TBTR4_THMg_A1) are smaller when the mechanical problem is also solved. The RH at the innermost point here only decrease to about 95%, which should be compared to the THg models, in which it decreased from fully saturated down to below 90% during the cooling phase at the end of the experiment. This also means that the final saturation profile is only marginally changed, as will be shown later on.

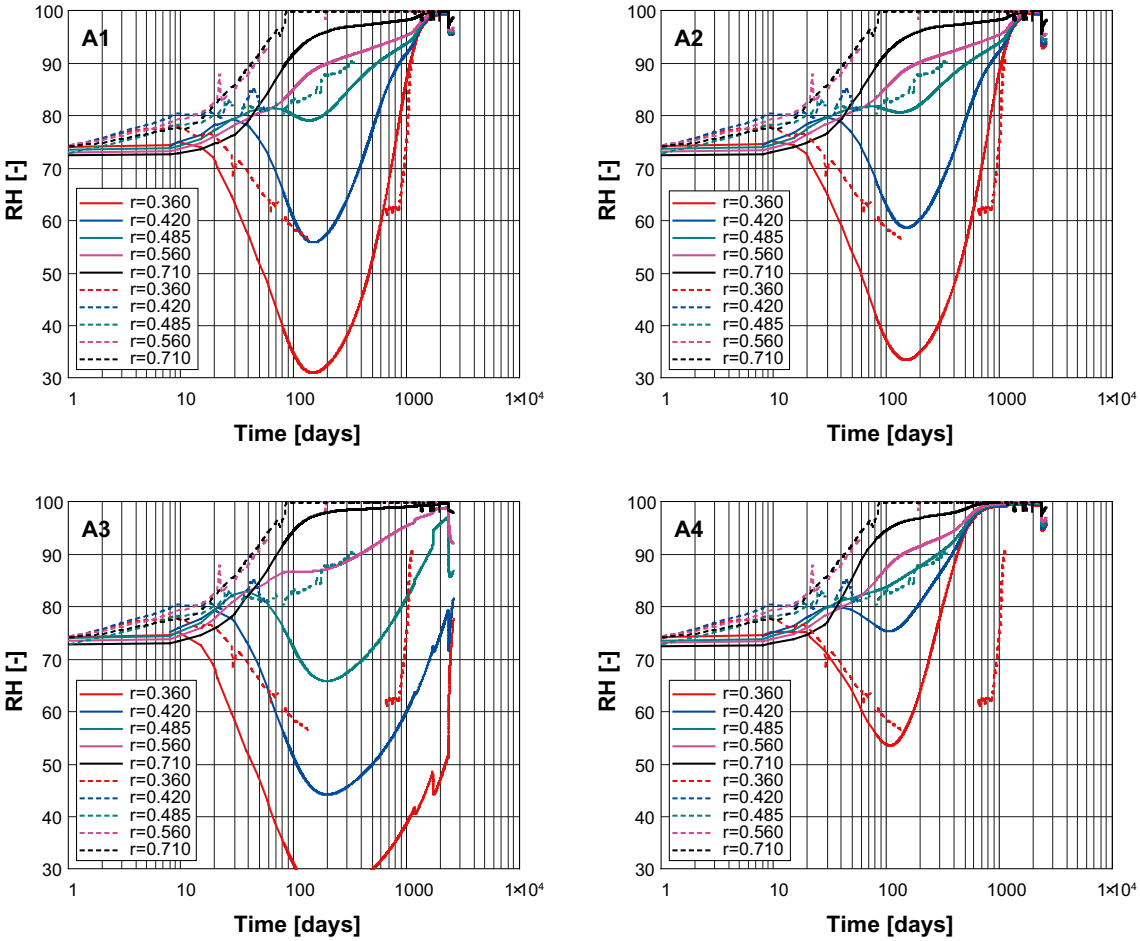

Figure 3-17. *The relative humidity evolution seen in the four THMg models done of R3/4 (solid lines) compared with the actual evolution as measured in TBT. No significant changes in the RH values are seen with respect to the models in which we do not solve the mechanical problem (i.e. models TBTR4_THg_A5, A6, A2 and A9 respectively).*

Stress evolution

In Figure 3-18 to Figure 3-20 we plot the radial, axial and tangential stresses measured in the models.

As can be seen in Figure 3-18, the radial stress in the models initially agree well with measured data. However, in all models, except TBTR4_THMg_A3 (the dry model), the results starts do deviate somewhat from the data after approximately 500 days. The model stresses reach values as high as 10 MPa, while in the field experiment the highest measured radial stresses are around 7 MPa. The dry model on the other hand, shows a very good agreement with measured data.

The axial stresses are plotted in Figure 3-19. At r = 0.585 m and r = 0.748 m model stresses are of the same magnitude as the stresses in the field experiment. However, at the innermost measuring point, r = 0.420 m, all models except TBTR4_THMg_A3 greatly overestimate the axial stress.

In Figure 3-20 we plot the tangential stresses measured in the model data (solid line) together with measured stresses in TBT (dashed lines). The agreement is very good in all models, except perhaps for TBTR4_THMg_A4, which slightly overestimate the magnitude of the stresses.

It should be noted that some of the stresses measured in the field experiment in R3/4 continue to grow until the heaters are turned off. This may indicate that the bentonite was close to, but not fully saturated in the inner region at this point in time, which could explain some of the differences between the models and the measured data. That TBTR4_THMg_A3, which is the by far the driest of all out models, best reproduce the measured stresses, adds some support to this explanation.

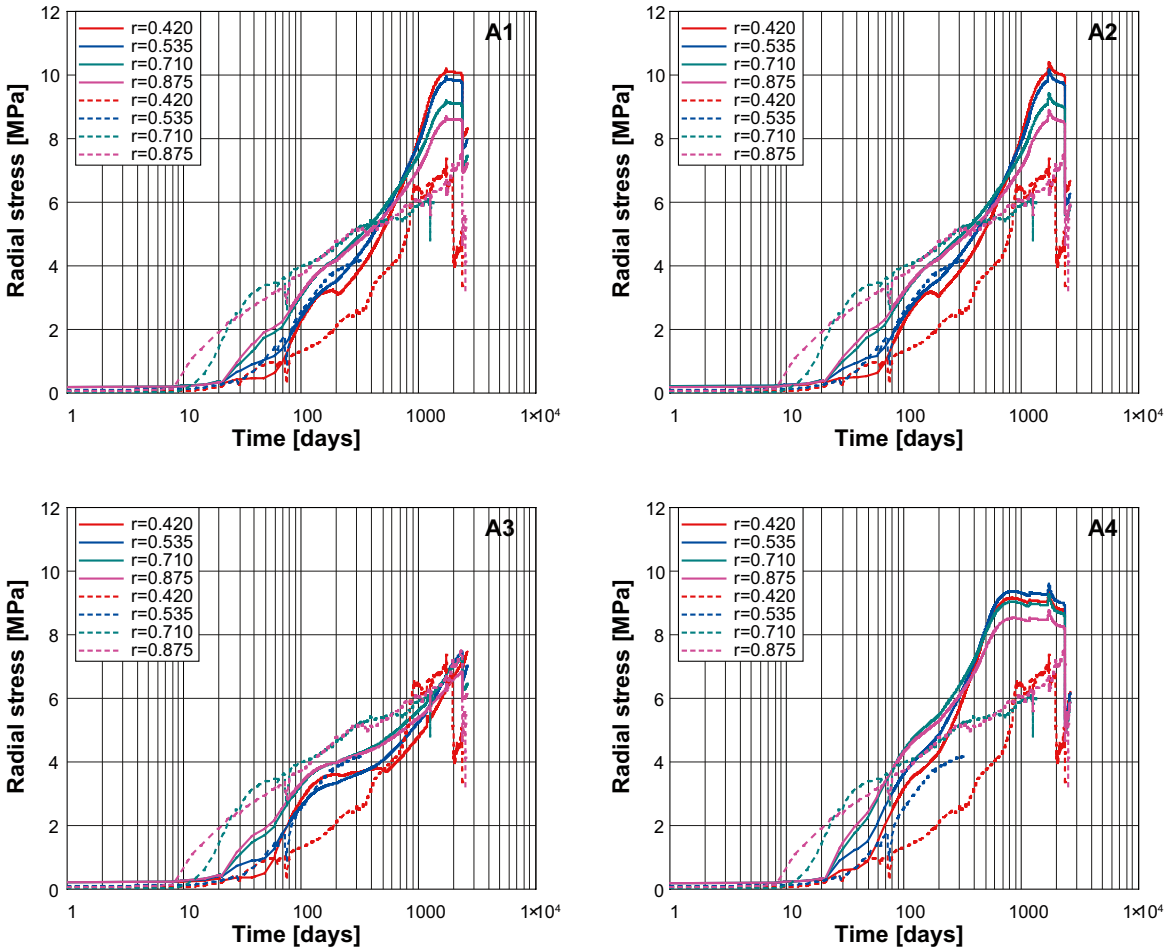

Figure 3-18. *Radial-stress evolution in the four THMg runs of R3/4. The stress-levels agree relatively well with the measured stresses during the first 600 days or so, where after all the models except TBTR4_THg_A3 display higher levels of stress, in particular model TBTR4_THMg_A4. It is worth to point out that TBTR4_THg_A3 is the driest of the models, showing significantly lower RH levels in the inner parts than what was actually measured. The discrepancy between model data and measured data, suggests that it might be necessary to refine the BBM parameters somewhat.*

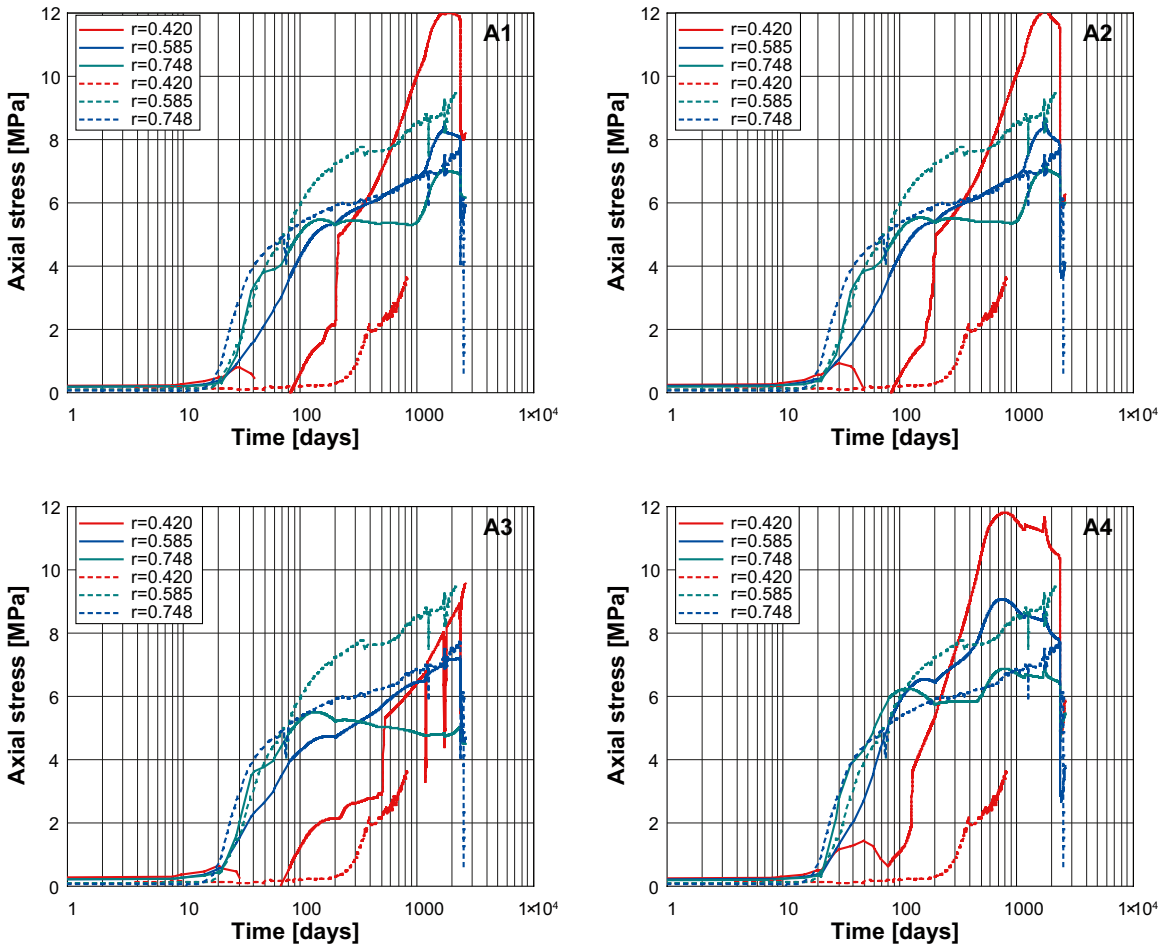

Figure 3-19. *Axial-stress evolution in the four THMg runs of R3/4.The magnitude of the axial stress at r = 0.585 and r = 0.748 m agree well with TBT data, while at r = 0.420 m, only model TBTR4_THMg_A3 reproduces the measured stress.*

Evolution in p'-q space

The measured evolution in p'-q space is shown in Figure 3-21 at two different radii; r = 0.535 m (red dashed line) and r = 0.710 m (blue dashed line). It is important to note that while the radial and tangential stresses were both measured at these radii, the axial stress was not. To calculate p' and q we have therefore used the measured axial stress at r = 0.585 m and r = 0.748 m respectively.

The evolution at these two points is quite different; at r = 0.535 m the bentonite in the field experiment reach a rather high deviatoric stress (q_{max}~3.5 MPa), while at the larger radius of r = 0.710 m, the maximum deviatoric stress reached is only about half as high (q_{max}~1.5 MPa). The models, on the other hand, show a rather uniform evolution at these two points, with a maximum deviatoric stress of about (q_{max}~2.5 MPa). The difference here can in part be attributed to that we use a yield surface which is independent of the void ratio. However, as the outer parts more quickly becomes saturated, and hence swells up (causing an increase in the void ratio) before the inner parts, the void ratio, and so also the yield surface, varies with both radius and time in the ring. This could give rise to the different evolution seen at the two points in the measured data. When modelling R10 we have investigated this effect further and considered yield surfaces which are not constant.

Final state

When dismantling the field experiment, both the saturation and void ratio was directly measured in all rings and cylinders. This gives us an excellent opportunity to compare the final state in our models with that of the experiment. Figure 3-22 shows the final void ratio, where the black diamonds are the measured points in R4. The final void ratio profiles from the four THMg modes are also included in the figure. Three of these models do a relatively good job of reproducing the measured profile, while

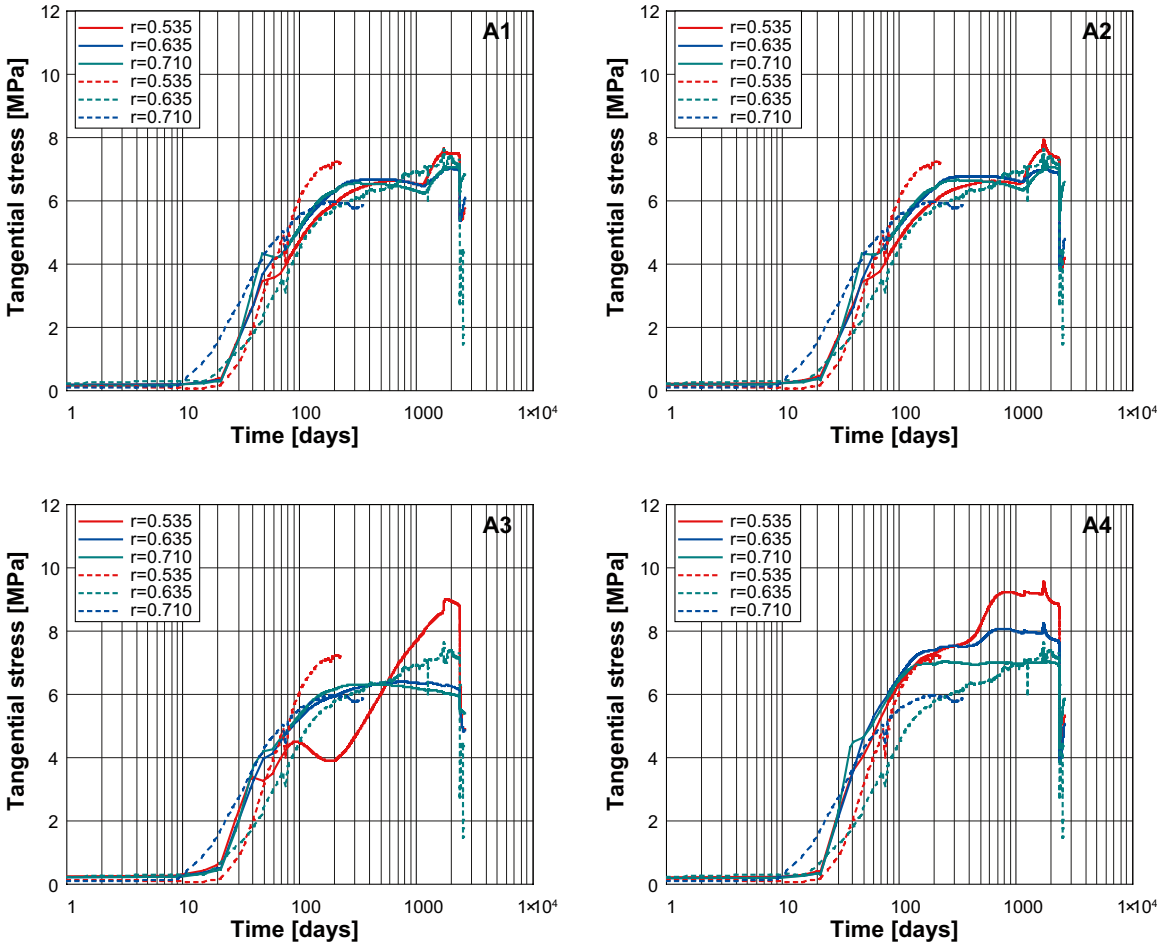

Figure 3-20. *Tangential-stress evolution in the four THMg runs of R3/4. All models reproduce the measured stresses reasonably well, in particular TBTR4_THMg_A1 and A2.*

the fourth model (TBTR4_THMg_A3) predicts a much too low void ratio inside r = 0.55 m. None of the models can reproduce the void ratio close to the sand filter. The cause of this is most likely how we treat the mechanical behaviour of the sand.

When the sand is being compressed, i.e. during the swelling of the bentonite, the linear elastic approximation is most likely rather good. However, as the heaters are turned off, and so also the water, the bentonite will start to shrink. This means that the outer radius of the bentonite will move inwards. In the models, this inwards motion means that the sand will expand again, however, this is not a realistic behaviour. In reality one would expect the sand to remain compressed even when the applied stress from the bentonite decrease. Due to the cooling, the bentonite might shrink, however, as there will still be some water in the filter, this can flow into the bentonite, leading to swelling in the outermost part. As the bentonite will not be confined by the sand filter during this swelling, one can expect the void ratio to reach rather high values in the bentonite close to the filter (see section 5.4).

The final saturation profiles are shown in the right panel of Figure 3-22, where again the measured values are represented by the black diamonds, and model data by the coloured lines. None of the models agrees well with the measured data. The saturation in the driest model (TBTR4_THMg_A3) is too low, while the final saturation in the other three models is too high. The decrease in saturation due to the change in liquid density during the cooling phase is less in these models than in the THg models presented earlier. For example, the model TBTR4_THMg_A2, in which the expansion was increased to better correspond with laboratory data exhibits only a modest decrease in saturation. The cause of the difference between this model and the THg model presented earlier is that the porosity of the bentonite now changes. As the model cools and the bentonite desaturates slightly, it shrinks. The result is that the total pore volume decreases, which in turn means that the effect on the final saturation profile is smaller here than in the case when the porosity was constant (e.g. model TBTR4_THg_A6).

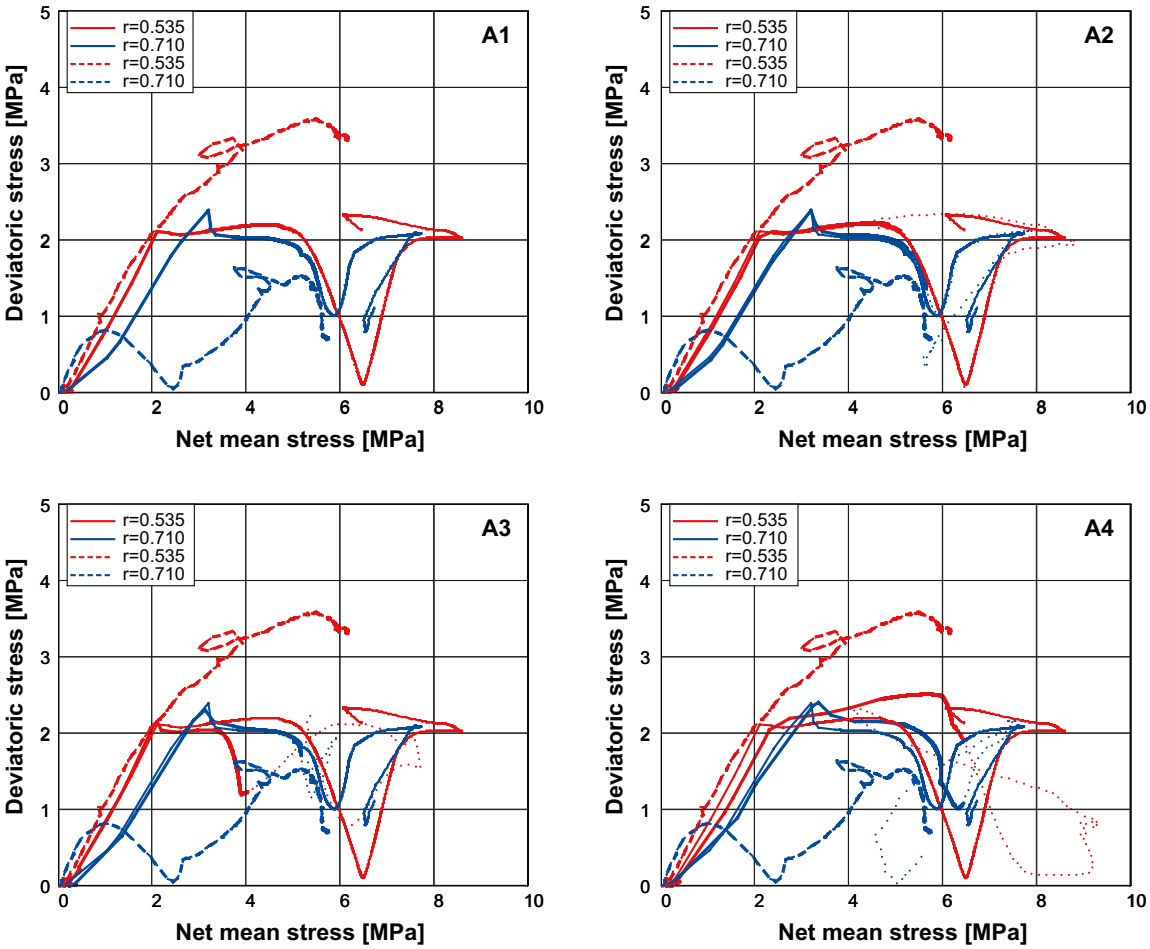

Figure 3-21. *Deviatoric and net-mean-stress evolution in the four THMg runs of R3/4. The axial stress was unfortunately not measured at r = 0.535 and r = 0.710 m. Thus, to calculate p' and q, we have used the measured axial stress at r = 0.585 m and r = 0.748 m respectively. For consistency, the same approach was used when calculating the stresses in the model data. The solid/dotted lines represent model data, while the dashed lines are the measured data. As measured data only exist up to day 228 at r = 0.535 and day 345 at r = 0.710, we have distinguished model data before these times (solid lines) with model data at later times (dotted lines).*

3.3.11 Summary of modelling R3/4

Modelling the evolution in R3/4 has shown that we cannot reproduce the measured RH evolution in the buffer with standard parameters (e.g. model TBTR4_THg_A1–A2). By changing the liquid flow parameters, as well as the vapour transport coefficients, we can, however, come rather close to the measured evolution (e.g. model TBTR4_THg_A9). The models which come closest to reproducing the measured RH, do, however, not provide a good match to the observed stresses (e.g. model TBTR4_THMg_A4). Only a much drier model can reproduce these (e.g. model TBTR4_THMg_A3). However, this latter model predicts a steeper radial void ratio profile than that measured.

One cause for these discrepancies might be that we have not included the gas leakage below R3/4 at a radius of about 0.4 m. Including this in our wet models would prevent the inner parts to become saturated before day 1,000, which could bring the results of the models closer to the measured data at r = 0.36 m, both in terms of RH and stresses. However, due to computational problems this was not possible. Another mechanism which might explain some of the discrepancy between stresses seen in the models as compared to the measured data is that the swelling properties of the bentonite might have been affected by the high temperatures near the heater (see e.g. Börgesson et al. 1995).

Finally, it should be noted that any discrepancies between the RH evolution in the models and measured data will significantly change the stresses in the models. This could be the most important cause of the differences between the model results and the data from the field experiment.

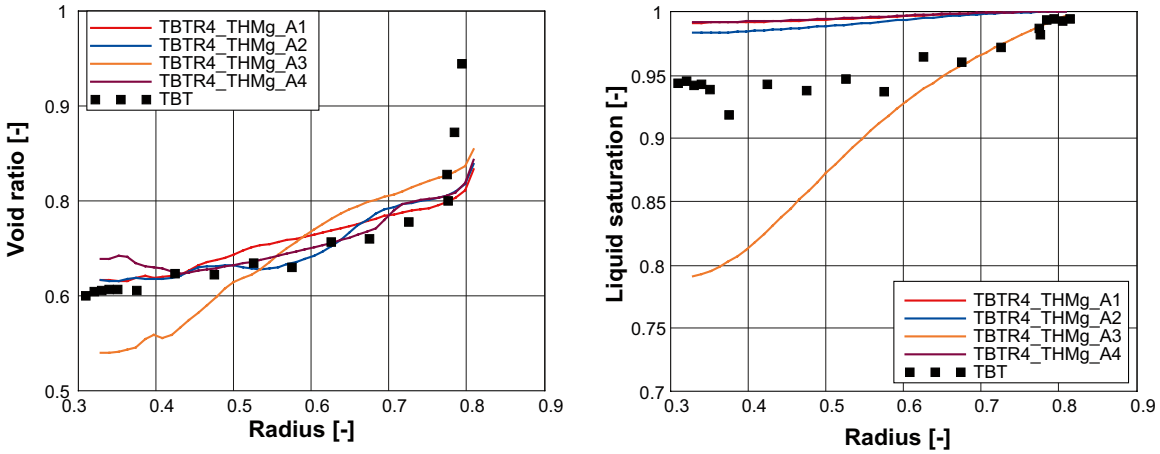

Figure 3-22. *Final void ratio (left) and saturation (right) as a function radius for models TBTR4_THMg_A1–A4. The black squares represent the actual values, measured after the dismantling of TBT. The void-ratio profile in TBT is reasonably well reproduced, although all models show too low values at the outer edge (r>0.78 m). The final saturation shows that models which reproduce the RH values in TBT (TBTR4_THMg_A1–A2, A4) are too wet, while, perhaps as expected, model TBTR4_THMg_A3 is too dry inside about r = 0.6 m.*

3.4 TBT – Task 2: Ring 9/10

The upper package differs significantly from the lower package modelled in the previous section in that the bentonite is separated from the heater by a 23 cm thick sand shield. This means, for example, that the maximum temperature in the bentonite stays below 100°C at all times.

3.4.1 Geometry

The geometry consists of a thin slice (1 cm high), with rotational symmetry around the y-axis, representing a thin disk at around the mid-height of the upper package (i.e. around R9/R10). The heater is not part of the geometry, instead its influence is handled as a boundary condition (heat flux) applied at the innermost radius (r = 0.305 m). The geometry, with assigned materials and mesh, is depicted in Figure 3-23. The mesh consists of 102 nodes, with 20 qL elements in the sand shield, 25 qL elements in the bentonite rings and 5 qL elements in the sand filter.

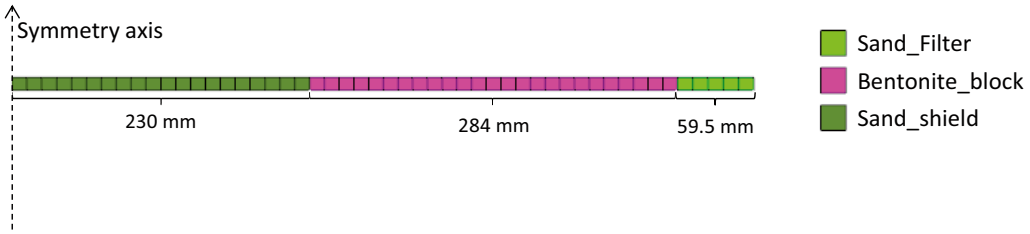

Figure 3-23. *Geometry used when modelling R9/10, including mesh and materials.*

Table 3-12. Hydraulic and solid phase properties.

Material	Solid density [kg/m^3]	Spec. heat cap. [J kg^{-1} K^{-1}]	Intr. perm. [m^2]	Liquid rel. perm. ($k_{rl} = S_{rl}^{\delta}$)	Gas rel. perm. ($k_{rl} = AS_{rl}^{\delta}$)		τ_v
				δ	A	δ	
Bentonite	2,780	800	1.2 x 10^{-21}		10^8		
Sand filter	2,650	800	1.0 x 10^{-15}	3	1	4	1
Sand shield	2,650	800	1.0 x 10^{-15}		1		

3.4.2 Material properties

The bentonite rings in the upper package have a different initial void ratio than the bentonite in the lower package. As such, the hydraulic properties are different, but still chosen in accordance with the suggested values in Åkesson et al. (2010b). We summarize them in Table 3-12.

The retention curve of bentonite used is based on the retention model of Fredlund and Xing (1994), where the fitting parameters were chosen so to agree with the experimental data as well as possible. This curve is almost identical to the extended can Genuchten curve with recommended parameters in Åkesson et al. (2010b), but behaves more realistically at high suction. The parameters for this retention curve, as well as for the retention curves of the sand, are summarized in Table 3-13.

Table 3-13. Water retention curves used when modelling R9/10.

Material	Law	P_0	λ_0	P_1	λ_1
Bentonite Fr4	$S_l = C(\Psi, P_1)\left\{\ln\left[e + \left(\frac{\Psi}{P_0}\right)^{\lambda_0}\right]\right\}^{-\lambda_1}$ $C(\Psi, P_1) = 1 - \frac{\ln(1 + \Psi/P_1)}{\ln(1 + 10^6/P_1)}$	284.288	1.347	9.854×10^7	6.148
Sand filter	$S_l = \left(1 - \left(\frac{\Psi}{P_0}\right)^{\frac{1}{1-\lambda_0}}\right)^{-\lambda_0}\left(1 + \frac{\Psi}{P_1}\right)^{\lambda_1}$	0.005	0.6	700	1.1
Sand shield		0.1	0.6	700	1.1

Regarding the thermal properties, the same conductive heat flux relation, and parameters as used when modelling R3/4 were used for the bentonite (see Table 3-2). The sand shield, however, requires a somewhat more elaborate treatment, in which λ_{dry} varies with time. This is done to match the measured temperature evolution in the shield. Varying λ_{dry} is motivated by the compression of the sand which decreases the average inter-particle distances (see section 6.2 for a more detailed description), thereby increasing the thermal conductivity. The values used are listed in Table 3-14 below.

Table 3-14. The thermal conductivity of the sand shield, at zero (λ_{dry}) and full (λ_{sat}) saturation, in the two different time-intervals, as used when modelling R9/10.

Time (days)	λ_{dry} (W m^{-1} K^{-1})	λ_{sat} (W m^{-1} K^{-1})
0–226	0.6	1.6
226–2,600	0.8	1.8

In models TBTR10A1–A5 the sand shield was not artificially hydrated, as was the case in the real experiment, and thus it remained dry. To achieve a correct temperature profile in the shield (and bentonite) at this point in time, λ_{dry} was set equal to 1.8 W m^{-1} K^{-1} for t>1,695 days in these models. In the remaining two models (TBTR10A6–A7) the shield was artificially saturated, and as such no modification of λ_{dry} was needed.

3.4.3 Mechanical parameters

We use the BBM model to describe the mechanical behaviour of the bentonite, and a linear elastic model for the sand in both the filter and the shield. The elastic parameters used were taken from Åkesson et al. (2010b) and are summarized here again in Table 3-15. The bentonite materials plastic parameters were initially determined from the target void ratio, calculated by assuming horizontal stress equilibrium in the model (see also section 3.3.6). However, these models did not provide a good match to the measured stresses in TBT, in particular with respect to the strong deviatoric stress that developed early on. As such, two additional sets of plastic parameters were used. They are summarized in Table 3-16.

Table 3-15. BBM model – Elastic parameter values.

Material	κ_{i0}	κ_{s0}	K_{min}	v	α_{ss}	α_{sp}	α_i	p_{ref}
Bentonite	0.12	0.3	20	0.2	–0.01	*	–0.021	1

* The αsp parameter is replaced by an in-house development of the code; see Åkesson et al. (2010b).

Table 3-16. BBM plastic parameters used to model bentonite.

Set	e_T	λ_0	r	β	ρ	k	p_{s0}	p_c	M	α	e_0	p_0*
P1	0.692	0.158	0	0		0	2.7	1	0.23			21
P2	0.620*	0.148	0	0	0	0	3.0	1	0.22	0.5	0.573	32
P3	0.573–0.692**	0.158	0.71	0.01		0.011	2.7	7.8	0.23			21

*Due to convergence problems, a lower target void ratio than 0.62 could not be modelled.

** The yield curve is constructed such that it at a suction of 46 MPa corresponds to the yield curve at e_T = 0.573 and for a suction of 0 MPa it corresponds to e_T = 0.692.

The mechanical parameter set labelled *P3* in Table 3-16 differs from the other sets used here in one important aspect. By setting r, β and k to non-zero values, we introduce a suction dependence on the yield surface. However, for buffer densities, the dependency is weak (see, for example, Figure 6-15 in Dueck 2010). The motivation for the introduction of a suction dependence is instead to mimic the change in yield surface with changing void ratio. This allows for a more realistic model of how the yield surface may have changed with time and radius in the field experiment.

The Young modulus and Poisson's ratio of the sand in the filter and shield respectively can be found in Table 3-17 below. Two parameter sets were used, one with linear elastic parameters as evaluated from oedometer tests (*S1*) and a second set, in which the sand was softened (see further discussion in section 3.4.5):

Table 3-17. Linear elastic materials – Parameter values.

Material	Parameter set	E [MPa]	v
Sand shield/filter	S1	95/60	0.20/0.20
Sand shield/filter	S2	55/25	0.25/0.25

3.4.4 Initial and boundary conditions

The initial conditions are chosen in accordance with the material data (Johannesson et al. 2010). The initial value of suction, 46 MPa, corresponds to the initial water content in the bentonite. All adopted values are summarized in Table 3-18.

Table 3-18. Initial conditions used when modelling R9/10.

Material	e/n	P_l (MPa)	P_g (MPa)	T (°C)	σ (MPa)
Bentonite	0.573/0.364				
Sand filter	0.533/0.348	–45.9	0.1	22	–0.11 ***I****
Sand shield	0.456/0.313				

*Here ***I*** is the unit matrix.

No horizontal displacement was allowed on the edges of the model, to mimic the effect of the heater and rock surfaces. Furthermore, as the model is one dimensional, no vertical displacement was allowed on the top and bottom boundaries. The mechanical boundary conditions are illustrated in the lower part of Figure 3-24.

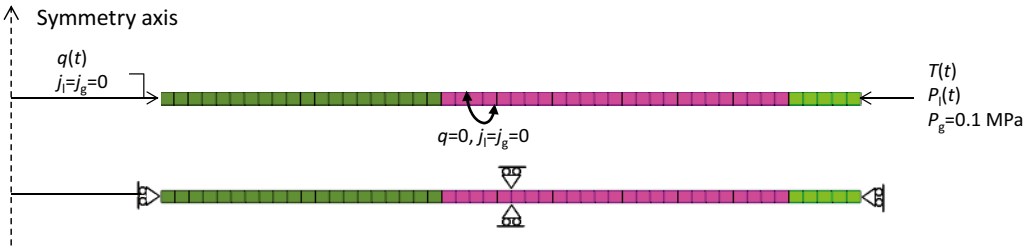

Figure 3-24. *Hydraulic and thermal (upper part), as well as mechanical boundary conditions (lower part), used when modelling R9/10. The time-dependence of the temperature, liquid pressure and heat flux boundary conditions are elaborated on in the text.*

To mimic the power output of the heater, as well as the cooling effect of the surrounding rock, we apply a heat flux on the "heater surface", hence on the left vertical boundary (see Table 3-9).

On the "rock surface", we apply a temperature boundary condition, derived from an analytical model described previously in Goudarzi et al. (2005), which takes into account the effect of the nearby CRT heater, as well as both of the TBT heaters. The temperature applied on the rock surface is illustrated in Figure 3-25 (left panel).

Table 3-19. Heater power (upper package), as well as heat flux boundary condition applied in the 1D model of R9/10, used to mimic the power output of the heater.

Time (days)	Heater Power (W)	q (W/m^2)
0–8	900	156.55
8–15	1,200	208.73
15–1,171	1,500	260.91
1,171–1,695	1,600	278.30
1,695–1,702	1,500	260.91
1,702–1,709	1,400	243.52
1,709–1,716	1,300	226.12
1,716–1,723	1,200	208.73
1,723–1,730	1,100	191.33
1,730–2,343	1,000	173.94
2,343–2,347	1,000–0	Linearly decreasing: 173.94–0
2,347–2,600	0	0

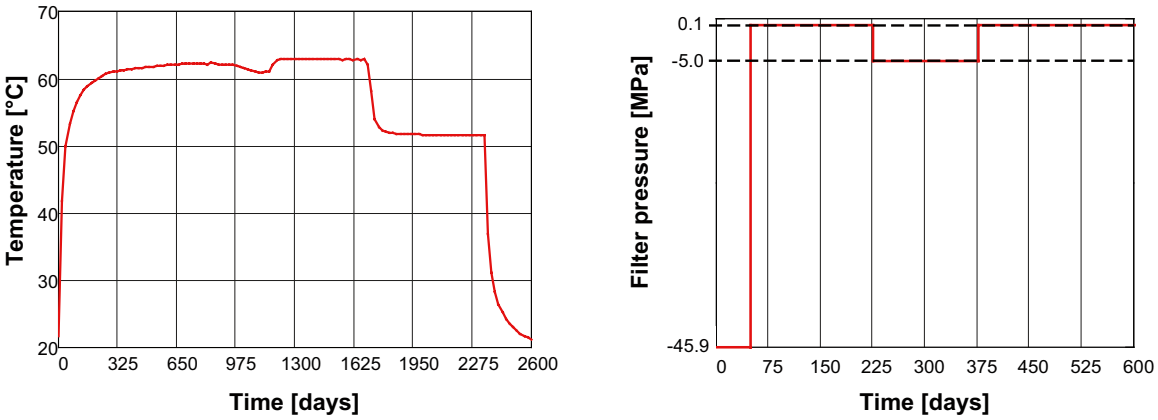

Figure 3-25. *Temperature boundary condition used in the models of R9/10 (left panel) and liquid pressure in the sand filter during the first 600 days (right panel). The temperature was calculated analytically following the model described in Goudarzi et al. (2005).*

Initially, the liquid pressure in the sand filter is kept at –45.9 MPa, as the filter was initially dry. At approximately day 50, the sand filter was artificially saturated, and hence at this time we increase the liquid pressure to 0.1 MPa. However, an important event during the field experiment was the apparent increase in suction in the bentonite between roughly day 200 and day 400. It has been suggested that this was due to a desaturation of the sand filter, although the cause of this is not determined. To mimic this behaviour we reduce the liquid pressure in the sand filter to $P_l = –5.0$ between day 225 and day 377 in the models. The liquid pressure applied over the sand filter during the first 600 days is illustrated in the right panel of Figure 3-25. After this time the pressure was kept at 0.1 MPa until the heaters were turned off on day 2,347, where after a no-flow boundary condition was applied on the filter.

The gas pressure in the model can reach rather high levels if gas is only allowed to escape through the sand-filter/rock interface. However, given the high permeability of the sand shield, and since it was not saturated until around day 1,700, gas could in principle move around freely inside it. If the gas was able to escape from the shield out into the rock or tunnel, this would mean that the gas pressure may have been kept close to atmospheric levels until the shield was filled with water. On top of the sand shield two bentonite cylinders (C3 & C4) are situated. They provide an excellent way for gas to escape as 1) they were not supplied with water until approximately day 700 (C3) and 2) C3 may have been fractured early on (see section 3.5.1), opening up an escape route to the bentonite pellets, allowing gas to leak directly from the sand shield into the surrounding rock.

To see how this may affect the time-evolution of the model, we have done one model (TBTR10A6) in which gas is allowed to leak through the horizontal boundaries of the sand shield. We do this by setting the gas pressure equal to 0.1 MPa, with $\gamma_g = –10^{–3}$. A negative value of γ_g means that only outflow of gas is allowed. The low value of γ_g means that the gas pressure can deviate slightly from the assigned value of 0.1 MPa. The evolution of this model is compared with another simulation (TBTR10A7), in which the gas pressure is kept constant at $p_g = 0.6$ MPa.

The inner part of the geometry in R9/10 was the sand shield. At approximately day 1,700, the sand shield was filled with water using two inlet pipes near the interface between the sand shield and the bentonite buffer material. To model this process, we raise the liquid pressure to 0.1 MPa in the sand shield at day 1,700 in models TBTR10A6–A7. However, for computational reasons, this is done using a liquid boundary condition on the surface of the heater (i.e. the left vertical edge of the geometry), rather than close to the sand/bentonite interface. Given the high permeability of the sand, this can be considered a good approximation.

3.4.5 Results

A total of 6 THMg models, and 1 THM model were simulated. They are summarized in Table 3-20 below:

Table 3-20. Overview of models done involving R9/10.

Model	Sand mech. parameters	Plastic parameters	Gas pressure	Wetting of sand shield
TBTR10A1	S1	P1	Gas flux only allowed through rock/sand boundary (P_g = 0.1 MPa).	No
TBTR10A2	S2	P1		No
TBTR10A3	S2	P2		No
TBTR10A4	S2	P3		No
TBTR10A5	S2	P3, M = M(p')		No
TBTR10A6	S2	P3, M = M(p')	Gas flux allowed through rock/sand boundary and in the sand shield.	Yes
TBTR10A7	S2	P3, M = M(p')	Gas pressure constant and equal to 0.6 MPa.	Yes

Models TBTR10A1–A2: Influence of the mechanical parameters of the sand

Model TBTR10A1 was done as a base case, in which the plastic parameters of the bentonite are derived using the procedure described in Åkesson et al. (2010b) and the elastic parameters of the sand is taken from the oedometer tests. The resulting stresses in this model are shown in Figure 3-26. As can be seen, the total swelling pressure in the model (~10 MPa) is much higher than what was measured (~ 8 MPa).

The cause for this could, for example, be either that the swelling pressure curve used is incorrect, or that the bentonite is too tightly confined in the model. Of these two possibilities, the latter seems to be more likely, given that the swelling pressure curve used here represents the scatter in the lower end of experimental data (see Figure 6-13).

In model TBTR10A2 we have changed the mechanical parameters of the sand, making it significantly softer than what was to be expected from the oedometer measurements. The cause for such a softening could, for example, be axial swelling of the bentonite, mixing of sand and bentonite, or the different geometry of the sand shield as compared to the geometry in the oedometer tests. Further discussions of the compressibility of the sand can be found in section 6.7.

The total stresses in model TBTR10A2 are shown in Figure 3-27. The final swelling pressure agrees well with the measured data. The softer sand allows the bentonite to swell to a higher void ratio than in model TBTR10A1, thus giving a lower final swelling pressure.

However, the evolution during the first 800 days or so is quite different from that measured. The axial and tangential stresses are much lower in the model as compared to the measured stresses. As the stresses in all three principal directions were continuously measured until day 827 at r = 0.635 m, we can construct a diagram of the p'-q evolution in this point. When doing so for model TBTR10A2 (see Figure 3-28, left panel) it is clear that the bentonite in the model plasticizes at a significantly lower point in the p'-q plane compared to the measured evolution. The cause of this is in part due to that the yield surface used (parameter set P1) is set according to the target void ratio (e_T = 0.695).

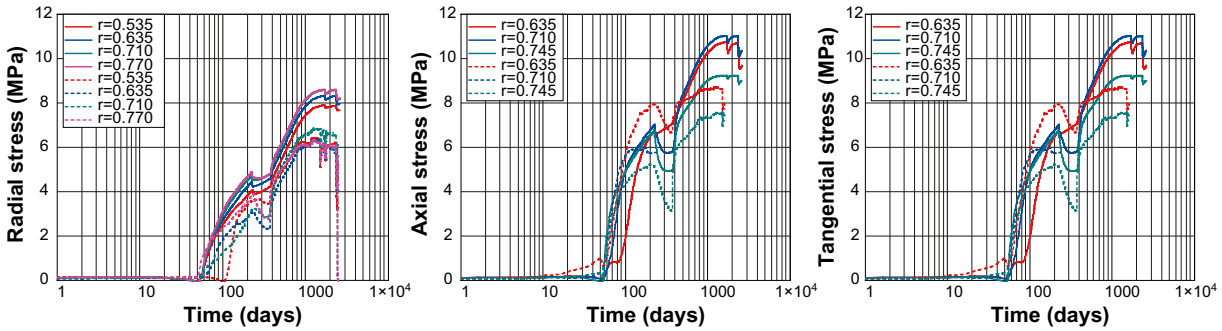

Figure 3-26. *Radial (left), axial (middle) and tangential (right) stresses from model TBTR10A1 as a function of time. Solid lines are model data, while the dashed lines are the corresponding measured data from TBT.*

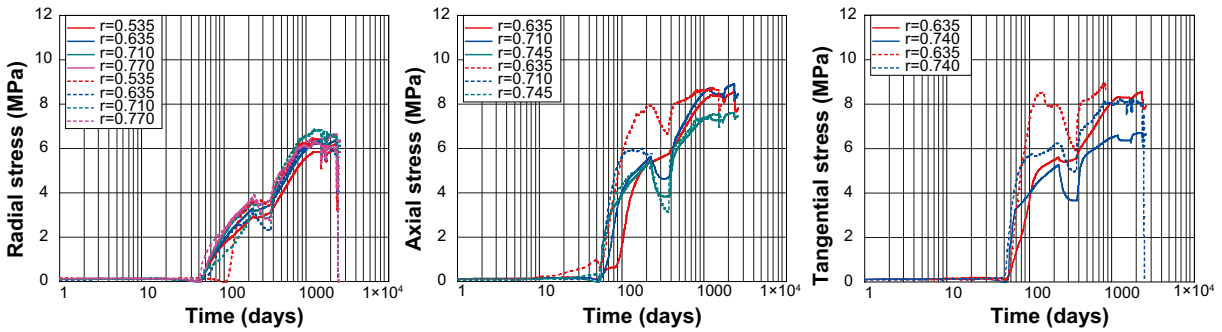

Figure 3-27. *Radial (left), axial (middle) and tangential (right) stresses from model TBTR10A2 as a function of time. Solid lines are model data, while the dashed lines are the corresponding measured data from TBT.*

However, when the bentonite starts to plasticize in the model, the void ratio is approximately 0.55 (see Figure 3-28, right panel), hence the yield surface is set too "low" in the p'-q plane. It is also worth pointing out, that the deviatoric stress in R9 starts to increase from day 0, with a very small corresponding increase in the net mean stress. This indicates a build-up of axial stress in R9 due to swelling in the lower part of TBT. This build-up can clearly be seen in Figure 3-27 (middle panel), where the axial stress at r = 0.635 starts to increase around day 10, well before any other pressure sensors in R9 indicates increasing stress levels.

Models TBTR10A3–A5: Bentonite plastic parameters

The high deviatoric stress reached before the bentonite plasticizes cannot be fully explained by the low void ratio at this point. The blue square in the left panel of Figure 3-29 is the point at which the bentonite plasticizes at r = 0.635 m, according to the pressure sensors in TBT. In Figure 3-29 we also plot the yield surface for the initial void ratio, e = 0.573 (left panel, orange line) and the yield surface at the target void ratio, e = 0.692 (left panel, grey line). As can be seen, the bentonite reached a much higher deviatoric stress than what can be explained in the models according to the TBT-data. In order to construct a yield curve which reaches the experimental point, one has to assume that the bentonite at this radius reached a void ratio close to 0.46, which seems highly unrealistic. Further discussion on this topic can be found in section 6.4.

Due to convergence problems, no model with a yield surface constructed from a constant void ratio of e = 0.573 could be done, but in TBTR10A3, the yield surface is constructed from a void ratio of e = 0.62 (see Figure 3-29, left panel, red line). The evolution in p'-q space at r = 0.635 m from this model is shown in Figure 3-29 (right panel, red line). A higher deviatoric stress is observed as compared to model TBTR10A2, but the discrepancy compared to the measured data is still large.

The plastic parameter set used in model TBTR10A3 is only valid early on in the model, when the void ratios in the bentonite are close to the starting values. It would therefore be useful if one could construct a yield surface which behaves more realistically during the full experiment. CODE_BRIGHT v3 does not include a void ratio dependence on the yield surface; however, a suction dependence can be introduced. The bentonite starts out dry (with suction, s = 46 MPa), and then swells (and hence the void ratio increases) due to a decrease in suction, reaching the final void ratio once the suction has decreased to zero, one can, to an approximation, use the suction dependence to mimic a void ratio dependence.

To construct such a suction-dependent yield surface, we require it to coincide with the yield surface for e = 0.573 at s = 46 MPa, and the yield surface for e = 0.695 at s = 0 MPa. The exact path of the yield surface between these two suction values is determined by several parameters; the values chosen for this modelling can be found in Table 3-16, and the resulting yield surface is shown in Figure 3-30.

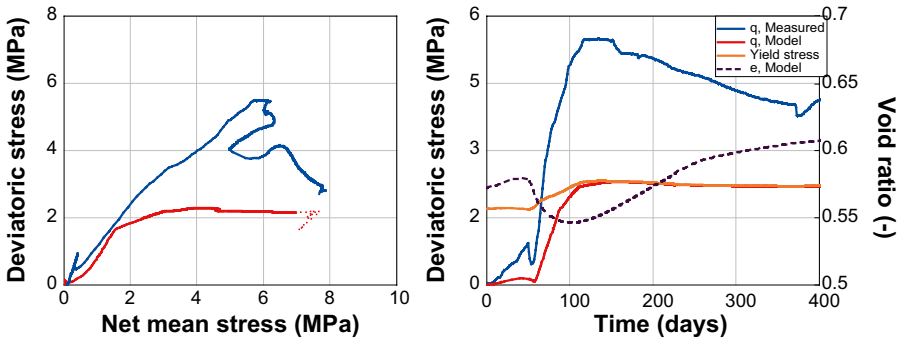

Figure 3-28. *Deviatoric stress at r = 0.635 m in R9 from model TBTR10A2 as a function of net mean stress (left) and time (right). The solid red line in the left panel correspond to the p'-q evolution before day 827. At this point, the pressure sensor measuring the tangential stress in TBT failed, and hence the measured data only goes to this point. The p'-q evolution in the model after day 827 is shown as the red-dotted line. In the right panel the yield stress is also plotted, as a function of the current net mean stress (orange line), as well as the void ratio at this point (black dashed line). When the bentonite plasticizes in the model, the void ratio is approximately 0.55.*

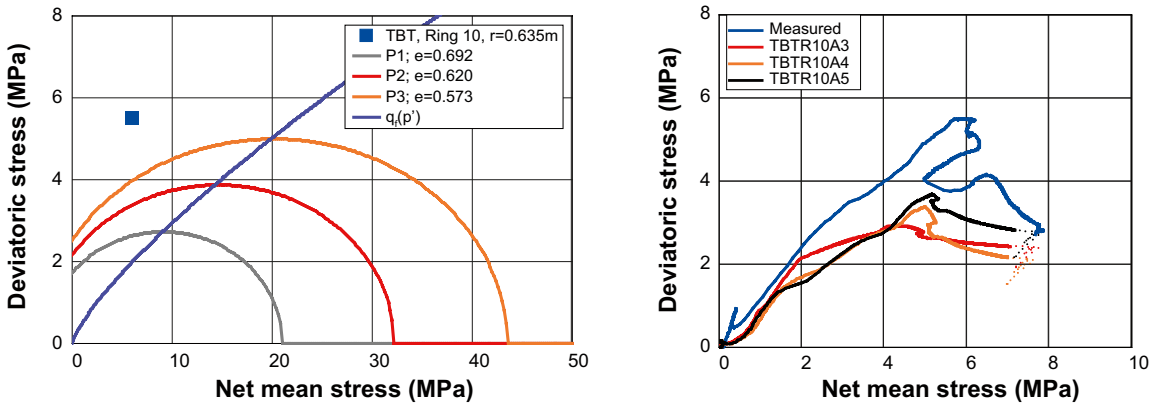

Figure 3-29. *Yield surfaces for the three different plastic parameter sets (P1, P2 & P3; see Table 3-16) to the left and deviatoric stress vs. net mean stress evolution at r = 0.635 m in R9 to the right. The blue square in the left panel is the point in p'-q space where the bentonite plasticized in TBT, a point which none of the yield surfaces used in the modelling can reproduce. At t = 827 d, the pressure sensor measuring tangential stress at r = 0.635 m in R9 failed. As such, in the right panel, model data for t<827 d are marked with solid lines, while data for t>827 d are marked with dotted lines.*

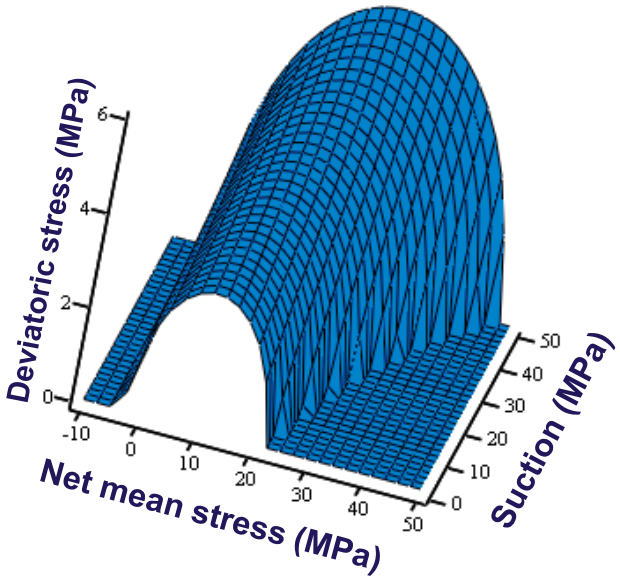

Figure 3-30. *The yield surface from the plastic parameter set P3 (see Table 3-16) in p'-q space, as function of suction. The yield curve at suction s = 0 MPa is identical to the yield curve using parameter set P1, while at s = 46 MPa, the yield curve is identical to that when e = 0.573, the initial void ratio.*

In model TBTR10A4 this yield curve is used. The evolution in p'-q space at r = 0.635 m from this model is shown in Figure 3-29 (right panel, orange line). Compared to previous models, the results are more in agreement with the measured evolution. However, as the implemented yield curve does not allow the measured combination of net mean stress and deviatoric stress (e.g. Figure 3-29) the discrepancy between the measured evolution and that of the model is still significant.

Critical state-line parameter

When introducing a suction dependence in CODE_BRIGHT, only p_S and p_0 changes with varying suction, s. Hence, the critical state-line parameter, M, is constant, and so the ratio between q_{max} and the sum p_0+p_S remains constant. However, this does not agree with the tensile yield stress relation as

measured in experimental data. As such, an improved handling of the behaviour of M with changing p_0 and p_s has been implemented in CODE_BRIGHT at Clay Technology, in which M follows the relation (Åkesson et al. 2010a):

$$M = a\left(\frac{p_0 + p_s}{2}\right)^{b-1} \qquad (3\text{-}18)$$

where a and b are experimentally determined parameters (see equation (3-6)), determined from measurements of the tensile yield strength of bentonite. In model TBTR10A5 equation (3-18) is used to determine M, while the remaining plastic parameters are taken from parameter set P3. The resulting p'-q evolution at r = 0.635 m is plotted in Figure 3-29 (right panel, black line), and a small improvement, with respect to previous models, can be seen in reproducing the measured evolution. We plot the time evolution of the stresses in the model, at all positions where a pressure sensor was placed in TBT, in Figure 3-31 below.

Final void ratio and saturation profiles

Figure 3-32 shows the final void ratio, where the black diamonds are the measured points in R10. The final void ratio profiles from models TBTR10A1–A5 are also included in the figure. Only model TBTR10A1, in which the sand was significantly stiffer, fails to reproduce the general shape and magnitude of the void-ratio profile. The other models does a relatively good job, except for outside r = 0.8 m, where the measured void ratios are significantly higher than the model data. The cause of this discrepancy is most likely the handling of the sand filter as a linear elastic material (see also discussion in 3.1.12).

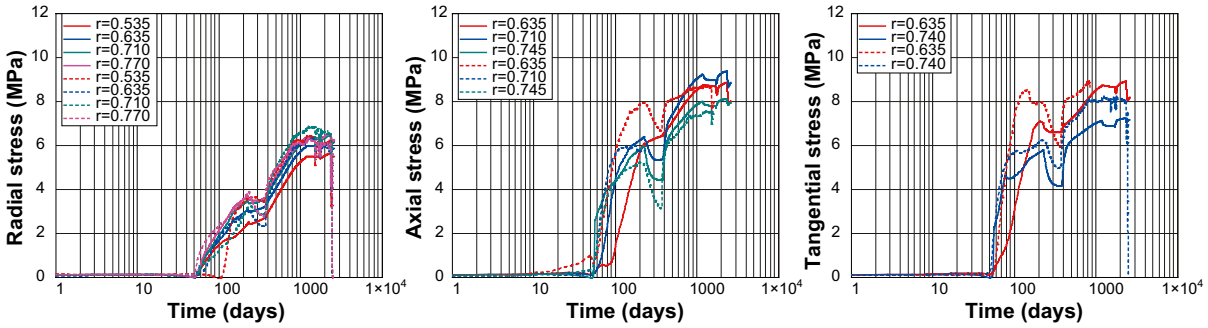

Figure 3-31. *The measured time-evolution of radial (left panel), axial (middle panel) and tangential (right panel) stresses in R9 of TBT (dashed lines) and from model TBTR10A5, at all pressure sensor positions. Aside from the early increase in axial and tangential stress in the inner parts of the bentonite rings, the model data generally agrees well with the measured evolution. A discrepancy of about 1 MPa in the final tangential stress at r = 0.740 is, however, present.*

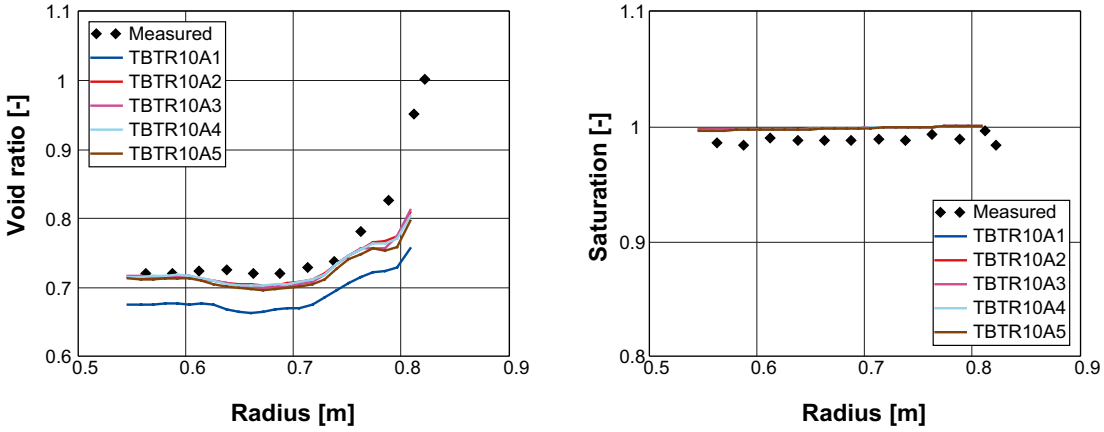

Figure 3-32. *Final void ratio and saturation radial profiles (snapshot at t = 2,600 d); both measured values (black diamonds) and model data (solid lines). The difference between the models is the stiffness of the sand (TBTR10A1) and the plastic yield surface parameters TBTR10A2–A5).*

The final saturation profiles are shown in the right panel of Figure 3-32, where again the measured values are represented by the black diamonds, and model data by the coloured lines. The final saturation in both the models and the field experiment is very close to one, and hence agree rather well.

Time evolution of temperature and relative humidity

The temperatures that the bentonite situated at mid-height around the upper canister experiences are below 100°C at all times throughout the experiment. This implies that the gas pressure in the bentonite should stay close to atmospheric conditions. However, the sand shield does experience high temperatures, and it can therefore be expected that high gas pressures may be attained there. However, the pore pressure sensor located in the sand shield (at a radius of 0.42 m) does not signal a build-up in pore pressure before the shield is artificially wetted at around day 1,700. This implies that the gas pressure stayed close to atmospheric in the shield throughout the experiment; hence the gas must have been able to leak from the shield. Perhaps this leakage took place through C3 and C4, or some other pathway was available. In order to simulate the prevailing conditions, we have varied the hydraulic boundary conditions, to see what the effect of maintaining a lower gas pressure is.

In the models previously presented, gas flow was only allowed through the outer vertical boundary (i.e. the rock/sand filter boundary). There, the gas pressure was kept at atmospheric levels (p_g = 0.1 MPa). We will use the model TBTR10A1 as the representative runs for this boundary condition.

To mimic the escape of gas, we have done one model (TBTR10A6) in which the gas pressure in the sand shield was kept atmospheric, by allowing gas to leak out in one point on both the upper and lower horizontal boundary, at a radius of r = 0.42 m.

One additional model was also done (TBTR10A7), in which the gas pressure was kept constant and equal to 0.6 MPa (i.e. the mass balance of air was not solved). This pressure corresponds to the water vapour saturation pressure at approximately 160°C.

The relative humidity in these three models are shown in Figure 3-33 (solid lines, A1 – upper left panel, A6 – upper right panel and A7 – lower left panel) together with the measured RH evolution in the field experiment (dashed lines).

As can be seen the RH evolution is not bad in the outer parts of the geometry in all three models. Inside r = 0.635 m, however, the models with varying gas pressure (upper row) produce somewhat too dry conditions during the first 600 days. The model with constant gas pressure equal to 6 bar (lower-left panel) behaves more similar to the measured evolution. Additionally, the response in RH to the increase in suction in the filter between day 225 and 377 differ quite significantly between the models.

3.4.6 Summary of modelling of R9/10

The bentonite in the upper package is not subjected to as high temperatures as in the lower package. As such, one might expect that the standard parameter set from Åkesson et al. (2010b) would provide results in good agreement with the measured data. With regards to the RH evolution this is in general true, even though the early evolution is not fully reproduced. One contributing factor here is the "dry period" between roughly day 225 and 377, which can only be schematically included in the modelling. The cause of the discrepancies between model and measured data can possibly be traced back to the inclusion of a varying gas pressure, and how the boundary condition for this is set.

The stresses produced in the models are quite different from the evolution in the field experiment. One part of this inconsistency comes from the handling of the sand, which, given the results presented here, behaved quite differently in the field experiment as compared to in the independent oedometer experiments in the lab. It is perhaps not too surprising that our 1D model has problems in this respect, as e.g. vertical expansion of the bentonite could increase the sand shield volume, effectively softening it, and lower the bentonite's density. However, the large shear stresses seen at a radius of 0.635 m presents a more serious challenge to the current mechanical model, since it in principle cannot reproduce them. Although we had some success in producing models more similar to the evolution seen at r = 0.635 m by mimicking a void ratio dependence on the yield surface, the discrepancy is still large. This behaviour of the bentonite, and the apparent inconsistency with the mechanical model used, is discussed further in section 6.4.

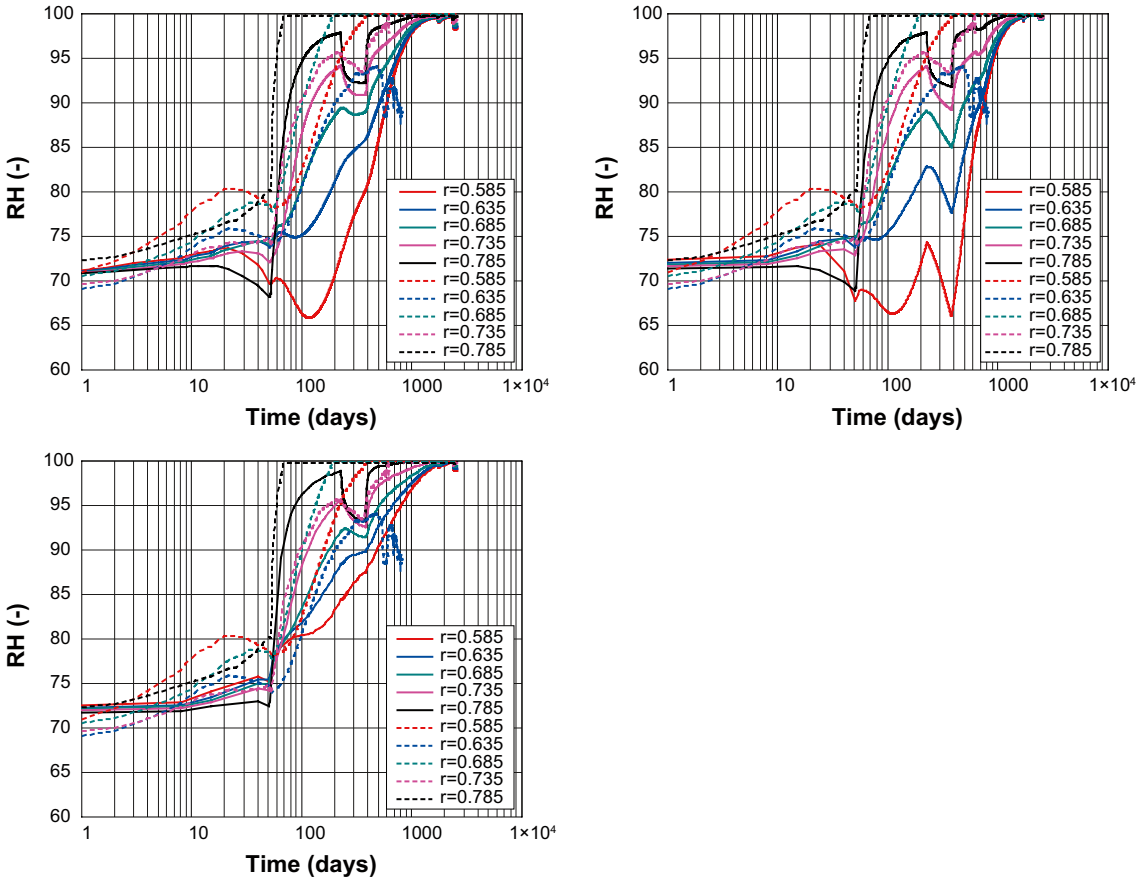

Figure 3-33. *RH-evolution in models TBTR10A1 (upper left), TBTR10A6 (upper right) and TBTR10A7 (lower left, between which how to solve for the gas evolution was varied. In TBTR10A5 gas was only allowed to escape along the outer vertical boundary, in TBTR10A6 gas was also allowed to escape through the sand filter, effectively keeping the gas pressure there atmospheric. Finally, in TBTR10A7, the gas pressure was kept constant and equal to 0.6, (equal to the vapour saturation pressure at T = 160°C).*

3.5 TBT – upper package

3.5.1 Background

During the dismantling of TBT, a fracture was found in C3. The cause of this fracture may be that significant shear stresses developed in C3 during the first 100 days of the experiment. Evidence for this comes from the measurements of stresses in C3 (see Figure 3-34). As can be seen, a spike in the axial stress occurs roughly 70 days after the heaters were turned on, several weeks before the build-up of swelling pressure at this location. This suggests that the spike in axial stress was not caused by the swelling in C3, but rather due to the build-up of axial stress further down (hence in the rings below). This has a straightforward explanation; while the rings (except the upper part of R12) are surrounded by sand, with high permeability, C3 is surrounded by pellets, with much lower liquid permeability. Hence, while the rings below essentially has free access to water at t = 80 days, C3 does not. The build-up of swelling pressure further down gives rise to strong axial stresses in C3, which, since C3 is not swelling at this point, are not accompanied by radial or tangential stresses. The result of this is a large shear stress, which is likely to be the cause of the fracture. To investigate this particular behaviour more closely, we have done models of the upper TBT package only, using a simplified model (only solving the hydraulic and mechanical problems) during the first 200 days. The set-up of this model exercise, as well as the result, is presented below.

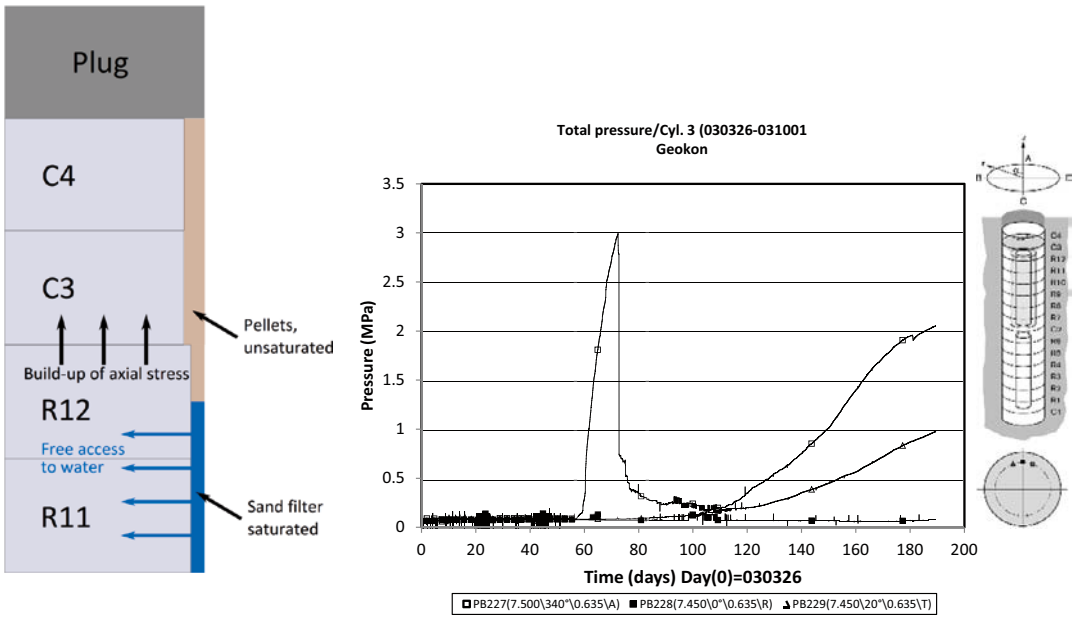

Figure 3-34. *Schematic overview of one possible cause for the shearing observed in C3. As R11 and R12 become saturated, they start to exert a swelling pressure. However, as the sand filter ends half-way up R12, C3 has no access to water (the pellets do not become saturated quickly), and hence does not swell. This means that C3 will be subjected to strong axial stress, originating in the rings below it, while at the same time producing very small, or zero, radial stress. The result of this is strong shear stresses, which may give rise to the observed fractures in C3 at dismantling. An additional piece of evidence in support of this theory is the measured axial stress in C3. At roughly 80 days (see right part of figure), a strong spike in the axial stress is measured, coinciding with the build-up of swelling pressure (and hence axial stress), which was measured further down in the experiment (at R9).*

3.5.2 Geometry

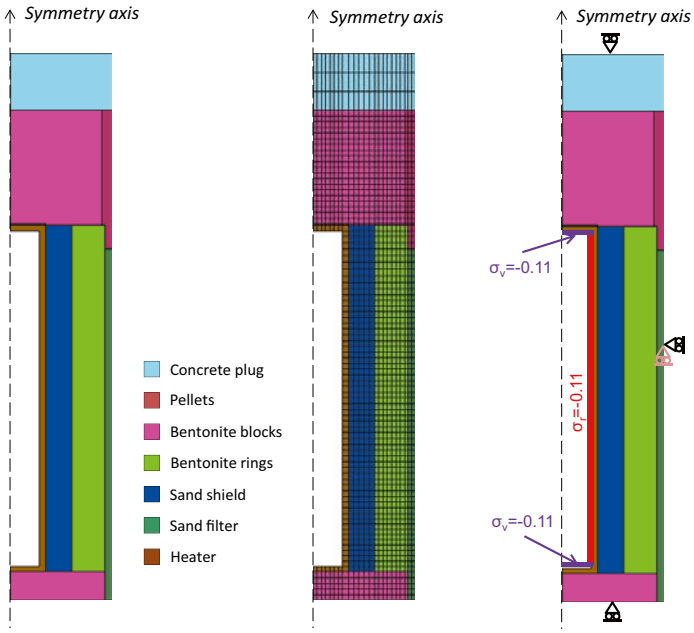

Figure 3-35. *Geometry/materials used (left panel), mesh (middle panel) and boundary conditions for the mechanical problem (right panel). NB: Two types of B.C. were used for the vertical rock wall. One rolling B.C where the outer edge of the sand is allowed to move freely in the vertical direction, and one locked B.C. where the outer edge of the sand has a fixed position.*

The geometry of the model (see Figure 3-35, left panel) includes all features of the upper package, except for the PEEK-plate at the bottom of the sand shield. The influence of this on the TH evolution was considered to be so small that neglecting it is justified. The mesh consists of 1,641 qL elements; with 1,761 nodes (see Figure 3-35, middle panel).

3.5.3 Material properties

The properties of the included materials are summarized in Table 3-21. They are chosen from the modelling of R10 (bentonite blocks) and R4 (bentonite rings). The hydraulic conductivity of the bentonite blocks were taken to be 2.4×10^{-14} m/s, two times the value suggested in Åkesson et al. (2010b). This gives a hydration rate during the first 200 days which agrees well with the measured rate.

3.5.4 Mechanical and hydraulic parameters

To correctly model the evolution of the upper package, the interaction (friction) between the sand filter and the rock wall and also the interaction between the bentonite rings and the sand filter, should be included in the model. However, CODE_BRIGHTv3 does not solve for frictional forces, and hence this was not possible. The bentonite and the sand are therefore assumed to be joined, while the interaction between the sand and the rock wall are handled at the two extremes (free rolling and no displacement along the wall respectively), using boundary conditions. Regarding the bentonite blocks, the plastic parameters were varied in the same way as when modelling R10. Hydraulic and mechanical parameters of the pellets are taken from Åkesson et al. (2010b). All these parameters are summarized in Table 3-22, Table 3-23, Table 3-24 and Table 3-25.

The plug's material parameters have to be handled in a special way. In reality, the plug was anchored into the rock using nine rods. As the swelling bentonite developed an axial stress on the plug, these rods were strained, leading to a displacement of the plug. The rods can be assumed to be "softer" than the concrete plug, and hence any displacement due to compression of the plug can be neglected.

In the models, the upper horizontal boundary of the plug is, however, fixed, as the rods are not included. To allow for the bentonite to swell upwards, we have therefore allowed for compression of the plug. The mechanical parameters were chosen so as to reproduce the measured stress-strain relationship of the plug in TBT. These parameters are given in Table 3-25.

Table 3-21. Hydraulic and solid phase properties.

Material	Solid density [kg/m^3]	Intrinsic permeability [m^2]	Liq. rel. Perm. ($k_{rl} = S_{rl}^{\delta}$)
Bentonite cylinders	2,780	2.0×10^{-21}	
Bentonite rings	2,780	2.4×10^{-21}	
Pellets	2,780	5.2×10^{-19}	
Sand filter	2,650	1.0×10^{-20}	δ=3
Sand shield	2,650	1.0×10^{-15}	
Concrete plug	2,800	1.0×10^{-18}	
Heater	7,800	1.0×10^{-30}	

Table 3-22. Retention properties.

Material	Law	P_0	λ_0	P_1	λ_1
Bentonite cylinders	$S_l = C(\Psi, P_1)\left\{\ln\left[e + \left(\frac{\Psi}{P_0}\right)^{\lambda_0}\right]\right\}^{-\lambda_1}$	69.228	1.811	2.544×10^4	1.872
Bentonite rings		284.288	1.347	9.854×10^7	6.148
	$C(\Psi, P_1) = 1 - \frac{\ln(1 + \Psi/P_1)}{\ln(1 + 10^6/P_1)}$				

Table 3-22. Continued.

Material	Law	P_0	λ_0	P_1	λ_1
Sand filter	$S_l = \left(1 - \left(\frac{\Psi}{P_0}\right)^{\frac{1}{1-\lambda_0}}\right)^{-\lambda_0} \left(1 + \frac{\Psi}{P_1}\right)^{\lambda_1}$	0.005	0.6	700	1.1
Sand shield		0.01	0.6	700	1.1
Pellets	$S_l = \left(1 - \left(\frac{\Psi}{P_0}\right)^{\frac{1}{1-\lambda_0}}\right)^{-\lambda_0}$	0.508	0.26		
Concrete plug		9.0	0.3		
Heater		50	0.3		

Table 3-23. BBM model – Elastic parameter values of bentonite.

Material	κ_{i0}	κ_{s0}	K_{min}	υ	α_{ss}	α_{sp}	α_i	p_{ref}
Bentonite cylinders					–0.01		–0.021	1
Bentonite rings	0.12	0.3	20	0.2	–0.01	*	–0.021	1
Pellets					0		–0.01	0.1

* The α_{sp} parameter is replaced by an in-house development of the code; see Åkesson et al. (2010b).

Table 3-24. BBM model – Plastic parameter values of bentonite.

Material	Set	e_T	λ_0	r	β	ρ	k	p_{s0}	p_c	M	α	e_0	p_0*
Blocks	P1	0.692	0.158	0	0		0	2.7	1	0.23		0.573	21
	P2	0.620	0.148	0	0		0	3.0	1	0.22		0.573	32
	P3	0.573–0.692	0.158	0.71	0.01	0	0.011	2.7	7.8	0.23	0.5	0.573	21
Rings	–	0.686	0.158	0	0		0	2.7	1	0.23		0.631	21
Pellets	–	0.77	0.330	0	0		0	0.05	1	0.55		1.780	0.88

Table 3-25. Linear elastic materials – Parameter values.

Material	E [MPa]	υ
Sand filter	25	0.25
Sand shield	55	0.25
Concrete plug	99.6	0.2
Heater	2.1×10^5	0.2

3.5.5 Initial conditions

The models are simulated with a constant temperature of T = 60°C, which corresponds reasonably well to the conditions during the first 200 days. The different void ratios/porosities, as well as the initial liquid pressure and stress, are shown in Table 3-26.

Table 3-26. Initial conditions.

Material	Void ratio/Porosity	Liquid pressure	Stress
Concrete plug	0.429/0.300		
Bentonite cylinders	0.626/0.385		
Bentonite rings	0.573/0.364		
Sand shield	0.456/0.313	–45.9	$\sigma = -0.11\ \boldsymbol{I}$*
Sand filter	0.534/0.348		
Pellets	1.780/0.640		
Heater	0.001/0.001		

*Here ***I*** is the unit matrix.

These were chosen in accordance with measured densities (sand and bentonite) or otherwise taken from previous modelling exercises in TBT (Åkesson 2006).

3.5.6 Boundary conditions

Hydraulic

The wetting of the sand filter is handled in a schematic way, where we saturate the sand in segments equal to the heights of the bentonite rings. Sand which is not saturated is given a suction of 46 MPa, corresponding to the initial suction in the bentonite. The transition between the two pressure states is handled by ramping up the liquid pressure from –45.9 MPa to 0.1 MPa in about one minute. An overview of the wetting scheme is given in Table 3-27 below. All other boundaries than the sand filter are assigned a no-flow condition.

Table 3-27. Overview of the scheme used to model the wetting of the sand. The cylinder/ring in the right column identifies the part of the bentonite up until which the sand was saturated.

Time (days)	Uppermost saturated bentonite cylinder/ring
0–20	No water
20–26	C2
26–33	R7
33–40	R8
40–47	R9
47–54	R10
54–63	R11
63–70	R12 (NB! The sand only reached half-way up R12)
70–200	Sand filter fully saturated

Mechanical

Two types of mechanical boundaries were used: A no displacement boundary and a boundary stress condition (see Figure 3-35).

For the inside of the heater, a boundary stress of $\sigma_r = –0.11$ MPa is placed on the vertical boundary and $\sigma_v = –0.11$ MPa is assigned to the horizontal boundaries.

A no vertical displacement criterion is assigned to the upper and lower part of the geometry. The vertical rock boundary is handled in two separate ways; with 1) a rolling boundary condition (i.e. the sand is allowed to move freely in the vertical direction) and 2) a locked boundary condition (the sand is not allowed to move in the vertical direction). In both cases, *no* horizontal movement of the outer edge of the sand filter is allowed. The purpose of these two boundary conditions is to explore the two extreme situations of 1) *no friction* between the sand and the rock wall, and 2) that the friction is so high that *no vertical movement* occurs at the rock/sand interface.

3.5.7 Results

Four models have been done, varying the mechanical boundary conditions and the yield surface of the bentonite blocks. They are summarized in Table 3-28 below:

Table 3-28. Models done of the upper package.

Model	Mechanical B.C on rock wall	Yield surface parameter set
TBTT3E1	Rolling	P1
TBTT3E2	Locked	P1
TBTT3E3	Rolling	P2
TBTT3E4	Rolling	P3

In Figure 3-36 we show the RH evolution in the model TBTT3E1 at the position of both R9 and C3, and compare it with measured data. As can be seen, the agreement in R9 is good, in particular at r = 0.735 m. At r = 0.635 m the model is slightly to dry. At the location of the RH sensors in C3, the measured data shows an increase in RH which is not seen in the model. This increase is probably due to vapour transport from the regions closer to the heater, which cannot be captured in this model.

In Figure 3-37 we plot the evolution of the axial stress at r = 0.635 m at the top of R9, both from model results and from the actual measurement. As in the 1D model presented earlier, the axial stresses are too low. Furthermore, the axial stresses are very similar between the models. As such, we can expect that the effect on the evolution in C3 should not differ significantly between the models.

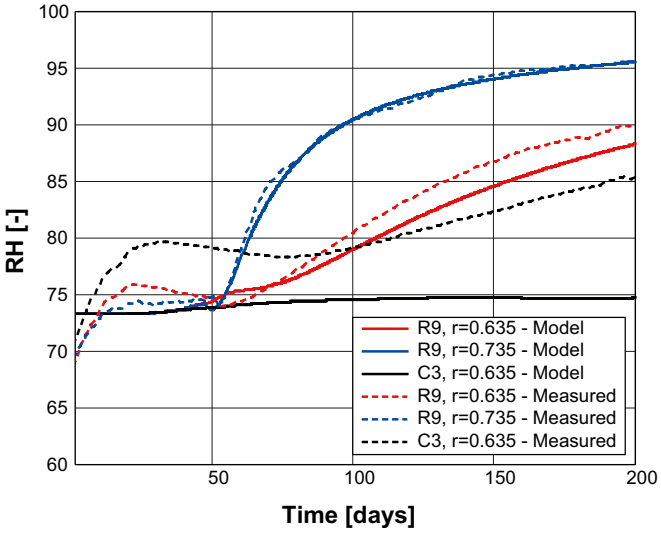

Figure 3-36. *RH evolution with time in R9 and C3, both the measured data (dashed lines) and data from the model TBTT3E1 (solid lines). The agreement is very good in the outer part of R9 (blue lines), relatively good further in at R9 (red line), and rather poor at C3. The discrepancy at C3 between the model and the measured data could be due to vapour transport caused by temperature gradients, which is not included here.*

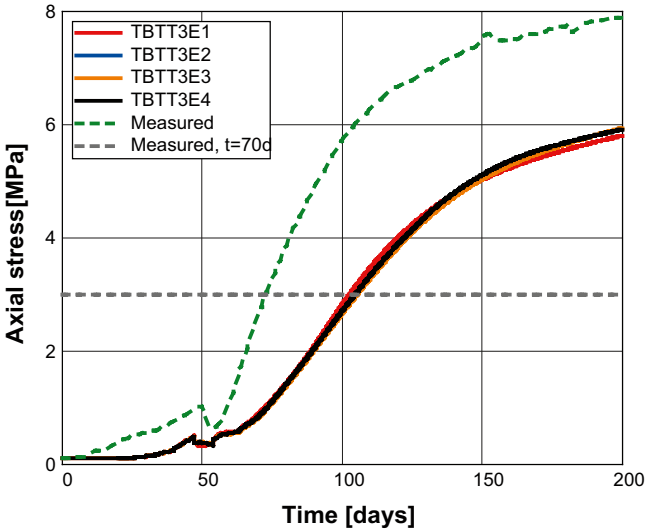

Figure 3-37. *Axial stress at r = 0.635 m at the height of R9, both from models (solid lines) and measured data (green dashed line). The grey line corresponds approximately to the axial stress in R9 at day 70, around the time at which the shearing in C3 occurred. This stress level is not reached until after day 100 in the models, hence any shearing at C3 in the models should occur after day 100.*

In Figure 3-38 we plot the radial, axial and tangential stress at r = 0.635 m on the top of C3. Also included are the measured stresses at this point. The different panels correspond to the four models done. The stress evolution is rather similar in all three models in which the sand is allowed to move freely in the vertical direction (TBTT3E1 and TBTT3E3–E4). In TBTT3E2 on the other hand the axial stress is considerably lower. In this model some of the axial stress is essentially taken up by the rock wall, explaining the decrease in axial stress in C3.

The axial stress produced in the models is comparable in magnitude to that seen around day 70 in TBT. However, the build-up of the axial stress in the models is considerably slower. The other two principal stresses (tangential and radial) show a somewhat stronger growth in the models (in particular the radial stress) than what was measured. CODE_BRIGHT cannot reproduce the brittle behaviour of bentonite, and hence we cannot capture the sudden decrease in axial stress around day 80 in the models.

However, we would expect to see an axial displacement of some parts of the bentonite, as well as signs that the bentonite has yielded in roughly the same place as where shearing was observed to have occurred when C3 was excavated. In Figure 3-39 we show the displacement seen at dismantling of TBT (left panel) and model results from TBTT3E4; in the middle panel the values of P0 at t = 200 d and in the right panel the displacements at t = 200 d.

A similar picture to that seen when dismantling TBT can be seen in the model. A triangular shaped area of C3 has been pushed upwards by the swelling pressure from the bentonite below. This has caused the bentonite to yield in a line starting close to the left edge of R12 and ending roughly at the upper and outermost point of C3. The angle of this line as measured during dismantling was in the range 65°–72°, while in the model it is somewhat lower, approximately 55°.

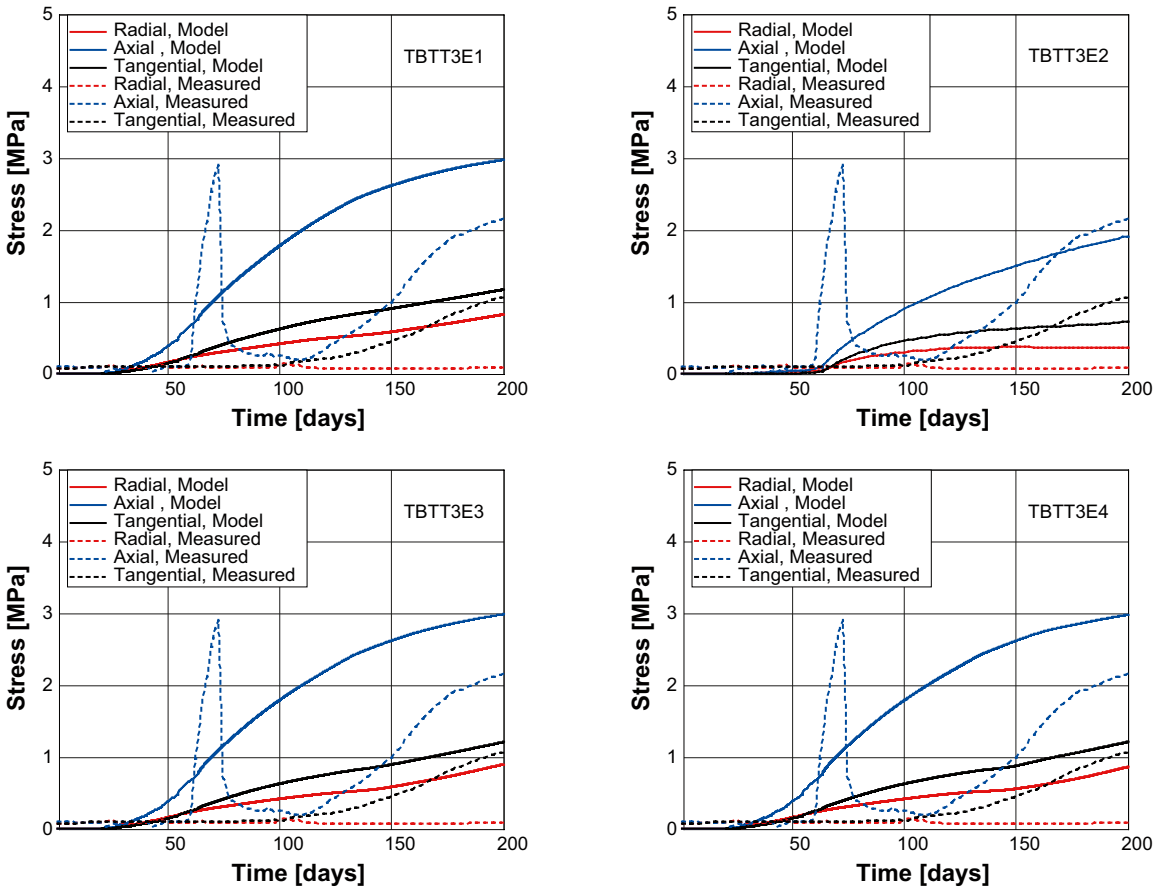

Figure 3-38. *Stress evolution at the top of C3 at a radius of r = 0.635 m in the four models TBTT3E1–E4. Solid lines correspond to model results, while dashed lines are measured data from TBT.*

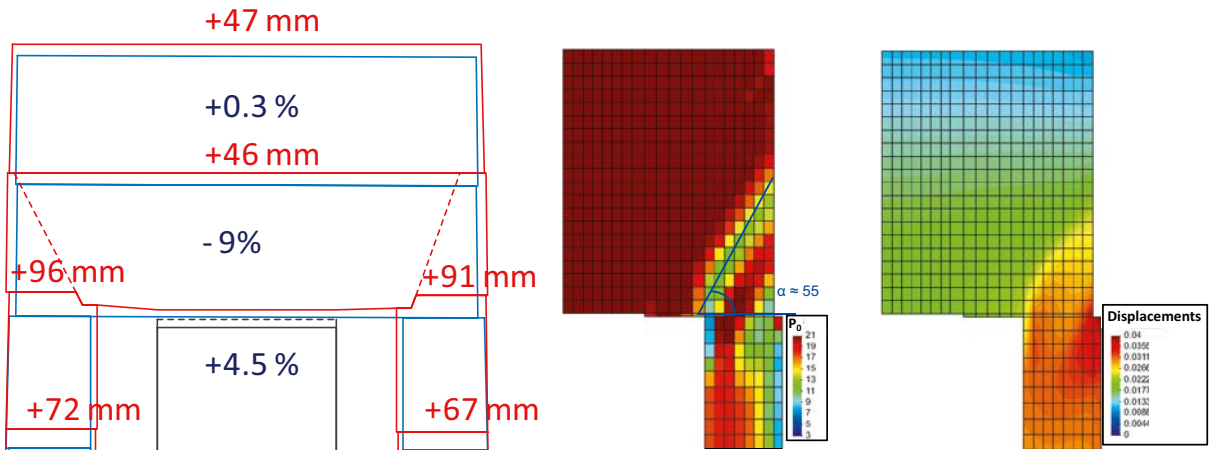

Figure 3-39. *In the left panel, the final displacements, as measured during the excavation of TBT, are illustrated. In the middle panel, the values of P_0, at time t = 200 d in model TBTT3E4 are plotted. Values lower than the initial (P0 = 2 MPa) indicates that, the material has hardened and hence that plasticisation has occurred.*

The model predicts and axial displacement of about 20 mm, much smaller than the ~50 mm seen at dismantling. This is, however, not surprising, as the sliding which occurred when the material failed in C3 cannot be captured in the model using CODE_BRIGHT and hence we cannot expect to reproduce the actual displacements.

3.5.8 Summary of modelling the upper package

This modelling exercise has shown that the shearing seen in C3 during dismantling agrees with model results. The axial swelling of the bentonite rings below leads to the build-up of a high deviatoric stress in C3, causing it to yield, forming a fracture in the bentonite. The actual displacements found when dismantling are larger than what the models predict, however this discrepancy may in part be due to later evolution.

The fracture in C3 may have been very important in the future evolution in TBT, as it may, for example, have acted as an escape path for gas. Understanding how it formed, as well as whether it "healed" or not at later times are therefore important. This modelling shows that the cause of the shearing and fracture formation is mostly due to the artificial wetting scheme. Hydrating the bentonite using a sand filter filled from below leads to a build-up of axial stress in the top parts, without any corresponding rise in radial or tangential stress, putting the bentonite there under a high deviatoric stress.

3.6 Task 4 – 2D-axisymmetric model of TBT

Below we present a 2D-axisymmetric model of the full TBT experiment. Only the T, H and g problem is solved, models also including M are not presented here, as it was too difficult to attain a correct solution to them (convergence problems).

The motivation here is to study how the hydration of the bentonite evolves if the gas pressure in the lower package is kept close to atmospheric levels. This may have been the case if gas could escape from the lower package into the sand shield, thereafter migrating out into the rock/tunnel via the upper cylinders.

3.6.1 Geometry and boundary conditions

The geometry consists of a 2D-axisymmetric cross section of the full TBT experiment (see Figure 3-40). All the materials used in TBT, except for the PEEK-plate at the bottom of the sand shield, are included. The mesh contains 2,286 nodes, with 2,132 qL elements in total.

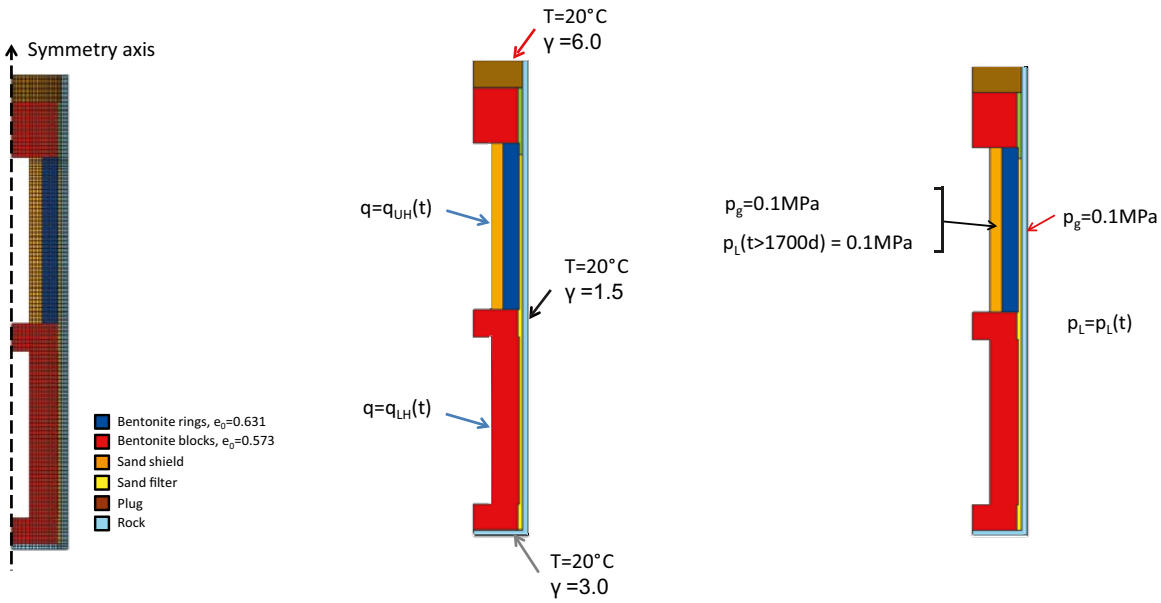

Figure 3-40. *Geometry, mesh and boundary conditions used to model Task 4. The time-dependent variables are described in the text.*

Thermal boundary conditions

The thermal problem is handled by two different boundary conditions. The heaters are replaced by an assigned heat flux on the left vertical boundaries of the upper ($q_{UH}(t)$) and lower package ($q_{LH}(t)$) respectively. The prescribed flux is varied with time in accordance with the actual output of the heaters in TBT; the exact values of the heat flux applied in the model are listed in Table 3-29.

The cooling effect of the surrounding rock and tunnel floor was handled somewhat differently from the 1D simulations presented above. An artificial rock material, 1 dm in thickness, was assigned around the lower and outer boundaries of the model. The material was given a very high heat capacity (c_V = 10,000 J kg^{-1} K^{-1}) and a high thermal conductance ($\lambda_{dry} = \lambda_{sat}$ = 60 W m^{-1} K^{-1}). On the outside of the material a Cauchy type boundary condition was prescribed, with temperature T = 20°C and γ = 1.5 on the vertical wall and γ=3 on the horizontal boundary respectively. On the tunnel floor a similar boundary condition was prescribed, with T = 20°C and γ = 6.0.

Table 3-29. The heat flux assigned to the left vertical boundaries of the lower and upper package respectively (see Figure 3-40).

t_1 [days]	t_2 [days]	q_{LH} [J/s]	q_{UH} [J/s]
0	8	900	900
8	15	1,200	1,200
15	1,171	1,500	1,500
1,171	1,695	1,600	1,600
1,695	1,702	1,700	1,500
1,702	1,709	1,800	1,400
1,709	1,716	1,900	1,300
1,716	1,723	2,000	1,200
1,723	1,730	2,000	1,100
1,730	2,343	2,000	1,000
2,343	2,347	2,000–0	1,000–0
2,347	2,600	0	0

Hydraulic boundary conditions

The inflow of water into the model was handled by a prescribed liquid pressure in the sand filter. The filling of the filter was handled in a schematic way, in which the sand was filled up to the top of each successive ring in 4 day intervals. The top of the water level in the sand filter, as function of time, is outlined in Table 3-30.

Table 3-30. Schematic overview of the water filling of the sand filter. The time here is the time at which the water level was at the top of the corresponding ring/cylinder.

Ring/Cylinder	C1	R1	R2	R3	R4	R5	R6	C2	R7	R8	R9	R10	R11	R12*
Time [days]	4	8	12	16	20	24	28	32	36	40	44	48	52	54

*R12 was only filled half-way up, as the transition between sand and pellets occurs at this height.

As no build-up of pore pressures are seen in the upper package before the filling of the sand shield, it would appear that the gas pressure remained atmospheric here. This is captured in the model, by applying a Cauchy-type boundary condition in one node there, with $p_g = 0.1$ MPa, and $\gamma = 0.1$. Due to the high conductivity of the material, this effectively keeps the gas pressure close to 0.1 MPa in the whole shield.

Also, in the model we, for computational reasons, allow gas in the sand filter to leak out by setting $p_g = 0.1$ MPa on the outer edge of the rock material.

The artificial saturation of the sand shield was not included for computational reasons. However, the effects of this saturation was mimicked by removing the gas leakage in the sand shield at t = 1,700 d.

3.6.2 Material properties

The material parameters for the bentonite in the models are chosen from the previous modelling of R3/4 and R9/10. To match the hydration as best we can, the permeability of the bentonite has been doubled for both the rings and blocks with respect to the "standard" values suggested in Åkesson et al. (2010b). They are, however, still within the limits of the sensitivity analyses suggested in the same report.

Table 3-31. Hydraulic and solid phase properties.

Material	Solid density [kg/m^3]	Spec. heat cap. [J kg^{-1} K^{-1}]	Intr. perm. [m^2]	Liquid rel. perm. ($k_{rl} = S_{rl}^{\delta}$)	Gas rel. perm. ($k_{rl} = AS_{rl}^{\delta}$)		Tortuosity
					A	δ	τ_v
Blocks	2,780	800	4.0×10^{-21}	3	10^8		
Rings	2,780	800	2.4×10^{-21}	3	10^8		
Pellets	2,780	800	5.2×10^{-19}	0	1		
Sand filter	2,650	800	1.0×10^{-15}	3	1	4	1
Sand shield	2,650	800	1.0×10^{-15}	3	1		
Plug	2,800	900	1.0×10^{-18}	3	1		
Rock	2,700	10,000	1.0×10^{-20}	3	10^{10}		

Table 3-32. Conductive heat flux.

Material	Law	λ_{sat} [W mK^{-1}]	λ_{dry} [W mK^{-1}]
Rings	$\lambda(S_l) = \lambda_{sat} sin^2(\pi S_l/2) + \lambda_{dry} cos 2(\pi S_l/2)$	0.5	1.3
Blocks		0.5	1.3
Pellets		0.5	1.3
Plug	$\lambda(S_l) = \lambda_{sat} S_l + \lambda_{dry}(1 - S_l)$	1.7	1.7
Rock		60	60
Sand filter		0.7	1.2
Sand shield		0.6/0.8*	1.6/1.8*

*In accordance with the results from Task 2, the conductivity of the sand shield was changed at t = 226 days. This change can most likely be attributed to the compression of the sand shield.

Table 3-33. Water retention curves.

Material	Retention curve	P_0 [MPa]	λ_0 [–]	P_1 [MPa]	λ_1 [–]
Rings	$S_l = C(\Psi, P_1)\left\{\ln\left[e + \left(\frac{\Psi}{P_0}\right)^{\lambda_0}\right]\right\}^{-\lambda_1}$	284.288	1.347	9.854×10^7	6.148
Blocks	$C(\Psi, P_1) = 1 - \frac{\ln(1+\Psi/P_1)}{\ln(1+10^6/P_1)}$	139.44	1.97	6.7	2.28
Pellets	$S_l = 10\left(1 - \left(\frac{\Psi}{P_0}\right)^{\frac{1}{1-\lambda_0}}\right)^{-\lambda_0}$	0.508	0.26		
Sand filter		0.1	0.6		
Sand shield		0.05	0.6		
Plug		9.0	0.3		
Rock		9.0	0.3		

The thermal expansion of liquid was shown to have a significant effect on, in particular, the final saturation profile in the modelling of R3/4 (see section 3.3). As such, we have used the parameters determined there that best match the actual behaviour of the liquid density in the temperature range in question. They are listed in Table 3-34 below.

Table 3-34. Liquid density.

Law	$\rho_{l,0}$ [kg/m^3]	α [°C^{-1}]
$\rho_l = \rho_{l,0}\, exp[4.5\times10^{-4}(P_l - 0.1) - \alpha T]$	1,010.0	6×10^{-4}

3.6.3 Initial conditions

The initial conditions are chosen in accordance with the material data given in the installation report (Johannesson et al. 2010). A suction of 46 MPa corresponds to the initial water content measured in the bentonite before installation. All adopted values are summarized in Table 3-8.

Table 3-35. Initial conditions.

Material	e/n	P_l (MPa)	P_g (MPa)	T (°C)
Rings	0.573/0.364			
Blocks	0.631/0.387			
Pellets	1.780/0.640			
Sand Filter	0.533/0.348	–45.9	0.1	20
Sand shield	0.456/0.313			
Plug	0.429/0.300			
Rock	0.001/0.001			

3.6.4 Results

The results of this modelling exercise are the temperature and RH evolution as compared to the sensor data, as well as the final liquid saturation, as measured during dismantling.

Temperature

The radial temperature profiles (solid lines) in the model for five different times, at the height of R4 and R10 respectively, are shown in Figure 3-41 and in Figure 3-42 we show the vertical temperature profile at r = 0.360 m and r = 0.685 m in the model (solid lines), at three different times; t = 200 d, 1,200 d and 1,900 d and compare them to measured data (symbols).

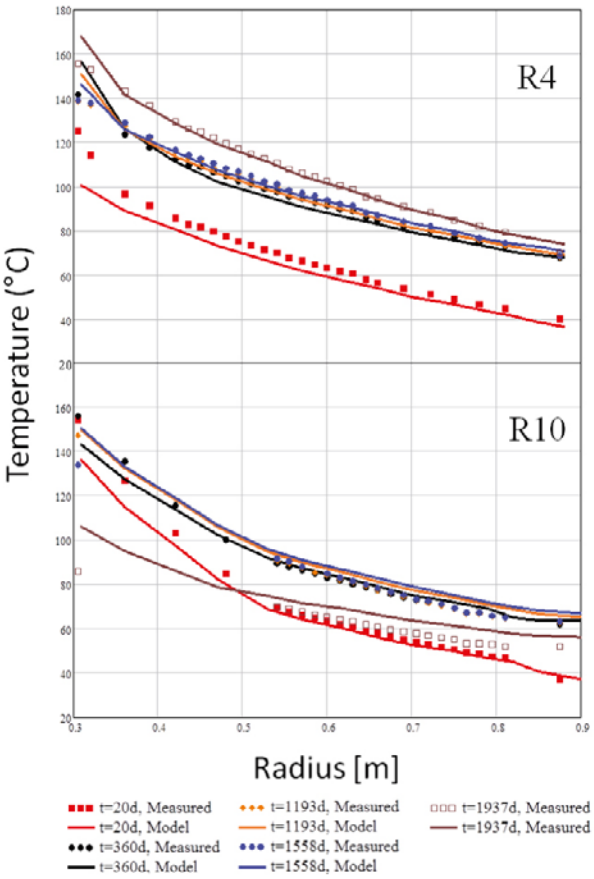

Figure 3-41. *Temperature profiles at five different points in time, at the position of R4 (upper panel) and R10 (lower panel). The measured temperatures are shown as symbols, while the temperature data from the models are shown as solid lines.*

The model temperatures in the bentonite agree rather well with the measured data, although the values are slightly too high in the upper package at later times. This could in part be due to the effect of neglecting the nearby CRT heater in the temperature boundary conditions used in the model.

In general, the temperature model, which in the case of the bentonite is based on the constitutive law and parameters recommended in Åkesson et al. (2010b), agrees well with measured temperatures. The ability to reproduce the measured temperatures without including a large body of rock surrounding the model allows us to use a much smaller number of elements than would otherwise have been needed.

RH

Aside from the temperatures, only the relative humidity evolution remains as a time-dependant variable to which we can compare the model behaviour. The RH evolution is strongly dependent on the behaviour of the gas in the experiment. If the gas pressure is below the water vapour saturation pressure somewhere in the model, it is not possible to saturate the material at that point. This means that the boundary conditions used when solving the mass balance of air is highly important for the RH evolution.

In Figure 3-43 we show the vertical RH profile at three different times in the model (solid lines, t = 200 d, 1,300 d and 1,900 d respectively), and compare it to the measured RH values (symbols). One note of caution here is that several RH sensors failed during the course of the field experiment, and in such cases no measured data exists to compare with.

At t = 200 d, the model is in general somewhat too dry, however, at later times (t = 1,300 d and 1,900 d) the agreement between the model and measured data is very good. The initial drying seen in the models, which does not appear to occur to the same extent in the field experiment, could in partly due to that the gas boundary conditions does not reflect the real situation. As we allow gas to escape

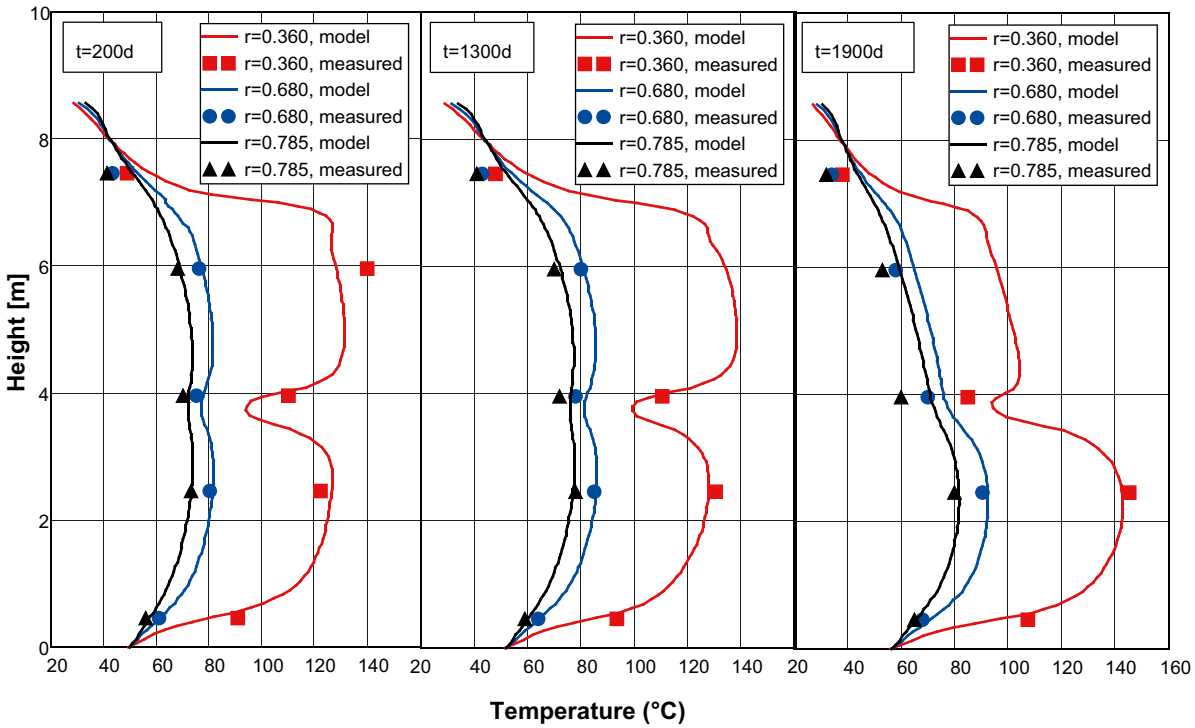

Figure 3-42. *Axial temperature distributions at three different times and radii. The solid lines represent model data, while the symbols correspond to measured data. The agreement is good, in particular in the lower parts, while in the upper part the temperatures are somewhat too high in the bentonite. The temperature in the sand shield, however, is considerably lower in the model than what was measured at r = 0.360 m, in particular at later times.*

freely through the sand shield, the latter will dry out considerably, causing the bentonite to also dry out. This is also consistent with the results from our modelling of R10 (see section 3.4).

The ability of gas to escape through the sand shield is also highly important for the evolution in the lower package. As long as C2 remains partially unsaturated, gas can migrate from the lower package into the shield. This keeps the gas pressure close to the lower heater below the vapour saturation pressure there, preventing the bentonite from taking up water and becoming saturated.

3.6.5 Final state

The final state of the model, in terms of liquid saturation, can be compared to the measurement done when dismantling the experiment. In Figure 3-44 we show the dismantling data (left panel) and compare it to model data just after the heaters have been turned off at t = 2,347 d (middle panel) and at the end of the simulation, i.e. at t = 2,600 d (right panel).

The agreement at t = 2,600 d with the saturation measured when dismantling the field experiment is good. Only in the inner parts of C2 (too dry) and in C3/C4 (too wet) is there a significant difference between the model results and the measured data. It is important to remember that we have not solved the mechanical problem here. If that was included, some shrinkage of the bentonite could be expected, as seen in particular when modelling R9/10. This would most likely lead to a somewhat higher degree of saturation around the lower heater due to the decrease in available pore volume.

3.6.6 Influence of gas boundary conditions

The purpose of this modelling exercise has been to understand how the evolution of the gas pressure may have influenced the hydration rate in bentonite. In most of the 1D models presented earlier, no gas was allowed to escape except via the rock/sand filter interface. As such, due to the high temperatures near the heaters, the gas pressure could reach values much higher than the vapour saturation pressure, allowing the bentonite to become water saturated.

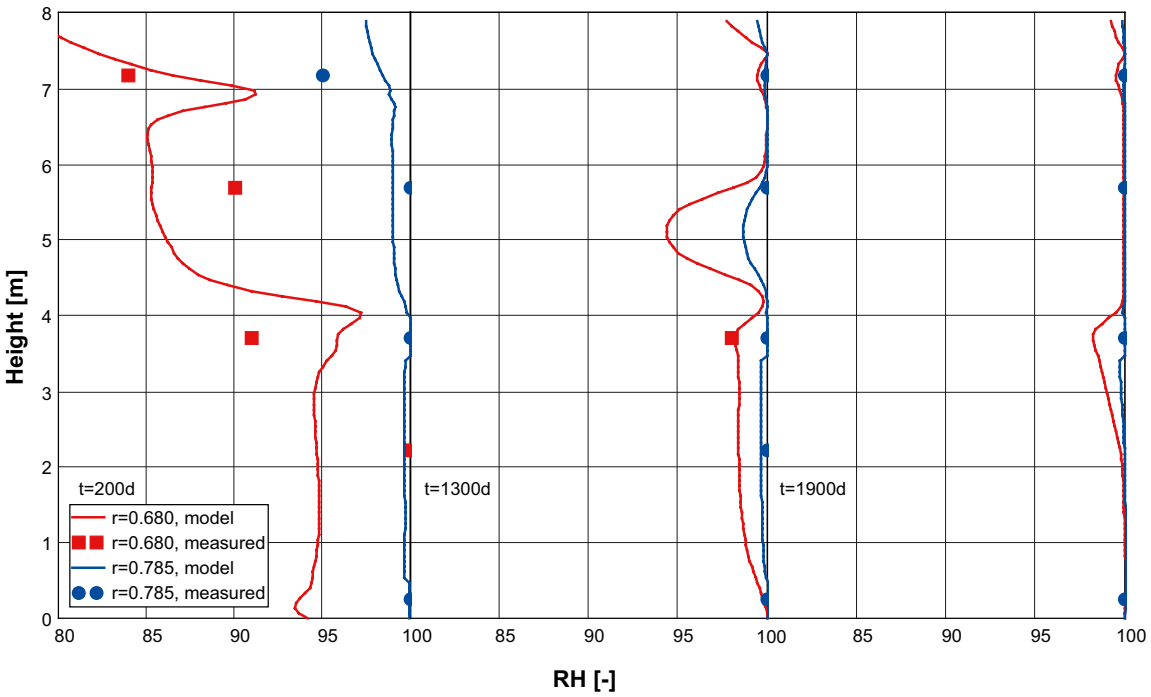

Figure 3-43. *Axial RH profiles at t = 200 d (left panel), t = 1,300 d (middle panel) and t = 1,900 d (right panel).The solid lines corresponds to model data, while the symbols represent measured data.*

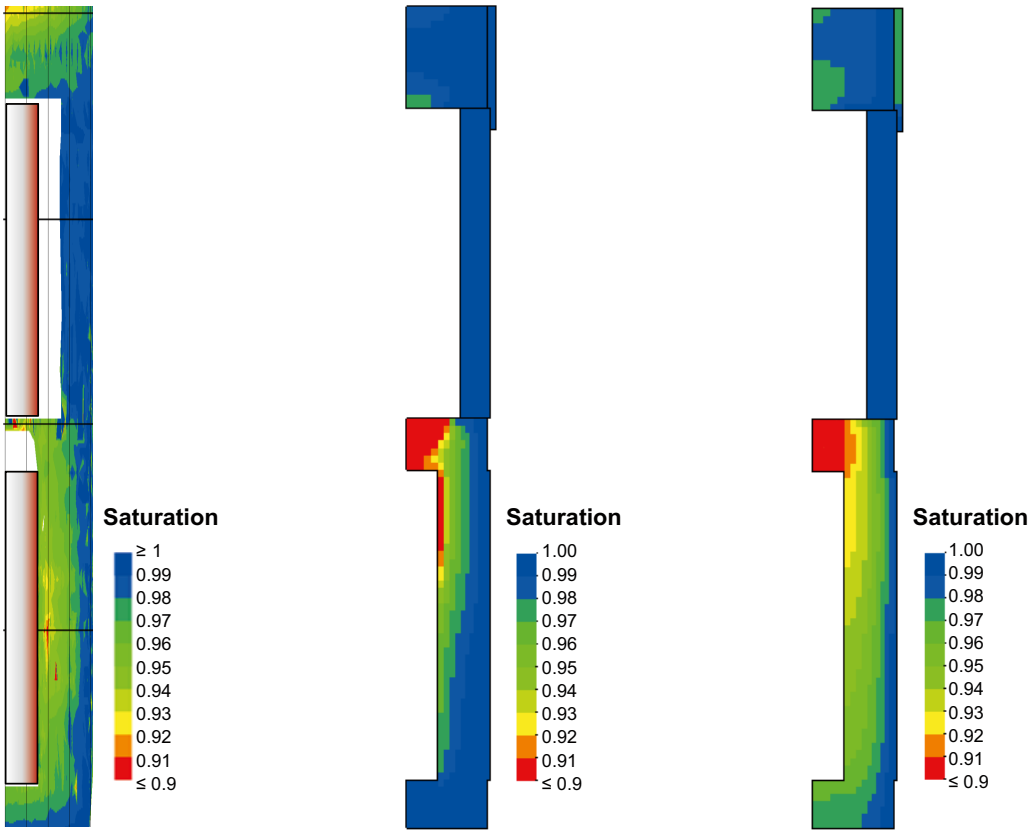

Figure 3-44. *The final liquid saturation in the field experiment as measured during dismantling is shown in the left panel. In the middle panel we show the results from the model (TBTT4F2) at t = 2,347 d, (i.e. at the day the heaters are switched off). In the right panel, the liquid saturation at t = 2,600 d in the model is displayed. The decrease in saturation between day 2,347 and 2,600 is due to the decrease in water volume, caused by the cooling of the material. No data currently exists for the final saturation in the inner parts of C2 in the field experiment, and as such it is unknown how the model data compares the measured data there. In the model the lowest saturation is found close to the symmetry axis in C2, with a value of S = 0.88.*

However, the high temperatures near the lower heater (T≈150°C) means that the water vapour saturation pressure there reached as high as 4.5 bars. However, none of the pore pressure sensors indicates that such a high gas pressure was ever reached in the field experiment.

In Figure 3-45 we plot the evolution of gas pressure, water vapour saturation pressure and liquid saturation at r = 0.36 m in both R3/4 and C2. In R3/4, the gas pressure is higher than the vapour saturation pressure already from day 650, and as such the bentonite is hydrated continuously. In C2, however, the gas pressure is similar to, or lower than, the saturation pressure until day 1,700. At this point the gas leakage, previously allowed through the sand filter, is removed, and hence the gas pressure in C2 starts to grow, at the same time as the system is cooled down, decreasing the water vapour saturation pressure. The result is a distinct increase in saturation.

The behaviour seen in Figure 3-45 illustrates how important the gas-pressure evolution is when modelling the hydration of the bentonite in TBT. One important discrepancy here is that the model predicts that the gas pressure close to the lower heater should have risen to above 4 bars after the increase in heater power to 2,000 W. No such strong increase is seen in the data from the pore pressure sensor situated at r = 0.420 m at this time. Instead, an instantaneous, but moderate, increase in the pore pressure is seen, where after the pressure starts to decrease steadily. If this data is correct, gas appears to have been able to leak from the region even after the sand shield was artificially saturated. It is worth pointing out that in the tests following the dismantling, the pore pressure sensor in question (UB201, situated at r = 0.420 m in R3) was deemed to be "Under specification" (Goudarzi et al. 2010), leaving some room for that the measured data at this particular point may be inaccurate.

Summary of modelling the full TBT

The 2D-axisymmetric model of the full TBT experiment presented in this section has shown that the evolution of the gas pressure in the field experiment played a crucial role in the hydration of the bentonite. The experimental data suggests that the gas pressure, p_g, remained close to atmospheric in all parts of the experiment until at least day 1,700, thereby possibly preventing the bentonite from becoming fully saturated in some regions near the lower heater where the water vapour saturation pressure was high.

The model presented here, which includes the leakage of gas through the sand shield, thereby keeping the gas pressures close to atmospheric levels until day 1,700 can reasonably well reproduce the measured RH evolution, as well as the final saturation state as measured during dismantling. Still, the model do predict a growth in gas pressure after day 1,700 (when the sand shield was artificially saturated) which is not seen in the measured data, perhaps suggesting that additional pathways through which the gas could escape may have been present.

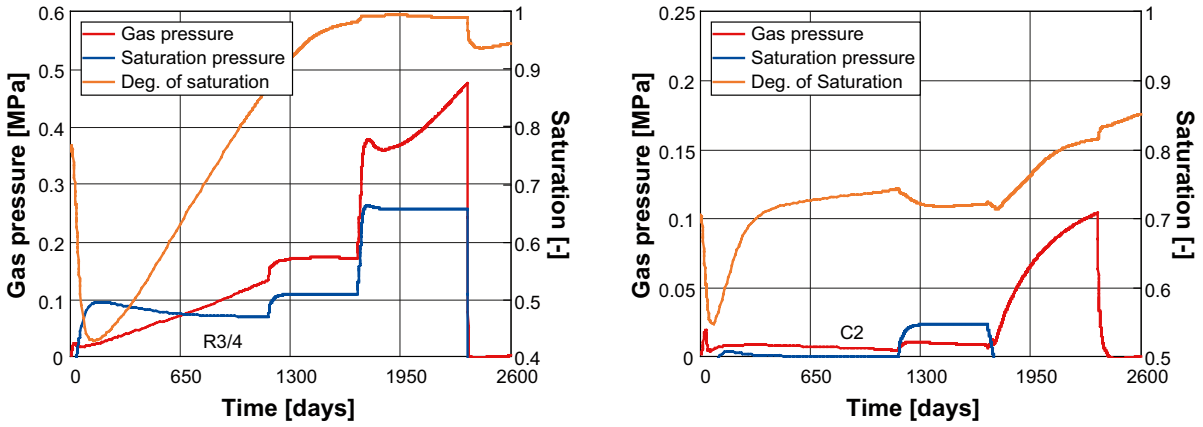

Figure 3-45. *The evolution of gas and vapour saturation pressure and liquid saturation at the height of R4 (left panel) and C2 (right panel). In both cases the evolution at a radius of r = 0.360 m is shown.*

4 ClayTechnology contribution – ABAQUS

4.1 Code ABAQUS

4.1.1 General

The finite element code ABAQUS contains a capability of modelling a large range of processes in many different materials as well as complicated three-dimensional geometry.

The code includes special material models for rock and soil and ability to model geological formations with infinite boundaries and *in situ* stresses by e.g. the own weight of the medium. It also includes capability to make substructures with completely different finite element meshes and mesh density without connecting all nodes. This technique has been used in the modelling of TBT. Detailed information of the available models, application of the code and the theoretical background is given in the ABAQUS Manuals.

4.1.2 Hydro-mechanical analyses in ABAQUS

The hydro-mechanical model consists of porous medium and wetting fluid and is based on equilibrium, constitutive equations, energy balance and mass conservation using the effective stress theory.

Equilibrium

Equilibrium is expressed by writing the principle of virtual work for the volume under consideration in its current configuration at time t:

$$\int_v \boldsymbol{\sigma}:\delta\boldsymbol{\varepsilon} dV = \int_S \mathbf{t}\cdot\delta\mathbf{v} dS + \int_v \hat{\mathbf{f}}\cdot\delta\mathbf{v} dV, \quad (4\text{-}1)$$

where $\delta\mathbf{v}$ is a virtual velocity field, $\delta\boldsymbol{\varepsilon} \stackrel{def}{=} \mathrm{sym}(\partial\delta\mathbf{v}/\partial\mathbf{x})$ is the virtual rate of deformation, $\boldsymbol{\sigma}$ is the true (Cauchy) stress, $\mathbf{t}$ are the surface tractions per unit area, and $\hat{\mathbf{f}}$ are body forces per unit volume. For our system, $\hat{\mathbf{f}}$ will often include the weight of the wetting liquid,

$$\mathbf{f}_w = S_r n \rho_w \mathbf{g}, \quad (4\text{-}2)$$

where S_r is the degree of saturation, n the porosity, ρ_w the density of the wetting liquid and $\mathbf{g}$ is the gravitational acceleration, which we assume to be constant and in a constant direction (so that, for example, the formulation cannot be applied directly to a centrifuge experiment unless the model in the machine is small enough that g can be treated as constant). For simplicity we consider this loading explicitly so that any other gravitational term in $\hat{\mathbf{f}}$ is only associated with the weight of the dry porous medium. Thus, we write the virtual work equation as

$$\int_v \boldsymbol{\sigma}:\delta\boldsymbol{\varepsilon} dV = \int_S \mathbf{t}\cdot\delta\mathbf{v} dS + \int_v \mathbf{f}\cdot\delta\mathbf{v} dV + \int_v S_r n \rho_w \mathbf{g}\cdot\delta\mathbf{v} dV, \quad (4\text{-}3)$$

where $\mathbf{f}$ are all body forces except the weight of the wetting liquid.

The simplified equation used in ABAQUS for the effective stress is:

$$\bar{\boldsymbol{\sigma}}^* = \boldsymbol{\sigma} + \chi u_w \mathbf{I}. \quad (4\text{-}4)$$

where $\boldsymbol{\sigma}$ is the total stress, u_w is the pore water pressure, χ is a function of the degree of saturation (usual assumption $\chi = S_r$), and $\mathbf{I}$ the unitary matrix.

Energy balance

The conservation of energy implied by the first law of thermodynamics states that the time rate of change of kinetic energy and internal energy for a fixed body of material is equal to the sum of the rate of work done by the surface and body forces. This can be expressed as (not considering the thermal part, which is solved as uncoupled heat transfer; cf Equation (4-15)):

$$\frac{\mathrm{d}}{\mathrm{dt}}\int_V \left(\tfrac{1}{2}\rho\mathbf{v}\cdot\mathbf{v} + \rho U\right)\mathrm{dV} = \int_s \mathbf{v}\cdot\mathbf{t}\mathrm{dS} + \int_V \mathbf{f}\cdot\mathbf{v}\mathrm{dV} \quad (4\text{-}5)$$

where

ρ is the current density,

v is the velocity field vector,

U is the internal energy per unit mass,

t is the surface traction vector,

f is the body force vector, and

Constitutive equations

The constitutive equation for the solid is expressed as:

$$d\boldsymbol{\tau}^{c} = \mathbf{H}: d\boldsymbol{\varepsilon} + \mathbf{g} \tag{4-6}$$

where $d\boldsymbol{\tau}^{c}$ is the stress increment, **H** the material stiffness, $d\boldsymbol{\varepsilon}$ the strain increment and **g** is any strain independent contribution (e.g. thermal expansion). **H** and **g** are defined in terms of the current state, direction for straining, etc., and of the kinematic assumptions used to form the generalised strains.

The constitutive equation for the liquid (static) in the porous medium is expressed as:

$$\frac{\rho_{\mathrm{w}}}{\rho_{\mathrm{w}}^{0}} \approx 1 + \frac{\mathrm{u}_{\mathrm{w}}}{\mathrm{K}_{\mathrm{w}}} - \varepsilon_{\mathrm{w}}^{\mathrm{th}}, \tag{4-7}$$

where ρ_w is the density of the liquid, ρ_{w}^{0} is its density in the reference configuration, $K_w(T)$ is the liquid's bulk modulus, and

$$\varepsilon_w^{th} = 3\alpha_w(T - T_w^0) - 3\alpha_{w|T^I}(T^I - T_w^0) \tag{4-8}$$

is the volumetric expansion of the liquid caused by temperature change. Here $\alpha_{\mathrm{w}}(T)$ is the liquid's thermal expansion coefficient, T is the current temperature, T^{I} is the initial temperature at this point in the medium, and T_{w}^{0} is the reference temperature for the thermal expansion. Both $\mathrm{u_w/K_w}$ and $\varepsilon_{\mathrm{w}}^{\mathrm{h}}$ are assumed to be small.

Mass conservation

The mass continuity equation for the fluid combined with the divergence theorem implies the point wise equation:

$$\frac{1}{J}\frac{d}{dt}(J\rho_{\mathrm{w}} S_r n) + \frac{\partial}{\partial \mathbf{x}} \cdot (\rho_{\mathrm{w}} S_r n \mathbf{v}_{\mathrm{w}}) = 0. \tag{4-9}$$

where J is the determinant of the Jacobian matrix of the skeleton motion and x is position. The constitutive behaviour for pore fluid is governed by Darcy's law, which is generally applicable to low fluid velocities. Darcy's law states that, under uniform conditions, the volumetric flow rate of the wetting liquid through a unit area of the medium, Srnvw, is proportional to the negative of the gradient of the piezometric head:

$$S_r n \mathbf{v}_{\mathrm{w}} = -\hat{\mathbf{k}} \frac{\partial \phi}{\partial \mathbf{x},} \tag{4-10}$$

where $\hat{\mathbf{k}}$ is the permeability of the medium and ϕ is the piezometric head, defined as:

$$\phi \overset{def}{=} \mathrm{z} + \frac{\mathrm{u}_{\mathrm{w}}}{\mathrm{g}\rho_{\mathrm{w}}} \tag{4-11}$$

where z is the elevation above some datum and g is the magnitude of the gravitational acceleration, which acts in the direction opposite to z. $\hat{\mathbf{k}}$ can be anisotropic and is a function of the saturation and void ratio of the material. $\hat{\mathbf{k}}$ has units of velocity (length/time). [Some authors refer to $\hat{\mathbf{k}}$ as the hydraulic conductivity and define the permeability as

$$\hat{\mathbf{K}} = \frac{\nu}{g}\hat{\mathbf{k}} \tag{4-12}$$

where ν is the kinematic viscosity of the fluid.]

We assume that g is constant in magnitude and direction, so

$$\frac{\partial \phi}{\partial \mathbf{x}} = \frac{1}{\mathrm{g}\rho_{\mathrm{w}}}\left(\frac{\partial \mathrm{u}_{\mathrm{w}}}{\partial \mathbf{x}} - \rho_w \mathbf{g}\right) \tag{4-13}$$

Vapour flow

Vapour flow is modelled as a diffusion process driven by a temperature gradient (coded as UEL user supplied routine with stiffness and flow).

$$\mathbf{q}_v = -D_{Tv}\frac{\partial T}{\partial \mathbf{x}} \tag{4-14}$$

where $\mathbf{q}_v$ is the vapour flux and D_{Tv} the thermal vapour diffusivity.

4.1.3 Uncoupled heat transfer analysis

Energy balance

The basic energy balance is (neglecting mechanical contribution; cf. Equation (4-5))

$$\int_V \rho \dot{U} dV = \int_S q dS + \int_V r dV \tag{4-15}$$

where V is a volume of solid material, with surface area S; ρ is the density of the material; $\dot{U}$ is the material time rate of the internal energy; q is the heat flux per unit area of the body, flowing into the body; and r is the heat supplied externally into the body per unit volume.

It is assumed that the thermal and mechanical problems are uncoupled in the sense that $U = U(T)$ only, where T is the temperature of the material, and q and r do not depend on the strains or displacements of the body. For simplicity a Lagrangian description is assumed, so "volume" and "surface" mean the volume and surface in the reference configuration.

Constitutive definition

The relationship is usually written in terms of a specific heat, neglecting coupling between mechanical and thermal problems:

$$c(T) = \frac{dU}{dT} \tag{4-16}$$

Heat conduction is assumed to be governed by the Fourier law.

$$\mathbf{f}_q = -\mathbf{k}\frac{\partial T}{\partial \mathbf{x}} \tag{4-17}$$

where $\mathbf{f}_q$ is the heat flux and $\mathbf{k}$ is the heat conductivity matrix, $\mathbf{k} = \mathbf{k}(T)$. The conductivity can be fully anisotropic, orthotropic, or isotropic.

4.1.4 Coupling of thermal and hydro-mechanical solutions

In ABAQUS the coupled problem is solved through a "staggered solution technique" as sketched in Figure 4-1 and below.

1. First a thermal analysis is performed where heat conductivity and specific heat are defined as functions of saturation and water content. In the first analysis these parameters are assumed to be constant and in the subsequent analyses they are read from an external file.
2. The hydromechanical model calculates stresses, pore pressures, void ratios, degree of saturation etc as function of time. Saturation and void ratio histories are written onto an external file.
3. The material parameters update module reads the file with saturation and void ratio data and creates a new file containing histories for saturation and water content.
4. The saturation and water content histories are used by the thermal model in the following analysis.
5. Steps 1–3 are repeated if parameter values are found to be different compared to those of the previous solution.

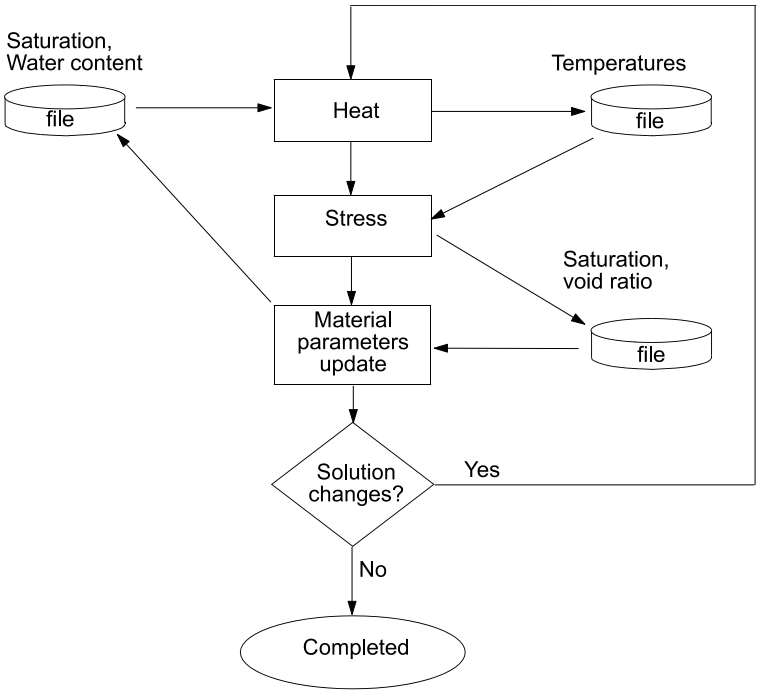

Figure 4-1. *In ABAQUS, heat transfer calculations and hydro-mechanical calculations are decoupled. By using the iteration procedure schematically shown above, the effects of a fully coupled THM model are achieved.*

Finite element model

The entire test is modelled with a axi-symmetric 2D model, that includes the rock, the heaters and the plug with anchors. Figure 4-2 shows the element mesh and some details of the mesh and Figure 4-3 shows the different property areas.

The model includes altogether two different bentonite materials (bentonite rings and bentonite blocks), an empty slot and seven other materials (heaters, rock, concrete plug, steel lid, sand shield, sand filter and anchors). In addition there is a row of water elements that are used to fill the sand filter with water in the measured filling sequence.

The geometry has been somewhat simplified compared to the geometry of field test. The upper small part of the outer slot that was filled with pellets has been exchanged to sand filter material and the thickness of the sand filter was made uniform to the same thickness (corresponding to the average thickness). The reason for these simplifications is problems with the water filling of the sand filter.

The dimensions and material names of the different parts in the model are shown in Table 4-1.

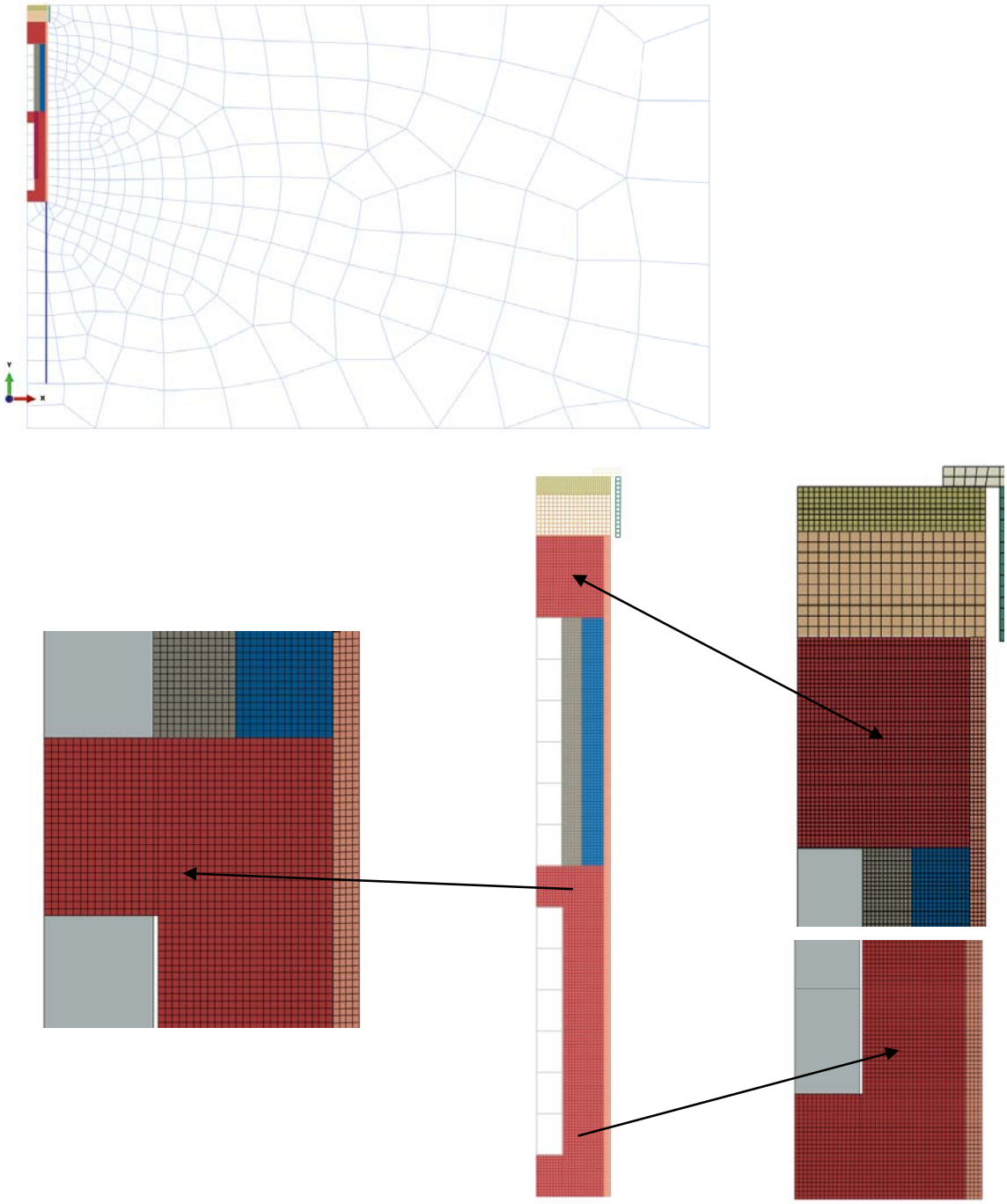

Figure 4-2. *Element mesh and some details. The water element is shown below the deposition hole in the upper figure.*

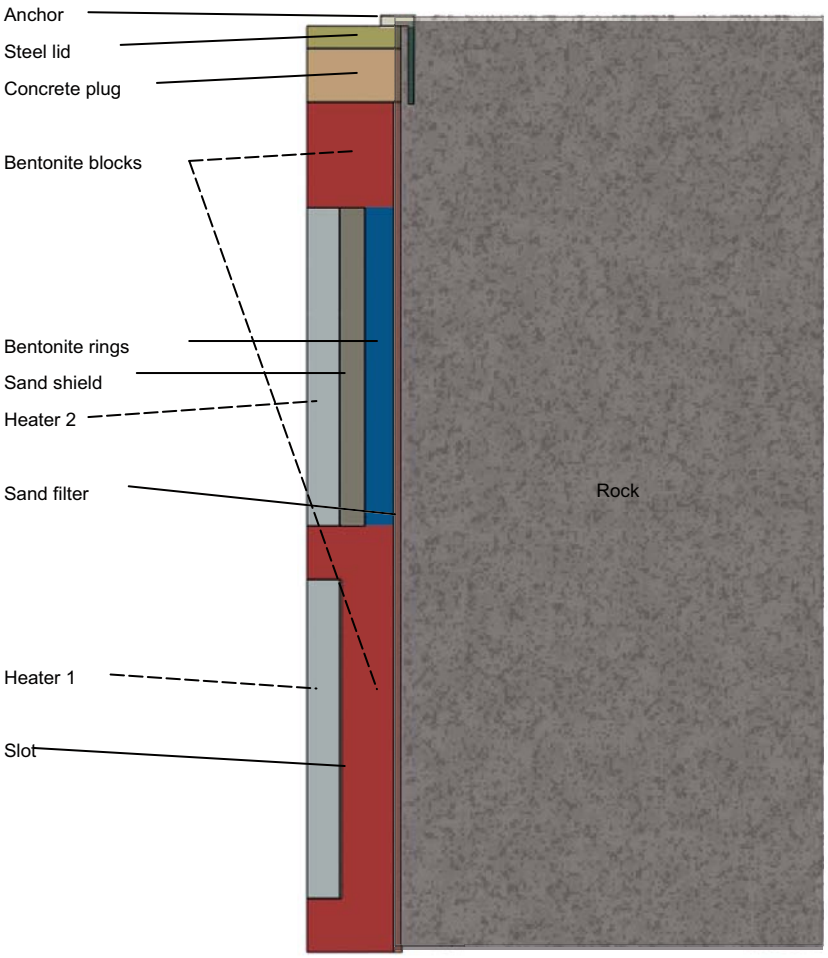

Figure 4-3. *Property areas.*

Table 4-1. Dimensions and material name of the different parts of the model listed from the top of the model.

Model part	Radial thickness (m)	Axial length (m)	Material name
Steel plug	r = 0.8785	0.21	Steel
Concrete plug	r = 0.8785	0.5	Concrete
Upper bentonite blocks	r = 0.805	1.0	Blocks
Sand filter	Δr = 0.0735	8.0	Sand filter
Upper heater (2)	r = 0.305	0.3	Heater
Sand shield	Δr = 0.23	0.3	Sand shield
Upper bentonite rings	Δr = 0.27	0.3	Rings
Intermediate bentonite block	r = 0.805	0.5	Blocks
Lower heater (1)	r = 0.305	0.3	Heater
Empty slot	Δr = 0.013	0.3	–
Lower bentonite rings	Δr = 0.487	0.3	Rings
Bottom block	r = 0.805	1.0	Blocks
Rock	r = 31	18.8	Rock

4.2 Material properties

4.2.1 General

The model is composed of eleven different materials, of which two are different bentonite models. The bentonite material MX-80 is used for all bentonite parts but with different densities and water contents, resulting in the same material model but different initial conditions. Table 4-2 shows the basic properties for the three bentonite parts.

The lower bentonite rings are made of solid blocks that have been tooled to yield the right geometry including the 0.318 m diameter hole for heater 1, which explains why they have the same properties as the bentonite blocks.

The two types of blocks are modelled as water unsaturated bentonite with the models developed for ABAQUS described in section 4.3.2. The other materials are described in section 4.3.3.

In addition there is a slot of 13 mm between the heater 1 and the lower bentonite rings that has been modelled by applying contact conditions to the inner surface of the lower bentonite rings.

4.2.2 Bentonite blocks and rings

General

This chapter contains a description of the material models for the two types of bentonite blocks and the parameters included in the models.

The following processes are modelled:

Thermal:

- Thermal flux from conduction.

Hydraulic:

- Water liquid flux.
- Water vapour flux.
- Hydraulic coupling between the pore water and the pore gas.

Mechanical:

- Mechanical behaviour of the structure.
- Thermal expansion.
- Mechanical behaviour of the separate phases.
- Mechanical coupling between the structure and the pore water.

The model includes complete coupling between all processes. Most processes are a function of the following variables:

- Temperature.
- Degree of water saturation.
- Void ratio.

Table 4-2. Basic properties of three of the bentonite parts.

Section	Density (kg/m^3)	Water ratio	Dry density (kg/m^3)	Void ratio	Degr. of saturation
Bentonite blocks	1,991	0,172	1,699	0,636	0,751
Upper bentonite rings	2,087	0,171	1,782	0,560	0,849
Lower bentonite rings	1,991	0,172	1,699	0,636	0,751

Required parameters

The required input parameters for the described THM model in ABAQUS are the following:

Thermal:

- Tables of thermal conductivity λ and specific heat c as function of void ratio e, degree of saturation S_r.

Hydraulic:

- Table of the hydraulic conductivity of water saturated material K as function of void ratio e and temperature T.
- Influence of degree of saturation S_r on the hydraulic conductivity K_p expressed as the factor δ in Equation (4-19).
- The basic water vapour flow diffusivity D_{Tvb} and the parameters a and b in Equations (4-21) to (4-23).
- The retention curve (table of the matric suction u_w as a function of the degree of saturation S_r.).

Mechanical:

- Porous bulk modulus κ according to Equation (4-26) and Poisson's ratio ν.
- Drucker-Prager plasticity parameters β, d, ψ, and the **yield function**.
- Bulk modulus and coefficient of thermal expansion of water (B_w, α_w) and bulk modulus solids (B_s).
- Bishops parameter χ in Equation (4-27) (usual assumption $\chi = S_r$).
- The volume change correction ε_v as a function of the degree of saturation S_r (the "moisture swelling" procedure).

Initial conditions

The following initial conditions of the elements in the structure need to be specified:

- void ratio e,
- degree of saturation S_r,
- pore pressure u (kPa),
- average effective stress p (kPa),
- the temperature T (˚C).

Material models of the ring-shaped blocks, solid blocks and the bricks

The models and data used for the buffer are essentially the same as used for modelling the wetting of KBS-3V for SR-Can (Börgesson et al. 2006), but the parameters used are mainly valid for the void ratios 0.7–0.9. In the CRT the initial void ratio is 0.56–0.72 (except for the pellets filling), which requires recalibration of some of the data.

Thermal flux from conduction

The only thermal flux that is included in the model is thermal conduction with the following parameters:

λ= thermal conductivity (W/m,K),

c = specific heat (Ws/K,kg),

ρ = bulk density (kg/m^3).

The *thermal conductivity* has been measured as a function of the degree of saturation and density (Börgesson et al. 1994). The parameter values for the ABAQUS model are shown in Table 4-3 (linear interpolation between the values).

Table 4-3. Thermal conductivity λ of the buffer material as a function of the degree of saturation S_r and the void ratio *e*.

S_r	λ (W/m,K)		
	e = 0.5	e = 0.78	e = 1.0
0	0.4	0.3	0.2
0.2	0.4	0.3	0.2
0.3	0.5	0.4	0.3
0.4	0.65	0.55	0.45
0.5	0.85	0.75	0.65
0.6	1.05	0.95	0.85
0.7	1.2	1.1	1.0
0.8	1.3	1.2	1.1
0.9	1.35	1.25	1.15
1.0	1.4	1.3	1.2

The *specific heat* has been calculated as the weight average of the specific heat of water c_w and particles c_p according to Equation (4-18).

$$c = c_w /(1+w)+ c_p\, w/(1+w) \qquad (4\text{-}18)$$

c_w = 4,200 Ws/K,kg

c_p = 800 Ws/K,kg

Equation (4-18) yields the input parameters shown in Table 4-4 (linear interpolation)

Table 4-4. Specific heat *c* of the buffer material as a function of the water ratio *w*.

w	*c* Ws/K,kg
0	800
0.1	1,109
0.2	1,367
0.3	1,585
1.0	2,500

Water liquid flux

The water flux in the liquid phase is modelled to be governed by Darcy's law with the water pressure difference as driving force in the same way as for water saturated clay.

The hydraulic conductivity K of saturated clay is a function of the void ratio and the temperature. The hydraulic conductivity K_p of partly saturated clay is assumed to be a function of the hydraulic conductivity K of saturated clay and the degree of saturation S_r according to Equation (4-19).

$$K_p = (S_r)^{\delta} K \qquad (4\text{-}19)$$

where

K_p = hydraulic conductivity of partly saturated soil (m/s).

K = hydraulic conductivity of completely saturated soil (m/s).

δ = parameter (usually between 3 and 10).

For the MX-80 the standard value

$\delta = 3$

has been found to be satisfactory according to the calibration calculations.

Water transport driven by gravity and density gradients is included in the model as well.

The *hydraulic conductivity* of water saturated bentonite has been measured at different temperatures and void ratios (Börgesson et al. 2006). Table 4-5 shows the values for the model.

Water vapour flux

The water vapour flux is modelled as a diffusion processes driven by the temperature gradient and the water vapour pressure gradient (at isothermal conditions) according to Equation (4-20).

$$q_v = -D_{Tv}\nabla T - D_{pv}\nabla p_v \qquad (4\text{-}20)$$

where

q_v = vapour flow,

D_{Tv} = thermal vapour flow diffusivity,

T = temperature,

D_{pv} = isothermal vapour flow diffusivity,

p_v = vapour pressure.

The isothermal vapour flow is neglected and thus $D_{pv}=0$.

The thermal water vapour diffusivity D_{Tv} can be evaluated from moisture redistribution tests by calibration calculations. The following relations were found to yield acceptable results (Börgesson and Hernelind 1999):

$$D_{Tv} = D_{Tvb} \qquad 0.3 \le S_r \le 0.7 \qquad (4\text{-}21)$$

$$D_{Tv} = D_{Tvb} \cdot \cos^{a}\left(\frac{S_r - 0.7}{0.3}\cdot\frac{\pi}{2}\right) \qquad S_r \ge 0.7 \qquad (4\text{-}22)$$

$$D_{Tv} = D_{Tvb} \cdot \sin^{b}\left(\frac{S_r}{0.3}\cdot\frac{\pi}{2}\right) \qquad S_r \le 0.3 \qquad (4\text{-}23)$$

a and b are factors that regulates the decreased vapour flux at high and low degree of saturation.

Table 4-5. Hydraulic conductivity *K* as a function of void ratio *e* and temperature *T*.

T °C	e	*K* m/s
20	0.4	0.035×10^{-13}
20	0.6	0.2×10^{-13}
20	0.8	0.65×10^{-13}
20	1.0	1.75×10^{-13}
40	0.4	0.05×10^{-13}
40	0.6	0.31×10^{-13}
40	0.8	1.0×10^{-13}
40	1.0	2.75×10^{-13}
60	0.4	0.07×10^{-13}
60	0.6	0.44×10^{-13}
60	0.8	1.45×10^{-13}
60	1.0	3.85×10^{-13}
80	0.4	0.1×10^{-13}
80	0.6	0.55×10^{-13}
80	0.8	1.8×10^{-13}
80	1.0	4.9×10^{-13}

The diffusivity is thus constant with a basic value D_{Tvb} between 30% and 70% degree of saturation. It decreases strongly to $D_{Tv} = 0$ at 0% and 100% saturation. The influence of temperature and void ratio on the diffusivity is not known and not considered in the model.

The *thermal vapour flow diffusivity* D_{Tvb} and the parameters a and b according to Equations (4-21) to (4-23) have originally been evaluated for the void ratio 0.8 and confirmed for lower void ratios in the Canister Retrieval Test. However, the high temperature in the TBT enforced a reduction from the value used in CRT.

$\boldsymbol{D}_{Tvb} = 0.4\times10^{-11}$ m^2/s,K
$a = 6$
$b = 6$

Hydraulic coupling between the pore water and the pore gas

The pore pressure u_w of the unsaturated buffer material, which is always negative, is modelled as being a function of the degree of saturation S_r independent of the void ratio (*water retention curve*).

$$u_w = f(S_r) \tag{4-24}$$

The pore air pressure is not modelled.

The water retention curves have been evaluated according to a method developed by Dueck (Dueck and Börgesson 2007). Since the void ratio differs in the different buffer blocks different curves are required. Figure 4-4 shows the evaluated retention curves.

Since the water transport in ABAQUS is governed by the pore water pressure u_w (kPa) but the measurements are in relative humidity (RH) a conversion from calculated negative pore water pressure to relative humidity has also been done. The conversion according to Equation (4-25), which is derived from thermodynamic considerations (see e.g. Dueck 2004), has been used.

$$\text{RH} = exp(u_w/462T) \tag{4-25}$$

where T = absolute temperature

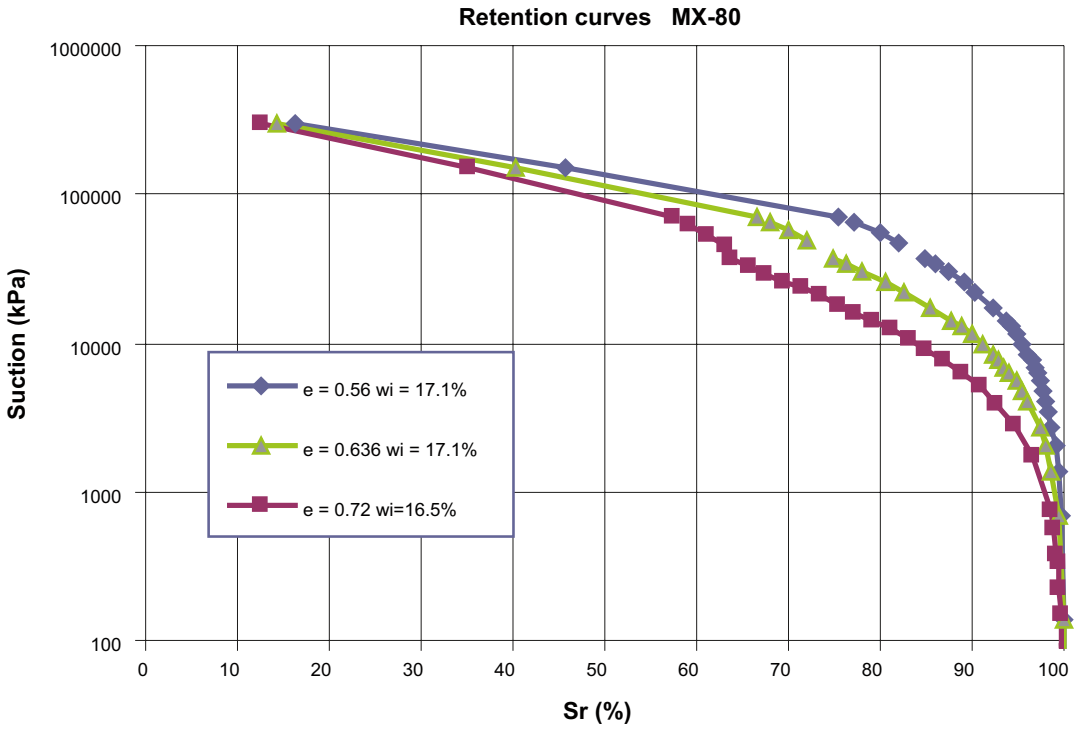

Figure 4-4. *Retention curve of MX-80 at the void ratio 0.56 (rings), 0.636 (blocks) and 0.72 (bricks, which are not used).*

Mechanical behaviour of the structure

The mechanical behaviour has been modelled with a non-linear Porous Elastic Model and Drucker-Prager Plasticity model. The effective stress theory is applied and adapted to unsaturated conditions and the shortcomings of this theory are compensated for by a correction called moisture swelling (see below).

The *Porous Elastic Model* implies a logarithmic relation between the void ratio e and the average effective stress p according to Equation (4-26).

$$\Delta e = \kappa \Delta \ln p \qquad (4\text{-}26)$$

where κ = porous bulk modulus.

Poisson's ratio v is also required.

Drucker-Prager Plasticity model contains the following parameters:

β = friction angle in the p-q plane,

d = cohesion in the p-q plane,

ψ = dilation angle,

$q = f(\varepsilon^d_{pl})$ = yield function.

The yield function is the relation between Mises' stress q and the plastic deviatoric strain ε^d_p at a specified stress path. The dilation angle determines the volume change during shear.

The following data has been used for the *Porous Elastic* model:

$\kappa = 0.20$,

$v = 0.4$.

The value of κ has been derived from oedometer and swelling pressure tests (Börgesson et al. 1995).

The following data was used for the *Drucker-Prager Plasticity* model:

$\beta = 0.001°$,

d = 3,000 kPa,

$\psi = 2°$.

Table 4-6. Yield function.

q (kPa)	ε_{pl}
3,000	0
3,200	0.1

The low friction angle and high cohesion are motivated by evidence that the strength is mainly a function of the void ratio, independently of the degree of saturation, and not the effective stress (Dueck 2010).

Thermal expansion

The volume change caused by the thermal expansion of water and particles can be modelled with the parameters:

α_s = coefficient of thermal expansion of solids,

α_w = coefficient of thermal expansion of water.

Only the expansion of the separate phases is taken into account. The possible change in volume of the structure by thermal expansion (not caused by expansion of the separate phases) is not modelled.

However, a thermal expansion in water volume will change the degree of saturation which in turn will change the volume of the structure. The following values have been used:

$\alpha_w = 3.0\times10^{-4}$

$\alpha_s = 0$

Mechanical behaviour of the separate phases

The water and the particles are mechanically modelled as separate phases with linear elastic behaviour. The pore air is not mechanically modelled. The following standard values have been used for the *properties of the water and solid phases*:

$B_w = 2.1\times10^6$ kPa (bulk modulus of water),

$B_s = 2.1\times10^8$ kPa (bulk modulus of solids),

$\rho_w = 1{,}000$ kg/m^3 (density of water),

$\rho_s = 2{,}780$ kg/m^3 (density of solids).

Mechanical coupling between the structure and the pore water

The mechanical behaviour is modelled to be governed by the effective stress theory and a procedure called moisture swelling.

Effective stress theory

The effective stress concept according to Bishop is used for modelling the mechanical behaviour of the water-unsaturated buffer material:

$$se = (s-u_a) + \chi(u_a-u_w) \qquad (4\text{-}27)$$

Equation (4-27) is simplified in the following way:

$u_a = 0$ (no account is taken to the pressure of enclosed air)

$\chi = S_r$

Moisture swelling

The shortcomings of the effective stress theory can be compensated in ABAQUS by a correction called "*moisture swelling*". This procedure changes the volumetric strain ε_v by adding a strain that can be made a function of the degree of saturation S_r.

The effective stress theory decomposes the total stress into pore pressure and effective stress (which only depends on deviatoric strains). However, the effective strain can be made dependent on saturation by using the concept of *moisture swelling* which modify the effective strain by this user defined saturation dependent volumetric strain (*moisture swelling*). In this application the moisture swelling contribution is calibrated by using the measured swelling pressure and assuming that the effective strain (after adding the moisture swelling) should be zero. Neglecting moisture swelling will imply an effective strain defined by the elastic material (porous elastic) and thus the moisture swelling strain can be calculated from Equations (4-28) and (4-29).

$$\Delta\boldsymbol{\varepsilon}_v = f(S_r) = \ln(p_0/p)\cdot\kappa/(1+e_0) \qquad (4\text{-}28)$$

$$p = p_{tot} - u_w\cdot S_r \qquad (4\text{-}29)$$

where

ε_v = volumetric strain,

p_0 = initial effective stress taken from the initial conditions,

p = actual effective stress,

κ = porous bulk modulus (from Equation (4-26)),

e_0 = initial void ratio,

p_{tot} = actual total stress,

u_w = pore water pressure,

S_r = degree of water saturation.

The moisture swelling relation (*M.S.*) that is needed as input is the logarithmic volumetric strain according to Equation (4-30) where $\Delta\varepsilon_v$ is taken from Equation (4-28).

$$M.S. = \ln(1+\Delta\varepsilon_v) \tag{4-30}$$

The data for the *moisture swelling procedure* is derived from the assumption that the relation between total stress and degree of saturation of a confined sample (constant volume) is linear when the degree of saturation is increased from its initial value to 100% (Dueck and Börgesson 2007). This relation is linked to the retention curve. The derivation of the retention curve and the moisture swelling relation is described in Åkesson et al. 2010a.

The derived moisture swelling relations are shown in Figure 4-5 for three bentonite block types. The bricks are not included in the model.

In order to check that the different bentonite block types behave according to the material model one element tests of drying and wetting have been simulated. The volume was kept constant and the degree of saturation stepwise changed from the initial conditions to 100% and to 0%. Figure 4-6 shows the calculated average stress in the element as a function of the degree of saturation.

Figure 4-6 shows that the bentonite block types behave according to the model. From the stress-less initial state the total average stress increases linearly with increasing degree of saturation until the swelling pressure at full saturation is reached at the degree of saturation 100%. The behaviour at decreasing degree of saturation is identical but merely theoretical since real samples cannot keep their original volumes but will shrink instead of having negative stress. In the real model high tensile average stresses will be kept but if they are transferred to the boundary the contact elements will open up, which leads to shrinkage of the buffer, since the contacts have no cohesion.

4.2.3 Other materials

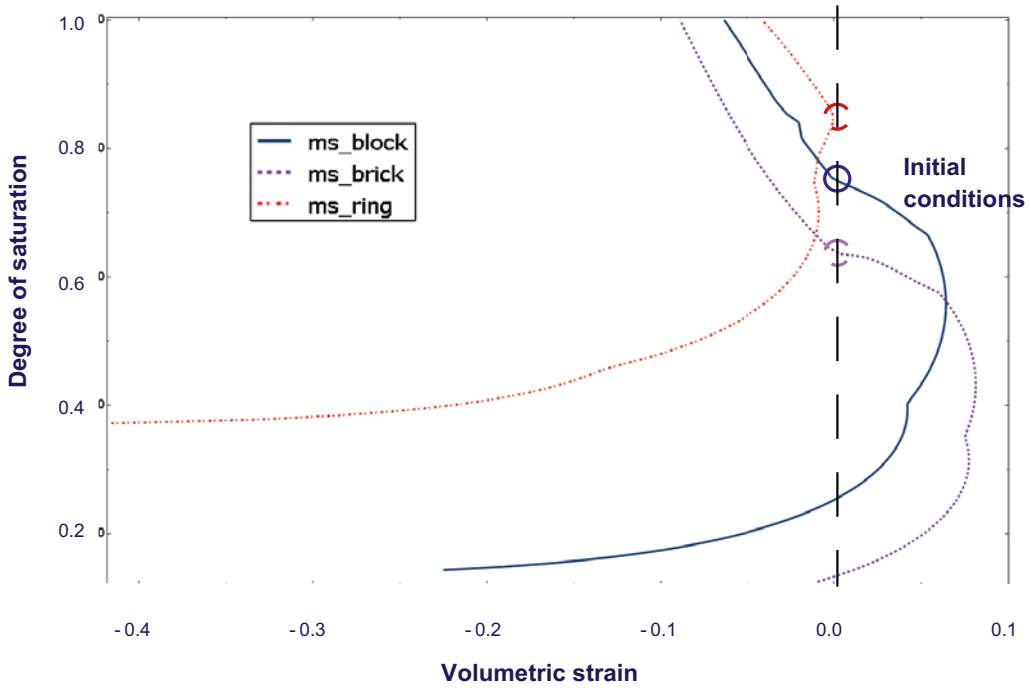

Figure 4-5. *Volume change correction $\Delta\varepsilon_v$ used in the moisture swelling procedure for three different bentonite block types. The initial conditions are also noted in the figure. Bricks are not included in the model.*

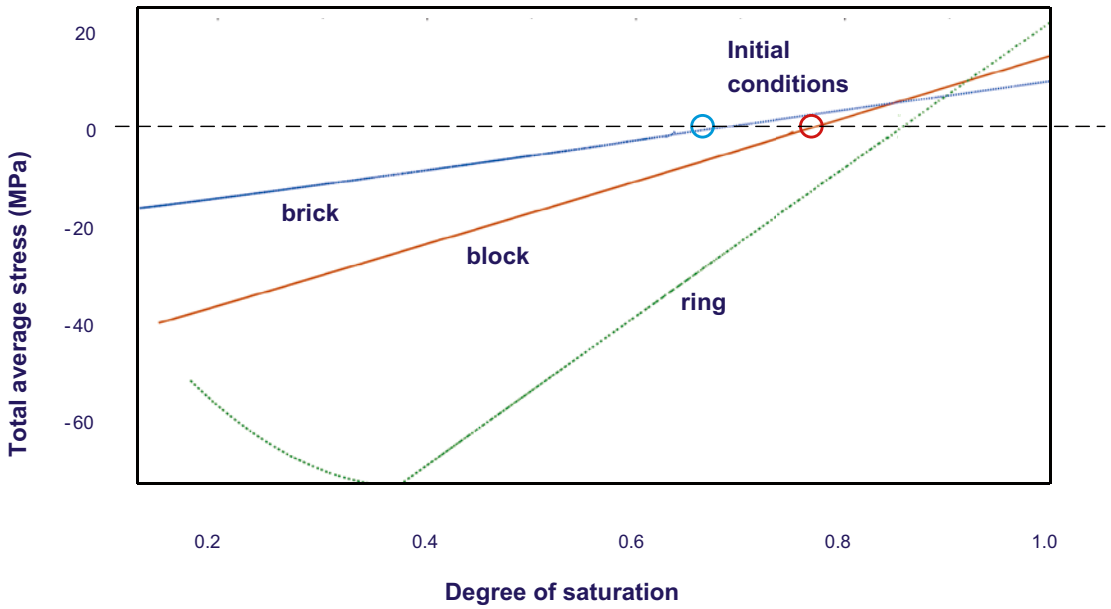

Figure 4-6. *One element tests of confined samples of three different block types. The initial conditions are also noted in the figure. Bricks are not included in the model.*

The heaters, the rock, theconcreyte plug and the steel lod have all been modelled as impermeable liear elastic materials. Table 4-7 shows the mechanical and thermal properties.

Table 4-7. Mechanical and thermal properties of various materials in the model.

Material\property	E (kPa)	v	λ (W/m,K)	c (Ws/K,kg)	ρ (kg/m^3)
Heaters	$2.1\cdot10^9$	0.3	60.5	435	7,850
Rock	$1.85\cdot10^8$	0.25	2.6	800	2,400
Concrete plug	$1.85\cdot10^6$	0.25	1.4	880	2,300
Steel lid	$2.1\cdot10^9$	0.3	60.5	435	7,850

Anchors

The steel lid is anchored by 9 anchor rods fixed to the top of the steel plate. In order to simulate the anchor rods a hook was placed on top of the steel lid and fixed to the rock as shown in Figure 4-3. Measurements of the force in the anchors and the displacement of the plug have yielded the following E-modulus that has been applied to the anchor hook.

$E = 1.44\cdot10^6$ kPa

$v = 0$

Sand shield and sand filter

The sand shield and the sand filter are *mechanically* modelled as an elastic material:

$E = 4.5\cdot10^4$ kPa,

$v = 0.2$.

Since the model is elastic the sand swells back elastically during the cooling phase. This is not a correct sand behaviour, since sand will stay in compressed state at unloading. In order to model the correct behaviour the sand filter and the sand shield were locked during the cooling phase.

The sand filter and sand shield were *thermally* modelled with a thermal conductivity that was changed with time according to the water filling process. The thermal conductivity was changed

from 0.5 W/m,K to 1.7 W/m,K in the same rate as the water column passed the actual element. Table 4-8 shows the protocol for the thermal properties.

Table 4-8. Thermal conductivity of the sand parts. Constant rate of water filling.

Sand part	Time days	λ W/m,K
Sand filter	0–70	0.5/1.7
	70–	1.7
Sand shield	0–1,642	0.5
	1,642–1,777	0.5/1.7
	1,777–	1.7

ρ = 7,850 kg/m^{3,}

c = 435 Ws/K,kg.

The time of the increase in thermal conductivity from the dry condition to water saturated condition agrees with the water filling.

Water filled column that simulates water filling of the sand shield and sand filter

The water filling of the sand shield and sand filter is *hydrualically* simulated by introducing a column of water elements into the sand filter as illustrated in Figure 4-3. The rate of the water column introduction is the same as specified in the protocol (see Table 4-9) and the same as the change in thermal conductivity shown in Table 4-8. The function of the water column is that it sets the pore water pressure to a constant value (0 kPa) in the same rate as the column is introduced.

4.3 Initial conditions

The following initial conditions have been applied for the bentonite parts (and regarding temperature for all parts):

Buffer rings

e = 0.56,

u = –37,000 kPa,

S_r = 0.849,

p = 31,413 kPa,

T = 17°C.

Buffer blocks

e = 0.636,

u = –37,000 kPa,

S_r = 0.751,

p = 27,787 kPa,

T = 17°C.

4.4 Boundary conditions and couplings

The structure is axi-symmetric around the centre line of the deposition hole. The following boundary conditions were applied:

Mechanical

- Fixed outer boundaries of the rock.
- Symmetry conditions at axis of symmetry.
- Pre-stress of the bolts 144 kN.
- Prescribed motion in vertical direction for sand and sand filter.
- Common nodes between bentonite materials.
- Contact surfaces with friction at the vertical boundaries between the buffer and heaters with $\phi_c = 5.7°$.
- All other contact surfaces: $\phi_c = 26.6°$.
- Canister free to move.

The contact surfaces between the sand shield and the buffer and between the sand filter and the buffer have low stiffness and a cut-off distance to allow flow between these surfaces even if they not are in contact.

Thermal

- The thermal boundary conditions at the outer rock boundary have been adapted to yield an acceptable temperature evolution. A constant temperature of 17 degrees and a heat transfer coefficient of $f = 1$ W/m^2,K were applied to the rock boundary and 5 W/m^2,K at the top of the steel lid.
- The field variable controlling the thermal conductivity of the sand filter is ramped from 0.05 to 1 from time 0 to 10,000 seconds. This corresponds to a variation of the conductivity from 0.5 to 1.7.
- A high coefficient of thermal conductivity has been defined (1,000) for all contact surfaces.

The power of the two heaters has been varied throughout the test. Figure 4-7 shows the power protocol. There is a small error in the applied protocol, since the power of heater 2 was raised from 1,550 watts to 1,600 watts at the same time as the power of heater 1 was raised from 1,500 watts to 1,600 watts. This 50 watts power raise of heater 2 was not modelled.

Hydraulic boundaries of the buffer

- At heater 1 (lower):
  - Inner: no flow.
  - Outer: in filter according to water pressure protocol.
  - No flow in buffer/rock and buffer/heater contacts.
- At heater 2 (upper):
  - Inner: in sand shield according to water pressure protocol.
  - Outer: in filter according to water pressure protocol.
  - No flow in buffer/rock and buffer/heater contacts.

The sand filter is modelled to reach along the entire buffer. The filter was filled with water during 70 days. The water filling was modelled by the introduction of the water column from bottom and upwards at a constant rate. Also the sand shield was filled with water using the same technique. Water filling was made according to the water pressure protocol shown in Table 4-9.

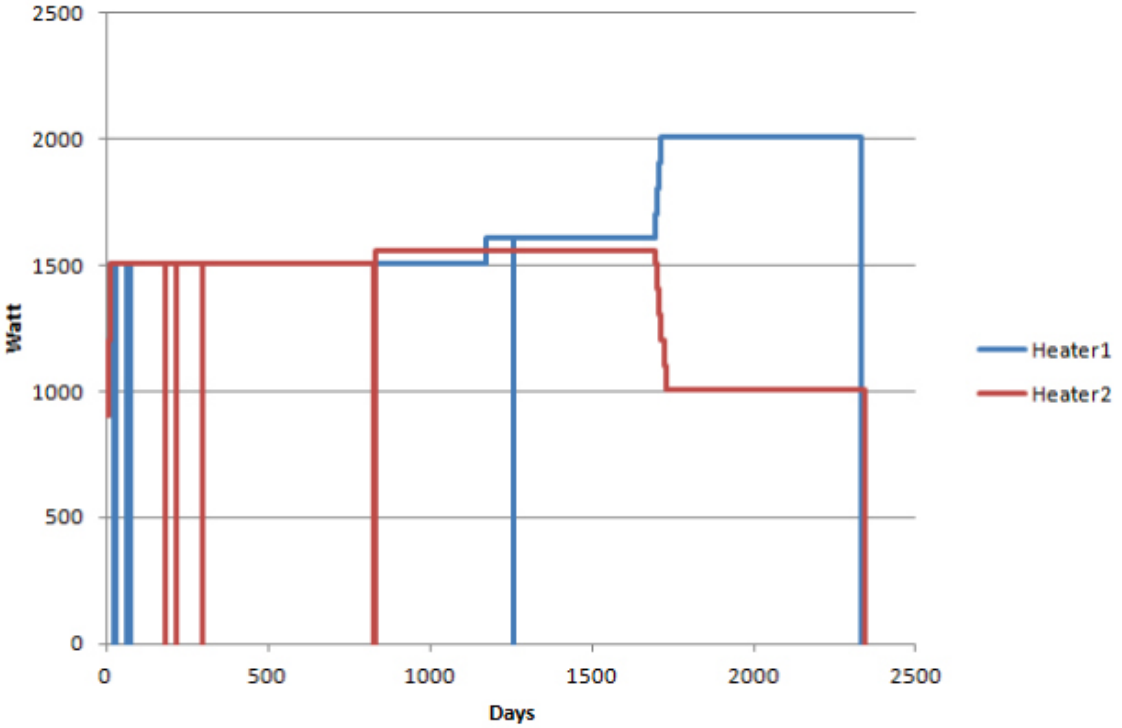

Figure 4-7. Power protocol of the heaters.

Table 4-9. Water pressure protocol for TBT.

Day	Action	Water pressure
0	Start water filling of filter	0
0–70	Successive introduction of water column in the filter	Hydrostatic
70	End water filling of filter	Hydrostatic
929	Water filling of mats between blocks C3 and C4	0
1,685	Start water filling of sand shield	0
1,642–1,777	Successive introduction of water column in the sand shield	Hydrostatic
1,775	End water filling of sand shield	Hydrostatic
2,407	End of test	
2,408	(Start dismantling)	

4.5 Calculation cases and sequences

The calculation has been done in the following steps:

1. Thermal calculation with the initial conditions of the materials.
2. Hydro-Mechanical calculation.
   - Establishment of equilibrium at initial conditions.
   - HM-calculation with temperature results according to step 1 and hydraulic boundary conditions according to the water pressure protocol.
3. Repetition of 1 and 2 until the results are identical.

At day 2,337, when the shutting off of heater 1 started, the nodes of the sand filter and the sand shield were locked so that no swelling of the sand could take place.

4.6 Results

4.6.1 General

The results will be structured as follows. At first the thermal results will be shown. They are separated from the HM-results since the thermal calculation is not very precise. Then the hydro-mechanical results will be shown. Comparison with measurements and some comments will be given together with the results.

4.6.2 Thermal results

The results of the thermal calculation stem from loop 2 i.e. the water uptake and swelling in the first stress calculation is taken into account. The modelled temperature evolution with time is shown in Figure 4-8 for some points in the buffer in a middle section of the lower heater 1 and in Figure 4-9 for some points on the heater surface. The corresponding temperature paths are shown in Figure 4-10. Both modelled and measured results are shown. The same results are shown in Figure 4-11 to Figure 4-13 for heater 2. Figure 4-14 shows a contour plot of the temperature at day 2,335 just before shutting off the heaters.

Comparison between modelled and measured temperatures shows that the agreement is fairly good but could probably be improved by fine-tuning the model by e.g. changing the heat transfer coefficient. The modelled temperature around heater 1 is underestimated with 5–15 degrees while the temperature in and around heater 2 is underestimated with 5–10 degrees.

The measaured temperature decrease with time on the surface of heater 2 is not modeled. There seems to be a process that increases the thermal conduction in the sand shield that is not modeled. A possible explanation is an increase in thermal conductivity caused by the compression of the sand shield from the swelling of the bentonite. The temperature agreement is though considered good enough for the purpose of the HM modelling exercise.

4.6.3 Hydro-mechanical results from the first loop

General

The results of the following HM-variables will be shown:

- Relative humidity.
- Pore pressure.
- Degree of saturation.
- Void ratio.
- Total axial and radial stress.
- Axial and radial displacements.

The results of the different HM variables will be shown in different plot versions, contour plots being used for all variables:

- Contour plots at different times.
- History plots.
- Paths.

In addition the force on the anchors and the displacement of the plug will be shown as history plots.

Due to convergence problems most HM-results are from the first calculation loop. The results after the second loop are only shown in the final stage in section 4.6.4.

Pore pressure

Figure 4-15 shows the pore pressure in contour plots at different times. The effect of the water filling of the sand filter is illustrated in the beginning of the test. The pore pressure development is also shown in Figure 4-16 as radial paths through bentonite rings R4 and R10.

The figures show that there is some drying around the lower heater and above and below the heaters but the wetting catches up after a few years. At the end of the test only a small part close to the plug is still slightly dried.

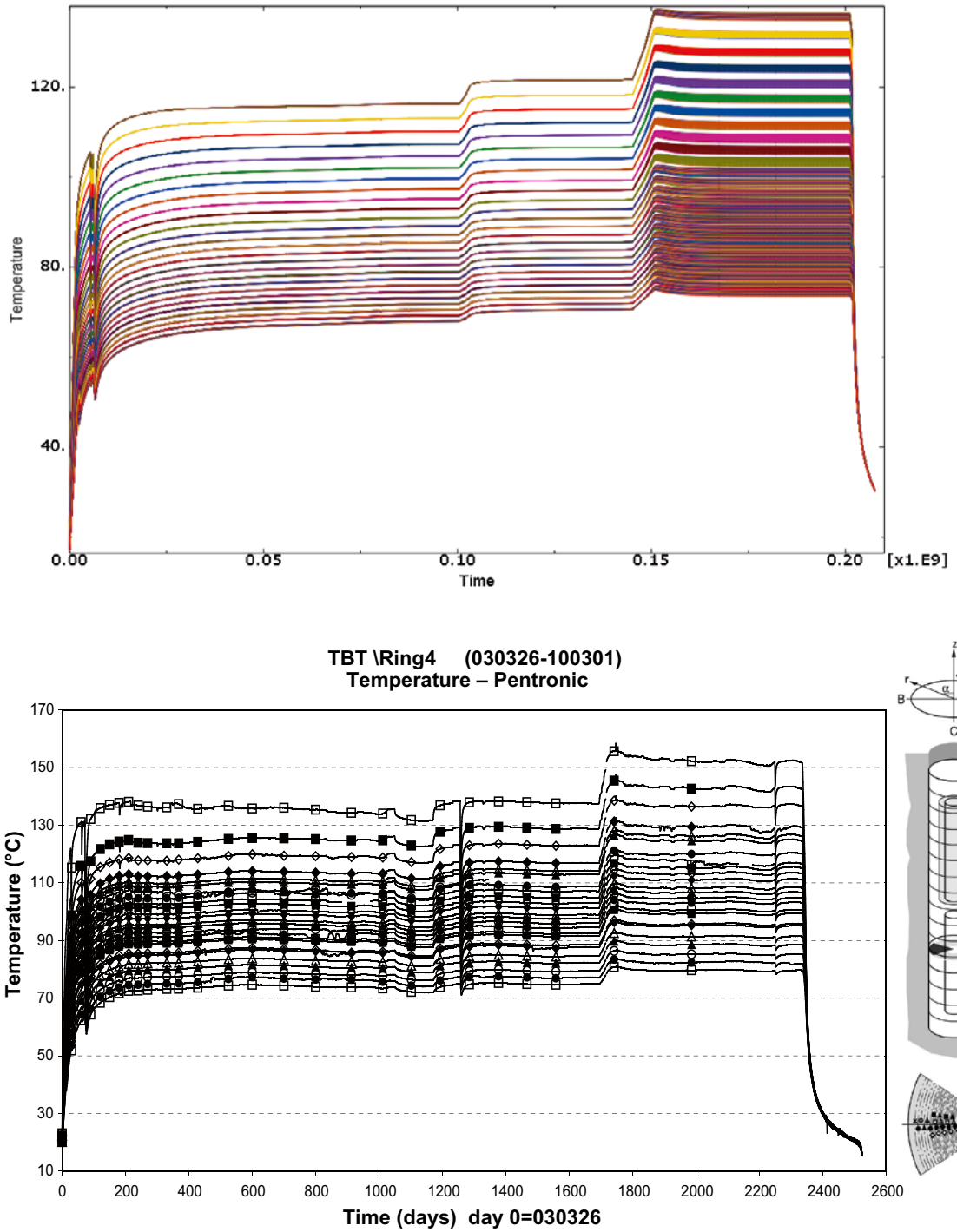

Figure 4-8. *Temperature (˚C) evolution in the buffer around heater 1 in a section through the centre of the heater. Modelled (upper) and measured results are shown. The modelled points are located equidistant from each other. The highest temperatures refer to the point closest to the heater. For detailed information about measured results see Goudarzi et al. (2010).*

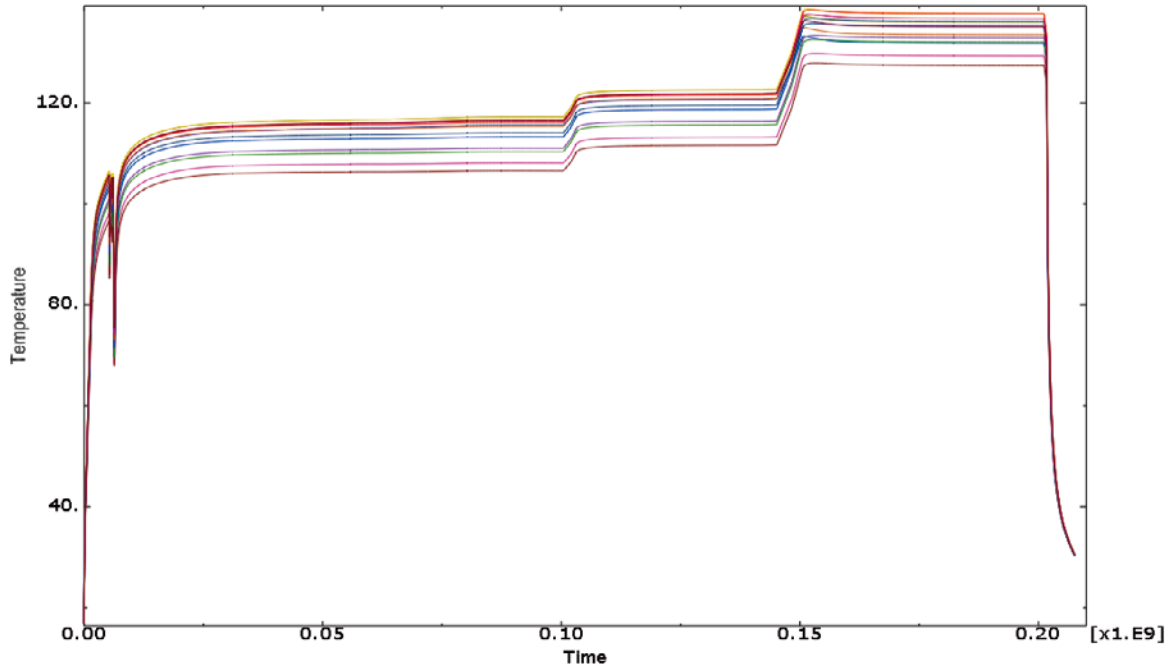

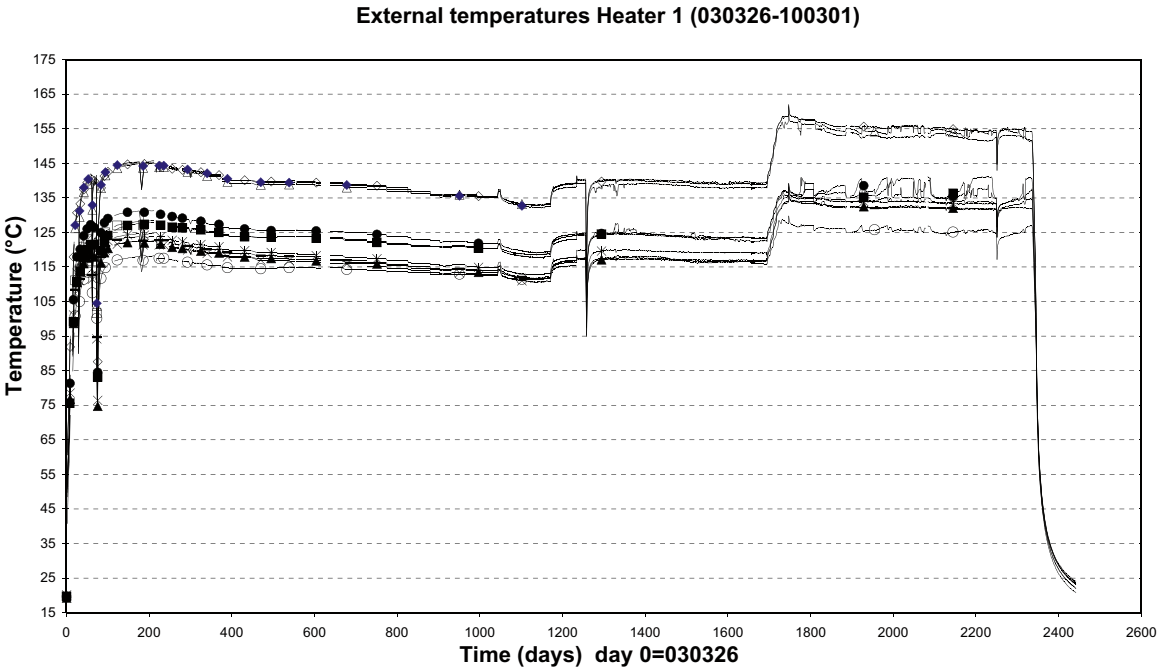

Figure 4-9. *Temperature (˚C) evolution on the surface of heater 1. Modelled (upper) and measured results are shown. For detailed information about measured results see Goudarzi et al. (2010).*

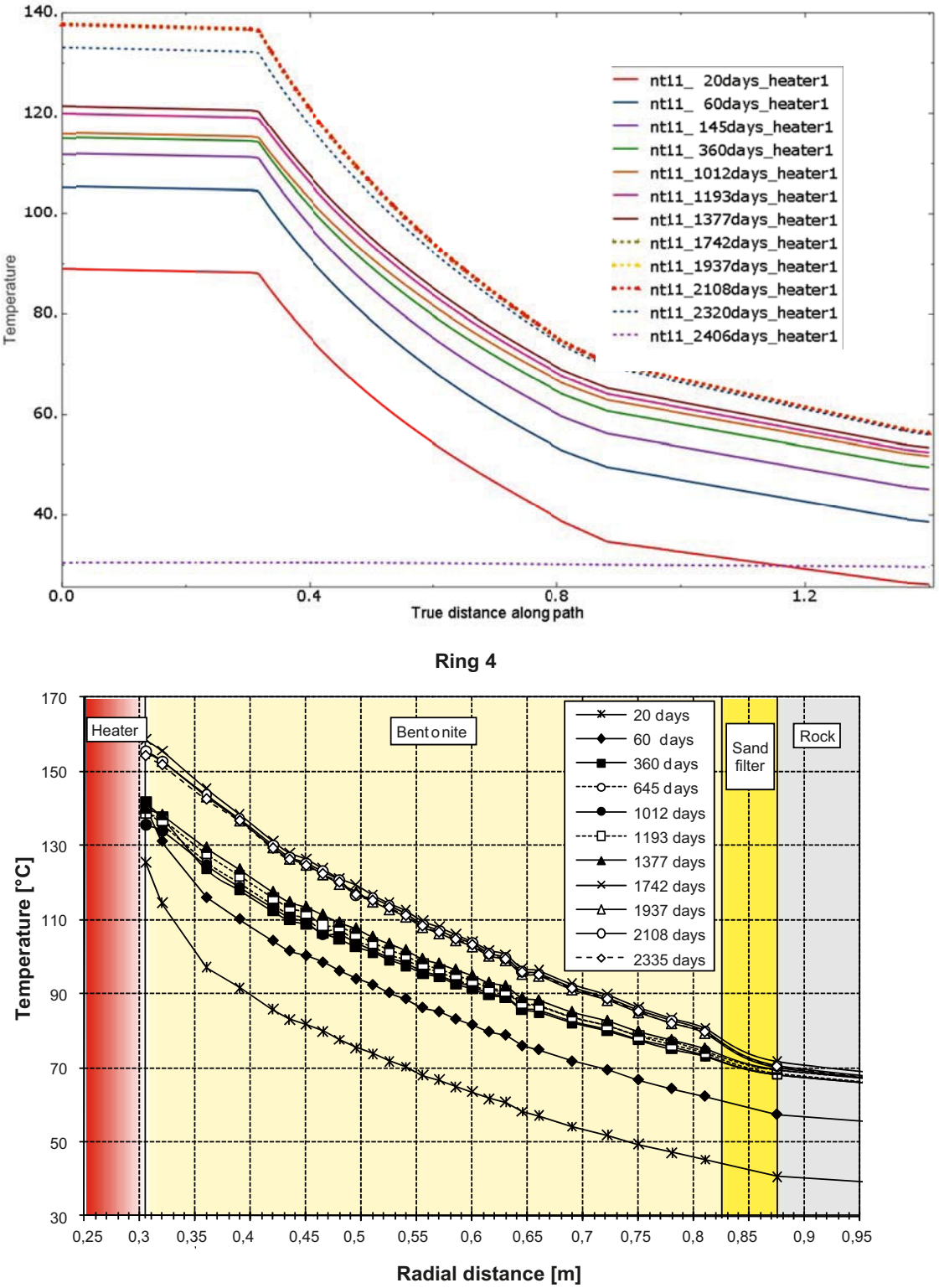

Figure 4-10. *Modelled (upper) and measured temperature in the buffer mid-height heater 1 at different times. Temperature (˚C) as function of the distance (m) from the centre line.*

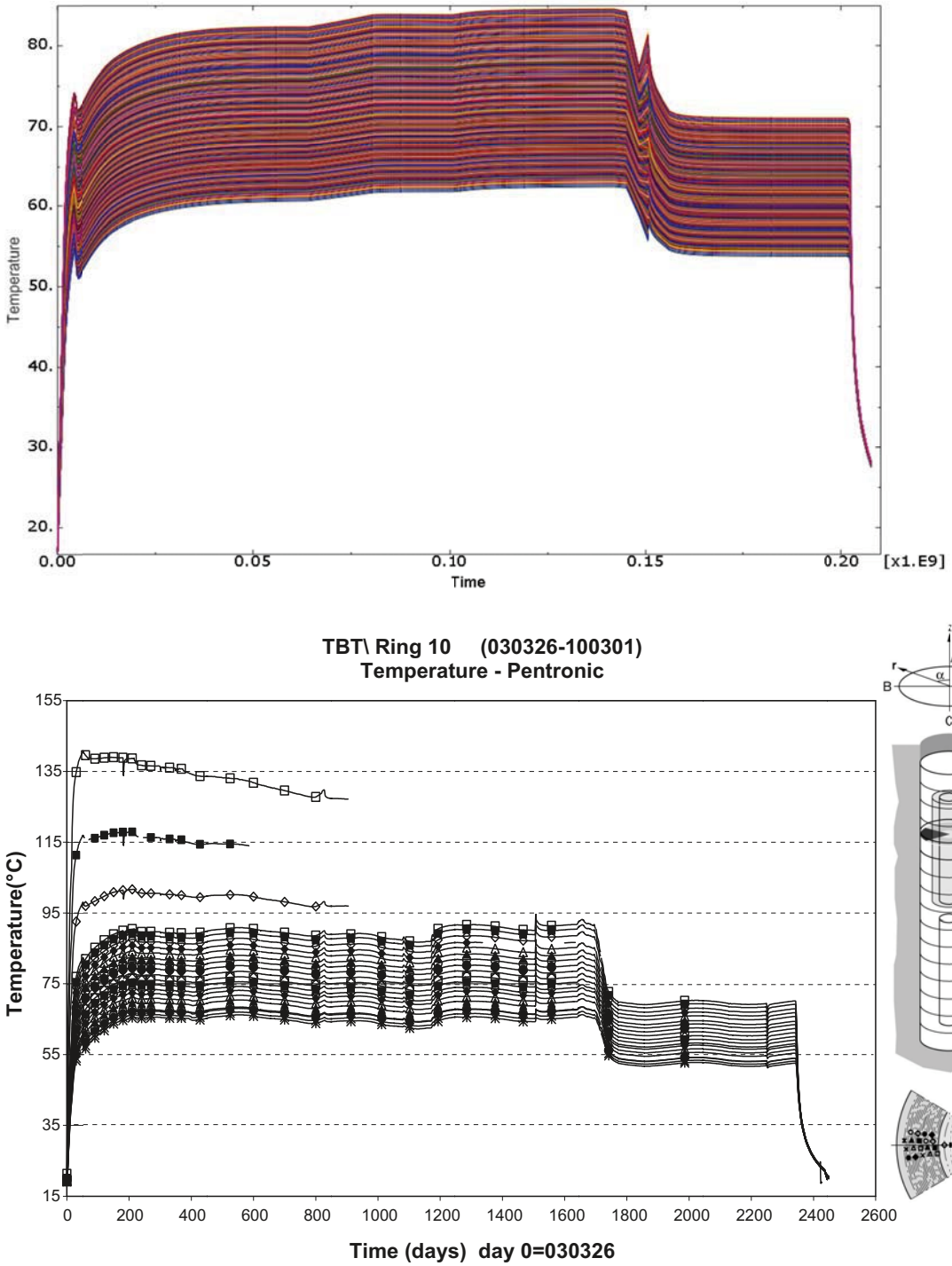

Figure 4-11. *Temperature (˚C) evolution in the buffer around heater 2 in a section through the centre of the heater. Modelled (upper) and measured results are shown. The modelled points are located equidistant from each other. The highest temperatures refer to the point closest to the sand shield except for the three curves with high measured temperatures, which refer to the sand shield. For detailed information about measured results see Goudarzi et al. (2010).*

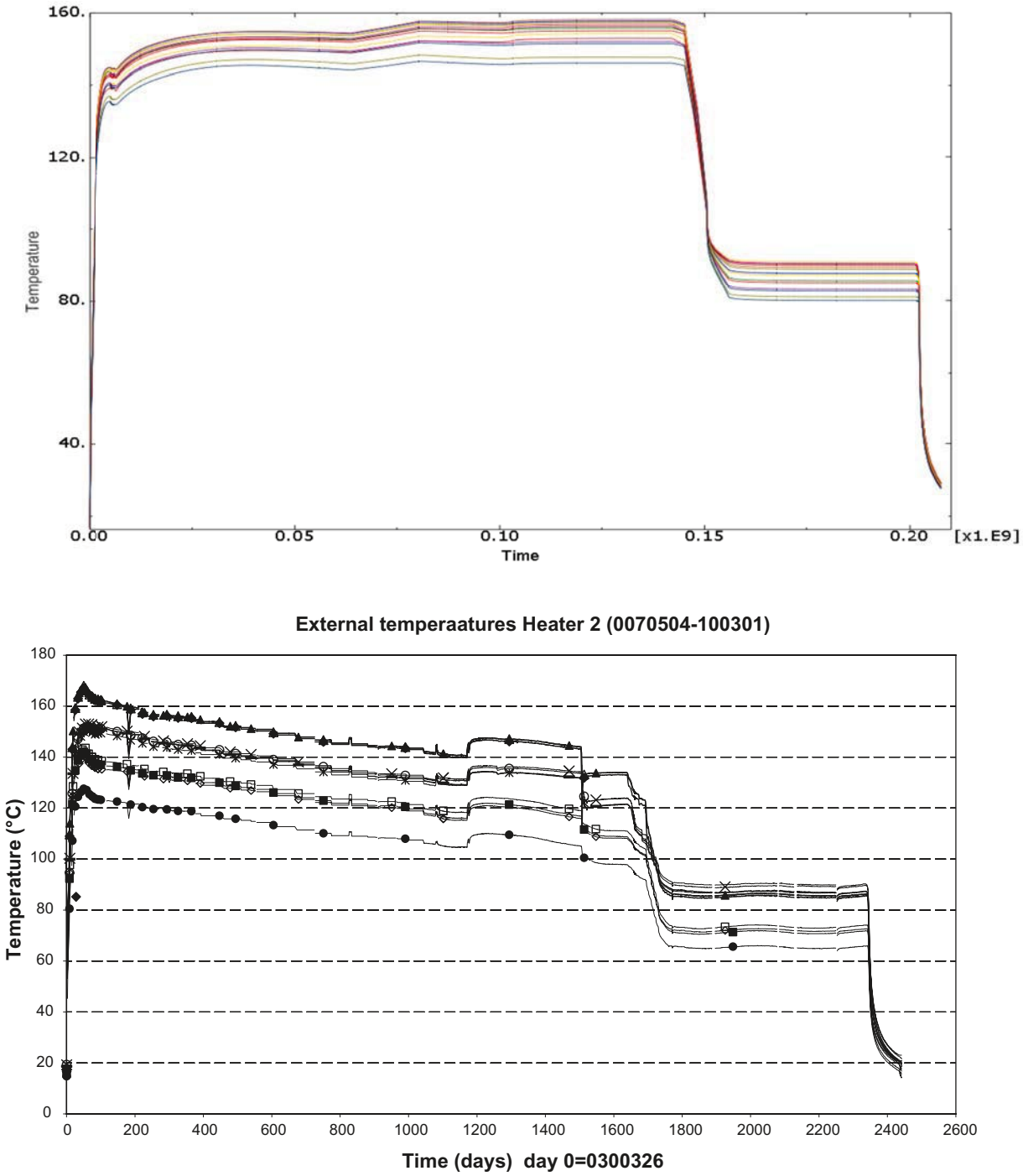

Figure 4-12. *Temperature (˚C) evolution on the surface of heater 2. Modelled (upper) and measured results are shown. For detailed information about measured results see Goudarzi et al. (2010).*

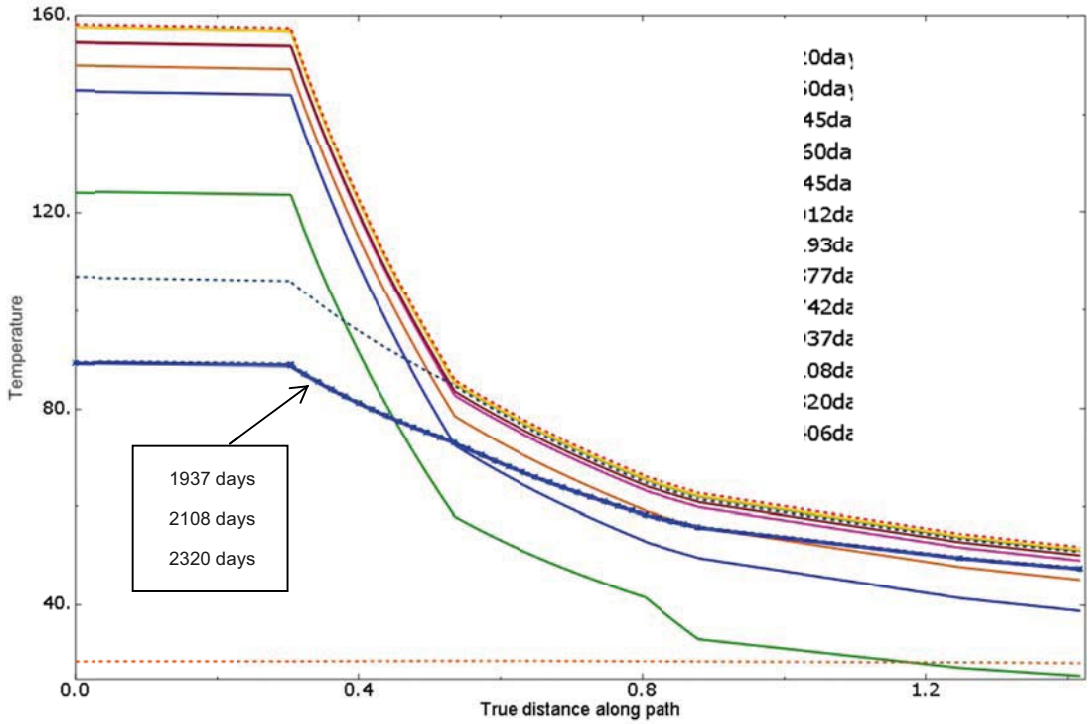

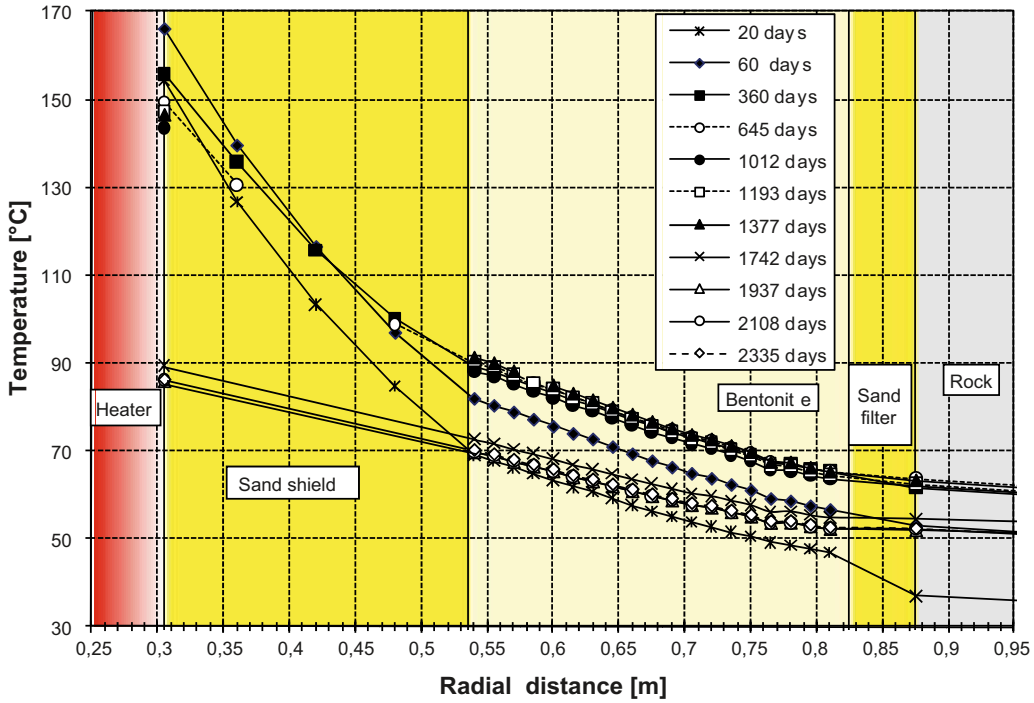

Figure 4-13. *Modelled (upper) and measured temperature in the buffer mid-height heater 2 at different times. Temperature (˚C) as function of the distance (m) from the centre of the heater.*

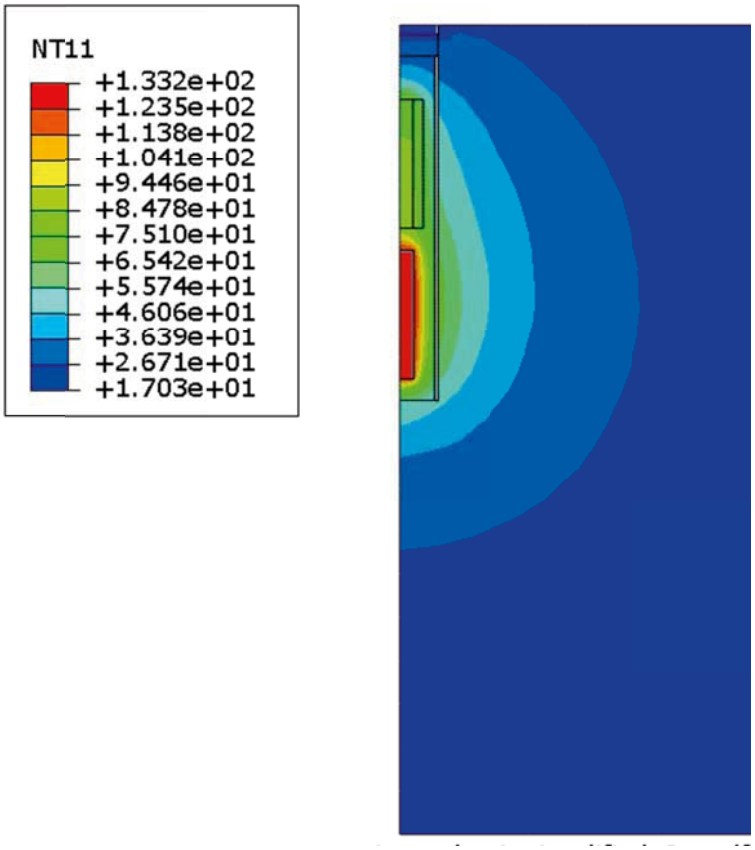

Figure 4-14. *Contour plot of the temperature (˚C) at day 2,320.*

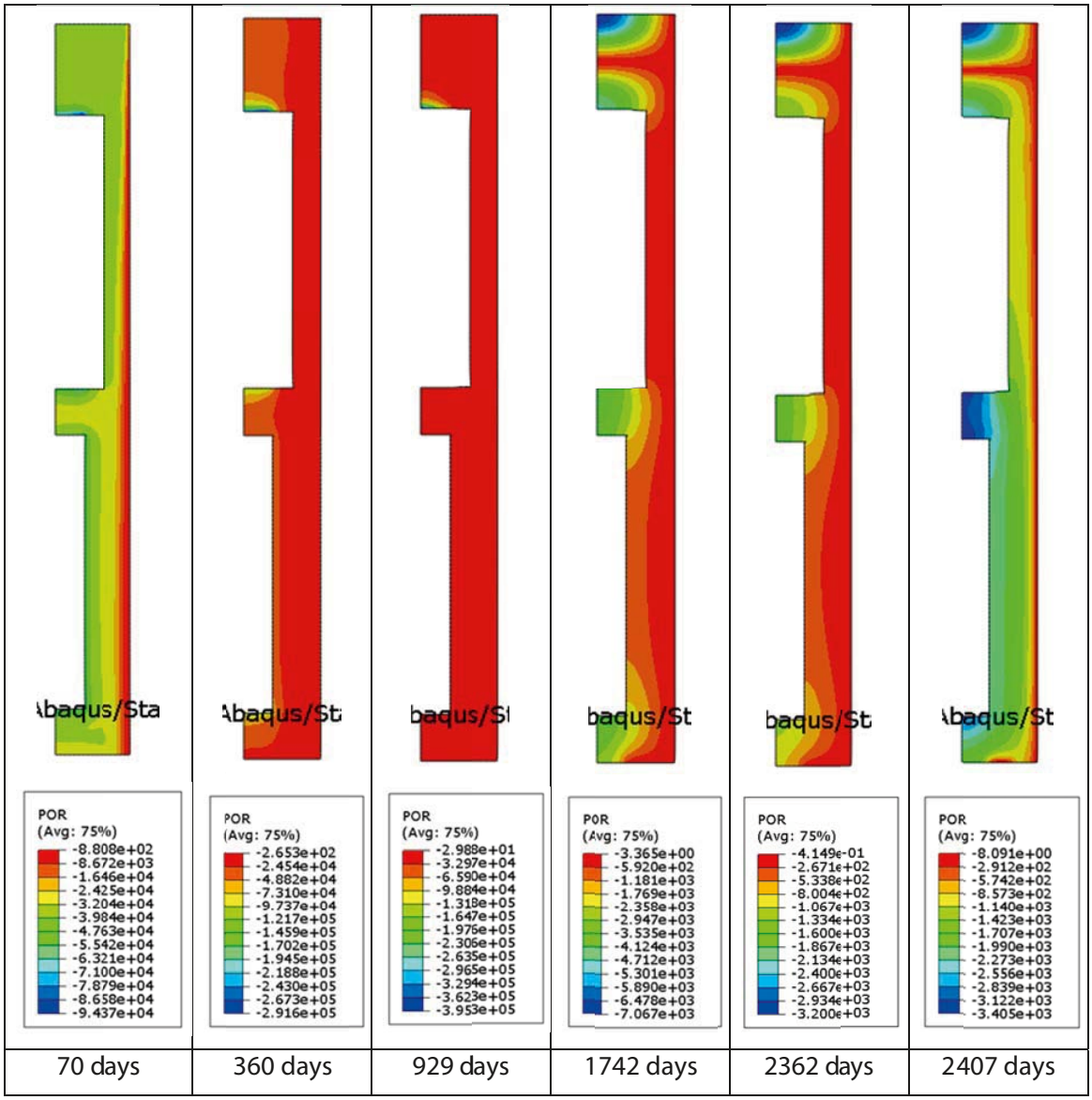

Figure 4-15. *Pore pressure (kPa) distribution in the buffer at different times. Observe the difference in scale.*

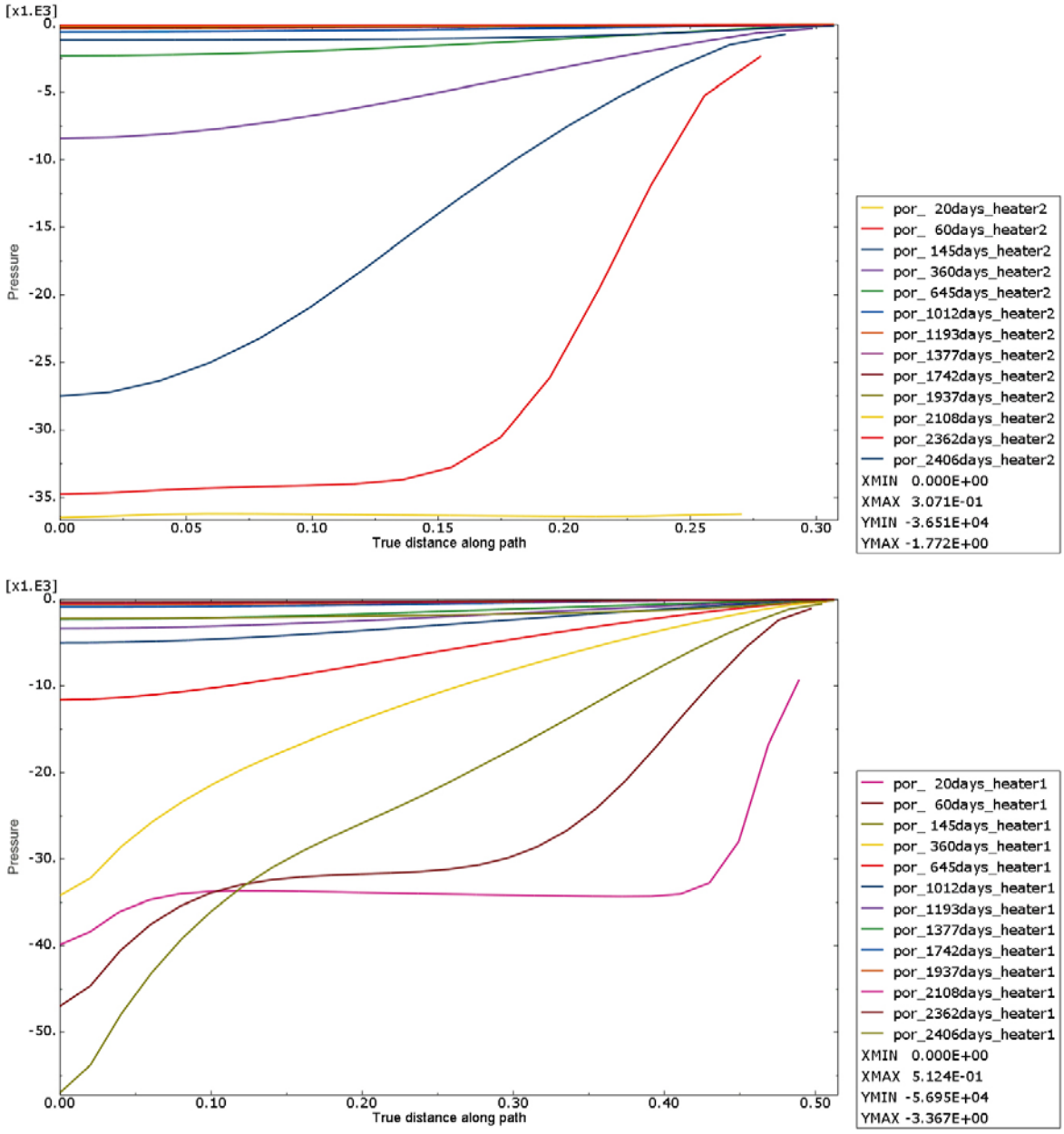

Figure 4-16. *Pore pressure (kPa) distribution at different times for radial sections through ring R10 (upper) and R4.*

Degree of saturation

The degree of saturation is illustrated in similar plots in Figure 4-17 and Figure 4-18. They confirm the pore pressure results.

The final distribution of degree of saturation can be compared to the measured one. This comparison is made in Figure 4-19 (measured results from Johannesson et al. 2010). The comparison shows that the appearance of the contour plots are similar in the respect that the unsaturated parts are similarly located but the comparison also shows that the degree of saturation is overestimated in the modelling especially close the lower heater. However, the disagreement is small (a few per cent close to the heater) and the entire buffer is close to full saturation (>95%). The overestimation may be due to that the stress release at excavation is not modelled and this stress release may have caused an expansion of the bentonite with a resulting small decrease in degree of saturation.

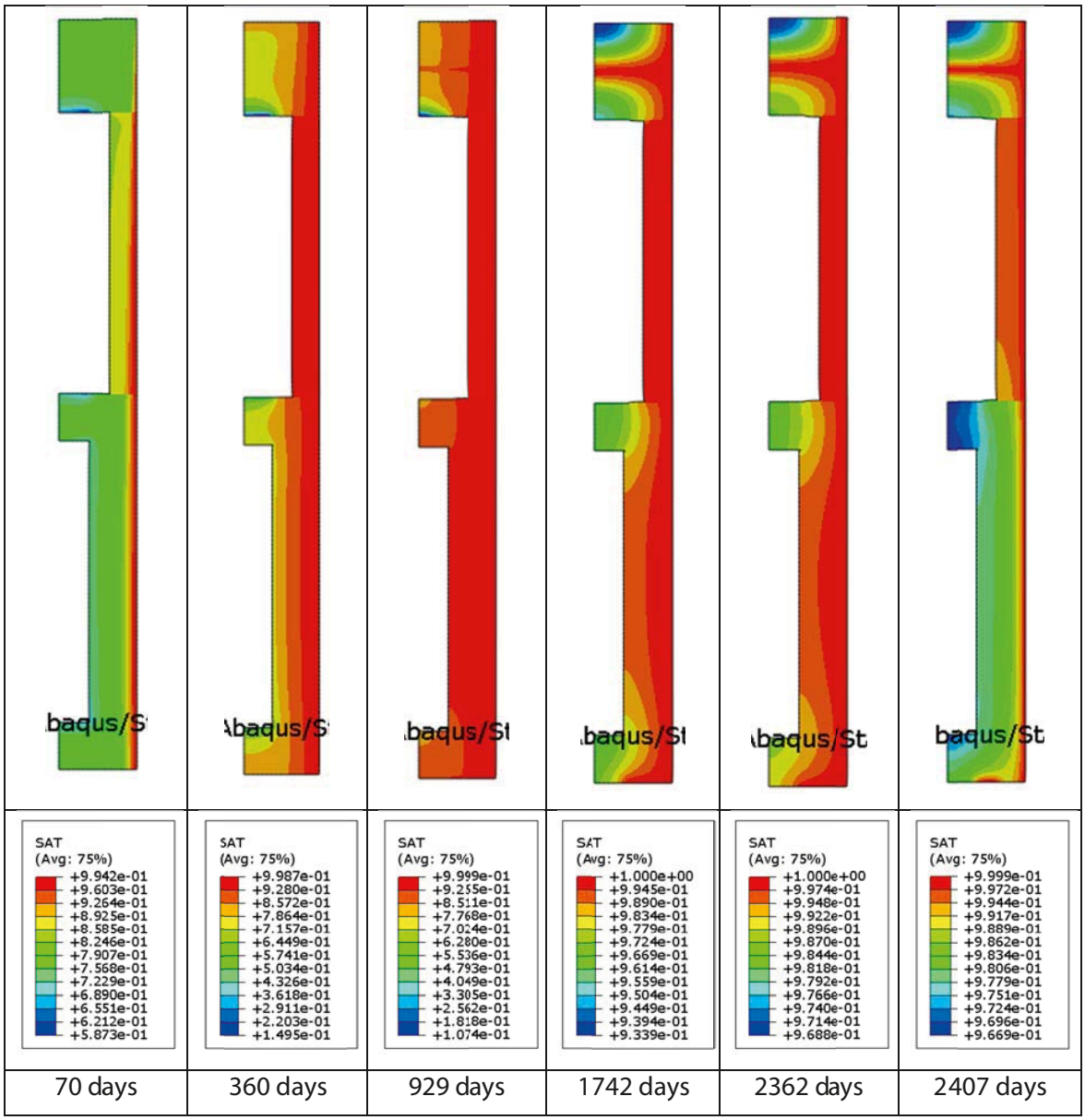

Figure 4-17. *Distribution of the degree of saturation in the buffer at different times. Observe the difference in scale.*

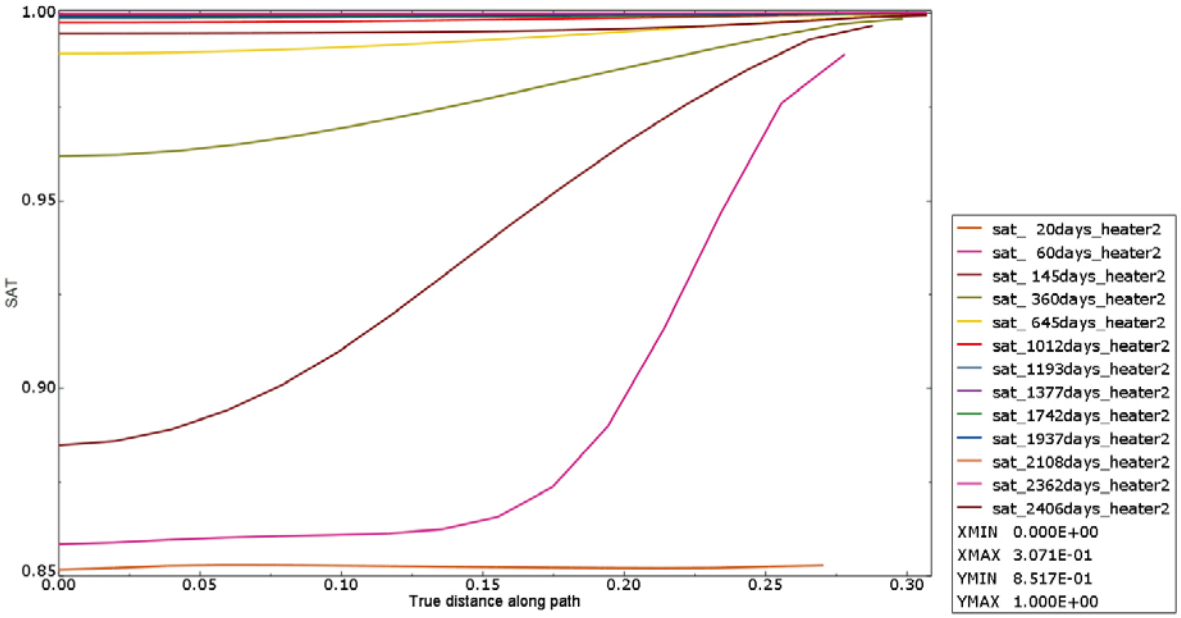

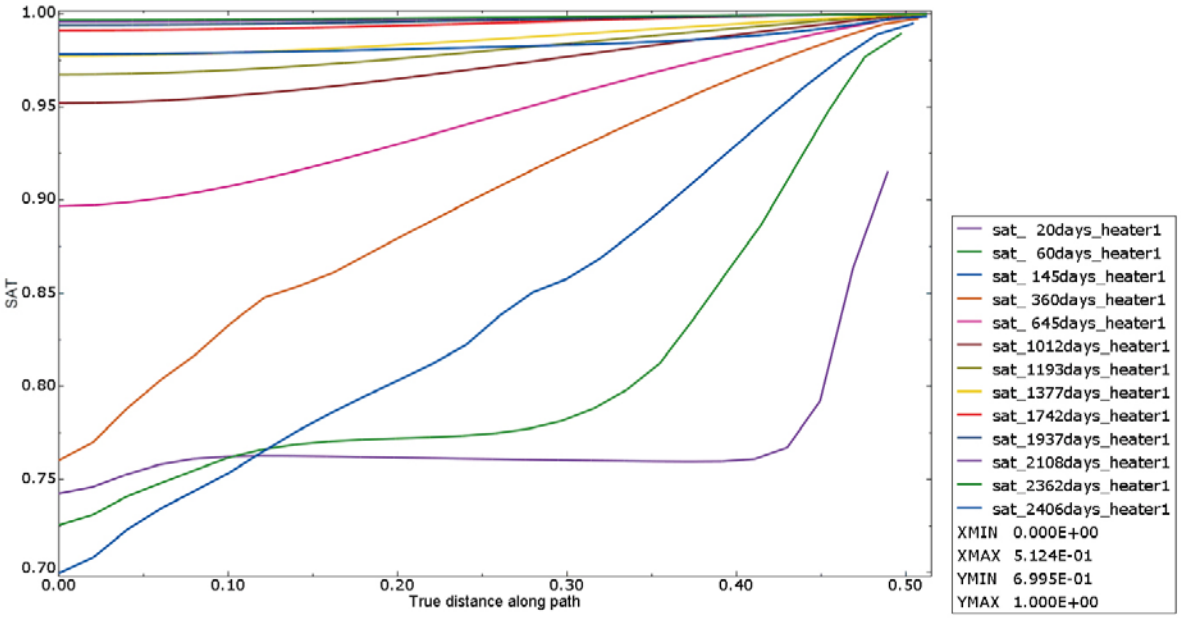

Figure 4-18. *Distribution of degree of saturation at different times for radial sections through rings R10 (upper) and R4.*

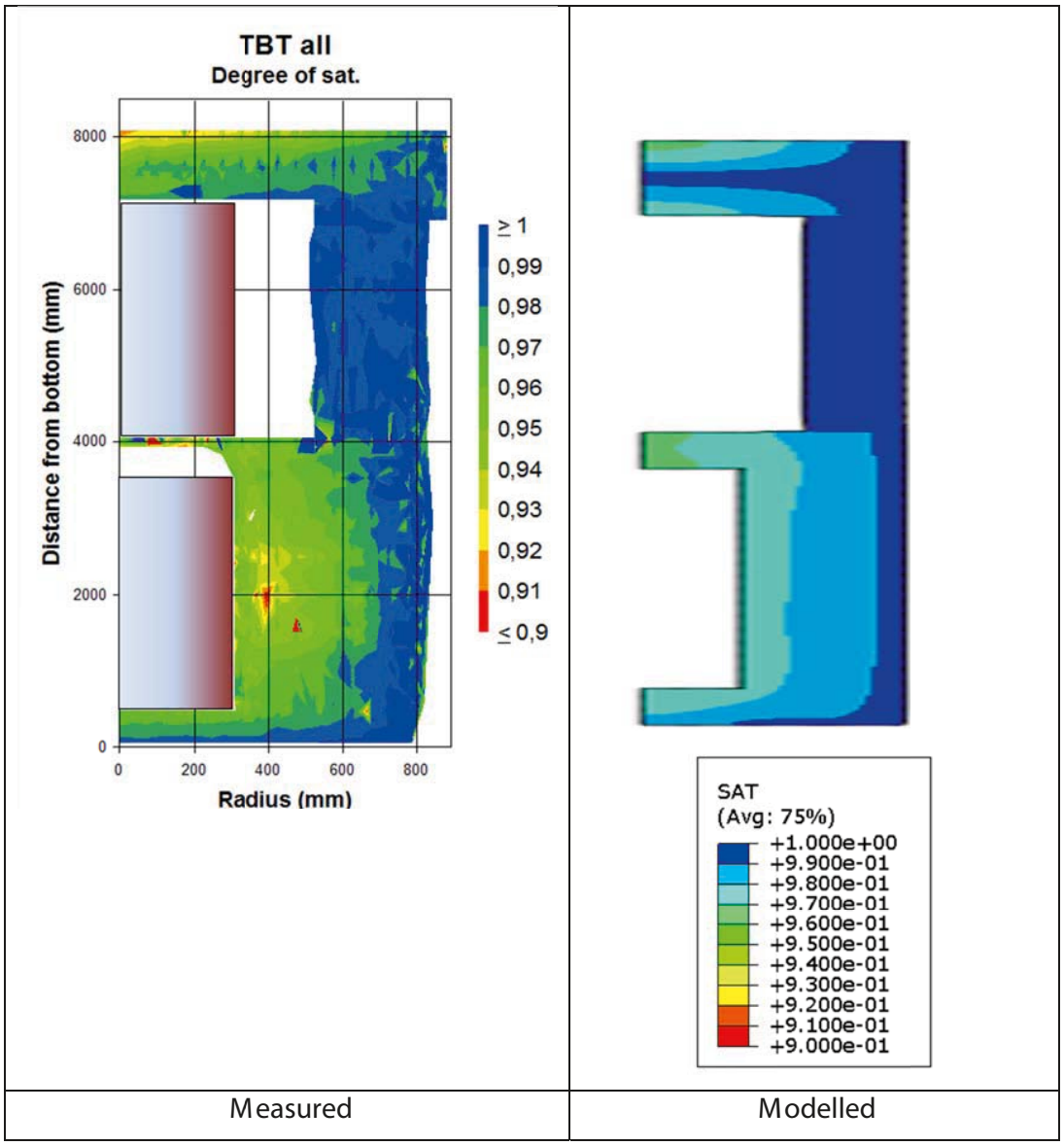

Figure 4-19. *Comparison between modelled and measured distribution of degree of saturation.*

Void ratio

Figure 4-20 shows the void ratio in contour plots at different times. The void ratio development is also shown in Figure 4-21 as radial paths across bentonite rings R4 and R10.

The figures show that there is some shrinkage around the lower heater and above and below the heaters but the wetting and subsequent swelling increases the void ratio after a few years. At the end of the test the bentonite is rather homogenised with exception of above and under the heaters where the void ratio locally is still rather low. There are also some corner effects (probably caused by ill conditioned element mesh) with high void ratio in the bentonite in contact with the upper and lower edge of the sand shield.

The final void ratio distribution can be compared to the measured one. This comparison is made in Figure 4-22 (measured results from Johannesson et al. 2010). The comparison shows that the agreement is rather good around the upper heater and below the lower heater. It is however not good around the lower heater where the measured very low void ratio is not modelled. The agreement is also very poor at the outer boundary to the sand filter. The large void ratio measured at the outer rim of the bentonite in contact with the filter is not modelled.

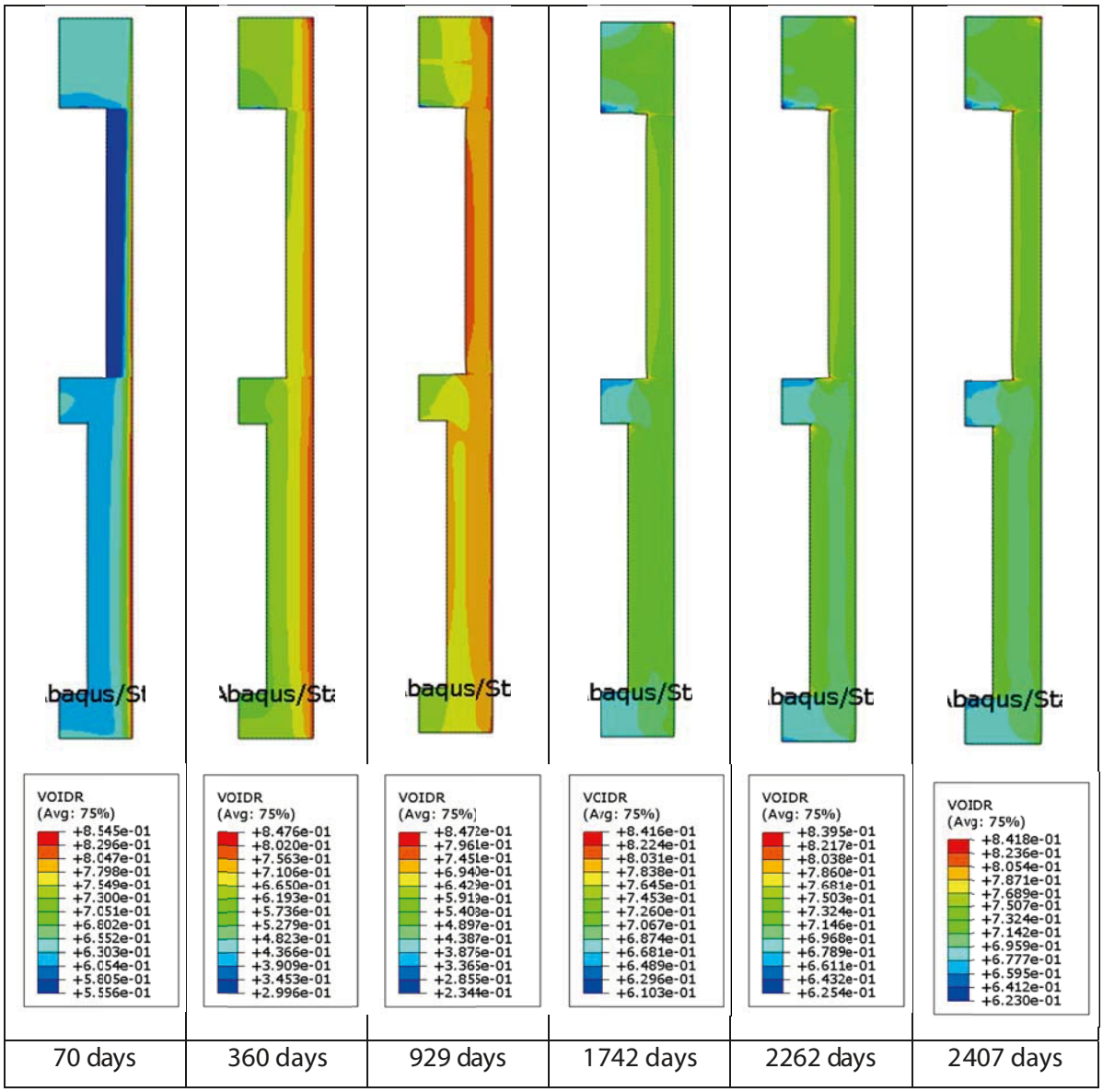

Figure 4-20. *Void ratio distribution in the buffer at different times. Observe the difference in scale.*

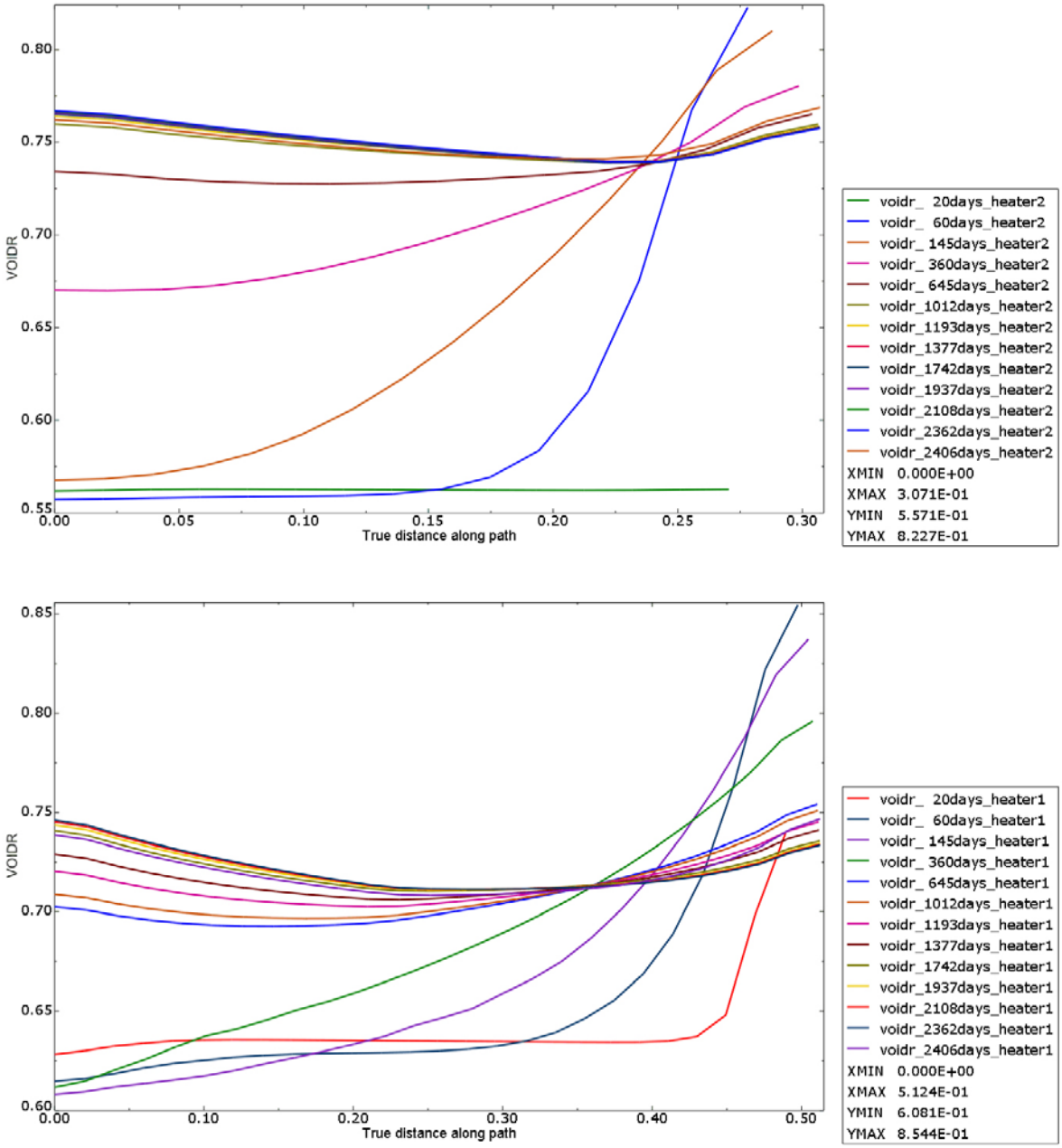

Figure 4-21. *Distribution of void ratio at different times for radial sections through rings R10 (upper) and R4.*

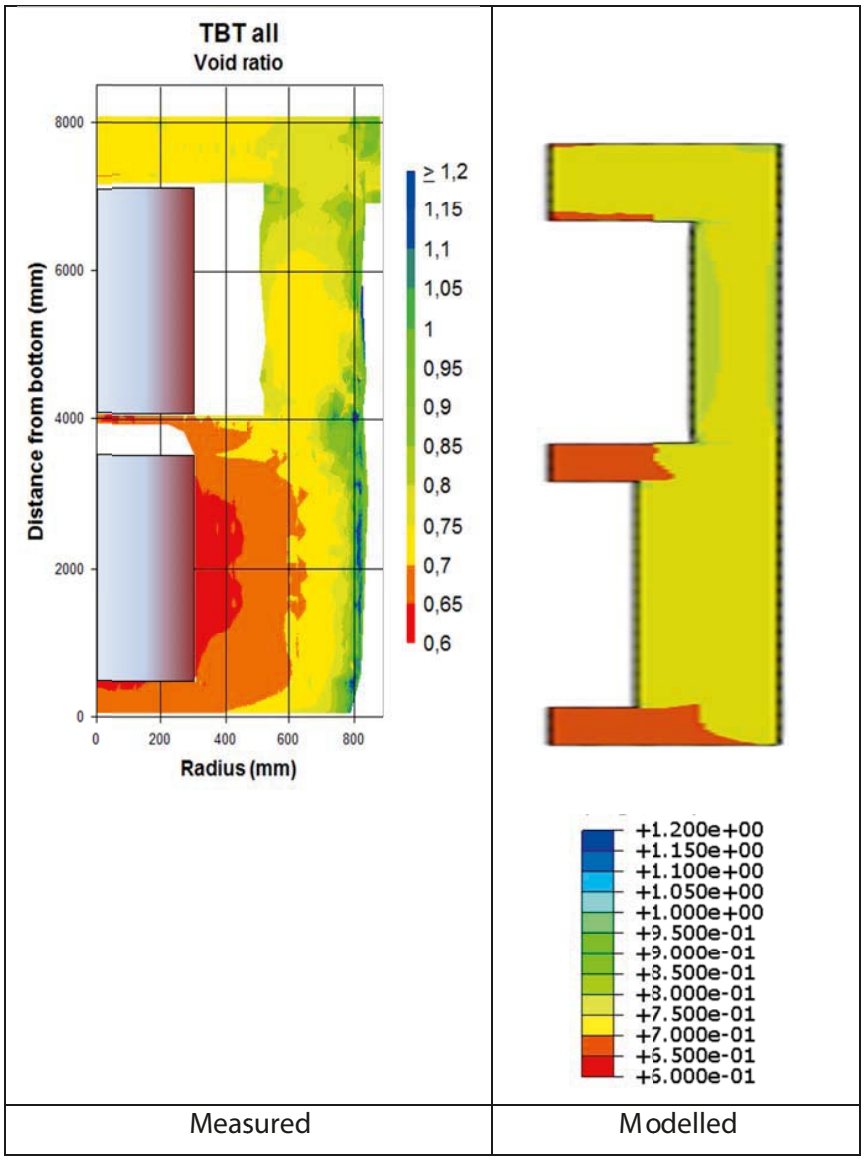

Figure 4-22. *Comparison between modelled and measured void ratio distribution.*

Total axial and radial stresses

Figure 4-23 shows the total axial and radial stresses in contour plots at different times. Figure 4-24 and Figure 4-25 show radial paths of the radial and axial stresses at mid heaters.

Around the upper heater the modelled radial stresses are clearly lower than the axial and agree very well with measured (6–7 MPa). The measured axial stresses (7.5–8.5 MPa) are in agreement with the calculated higher than the radial but a little lower than the calculated. Around the lower heater the modelled radial stresses (7–9 MPa) are also lower than the axial (9–11 MPa). The measured (radial: 6–7 MPa; axial 7.5–9.5 MPa) are also a little lower than the modelled.

A comparison between measured and modelled evolution of the total axial and radial stresses around heater 1 are shown in Figure 4-26 (measured results from Goudarzi et al. 2010). The results confirm what was stated earlier that the modelled stresses are higher than the measured. A general trend is that the modelling underestimates the total stress during the first about 1.5 years and then overestimates it during the rest of the test.

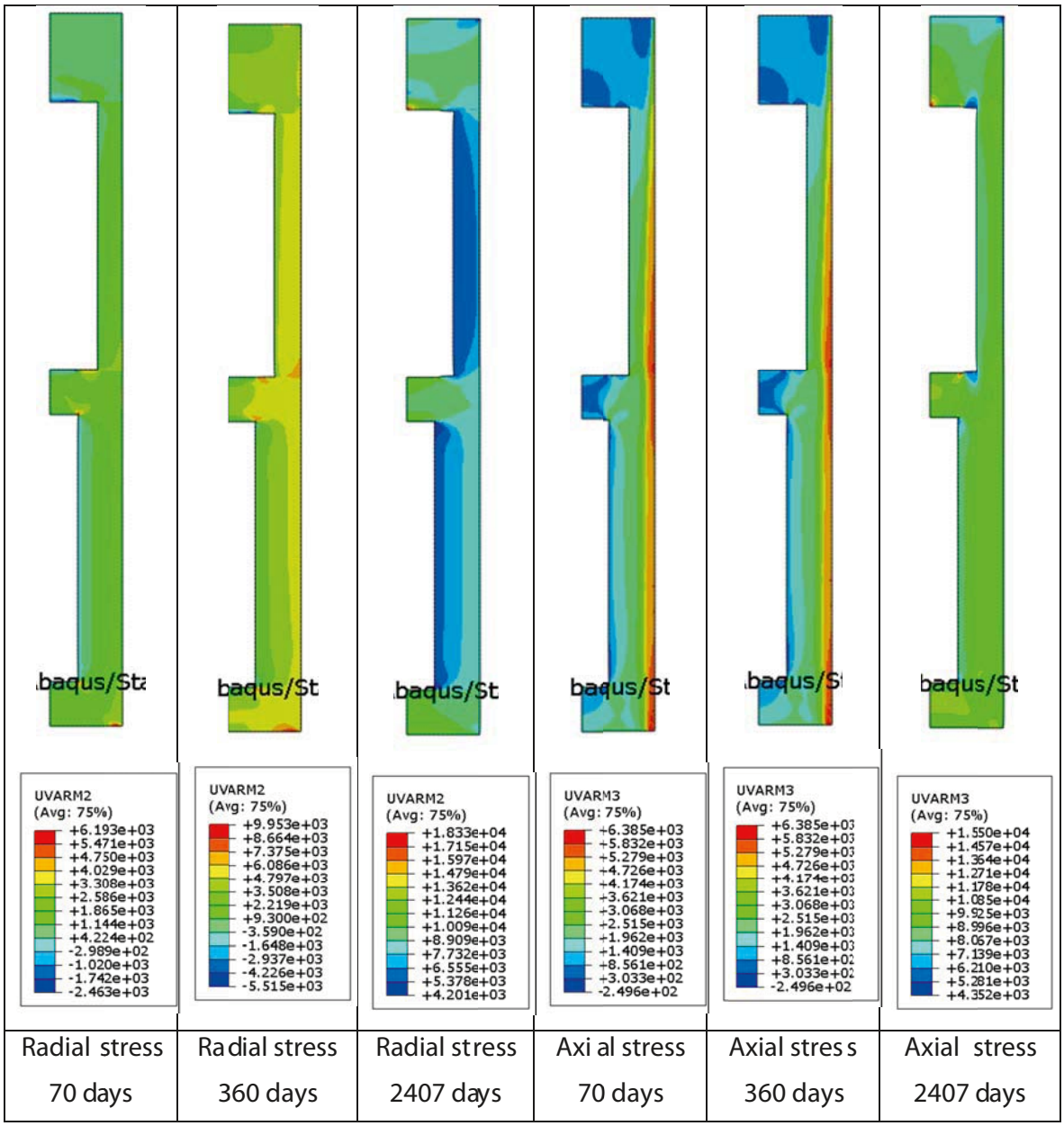

Figure 4-23. *Distribution of the total radial and axial stress (kPa) in the buffer at different times. Observe the difference in scale.*

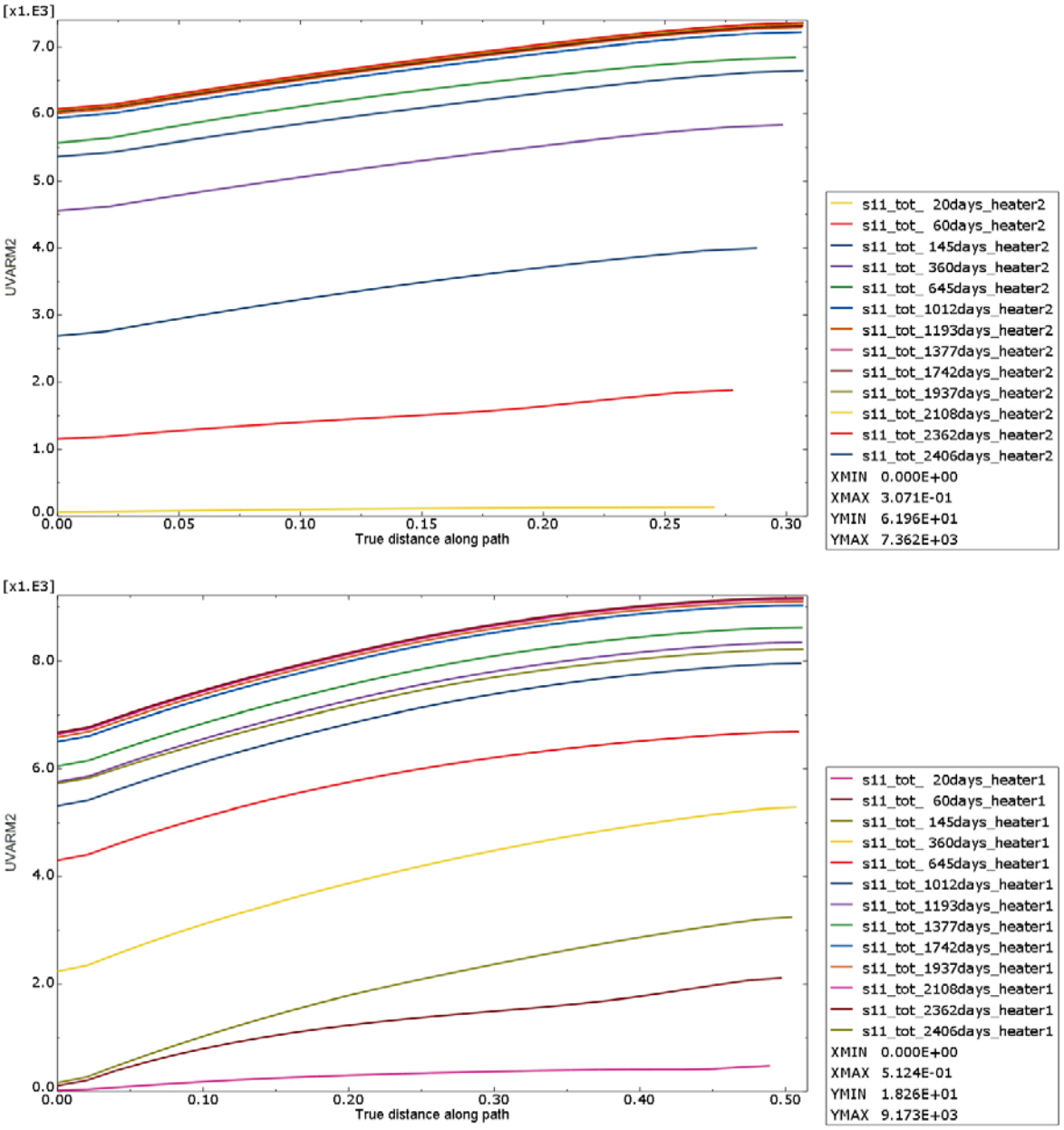

Figure 4-24. *Radial distribution of total radial stresses (kPa) at different times at mid height heater 1 (lower) and heater 2.*

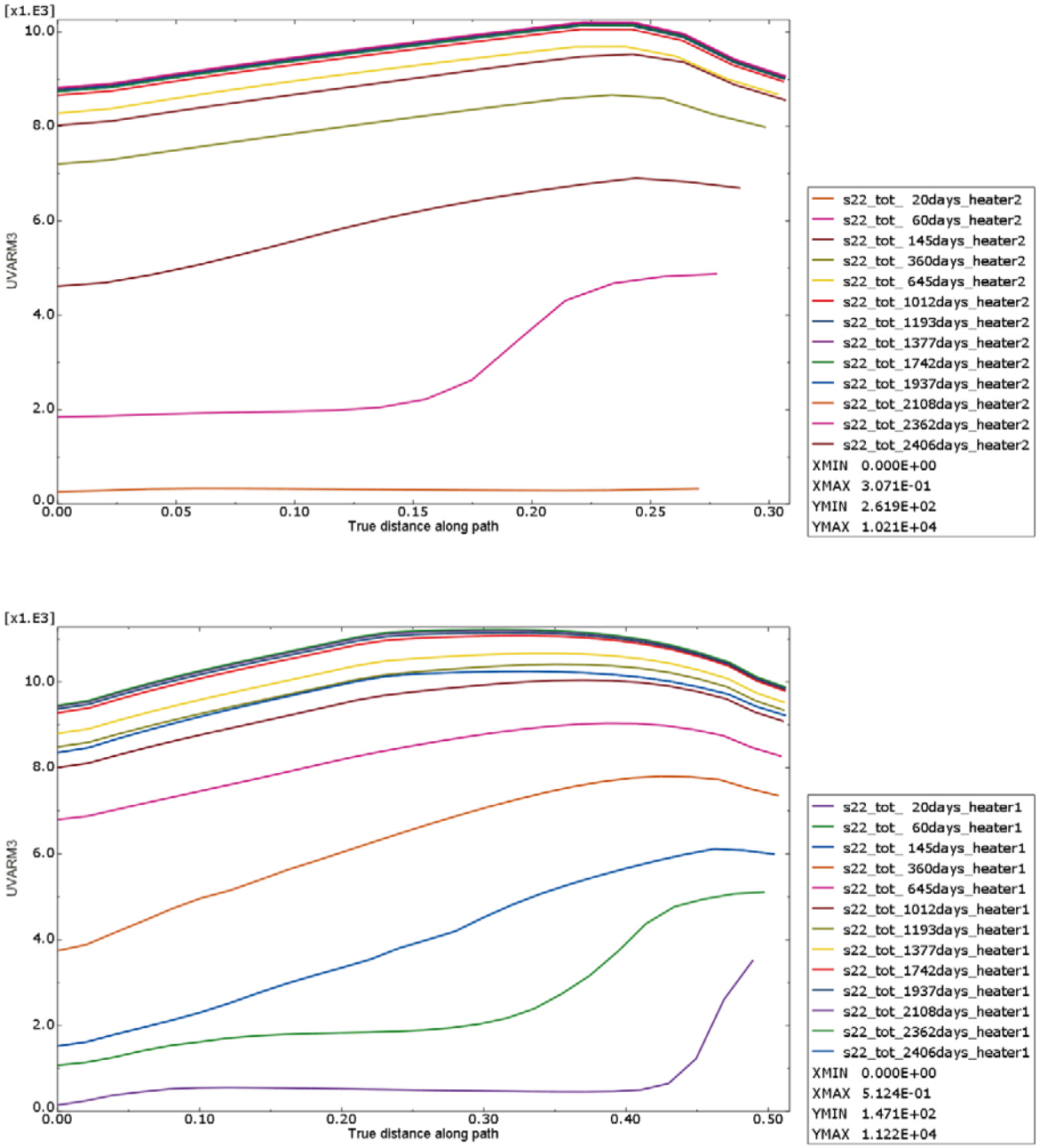

Figure 4-25. *Radial distribution of axial stresses (kPa) at different times at mid height heater 1 (lower) and heater 2.*

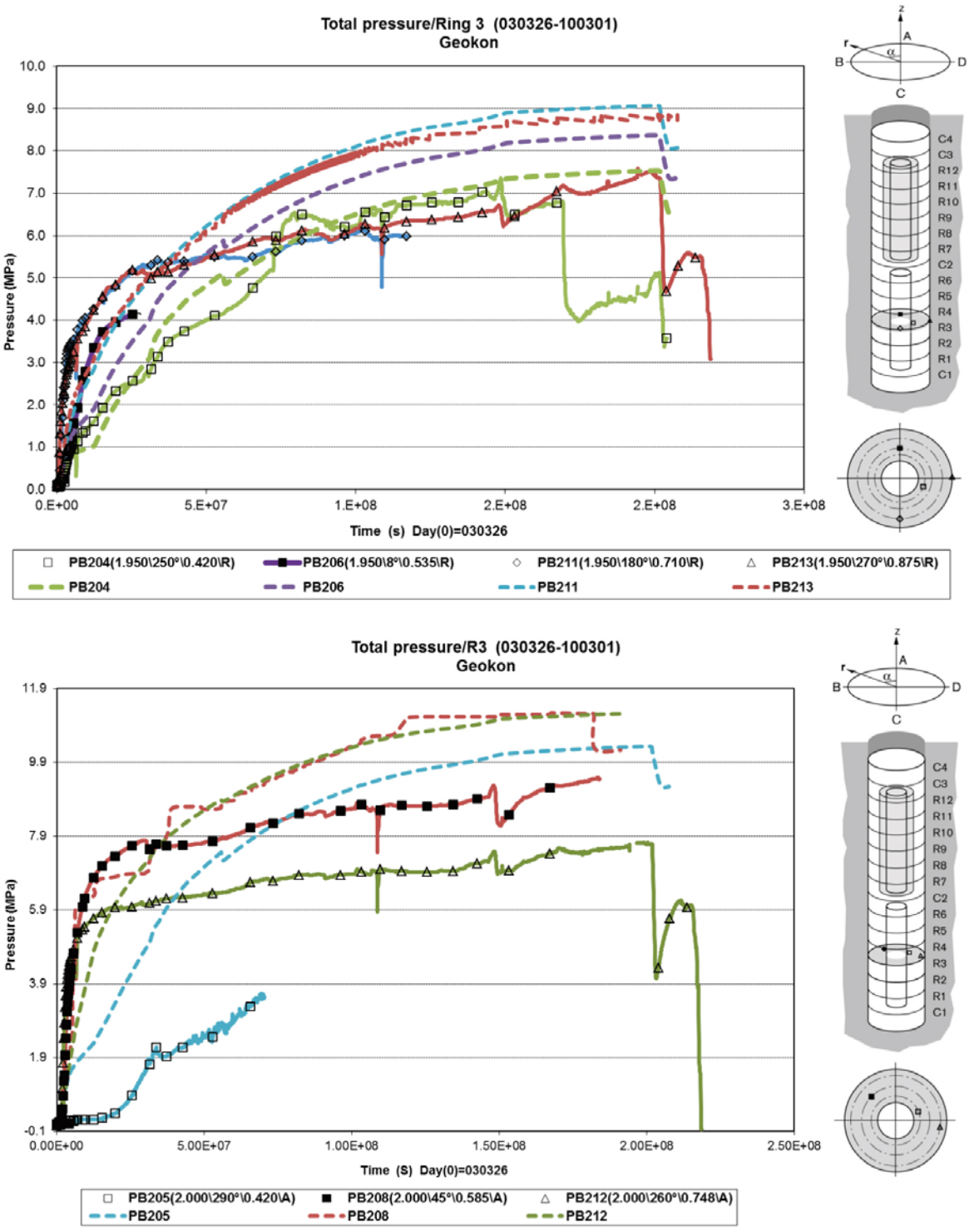

Figure 4-26. *Measured and modelled evolution of radial (upper) and axial (lower) total pressure (MPa) in the buffer around heater 1. The dashed lines are modelled results and the same colour represent the same location. The locations of the transducers are shown both in the figures and in the legends.*

Axial and radial displacements

Figure 4-27 shows the radial and axial displacements at mid heaters as radial paths at different times. The results show that there is a strong compression of the sand shield of more than 2.5 cm. The compression is completed after less than 1,000 days. They also show that the gap between the lower heater and the bentonite ring is closed after about 360 days.

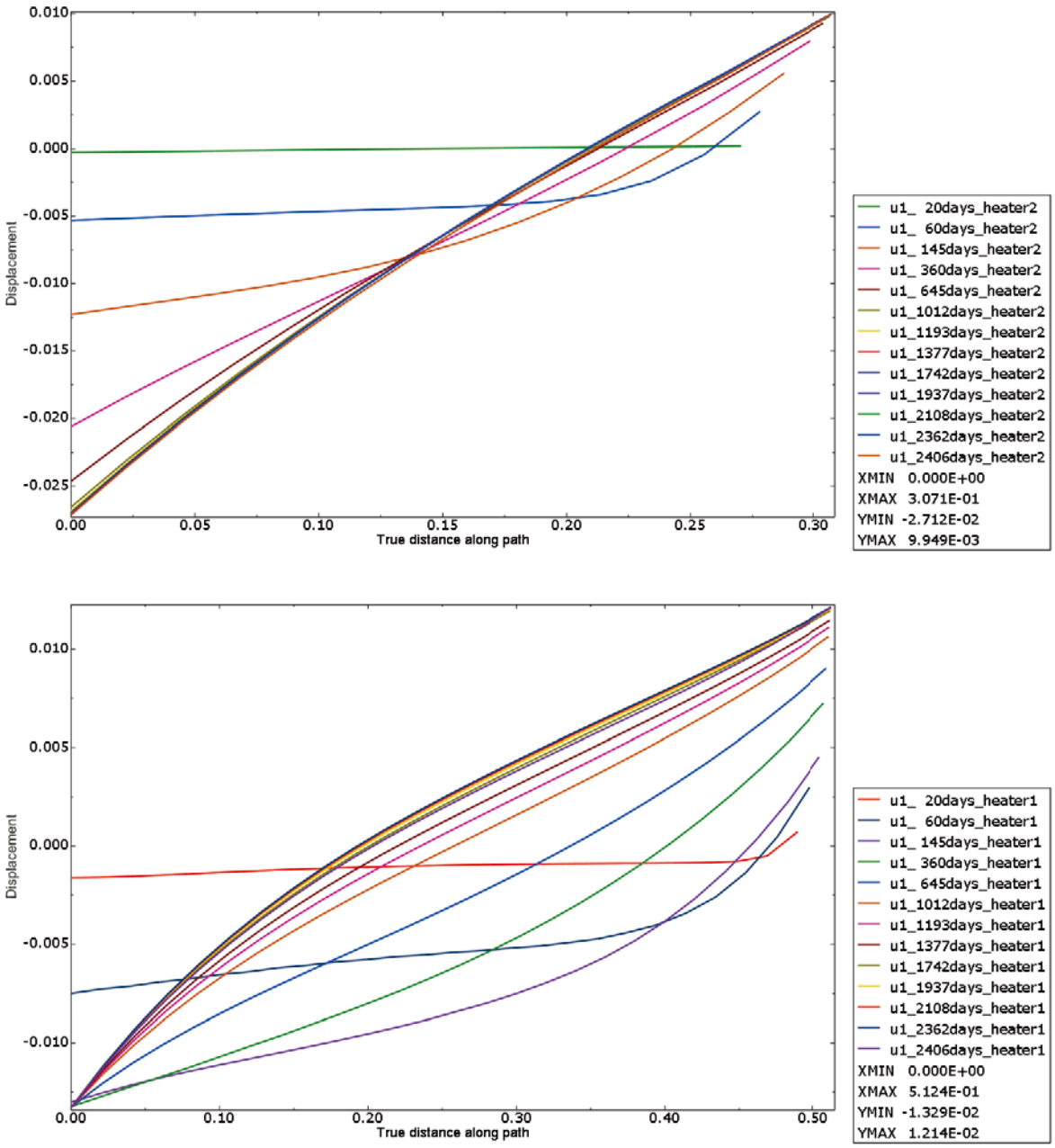

Figure 4-27. *Radial distribution of radial displacements (m) at different times at mid height heater 1 (lower) and heater 2.*

Displacements of and forces on the plug

Figure 4-28 shows the modelled and measured displacement of the plug. The measured displacement of the plug before heater shut off was 25 mm, which can be compared to the modelled displacement 21.2 (if the zero value is corrected).

Figure 4-29 shows the modelled and measured forces on the plug. The force was measured in three out of nine bolts. The total force on the plug is the sum of the three upper curves yielding a total maximum force before the power switch off of 14,990 kN, which can be compared to the total maximum modelled force of 13,180 kN.

The agreement between modelled and measured displacements of and forces on the plug is thus rather good. The model overestimates the force a little (12–13%), just as the total stresses, but not as much as the total stresses.

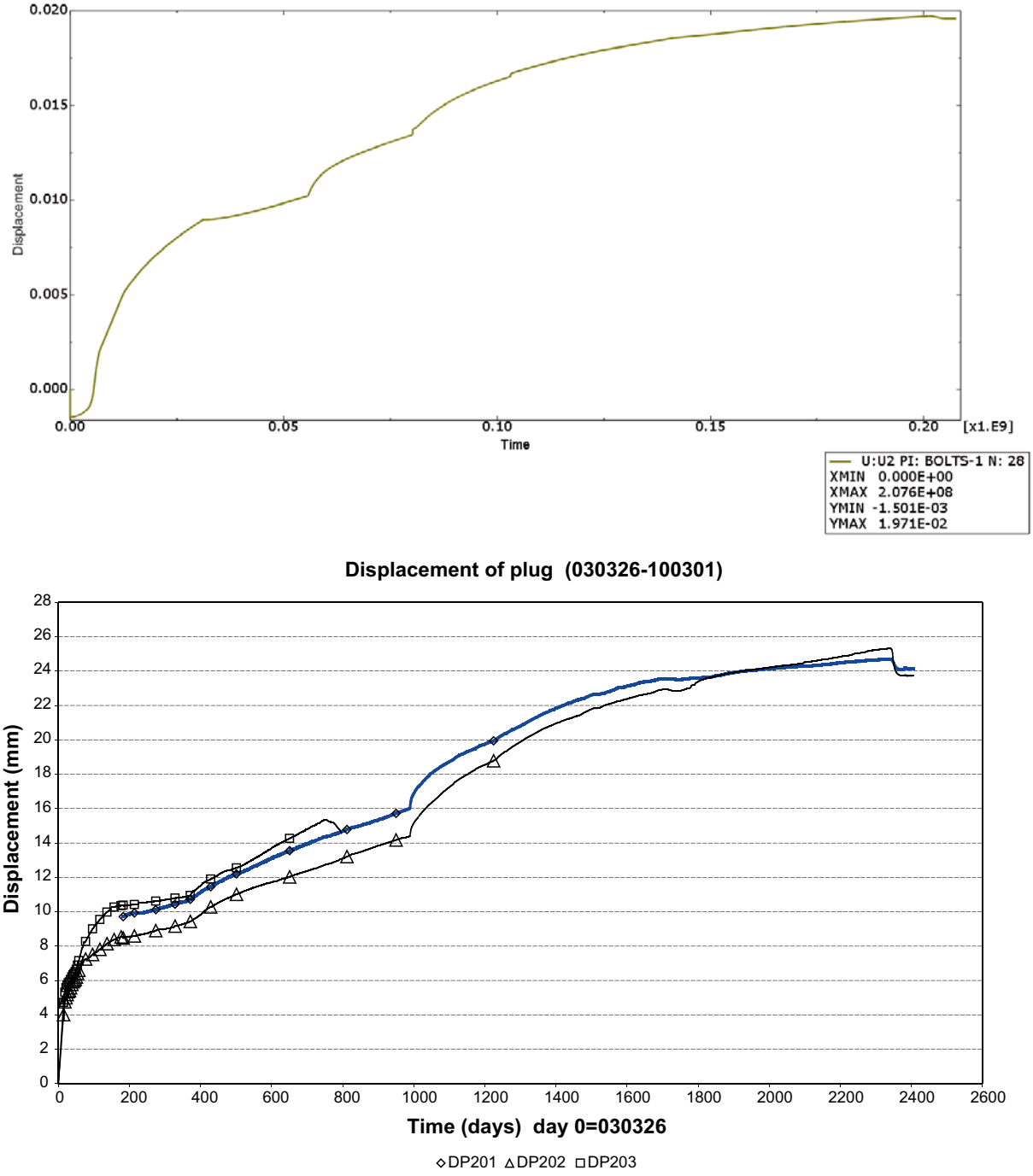

Figure 4-28. *Modelled (upper) and measured displacements of the plug.*

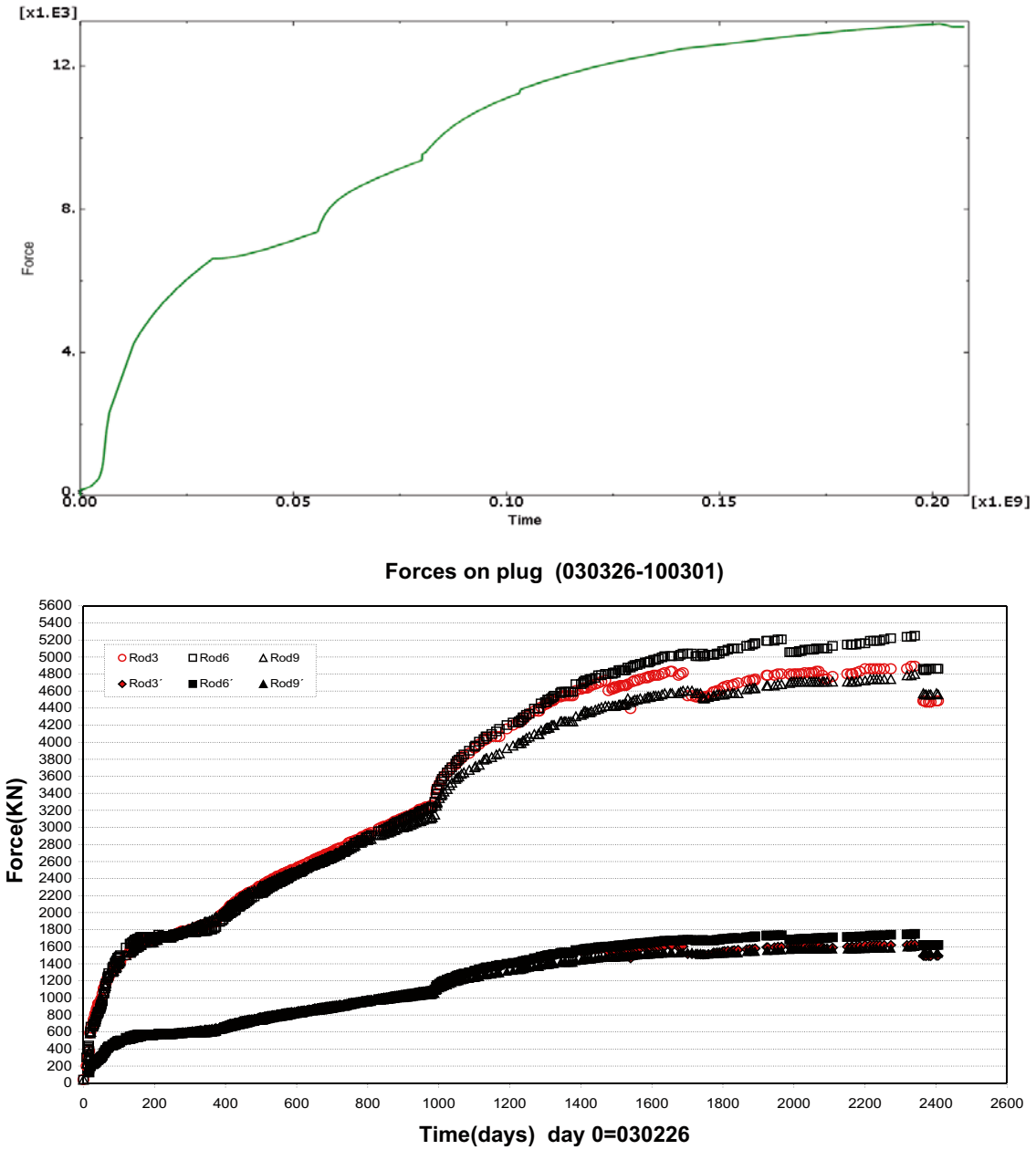

Figure 4-29. Modelled total force (kN) on the plug (upper) and measured force (kN) on three of the nine bolts. The total measured force is the sum of the three upper curves.

4.6.4 Hydro-mechanical results from the second loop

The second loop of the hydro-mechanical calculation (based on the second loop of the thermal calculation that was shown in section 4.6.2) was very difficult to complete due to convergence problems. Increasing the damping forces for the most difficult steps combined with continuing the analysis by using one or more restarts from last successfully converged step made the analysis to complete. However, the damping coefficient was increased so much that the results for those steps more or less gave no displacement changes implying that the swelling process became delayed even though the wetting process was marginally affected. At the end of the analysis no damping forces were required to have a converged solution and by comparing two successfully analysis using different levels of damping forces during the difficult steps show no final difference in the results presented in Figure 4-30. The analysis with highest value of the damping force required only one restart and with a smaller value two restarts were required to complete the analysis.

The damping forces (STABILIZE in ABAQUS) is normally an automatic procedure producing damping forces proportional to the velocity (incremental displacements dived by the time increment) and will

reduce the oscillations of the incremental solution and will in most cases make it possible to have a converged solution. However, if the damping coefficient is too high the solution might be wrong. It's up to the user to validate the obtained solution. It seems as in this case the solution is strongly affected in those steps where a high damping coefficient is used but when the damping coefficient later is reduced to zero the obtained final solution will be more or less the same regardless of the high damping coefficient earlier in the process.

The results of using these two help functions are illustrated by the results of the force on the plug. Figure 4-30 shows a comparison between the force evolution in loop 1 (same as in Figure 4-29) and two cases when damping forces and restarting have been used.

Figure 4-30 shows that the stress path is quite different when damping forces are used. The counter forces don't stop the wetting process but they delay the swelling and thus the force on the plug. However, the end results do not seem to differ and the results also show that the damping forces are zero at the end of the calculations, which means that the end results should be relevant. Damping forces were also used in loop 1 which explains the jerks in that curve. It thus seems that the mechanical evolution in loop 2 cannot be trusted but also that the end results are rather unaffected. This conclusion is further confirmed below.

Comparison between results after loop 1 and loop 2 (2 restarts) are shown in Figure 4-31 to Figure 4-33.

Figure 4-31 shows that there is some difference in temperature between loop 1 and 2 that clearly motivates the use of loop 2 for the temperature evolution. The largest difference is caused by the water filling of the sand shield and the wetting of the buffer around heater 1.

Figure 4-32 and Figure 4-33, which compare the degree of saturation, the void ratio and the total stresses in the buffer, show that the influence of the updated temperature calculation in loop 2 on these variables is very small. The results thus show that the hydro-mechanical calculations can be done without coupling to the thermal calculation.

The conclusion is thus that the hydro-mechanical results and comparisons shown in section 4.6.3 are relevant.

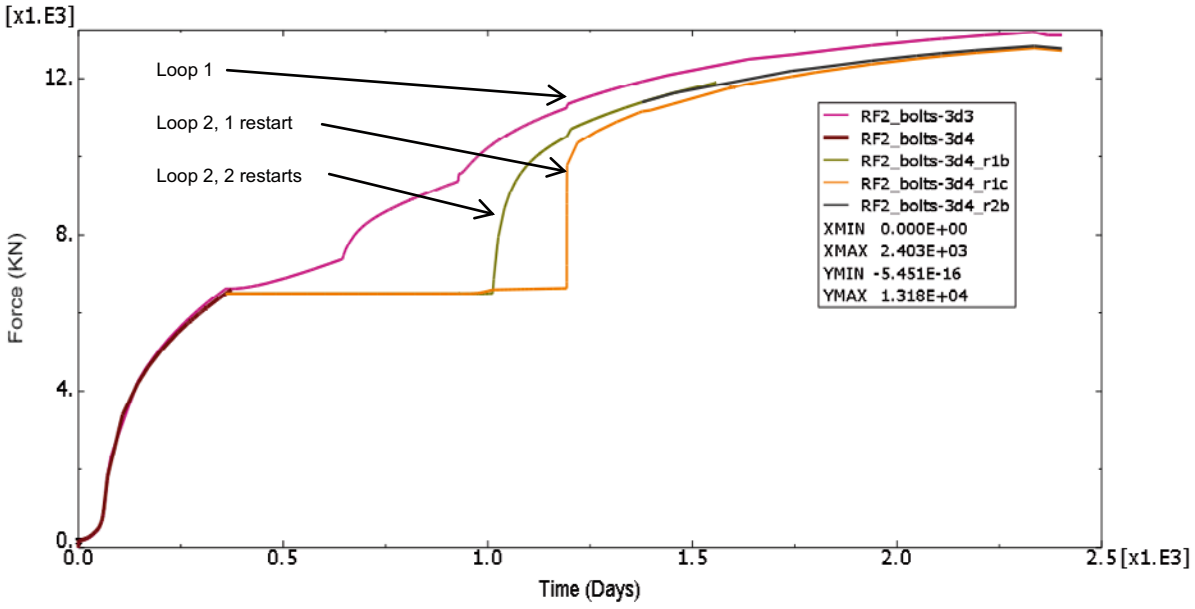

Figure 4-30. *Modelled force on the plug for three cases.*

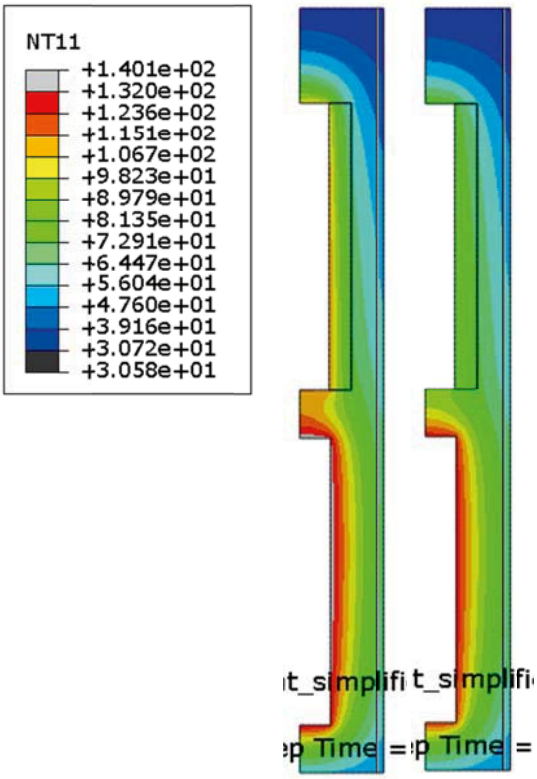

Figure 4-31. *Comparison of temperatures between loop 1 (left) and loop 2.*

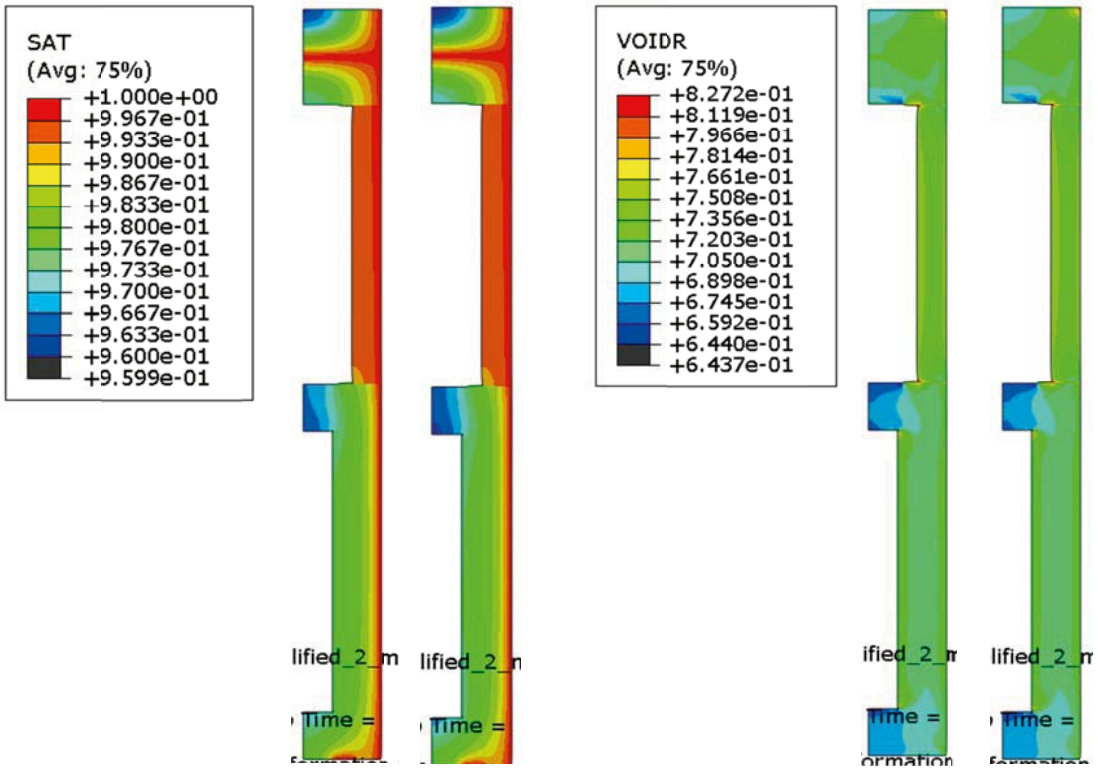

Figure 4-32. *Comparison of degree of saturation (left) and void ratio (right) between loop 1 (left) and loop 2 (right).*

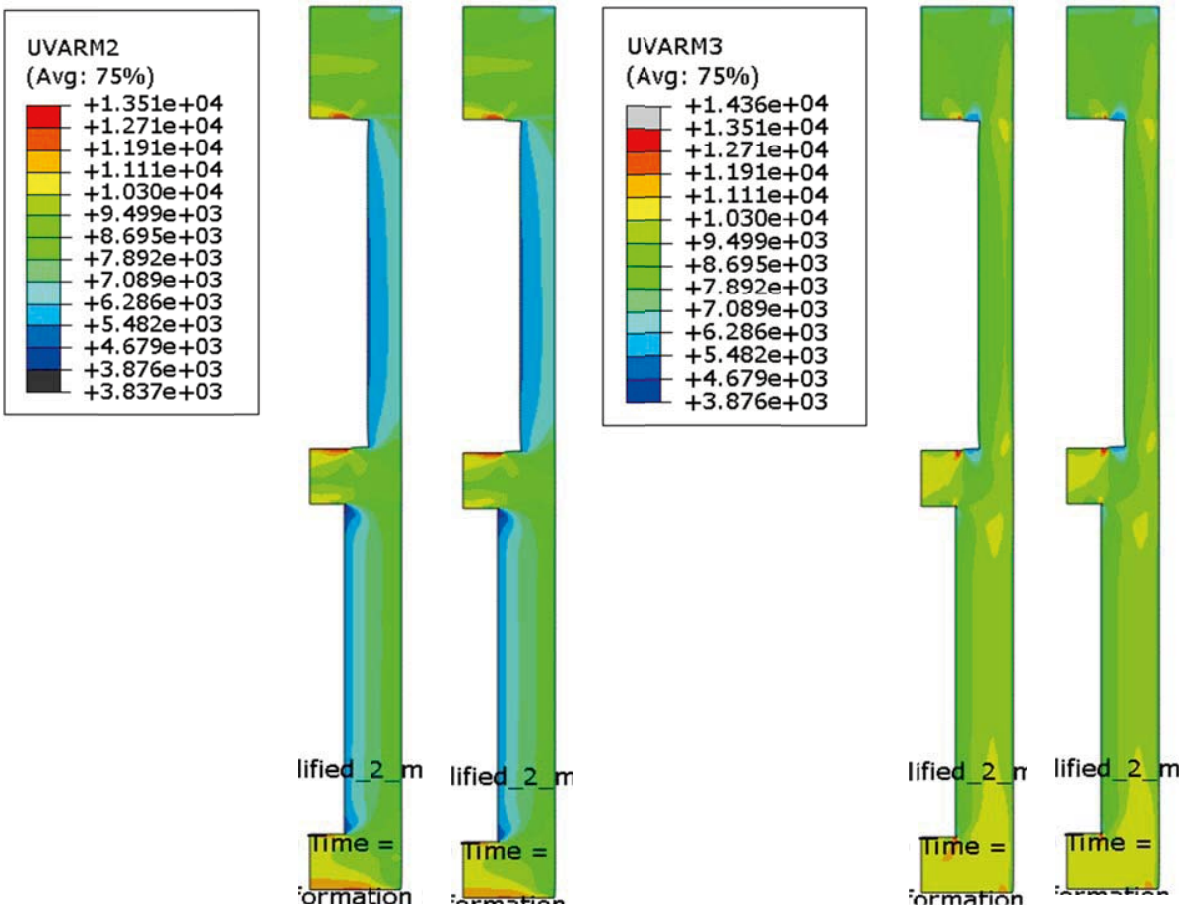

Figure 4-33. *Comparison of radial stresses (left) and axial stresses (right) between loop 1 (left) and loop 2 (right).*

4.7 Conclusions and comments

The thermo-hydro-mechanical modelling was done with a staggering technique since ABAQUS cannot at present couple temperature to hydro-mechanics. The temperature is thus in the first loop calculated with the thermal properties of the initial conditions of the buffer. The first loop of the hydro-mechanical calculation is then done using these temperature results. In the second loop of the temperature calculation the new thermal properties created by the hydro-mechanical evolution are used, which resulted in a somewhat different temperature evolution. However, the second loop of the hydro-mechanical calculation based on the new temperature results implied insuperable problems that could only be solved by introducing damping forces and restarts. However, comparing the results of loops 1 and 2 of the hydro-mechanical calculations showed that the difference was very small and that the results of loop 1 actually could be used.

In general the thermal results were decent although the boundary conditions have not been fine tuned. The largest discrepancy between modelled and measured temperature is the temperature of heater 1. The thermal problem is 3-dimensional and such a model has not been made with ABAQUS. However, the thermal results were considered good enough for the HM-calculation. The difference between the results of loop 1 and loop 2 were not strong but large enough to motivate the use of loop 2.

The hydro-mechanical modelling results were both good and bad, when compared to measured. The evolution of the buffer wetting and buffer swelling pressure has been rather well modelled. Theagreement between modelled and measured force and displacement of the plug is also very good. However, there are some parts of the void ratio distribution that were not well captured. The low void ratio close to heater 1 was not modelled. The high temperature (>100°C) and the HM effects of this high temperature are not well modelled. Neither was the very high void ratio measured at the boundary between the buffer and sand filter modelled. The reason of these discrepancies is not clear and should be further scrutinized.

5 Evaluation of experimental data

5.1 Introduction

The TBT experiment has generated large sets of experimental data which are used for interpretations of the processes and for comparison with results from THM models. Since the experimental data constitute the core for the understanding of the THM processes, it is necessary to somehow assess the validity of these data sets. Different data sets have however different sources, and may be affected by different conditions and factors. There is therefore no single method for such a task.

The *validity of the sensors data* have to some extent already been assessed through the sensor function control (Goudarzi et al. 2010), and the main results from these test are summarized in Table 5-1. Some sensors have evidently produced accurate results since the sensors exhibited a correct behavior when they were subjected to controlled conditions. A correct function was generally found for the thermocouples and the pore-pressure sensors. The total pressure sensors were in contrast generally graded as "under specification" which in most cases was due to a linear error higher than 5%. This grade appears to be slightly pessimistic, since 5% is virtually negligible for a typical swelling pressure of 8 MPa. The least accurate among the investigated were sensors were the capacitive RH-sensors.

The *validity of the dismantling data,* (i.e. the profile of water saturation and void ratio by (Johannesson 2010); as well as block levels and radial positions of interfaces (Åkesson 2010)) cannot be assessed by any direct means. Instead, one has to rely on methods in which independently determined data sets are compiled and evaluated with the aim of demonstrating some form of consistency. However, simply by visual inspection it can be made clear that the dismantling data was affected by the dismantling operation itself, especially regarding the high void ratio gradients close to the sand filter (see Figure 5-1 and Figure 5-2). These influences will unavoidably complicate the assessment of the validity.

Table 5-1. Brief remarks on the validity of the experimental data.

	Measurements	Sensors data	Dismantling data
T	Thermocouples	Accurate results	
H	Thermal conductivity	–"–	
	Psychrometers	–	
	Capacitive RH-sensors	Limited accuracy	
	Pore-pressure sensors	Accurate results	
	Saturation profiles		Affected by cooling and water in filter during dismantling operation
M	Total pressure sensors	Mostly "under specification"	
	Cable forces & lid displacements	–	
	Void ratio profiles		Affected by cooling and water in filter during dismantling operation
	Levels & interfaces		Affected by dismantling operation

Apart from the task of validating the available data sets, there are some major questions regarding *the conditions of the bentonite before the dismantling operation* in general and before the termination of the heaters in particular: what were the displacement fields (axial as well as radial) and what was the state of saturation? This information is of interest for the THM modelling and the general interpretation of the test, but was distorted by the cooling and the dismantling.

These two objectives, to validate the data sets and to assess the conditions before the dismantling, are addressed jointly in this chapter. The evaluation has been made in five different tasks:

i. Evaluation of i) void ratio profiles at compaction and dismantling; ii) initial block heights; and iii) results from the leveling at installation and dismantling. The goal of this task is to demonstrate consistence between these quantities, which thereby can be validated. This is made through quantification of relative changes of dry masses per unit height and relative changes of the height of each block. This task arrives at an assessment of the axial displacement field prior to the unloading of the lid.

ii. Evaluation of i) void ratio profiles at dismantling; ii) the final total pressure readings; and iii) swelling pressure curves. The goal of this task is to demonstrate consistency between these quantities and relations, which thereby can be validated. This is made through a compilation of intervals (with minimum, mean and maximum values) for the final total pressure readings and the void ratios representative for the radial positions of the sensors.

iii. Evaluation of i) void ratio profiles and saturation profiles at dismantling; and ii) the temperature profile before the termination of the heaters. The goal of this task is test the assumption that the bentonite was totally water saturated before the termination of the heaters, and that the observed saturation profile was caused be the thermal "contraction" of water when the bentonite was cooled. This is made through an indirect procedure in which distributions of radial displacement and changes in water content are defined and used to calculate profiles and saturation profiles. The temperature dependence of the water density is directly taken into account for this. The task also sheds light on the high void ratio gradient observed close to the sand filter.

iv. Evaluation of a radial displacement field and its influence on evaluated thermal conductivity values for Ring 4. The goal of this task is to obtain a correction factor for these conductivity values.

v. Evaluation of different experimental observations (saturation profiles; temperature profiles and evaluated thermal conductivities; pore-, filter- and saturated vapor pressures; total pressures; and relative humidity evolutions) as either supportive or refutable to different hypothetical saturation profiles around the lower heater. The goal of this task is to characterize the final saturation state, before the termination of the heaters, and the progress of saturation.

Some issues and aspects have not been considered in the evaluations. For instance, the question whether the fracturing of the upper rings occurred during the test, or as a result of the retrieval test, has not been investigated, simply because there is no data that could be used to make such an interpretation. Moreover, no attempt has been made to calculate the total water uptake in the bentonite. This volume could for instance be compared with the total injected water volume, but there is no motive for such a comparison since the injected volume obviously surpassed the available pore volume at the start of the test. Finally, all variables are considered to be axis-symmetric, and no azimuthal variability has therefore been addressed.

5.2 Evaluation of void ratio profiles and leveling results

This section describes an evaluation of i) void ratio profiles at compaction and dismantling; ii) initial block heights; and iii) results from the leveling at installation and dismantling. The goal of this task is to demonstrate consistence between these quantities, which thereby can be validated. This is made through quantification of relative changes of dry masses per unit height and relative changes of the height of each block. This task arrives at an assessment of the axial displacement field prior to the unloading of the lid.

The first and most laborious step in this evaluation is to quantify the bentonite dry mass per unit height (m') for each block:

$$m' = \int_{r_i}^{r_o} 2\pi r \cdot \rho_d(r)\, dr \qquad (5\text{-}1)$$

where ρ_d is the dry density and r is the radius, with indices i and o corresponding to inner and outer radius, respectively.

The following procedure has been used for calculating this quantity for the dismantled bentonite (m'_D):

i. Compilation of all analyzed samples from each block.

ii. Definition of radial intervals, 50 mm wide in the interior of the blocks (e.g. $650 < r \leq 700$ mm) and narrower close the sand filter.

iii. Calculation of mean values of void ratio of all samples within the defined intervals. These mean values are shown, at the mid-point of each radial interval, together with the original measured values in Figure 5-1 and Figure 5-2.

iv. Mean void ratios are converted to dry densities. The dry mass per unit height is calculated for each annulus defined by the intervals. The sum of the masses of all annuli is the dry mass per unit height (m'_D) for the block. This value is given in Table 5-2.

The corresponding dry mass per unit height at the compaction of the blocks (m'_C) is simply calculated as $\rho_d \cdot (\pi r_o^2 - \pi r_i^2)$ and is also given in Table 5-2. Void ratios for each block at compaction were reported by Johannesson et al. (2010).

The dry mass of each block at compaction should be equal to the dry mass of the corresponding block at dismantling:

$$m'_D \cdot h_D = m'_C \cdot h_C \tag{5-2}$$

h_C and h_D are the height of the blocks at compaction and dismantling respectively.

This balance can be evaluated through rearranging the expression and by introducing the height of the blocks at installations (h_I):

$$1 = \frac{m'_D}{m'_C} \cdot \frac{h_I}{h_C} \cdot \frac{h_D}{h_I} = (1+\mu_{CD})(1+\varepsilon_{CI})(1+\varepsilon_{ID}) \tag{5-3}$$

Each ratio is here expressed as relative changes in height (ε) or in dry mass per unit height (μ), and the sum of these relative changes should be close to zero:

$$\mu_{CD} + \varepsilon_{CI} + \varepsilon_{ID} = \frac{m'_D - m'_C}{m'_C} + \frac{h_I - h_C}{h_C} + \frac{h_D - h_I}{h_I} \approx 0 \tag{5-4}$$

Relative changes in dry mass per unit height (μ_{CD}) can thus be calculated from the m'_C and m'_D values (see Table 5-2). Blocks heights at compaction and installation are given together with calculated relative changes of these heights (ε_{CI}) in Table 5-2. The corresponding strain from heights at installation and dismantling (ε_{ID}) were evaluated by Åkesson (2010) and are also shown in Table 5-2.

Finally, the sum of all relative changes is calculated for each block (see Table 5-2).This sum is fairly small ($\leq 1\%$) for blocks C1, R1, R2, R5, R6, R7, R11 and C4. A joint evaluation of R12 and C3, which is relevant due to the complicated interface between these blocks, also shows a small total sum. The void ratio profiles and the leveling results are thus consistent for a majority of the blocks.

High positive values of the sum (i.e. for C2 and R8) could possibly be caused by fractures. High negative values (R3 and R4) could be caused by swelling during dismantling which would underestimate the heights at dismantling.

The axial displacements ($h_D - h_I$) for the top surface of each block are illustrated in Figure 5-3. Two data sets are illustrated: the actually measured heights ($\Sigma\, h_I^i \cdot \varepsilon_{ID}^i$), and the one implied by relative changes in dry mass per unit height, together with the relative changes in blocks heights from compaction to installation ($-\Sigma\, h_I^i \cdot (\varepsilon_{CI}^i + \mu_{CD}^i)$).

An estimated displacement field for the conditions before the unloading of the lid is also shown in Figure 5-3. This is based on the following conditions and assumptions:

- The displacement of the top surface of C4 was 48 mm during the dismantling. The corresponding displacement for the conditions before the unloading of the lid is assumed to be the same as the final readings from the displacement sensors, i.e. 24 mm. The increase of the displacement of this surface was thus 24 mm.
- This elastic spring effect is assumed to be caused by the lower package, i.e. C1–C2, and to be evenly distributed over these blocks. This can be motivated by the fact that these blocks had the lowest void ratios and the lowest saturation degrees (although C3 and C4 also were relatively dry).
- The estimated displacement field for the upper eight blocks is based on leveling results (ε_{ID}), while for the lower eight blocks the field is based the void ratio profiles (ε_C). This is sensible considering that the uncertainty of the leveling results increase with depth, while the void ratio profile uncertainties are higher in the upper rings with the extensive fallout of material during the dismantling.

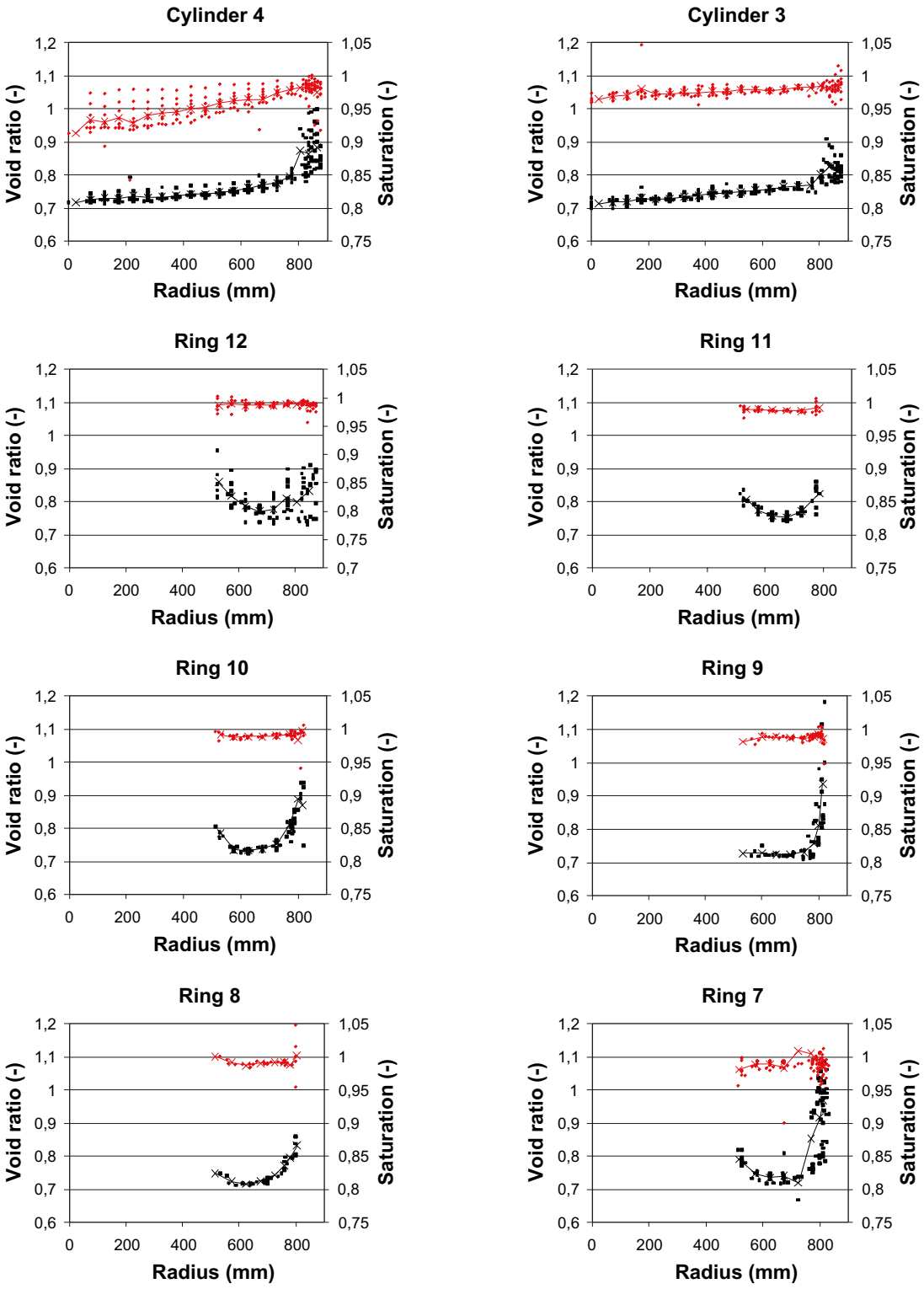

Figure 5-1. *Void ratio (black) and saturation degree (red) for different bentonite blocks. Measured values (dots) and averaged values within defined radial intervalls (lines with crosses).*

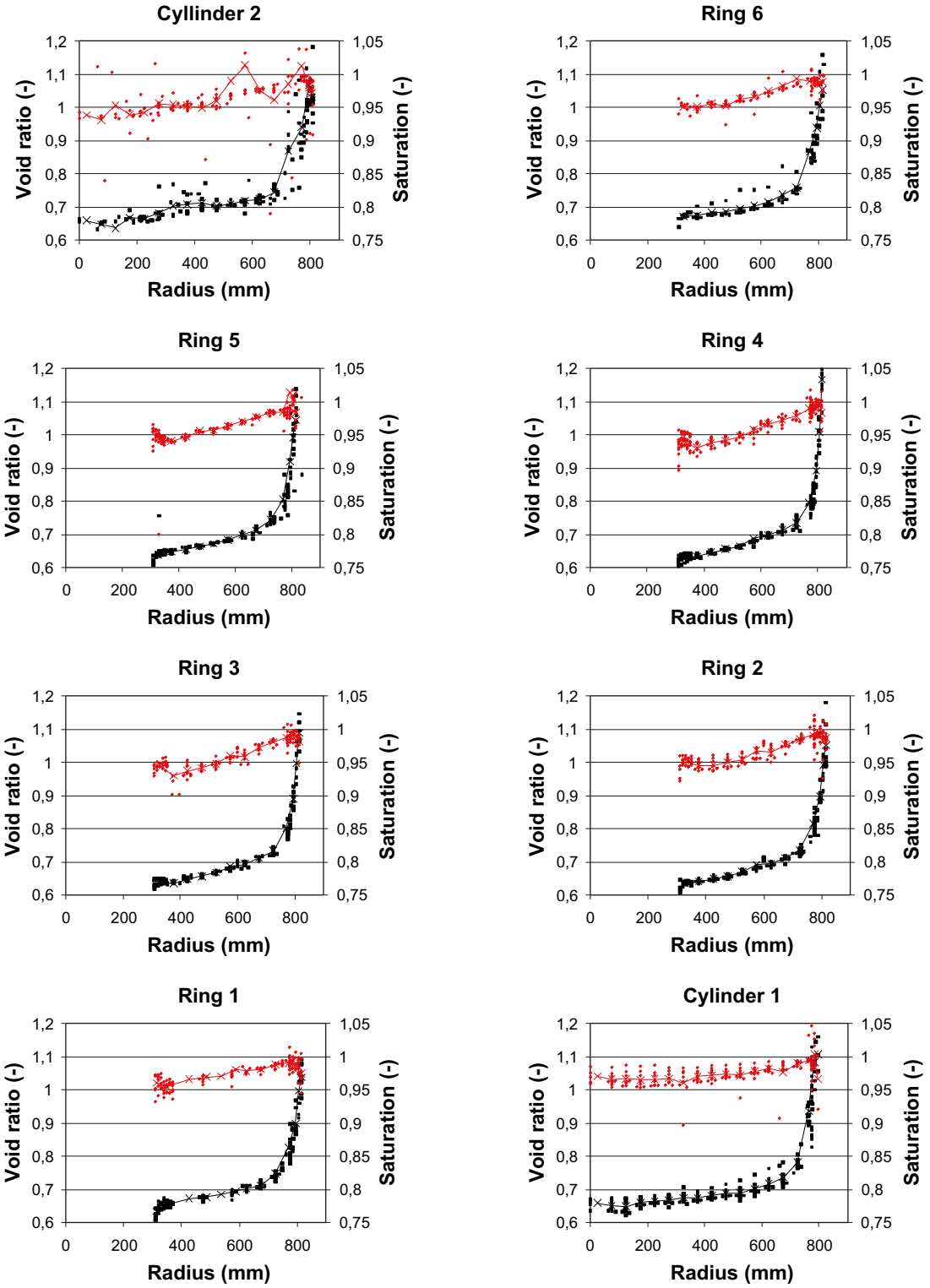

Figure 5-2. *Void ratio (black) and saturation degree (red) for different bentonite blocks. Measured values (dots) and averaged values within defined radial intervalls (lines with crosses).*

It should be stressed that this is an estimate that shouldn't be regarded as an empirical result, but rather as a best guess. Still, it implies a number of interesting observations:

- The large difference between the displacements at the top surfaces of R12 and C3 remains. This is plausible given the 5 cm shelves observed during dismantling and the unlikelihood that these were caused by the dismantling itself.
- Large axial strains are found for R10–R12 (in average approx 4%).
- The axial strains of R7–R9 are virtually zero or negative. This appears to correspond with the extensive inward radial swelling of these blocks observed during the dismantling.
- The axial strains of C1–C2 are found to be quite low and homogenous (in average 0.8%).

These observations have relevance for the THM modelling and the issue of explaining the stress-levels found in the experiment.

Table 5-2. Dry masses per unit height, blocks heights, and relative changes of different quantities for each bentonite block.

Block	m'_C (kg/m)	m'_D (kg/m)	μ_{CD}	h_C	h_I	ε_{CI}	ε_{ID}	$\mu_{CD}+\varepsilon_{CD}+\varepsilon_{ID}$*
C4	3,823	3,793	–0.8%	494	499	1.0%	0.3%	0.4%
C3	3,845	3,825	–0.5%	504	507	0.6%	–9%	–9.0%
R12	2,391	2,466	3.1%	502	505	0.5%	4.5%	8.0%
R11	2,091	2,000	–4.4%	501	504	0.7%	4.7%	1.0%
R10	2,081	2,053	–1.3%	498	503	0.9%	2.4%	2.0%
R9	2,089	2,150	2.9%	504	507	0.5%	–0.5%	2.9%
R8	2,087	2,183	4.6%	506	509	0.6%	0.4%	5.6%
R7	2,070	2,123	2.6%	504	506	0.4%	–3.3%	–0.4%
C2	3,308	3,272	–1.1%	498	504	1.3%	4.4%	4.6%
R6	3,039	2,919	–3.9%	497	501	0.9%	1.9%	–1.0%
R5	3,016	2,947	–2.3%	503	507	0.8%	0.8%	–0.6%
R4	3,019	2,940	–2.6%	498	502	0.9%	–0.5%	–2.2%
R3	3,013	2,954	–2.0%	502	506	0.9%	–1.3%	–2.4%
R2	3,017	2,944	–2.4%	501	506	1.1%	1.6%	0.2%
R1	3,030	2,934	–3.2%	499	504	1.1%	1.9%	–0.2%
C1	3,318	3,242	–2.3%	494	502	1.5%	1.5%	0.8%

* Sum is based on μ and ε-values with more than one decimal figure.

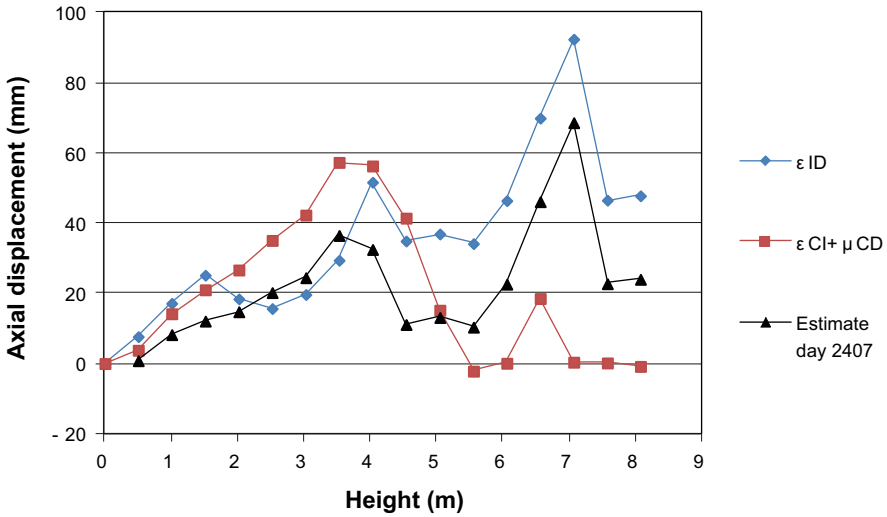

Figure 5-3. *Axial displacements (installation to dismantling) versus height. Each symbol represents the top surface of each block. Blue line denote measured data from levelling. Red line denote data evaluated from density profiles, initial density and initial block heights. Black line is an estimate for the conditions before the unloading of the lid.*

5.3 Evaluation of void ratio profiles and final total pressures

This section describes an evaluation of i) void ratio profiles at dismantling; ii) the final total pressure readings; and iii) swelling pressure curves. The goal of this task is to demonstrate consistency between these quantities and relations, which thereby can be validated. This is made through a compilation of intervals (with minimum, mean and maximum values) for the final total pressure readings and the void ratios representative for the radial positions of the sensors.

For evaluation of representative data on total pressures the following procedure has been used (see Table 5-3):

i. The last sensor readings have been listed. The first choice of date for this was day 2,335, i.e. the day before the start of the termination of the heaters if the sensor in question was still functional at the time. If the sensors had failed prior to this date, then the last representative sensor reading was chosen. For some sensors (PB 205, 206, 211, 207,210,221, 226, 227 & 228), no reading was considered to be representative for the final state of the investigated blocks.

ii. The rings had in several cases representative readings from more than one sensor in a certain direction (axial, radial or tangential). In these cases, an average stress was calculated for the direction in question. The cylinders had only one sensor each in the different directions and therefore no averages were calculated for these blocks.

iii. For each block, the minimum and maximum stress is identified from the individual sensor readings. A mean stress is calculated from the stresses in different directions; for the rings this is based on the average stresses, while for the cylinders this is based on individual readings. For Cylinder 3, only one representative reading is available, and this value is therefore treated as the mean stress.

For evaluation of representative data on the void ratio the following procedure has been used (see Figure 5-4 and Table 5-4):

i. Radial intervals of void ratio data (following the definitions presented in section 5.2) were selected in order to cover the radial positions of the pressure sensors, excluding the sensor at the rock wall outside Ring 3 (PB213). For the cylinders only one interval (600–650 mm) was sufficient to cover the interval positions in these blocks. Seven and five intervals were needed to cover the positions in Ring 3 and 9, respectively.

ii. For all the selected intervals in each block, a minimum and a maximum void ratio were identified from the individual measurements. A mean dry density was calculated as the weighted mean ($\Sigma A^i \cdot \rho_d^i / \Sigma A^i$, where A^i = area and ρ_d^i = mean dry density for interval i), from which a mean void ration was calculated.

Finally, all evaluated data, i.e. minimum, mean and maximum values, for total pressures as well as void ratios are compiled as crossed bars for each block (see Figure 5-5). Two swelling pressure curves for MX-80 bentonite are shown for comparison, denoted TR-95-20 curve and TR-10-44 curve, respectively, and were evaluated by Börgesson et al. (1995) and Åkesson et al. (2010b), respectively. The latter one is based on retention data, i.e. measurements of water content at different relative humidity for free swelling conditions, and the lower end of the scatter of swelling pressure data.

A second type of evaluation has been made through comparison of each individual pressure readings with the mean void ratio for the radial interval which covers the position of the individual sensors. These void ratios are presented in Table 5-3. A compilation of pressure readings and representative void ratios is shown in Figure 5-6.

The crossed bars for C1 and C2 in Figure 5-5 generally fall between the two swelling pressure curves, whereas the bars for R9 and C3 tend to agree more with the TR 10-44 curve. The crossed bars for R3 generally fall below both curves. The void ratio profiles and the total pressure readings are therefore quite consistent with the swelling pressure curves. The overall agreement illustrates that the total pressure sensors have produced quite accurate results, although the Sensor function control of Goudarzi et al. (2010) in most cases graded the investigated sensors as “under specification”.

An explanation for the slightly lower total pressures of R3 could be that the bentonite wasn’t totally water saturated at the end of the test, or it could be an indication that the properties of the bentonite had changed, perhaps due to the thermal load.

Table 5-3. Evaluation of final stress levels in different blocks.

Block	Last sensor readings/void ratio representative for sensor positions	Time/radius	Average stress in different directions	Minimum stress	Mean stress	Maximum stress
C1	PB201 (A): 9.1/0.717	d2,335/635		8.1	8.8	9.3
	PB202 (R): 9.3/0.717	d2,335/635				
	PB203 (T): 8.1/0.717	d1,695/635				
R3	PB208 (A): 9.5/0.687	d2,130/585	A: 8.6	5.1	7.3	9.5
	PB212 (A): 7.7/0.734	d2,335/748				
	PB204 (R): 5.1/0.649	d2,335/420	R: 6.2			
	PB213 (R): 7.4/–*	d2,335/875				
	PB209 (T): 7.1/0.693	d2,335/635	T: 7.1			
C2	PB214 (A): 7.8/0.724	d2,335/635		7.8	8.2	8.6
	PB215 (R): 8.6/0.724	d2,239/635				
	PB216 (T): 8.2/0.724	d2,239/635				
R9	PB218 (A): 8.6/0.724	d1,504/635	A: 8.1	5.9	7.5	8.6
	PB223 (A): 7.6/0.731	d1,504/745				
	PB217 (R): 6.2/0.728	d2,335/535	R: 6.2			
	PB219 (R): 5.9/0.724	d2,335/635				
	PB222 (R): 6.6/0.724	d2,335/710				
	PB224 (R): 6.0/0.731	d2,335/770				
	PB220 (T): 8.6/0.724	d836/635	T: 8.4			
	PB225 (T): 8.1/0.731	d2,335/740				
C3	PB229 (T): 6.0/0.757	d2,335/635			6.0	

* Located at the rock wall

Table 5-4. Evaluation of final void ratio levels in different blocks.

Block	Inner radius	Outer radius	Minimum void ratio	Mean void ratio	Maximum void ratio
C1	600	650	0.700	0.717	0.764
R3	400	750	0.642	0.690	0.745
C2	600	650	0.711	0.724	0.734
R9	492	775	0.709	0.727	0.780
C3	600	650	0.745	0.757	0.767

Figure 5-6 illustrates the scatter of total pressure for R9, which reflects the difference between radial stresses on one hand, below the TR 10-44 line, and axial and tangential on the other, above the line. For R3, two points falls below the swelling pressure curve: one radial sensor at 420 mm radius, and one tangential sensor at 635 mm radius. This illustrates that the low pressures of R3 primarily is registered by the innermost sensor.

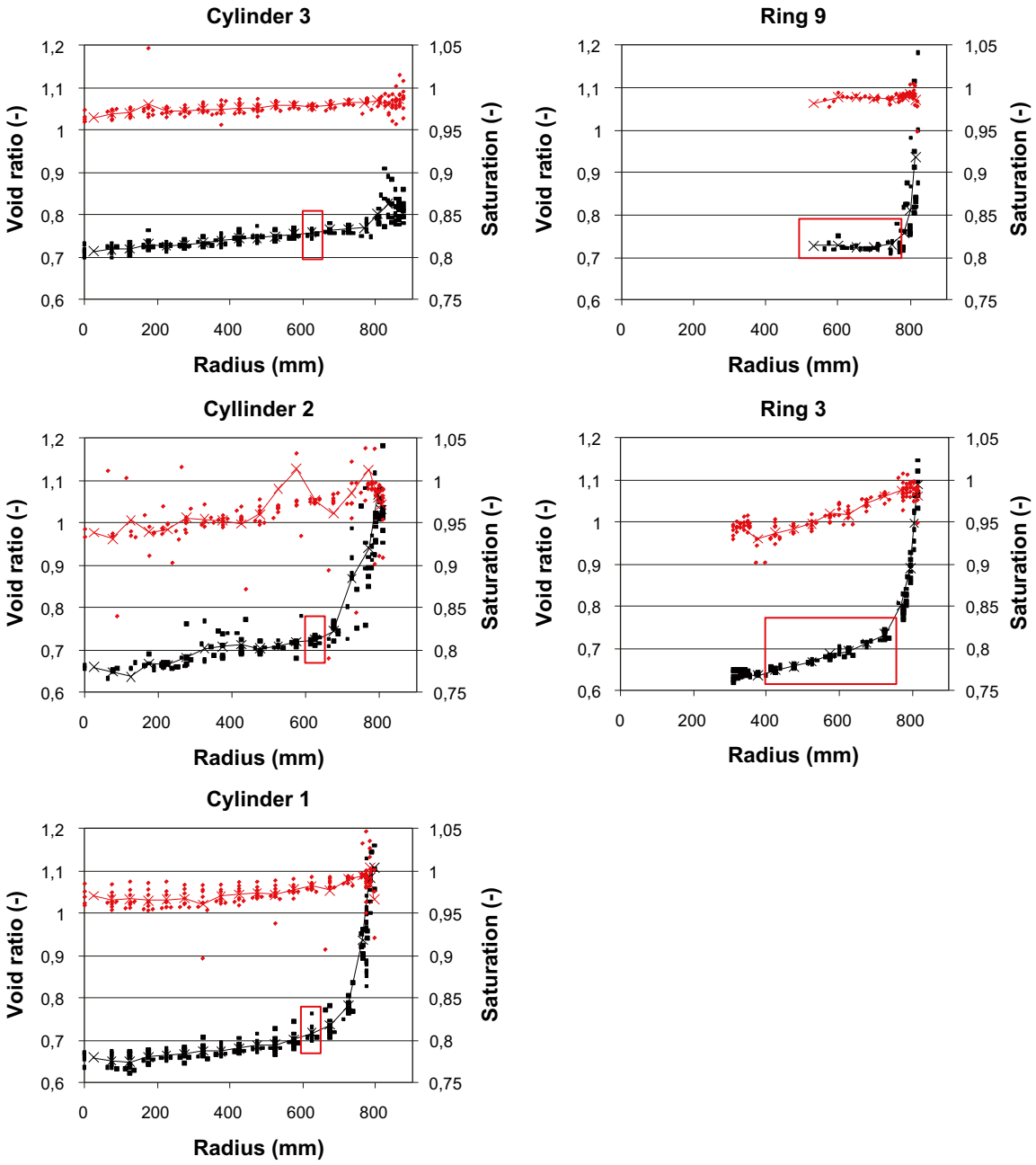

Figure 5-4. *Void ratio (black) and saturation degree (red) for different bentonite blocks. Red boxes denote instrumented sections for which representative void ratio data is evaluated.*

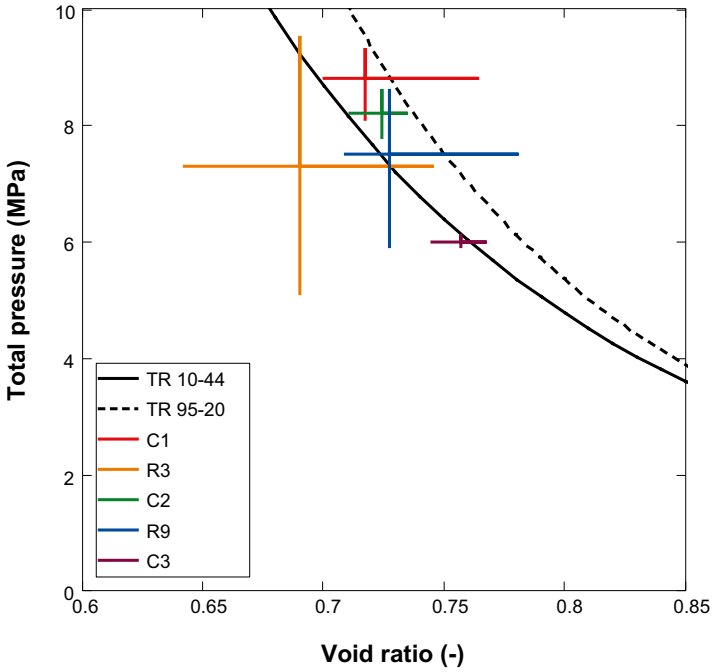

Figure 5-5. *Compilation of final pressures (minimum, mean, maximum) for each instrumented block versus the corresponding void ratios at dismantling (minimum, mean, maximum). Two swelling pressure curves shown for comparison.*

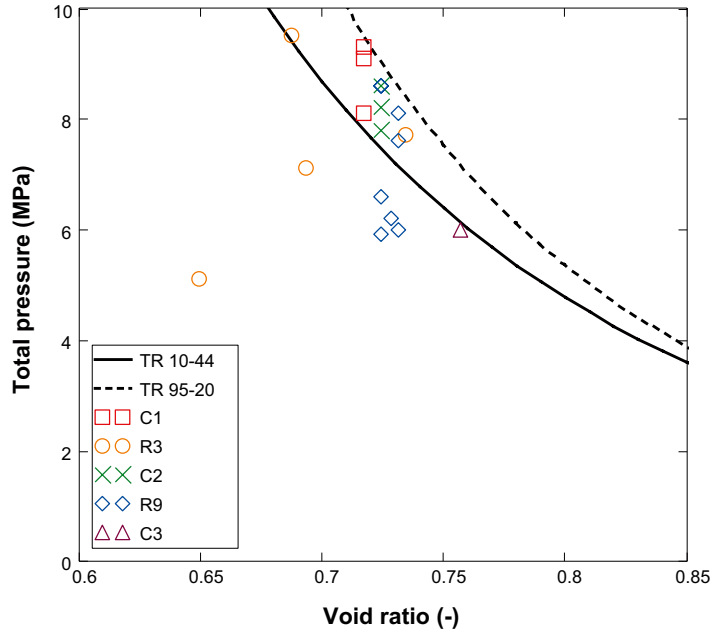

Figure 5-6. *Compilation of final pressures and representative void ratios for each individual pressure sensors. Two swelling pressure curves shown for comparison.*

5.4 Effects of cooling and conditions during dismantling

The results from the measurements of density and water content in the lower package of TBT display some unusual features that call for an explanation. The most exceptional result is the steep void ratio profile close to the sand filter (see Figure 5-2). The outermost values are in the order of 1.0–1.1, and it is unlikely that these could reflect the earlier conditions with swelling pressures around 7–9 MPa. A second observation is the saturation profiles with values from 93–94% at the heater to 100% at the filter. This should not be regarded as significant in itself. But given the extensive cooling that took place just prior to the dismantling operation and the thermal expansion of water, it appears to be possible that the buffer was water saturated prior to the cooling event.

In order to have a simple description of the changes associated with the cooling and the dismantling, a framework with five states has been defined. These states are denoted *initial*, *hot*, *cool*, *wet* and *final* (see Figure 5-7 and Figure 5-8). The initial state corresponds to day zero, i.e. the original bentonite block. The hot state corresponds to day ~2,300, i.e. just prior to the termination of the heating. The cool state represents the conditions immediately after the cooling of the bentonite. The wet state represents the conditions prior to the release of the material during dismantling, but after a period with access to some water in the filter. Finally, the final state corresponds to the sampled material.

The inner gap was probably closed before the hot state was reached, and the inner radius should therefore have decreased to the heater surface where it stayed until the final state. The outer radius, on the other hand, should have increased from the initial to the hot state, whereas it is assumed to have decreased during the cooling from the hot to the cool state. After this, it should have increased again due to water uptake during the transition from the cool to the wet state.

The final transition (from wet to final) is assumed to only be associated with an axial displacement field and this is therefore omitted from this evaluation.

The transitions between the different states are described by radial displacement fields and changes in the water content. The following characteristics can be noted for the different transitions:

- Initial/Hot: major displacements and increase in water content.
- Hot/Cool: minor negative displacement, but no change in water content.
- Cool/Wet: minor positive displacement and increase in water content, but only in the outer parts (say, beyond 750 mm).

It should be noted that these descriptions are simplification and that some transitions could very well take place in parallel.

The chosen approach is to define three radial displacement fields (u_{IH}, u_{HC} and u_{CW}). For example, the first field is defined as:

$$u_{IH}(r_i) = r_h(r_i) - r_i \tag{5-5}$$

These are functions of the initial coordinate (r_i), i.e. some radius between the initial inner and outer radii. For Ring 4 these were 317 and 815 mm, respectively.

The following functions have been adopted (mainly through trial-and-error):

$$\begin{aligned} u_{IH}(r_i) &= -0.041 + 0.162 \cdot r_i - 0.275 \cdot r_i^2 + 0.187 \cdot r_i^3 \\ u_{HC}(r_i) &= -0.002 \cdot \left(\frac{r_i - 0.317}{0.815 - 0.317} \right)^{0.7} \\ u_{CW}(r_i) &= 0.002 \cdot \left(\frac{r_i - 0.75}{0.815 - 0.75} \right)^{5} \cdot \Phi(r_i - 0.75) \end{aligned} \tag{5-6}$$

Φ is here the Heaviside step function. This approach is convenient since the different fields can be readily superimposed.

$$u_{IC}(r_i) = u_{IH}(r_i)+u_{HC}(r_i)$$
$$u_{IW}(r_i) = u_{IC}(r_i)+u_{CW}(r_i) \quad (5\text{-}7)$$

The three original fields are shown together with the final total field (u_{IW}) in Figure 5-9 (left).

Expressions for the void ratio profiles for the subsequent states (H, C and W) can be derived from the mass balance:

$$\frac{r_i}{1+e_i(r_i)}dr_i = \frac{r_h}{1+e_h(r_h)}dr_h \quad (5\text{-}8)$$

Through rearranging this expression, and by substituting r_h by $u_{IH} + r_i$, according to (5-5), the following expression can be derived:

$$e_h(r_i + u_{IH}(r_i)) = [1+e_i(r_i)]\cdot\left[1+\frac{u_{IH}(r_i)}{r_i}\right]\cdot\left[1+\frac{du_{IH}(r_i)}{dr_i}\right]-1 \quad (5\text{-}9)$$

Similar relations can be derived for u_{IC} and u_{IW}. Void ratio profiles, based on the displacement fields in (5-6), are shown in Figure 5-9 (right) together with experimental data.

The water content for the hot state is calculated to yield total saturation (i.e S=1). The water density profile $\rho_w(r_h)$ is taken into account for this:

$$w_H(r_i) = \frac{e_H(r_i)\cdot\rho_w(r_i+u_{IH}(r_i))}{\rho_s} \quad (5\text{-}10)$$

The water density profile was based on tabulated values for the specific volume of water (at 6.5 bar in order to get a value at 160°C) and thermocouple readings for day 2,335.

For the transition from cool to wet a function, similar to the one for the displacement field, is adopted for the change in water content:

$$\Delta w(r_i) = 0.097\cdot\left(\frac{r_i-0.75}{0.815-0.75}\right)^4\cdot\Phi(r_i-0.75) \quad (5\text{-}11)$$

These functions are illustrated in Figure 5-10 (left). The saturation degrees are calculated from water contents, void ratio and water density.

$$S_H(r_i) = \frac{w_H(r_i)}{e_H(r_i)}\cdot\frac{\rho_s}{\rho_w(r_i+u_{IH}(r_i))}$$
$$S_C(r_i) = \frac{w_H(r_i)}{e_C(r_i)}\cdot\frac{\rho_s}{1000} \quad (5\text{-}12)$$
$$S_W(r_i) = \frac{w_H(r_i)+\Delta w(r_i)}{e_W(r_i)}\cdot\frac{\rho_s}{1000}$$

These functions are shown in Figure 5-10 (right).

The total displacement of the interface towards the sand filter was with the presented calculations 9.5 mm. This is more than the measured value of 4 and 6 mm for Ring 4 and 3, respectively. This deviation reflects the observation that the blocks have expanded axially during the test and the dismantling (see Figure 5-3), but this has been omitted from this exercise.

The evaluation shows that it is possibly that the bentonite was water saturated in state H, although the displacement fields probably could be improved. There are however alternative routes to reach the final water saturation profile; this would either require that the water uptake during the dismantling operation (i.e. the Δw function) reached further in towards the heater, or it would require a more extensive shrinkage (i.e. the u_{HC}-field would be more negative). An alternative route which also comprises water redistribution from the outer to the inner parts could also be possible.

In order for the bentonite in the outer part of the block to swell out to a void ratio of 1.0–1.1, there should be some free space available at the sand filter. This can very well be the case if the bentonite "shrinks" during the cooling, as implemented with the u_{HC}-function, and if the sand filter remains compressed against the rock wall.

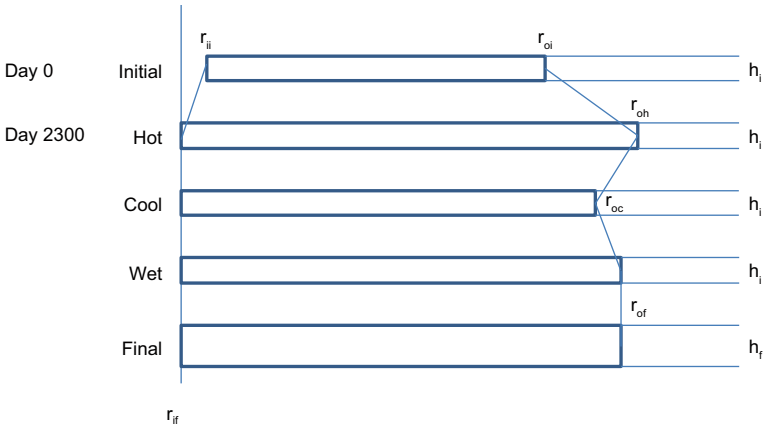

Figure 5-7. *Schematic outline of radii and heights of the blocks during the different states.*

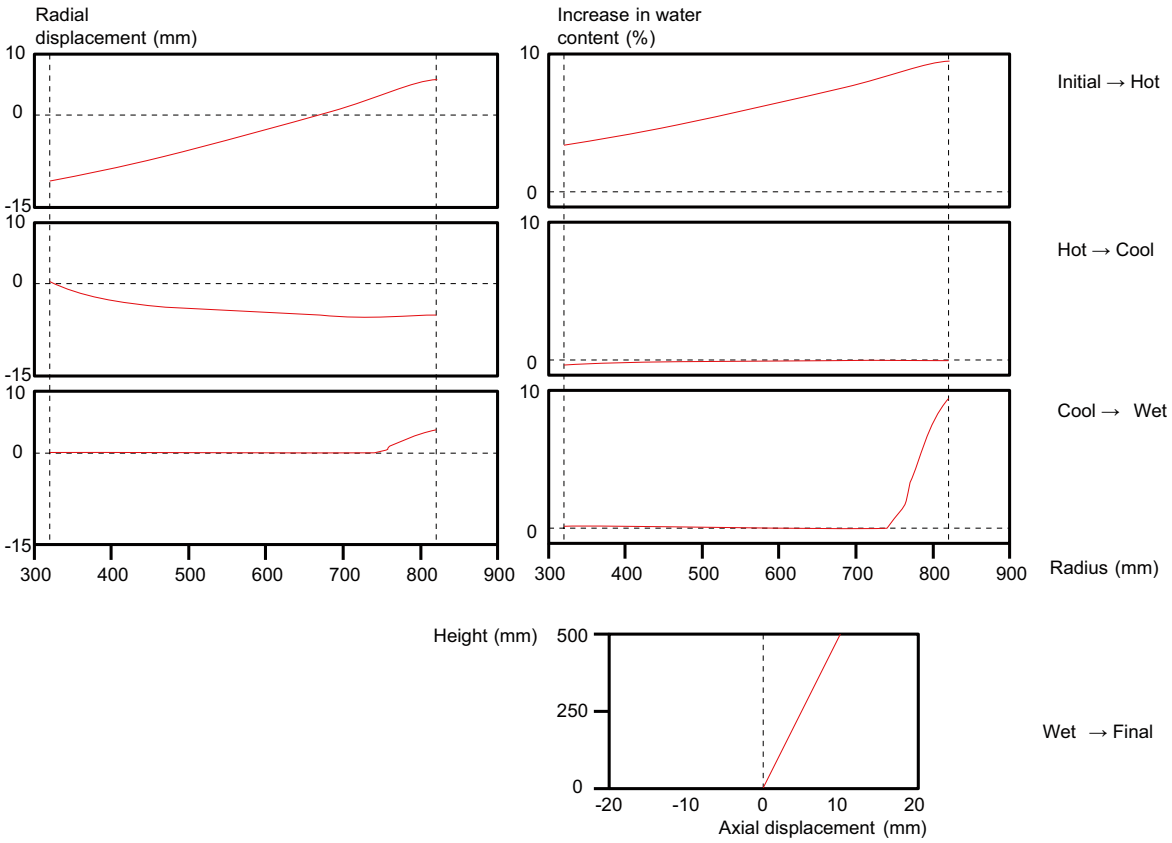

Figure 5-8. *Schematic outline of displacement fields and changes in water content during the transitions between different states.*

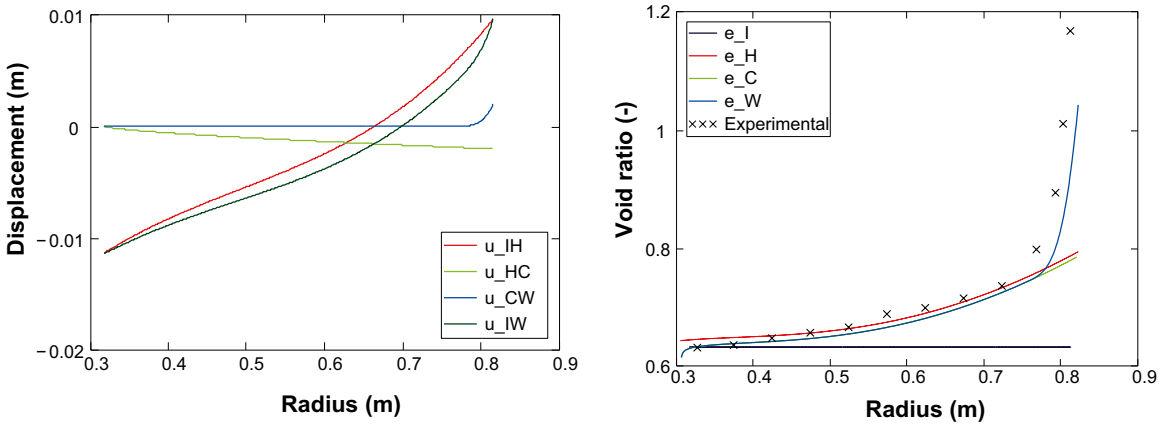

Figure 5-9. *Adopted displacement fields (left), and calculated void ratio profiles (right). Experimental data from Ring 4 evaluated as mean values for different radial intervals.*

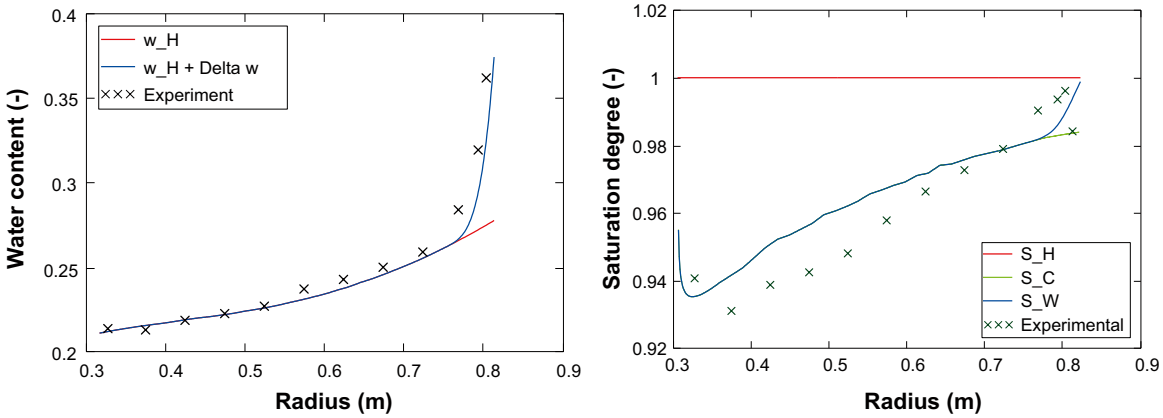

Figure 5-10. *Adopted water content profile and increase (left), and calculated saturation profiles (right). Experimental data from Ring 4 evaluated as mean values for different radial intervals.*

5.5 Effects of displacements on evaluated thermal conductivity values

The temperature profile in the lower package (R4) has been used to evaluate the evolution of the thermal conductivity (Goudarzi et al. 2010 and Figure 6-1, right). These evaluations have been based on the initial radius at installation of each thermocouple. However, all thermocouples have moved apart, since the bentonite has undergone swelling and radial displacement. It can therefore be assumed that the evaluated conductivities are underestimated.

Each thermal conductivity value is basically evaluated from two temperature readings, and is proportional to the factor $\ln(r_{out}/r_{in})$, where r_{out} and r_{in} are the radii of the outer and inner thermocouple, respectively. The ratio between a corrected and a directly evaluated conductivity value can be expressed as:

$$r_{corr} = \frac{\lambda_{corr}}{\lambda_{eval}} = \frac{\ln\left(\dfrac{r+\Delta r+u(r+\Delta r)}{r+u(r)}\right)}{\ln\left(\dfrac{r+\Delta r}{r}\right)} \qquad (5\text{-}13)$$

where r and r+Δr correspond to an inner and outer sensor radius, respectively, and where a displacement (u) is added to each radius for the corrected conductivity. For small values of Δr, this ratio can be simplified as:

$$r_{corr} = \frac{\ln\left(1+\dfrac{1+u'(r)}{r+u(r)}\cdot\Delta r\right)}{\ln\left(1+\dfrac{\Delta r}{r}\right)} = \frac{1+u'(r)}{1+\dfrac{u(r)}{r}} \qquad (5\text{-}14)$$

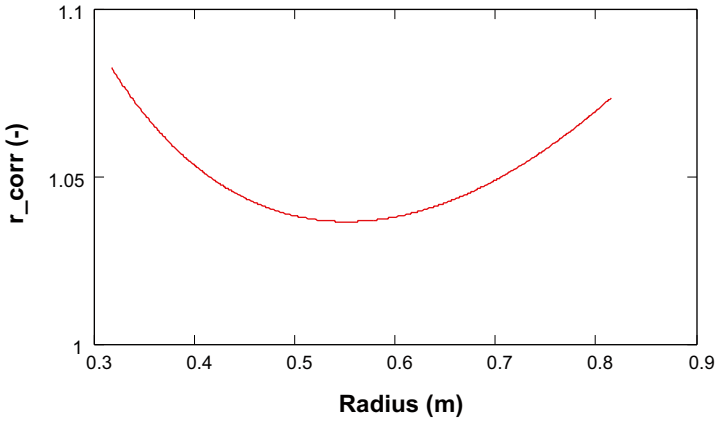

Figure 5-11. *Correction factor r_{corr} for different radii.*

This ratio can be readily calculated for the displacement field u_{IH} in Equation (5-6) and is shown in Figure 5-11. The corrected thermal conductivity values would thus be 4–8% higher than the evaluated values, which is negligible. It should be noted however that the main uncertainty of the conductivity values is related to the assumed heat flux which isn't addressed in this evaluation.

5.6 Interpretation of the saturation process

A relevant interpretation of the state of saturation is necessary for the process understanding and for the THM modelling, especially for the midsection around the lower heater. The experimental data can however be interpreted in different ways, and this therefore calls for a systematic evaluation.

A number of hypothetical saturation profiles are given in Figure 5-12. The left graphs show three different profiles of the final state, i.e. around day 2,200 and just before the termination of the heating. The right graphs shows two different types of progress of the saturation processes.

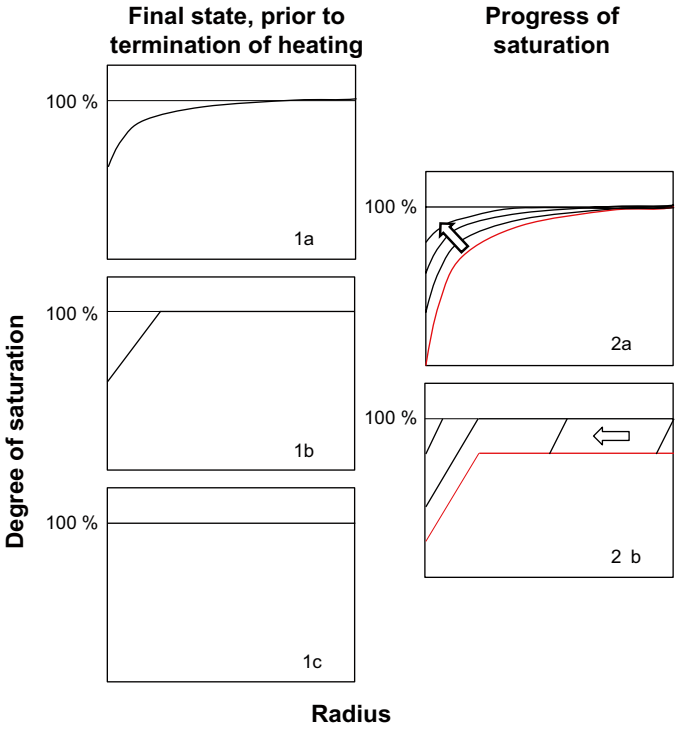

Figure 5-12. *Schematic illustration of different saturation profiles. Left column: alternative final states; right column: progress of saturation (red lines illustrate the profiles subsequent to the initial moisture redistribution).*

The two upper graphs (1a and 2a) illustrate a state and a saturation progress with smooth asymptotic saturation profiles. This type of behavior is quite typical for the behavior obtained with the standard THM models. The next two graphs (1b and 2b) show a state and saturation progress with a broken saturation profile, i.e. a saturation front, in which the outer part is water saturated whereas the inner part is unsaturated. The inner slope represents the saturation profile for a given vapor pressure (see section 6.3). The last graph (1c) shows a completely water saturated state, and this state can be reached irrespectively of the type of progress of saturation. These hypothetical profiles have been qualitatively compared with different sets of experimental data, and the results are summarized in Table 5-5 and Table 5-6. The different profiles have been graded for each set of experimental data of relevance. Two different grades have been made: supportive (+) and refutable (–). If no grade is given, this implies that the data is inconclusive for the profile, but that the profile still is possible.

Experimental saturation profiles

Measurements of density and water content after the dismantling operation have resulted in experimental saturation profiles (Johannesson 2010). These profiles show that the water saturation around the lower heater varied from 93–94% at the heater to 100% at the sand filter, and are very similar to the state 1a in Figure 5-12. In section 5.4 it was shown that the experimental data can be compatible with a totally saturated state (1c) if the thermal contraction of water is taken into account. The state 1c is therefore given a supportive grade. Still, a similar profile could possibly be expected for states 1a and 1b, if a water uptake took place during the dismantling operation, and these two states are thus regarded as possible.

Temperature profiles and thermal conductivities

The temperature profile around the lower heater just prior to the termination of the heating suggests that the thermal conductivity of the bentonite was quite high and homogenous at that time. This is illustrated by the evaluated thermal conductivity evolution presented by Goudarzi et al. (2010) (see Figure 6-1, right). This therefore supports the notion that the bentonite was water saturated in the final state (1c). Still, the possibility that some parts remained unsaturated (1a and 1b) should not be excluded, given the uncertainties of an evaluation of the thermal conductivity.

The evaluated conductivity evolution displayed a rapid decrease close to the heater surface during the first few months (before day 115). After this, the conductivity increased steadily until approx. half a year before the termination of the heating. This steady increase supports the notion of a steady rate of water uptake in the inner parts of the bentonite, which in turn supports the outlined saturation progress with smooth saturation profile (2a). In contrast, a saturation progress with a broken saturation profile (2b) should imply that the water uptake in the inner parts would be quite low until the outer parts had been filled up. Such a process is refuted by the evaluated conductivity evolution.

Table 5-5. Evaluation of hypothetical final states.

Observation	Smooth profile, 1a	Saturation front 1b	Saturation total, 1c
Measured saturation profile & thermal contraction			+
Temperature profile and conductivity			+
Pore pressures		+	
Rapid homogenous pore pressure response	+		
Filter pressures & local saturation vapor pressures			–
Increasing total pressures			–

Table 5-6. Evaluation of hypothetical types of progress of saturation.

Observation	Smooth profile, 2a	Saturation front, 2b
Temperature profile and conductivity	+	–
Pore pressure, filter pressures & local saturation vapor pressures	–	+
RH reading inner sensor	+	–
RH reading outer sensors	–	+

Pore pressures, filter pressures and saturated vapor pressures

The final pore pressure profile as recorded by the pore pressure sensor (see Figure 6-9) supports the notion of a broken saturation front (1b).

The increase in power output around day 1,700 was followed by a buildup of pore pressures at the three innermost sensor positions in Ring 3 (see Figure 6-5). The equilibration of these pressures to the same level, and the rate by which this equilibration occurred, suggest that a gas phase was involved in the process. This would support the notion of a widespread gas phase, which corresponds to a smooth saturation profile (1a). Still, the possibility that water saturated parts (as in 1c and outer parts of 1b) can transmit pore pressures at a high rate should not be excluded.

The level of the pore pressure in the sand filter can be compared with the local saturation vapor pressure, which is given by the temperature profile through the block (Figure 6-9). During the last 500 days the filter pressure corresponded to the saturation vapor pressure at a few centimeters from the heater surface. This would therefore refute the state with total water saturation (1c).

The evolution of the pore-pressure in Ring 3(see Figure 6-5) shows that sensors have responded at different times and display some minor correlation with the filter pressures. This behavior supports the notion of a discrete progressing saturation front (2b) and refutes a progress with a smooth saturation front.

Total pressures

Three total pressure sensors in Ring 3 (PB208, 212 and 213) displayed increasing values during the last 500 days (see Figure 5-13 and Figure 5-14), which implies that a water uptake still took place at that time. This would therefore refute the state 1c. The relatively low total pressures that were measured in the inner part of Ring 3 (see Figure 5-5 and Figure 5-6) can also be interpreted as the bentonite wasn't totally water saturated.

Relative humidity measurements

The results from the innermost RH sensor in Ring 4 (WB206) were quite fragmentary (see Figure 5-15), but from the recorded data the following observations can be made: At first the sensor displayed a rapid decrease down to 56% at day 139, after which no results were obtained until day 642 when it showed 62%. This level was sustained until day 860, when the tubing of a nearby pressure sensor (PB230) was cut and plugged, due to a leakage. After this the RH sensor showed a fairly rapid increase to 90% at day 1,138. After this, no more results were obtained. The distinct RH increase at day 860 can be interpreted as the vapor pressure were allowed to increase after a period during which is has been kept low (see Figure 6-21 right) as a result of the leakage nearby. It is therefore possible that the RH evolution at the same radius, but farther away from the leakage would have increased more rapidly. Such an evolution would thereby resemble the evolution of the thermal conductivity and therefore also support the smooth saturation progress (2a) and refutes a broken saturation progress (2b).

The results from the four RH sensors closest to the rock wall (i.e. for radii $\geq$ 560 mm) indicate that the relative humidity in these outer parts reached 100% before day 100 (Figure 6-3). These observations are discussed at length in section 6.3, in which it is shown that this very well can reflect a behavior where the moisture redistribution is limited due to particular water retention properties. The water saturation would thereby be limited to a level between the initial saturation degree and water saturated conditions. This would thereby support the broken saturation progress (2b) and refutes a smooth saturation progress (2a).

Summary

The analysis is apparently non-conclusive, since all alternatives can be supported and in many cases refuted by the experimental data (see Table 5-5 and Table 5-6).

Still, it appears to be clear that the bentonite wasn´t totally water saturated during the final state, given the evidence by the different pressures (filter pressure, local saturated vapor pressure, pore pressures and total pressure. This would mean that either 1a or 1b would be true.

It can also be noted, that the only evidence against a broken saturation progress (2b) are based on: i) one RH-sensor, which was clearly affected by a leakage, and ii) the evaluated thermal conductivity evolution which suggests that the re-saturation of the innermost part began already after a few months. In contrast, the evidence that supports a broken saturation progress are based on: i) approx. four RH-sensors which displayed a behavior which has also been observed in independent tests (see Figure 6-6), and ii) the data from pore pressures sensors, which evidently has shown to be reliable according to the sensor function control. The broken saturation profiles (1b and 2b) therefore appear to be the most plausible interpretation.

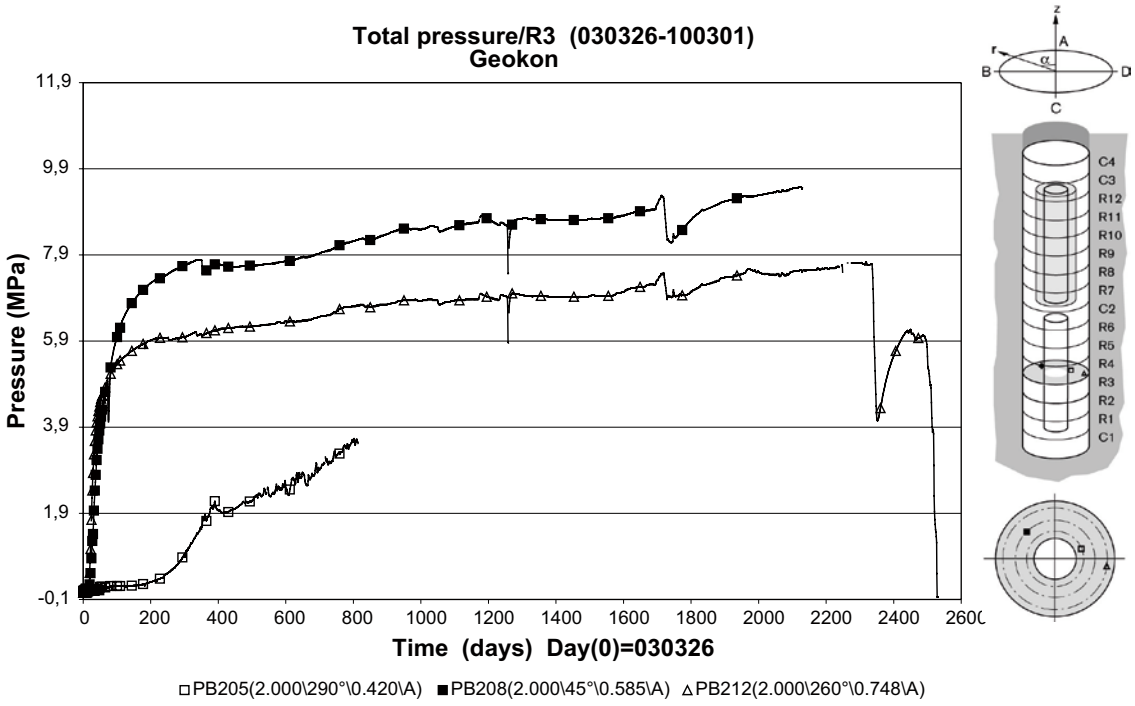

Figure 5-13. *Evolution of axial total pressures in Ring 3 (from Goudarzi et al. 2010).*

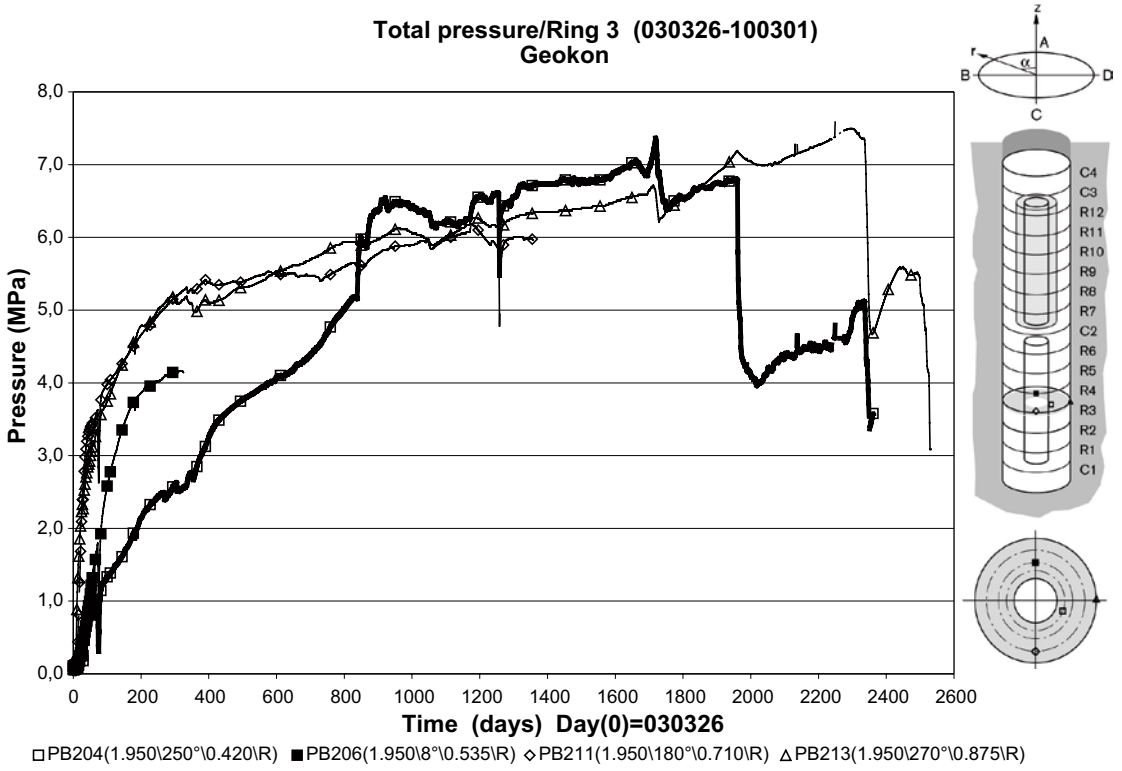

Figure 5-14. *Evolution of radial total pressures in Ring 3 (from Goudarzi et al. 2010).*

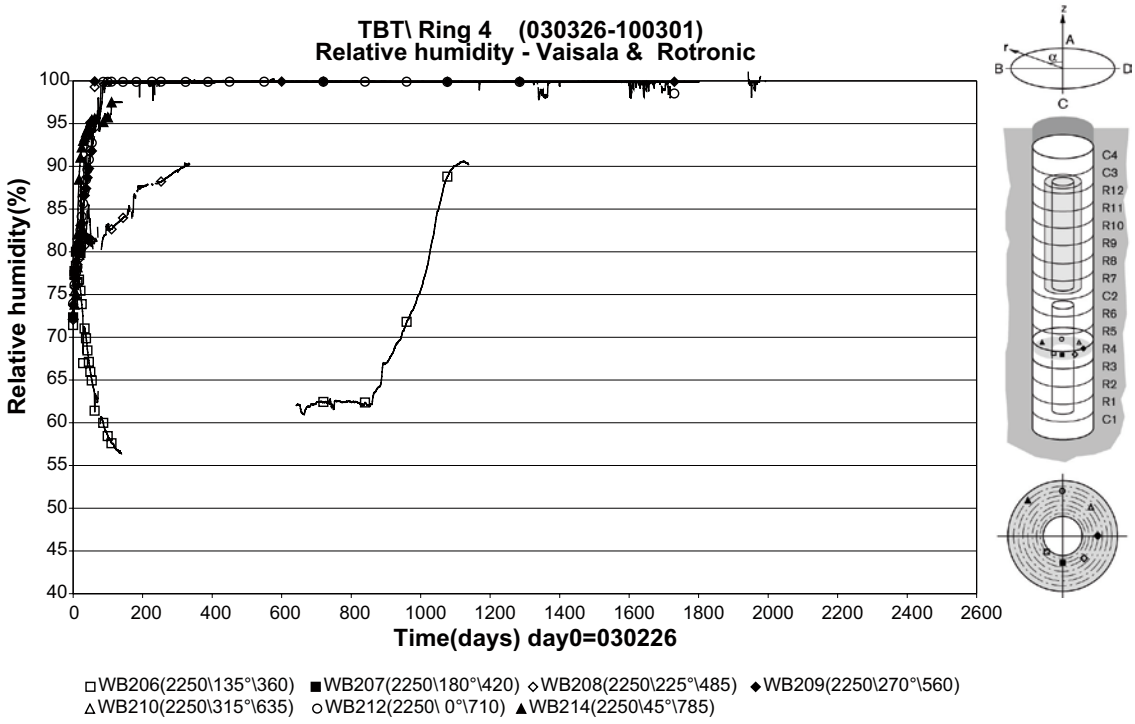

Figure 5-15. *Evolution of relative humidity in Ring 4 (from Goudarzi et al. 2010).*

5.7 Conclusions

The following conclusions can be made from the presented evaluations:

- The void ratio profiles measured during the dismantling are for several blocks (10 out of 16) consistent with the dry density of the blocks after compaction (relative error ≤ 1%), if the initial block heights as well as the results from the leveling at installation and dismantling are considered. Discrepancies can be caused by fractures through the blocks, and swelling of blocks during the dismantling. The relative changes of dry masses per unit height were used together with the leveling results to estimate the axial displacement field before the unloading of the lid.
- The void ratio profiles measured during the dismantling and the final total pressure readings are generally consistent with current swelling pressure curves. The final pressures in Ring 3, especially for the innermost sensor, are however slightly lower than swelling pressure curves. An explanation for this could be that the inner part wasn't totally water saturated at the end of the test, or it could be an indication that the properties of the bentonite had changed.
- The calculation indicates the measured saturation profile could be caused by the thermal contraction of water if the bentonite was water saturated prior to the termination of the heating. The temperature dependence of the water density was directly taken into account in the evaluation without the adoption of any specific thermal expansion value. Still, the possibility to reach the final saturation profile through an alternative route should not be excluded. The defined displacement fields and changes in water contents for the transitions between different states provides a means to explain the void ratio profiles measured during the dismantling.
- The radial displacements in Ring 4 imply that the evaluated thermal conductivity values are underestimated. The presented calculation shows that a correction would yield values approx 4–8% higher than the evaluated values. It should be noted that the main uncertainty of the conductivity values is related to the heat flux which isn't addressed in this evaluation.
- Different experimental observations from the mid-section around the lower heater have been identified as either supportive or refutable to alternative hypothetical final states and types of progress of saturation, with either smooth or broken profiles. The analysis is apparently non-conclusive, since all alternatives can be supported and in many cases refuted by the experimental data. Still, it appears to be clear that the bentonite wasn´t totally water saturated during the final state. Moreover, by assessing different experimental data it appears that the most plausible interpretation would be that the progress of saturation would be characterized by a broken saturation front.

6 Validity of the material models

6.1 Introduction

The reproduction of the experimental data from the TBT experiment constitutes a great challenge for the current material models. This chapter describes what lessons can be learnt from the modelling tasks presented in this report, and is thereby an assessment of the validity of the material models. This notion encompasses the diverse components such as chosen constitutive laws, adopted parameter values and code features, such as friction elements.

One means to evaluate the material models is through comparison of model results with experimental data, i.e. ability to reproduce evolutions of temperature, RH and total pressure, and the final distributions of degree of salutation and void ratio. The outline of the presentation basically follows the different parts of the material model which are of relevance for the TBT experiment:

- The thermal model, i.e. the thermal conductivity.
- The thermo-hydraulic model, i.e. the two flow coefficients and the retention properties.
- The mechanical model and especially the plastic model.
- The thermal expansion of water, which currently is a constant in the used codes.
- The gas transport, and the significance of its inclusion.
- The sand compressibility.
- The friction along the rock wall.

The comparisons of model results with experimental data are primarily presented by the modelling teams in the respective chapters, i.e. Chapter 2, 3, and 4. The ambition has been to address these comparisons in the different sections of this chapter, and also to summarize the findings in the conclusion at the end of the chapter.

A rigorous comparison of the different model contributions has been considered to be of limited value. For instance, the presented models have not been blind predictions, but rather evaluations in which the modelling teams during the course of this work have tried different approaches and adaptations in the material models, at least to some extent. The evaluations presented in this chapter aim at the core of the different constitutive laws: what they can do, and what their limitations are. The discussion has focused on the ClayTech's CODE_BRIGHT contribution in particular. The reason for this is to some extent that the main author has largely been responsible for the adoption of this material model (see the data qualification for the SR-Site (Åkesson et al. 2010b)), and therefore has the most insight into the capabilities of it. Nevertheless, all contributions are referred to, especially at the end of the chapter.

Due to the nature of the process in question, the lessons that can be learnt tend to vary in character. For some cases, such as parts of the mechanical model, the lessons can be directly applicable, while for others, such as the gas transport, the lesson is limited to general observations of the problem. Finally, for some processes (such as the thermo-hydraulic model) there is an apparent need for further investigations of the fundamental mechanisms.

6.2 Thermal model

The most important parameter of the thermal model for the TBT experiment is the thermal conductivity, especially for the bentonite blocks and the sand-filled slots. The specific heat is another parameter of the thermal model, although the processes are quite insensitive to the value of this parameter for the bentonite and the sand. It is therefore not considered in this evaluation. It should be noted however that the conductivity as well as the specific heat for the rock influence the temperature at the wall of the deposition hole.

For compacted MX-80, the thermal conductivity displays a dependence of the degree of saturation, as well as the void ratio. Independent measurements of thermal conductivity are shown in Figure 6-1 (left) together with a number of adopted functions of the degree of saturation, among which the Relation 3 has been used in the numerical models. These functions are apparently relevant, since the calculated temperatures profiles in general show good agreement with measured profiles (see ClayTech CODE_BRIGHT contribution in Figure 3-10, Figure 3-41 and Figure 3-42). Similar results were found by the other teams. However, the ABAQUS model under-predicted the temperatures, especially in the inner parts (see Figure 4-8 and Figure 4-11), while some of the UPC CODE_BRIGHT models over-predicted the temperatures in the peripheral parts of the lower package (see Figure 2-6 and Figure 2-11). Still, these deviations appear to be caused by the geometry and boundary conditions, rather than by limitations in the material model.

A more direct indication of the relevance of the thermal model can be gained through an evaluation of the thermal conductivity from the readings of the thermocouples in Ring 4 (see Figure 6-1, right). Values are presented as evolutions at six different distances from the heater surface. It can be noted that all points outside a radius of 460 mm display conductivity values between 1.1 and 1.3 W/mK, whereas the conductivity at the innermost point (radius 340 mm) dropped to 0.5–0.6 W/mK at an early stage, after which it increased steadily during the test period to 1.1–1.2 W/mK. This suggests that the inner part, within approx. 0.1 m from the heater, was dehydrated at the beginning of the test, and that the saturation degree close to the heater decreased significantly. According to the independent conductivity measurements (Figure 6-1, left graph), the lowest saturation degree could very well be in the order of 20–30%. Such levels have also been found in the numerical models (see Chapter 3).

The thermal conductivity of the sand has had some influence on the thermal processes in TBT, especially in the shield around the upper heater. The shield remained virtually dry until the filling of this part with water, and this operation started day 1,505. The external temperature of the upper heater displayed a significant decrease from the beginning of the test (166°C at day 60) to the 1,500/1,600 W increase of power output (144°C at day 1,012). In order to reproduce this temperature decrease it is necessary to increase the thermal conductivity. Such a conductivity increase cannot however be caused by any increase in the degree of saturation since the shield remained dry during this period. In one of the model contributions (Chapter 3), the conductivity was increased manually from 0.6 to 0.8 W/mK, in order to mimic the measured temperature evolution. Such a conductivity increase can possibly be caused by the compression of the sand shield.

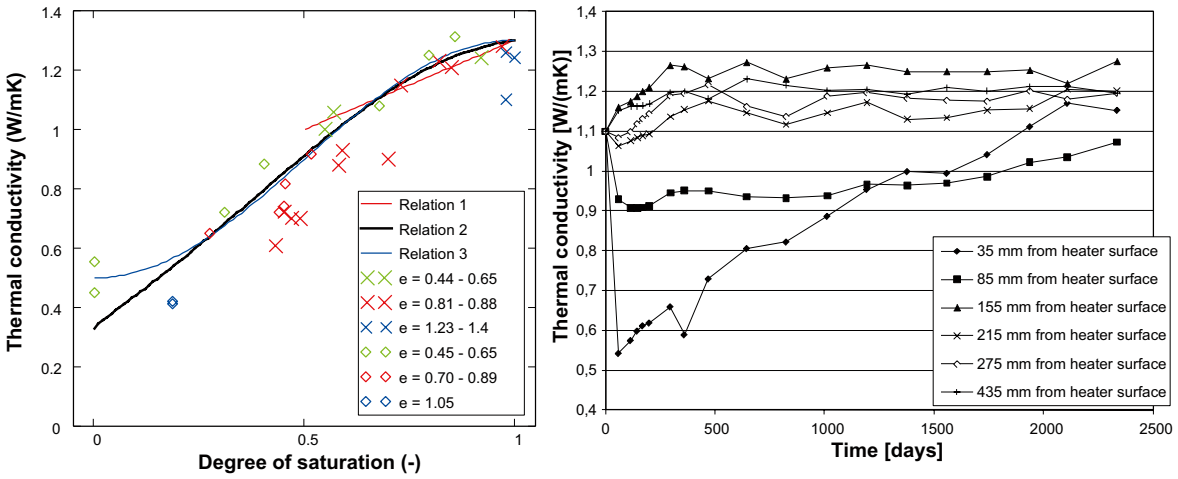

Figure 6-1. *Thermal conductivity of MX-80 bentonite. Left: independent measurements and adopted functions, from Åkesson et al. 2010b. Right: evaluated values from Ring 4 in TBT (from Goudarzi et al. 2010).*

The following saturation and porosity dependent function for the thermal conductivity was reported by Börgesson et al. (1994):

$$\lambda = \lambda_s^{1-n} \cdot \lambda_w^{n \cdot Sr} \cdot \lambda_a^{n \cdot (1-S_r)} \quad (6\text{-}1)$$

where λ is the thermal conductivity, n is the porosity and S_r is the saturation degree. The indices s, w and a denote solids, water and air, respectively. If the material is dry, i.e. S_r=0, then the expression can be simplified as:

$$\lambda = \lambda_s^{1-n} \cdot \lambda_a^{n \cdot} \quad (6\text{-}2)$$

Börgesson et al. (1994) states that the value for λ_s and λ_a is 2.6 and 0.024 W/mK, respectively. The function and the parameter values were adopted from a study on the French natural clay Fo-Ca. The value of 2.6 W/mK was stated to coincide well with what is considered to be an average of soil minerals containing an insignificant amount of quartz.

This model has been tested for a case which corresponds to the sand shield. The porosity of the shield is treated as a function of the sand-bentonite interface radius (Figure 6-2), and the thermal conductivity is in turn calculated from the porosity. The initial radius of the sand/bentonite (at 535 mm) corresponds to a conductivity of 0.6 W/mK, whereas a 15 mm radial displacement towards the heater would yield a conductivity value of 0.8 W/mK. This exercise therefore supports the values used in the model, although the highest value (0.8 W/mK) corresponds to a density of 1,980 kg/m^3, which appears to be a bit high in comparison to independent compression tests (see section 6.7).

6.3 Thermo-hydraulic model

General

The resaturation of the bentonite is mainly a thermo-hydraulic problem, and this process is in the model basically determined by the two flow coefficient (permeability/hydraulic conductivity and vapour diffusivity) and the retention properties.

The models can to some extent mimic the experimental results with independently determined parameter values. The agreement is fairly good for the conditions around the upper heater with moderate temperatures (UPC CODE_BRIGHT contribution: Figure 2-26 and Figure 2-27; ClayTech CODE_BRIGHT contribution: Figure 3-33; and ClayTech ABAQUS contribution Figure 4-18). Some discrepancies are however noticeable for the conditions around the lower heater with very high temperatures. The CODE_BRIGHT models tended to exaggerate the dehydration and delay the re-saturation process

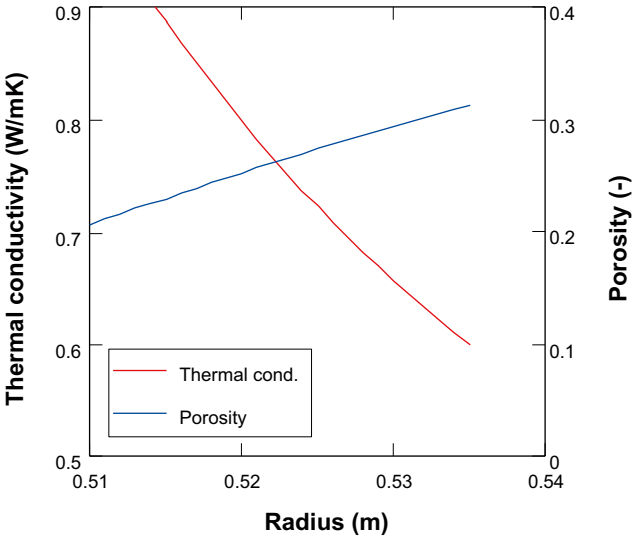

Figure 6-2. *Porosity and thermal conductivity of sand in shield as function of sand/bentonite interface position.*

(e.g. UPC CODE_BRIGHT contribution: Figure 2-12 and Figure 2-13; ClayTech CODE_BRIGHT contribution: Figure 3-33, Figure 3-11 and Figure 3-16). The ClayTech ABAQUS contribution did not exhibit any exaggerated dehydration, at least not according to the final saturation profile (Figure 4-19).

Still, all modelling teams found that the use of standard values for vapour diffusivity tended to over-estimate the extent and rate of the dehydration in hot parts, and that the agreement could be improved by using lower values (see sections 2.2.3, 3.4.1 and 4.3.2). It was also found that an independent determined intrinsic permeability value tended to delay the hydration, and that the agreement could be improved by using higher values (see section 3.3.9). Such an increase could very well be motivated given the uncertainty of the measured hydraulic conductivities at the dry density in question. The resaturation process is sensitive to the used retention curve and some parameter variations have therefore been performed, basically by varying the slope of the curve on the wet and the dry side of the initial point, respectively. Some improvements can be obtained in this way (see sections 2.2.3 and 3.3.9), although it is uncertain if any new information can be gained by this type of variations.

Two characteristic results which to some extent have occurred around both heaters, but in particular around the lower heater, are generally not captured by the models: the early evolution of relative humidity during the first 100 days (Figure 6-3), and the occurrence of pore pressures (Figure 6-4 and Figure 6-5). The implications of these two observations are discussed below.

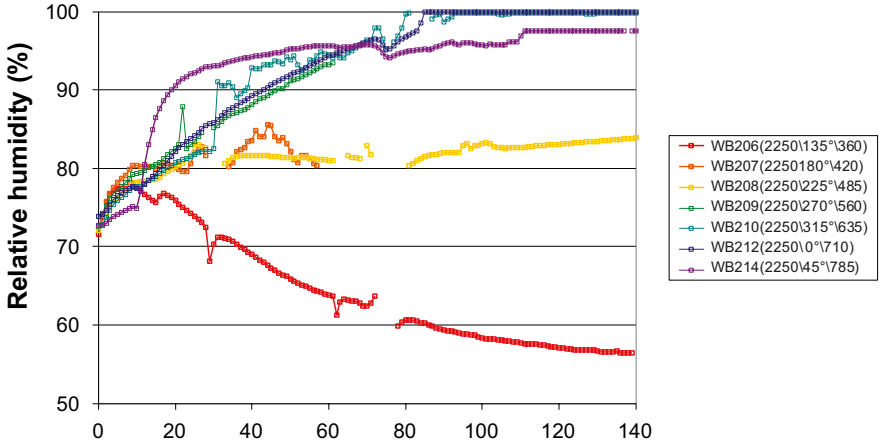

Figure 6-3. *Early evolution of relative humidity in Ring 4.*

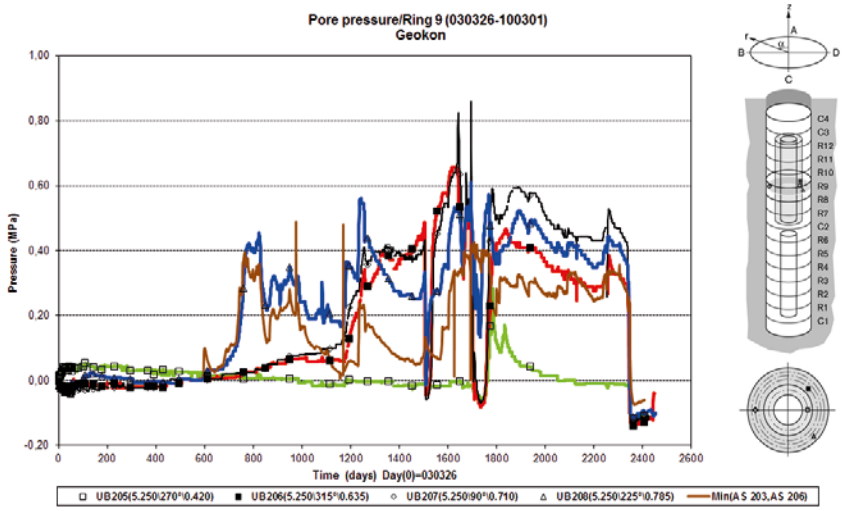

Figure 6-4. *Evolution of pore pressure in Ring 9 and filter pressure (from Goudarzi et al. 2010).*

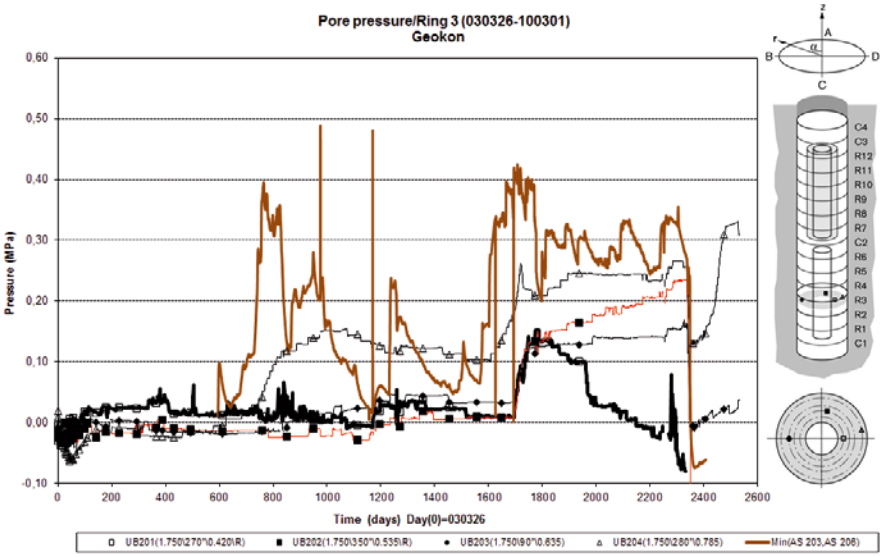

Figure 6-5. *Evolution of pore pressure in Ring 3 and filter pressure (from Goudarzi et al. 2010).*

RH evolution

The early evolution of relative humidity in Ring 4 is consistently not captured by the models. The four capacitive sensors closest to the rock wall (i.e. for radii ≥ 560 mm) indicate that the relative humidity in these outer parts reached 100% before day 100 (Figure 6-3). It should be noted that some exception and uncertainties exist:

i. the outermost RH-sensors at 785 mm radius showed 96%.

ii. the sensor at 560 mm radius didn't show any results between day 61 and day 177, at which times the sensor showed 93 and 100%, respectively.

iii. two of the capacitive sensors were of the Rotronic type, whereas the other two were of Vaisala type. These types of sensors generally exhibited a function outside the stated specifications during the sensor function control performed subsequently to the dismantling (see Goudarzi et al. 2010). This should however not discredit the data from the initial phase, considering the succeeding exposure of heat and water pressure on these sensors.

If the observed evolution on the other hand was correct, then this would imply that the outer parts would be water saturated at day 100, given that the standard retention curves also are correct. This would either mean that a significant volume of water had to be taken up from the filter, or it would mean that this water volume had been distributed from the inner part. In the latter case this would imply that the inner part would be extensively dehydrated. Some water uptake had surely occurred at day 100, but it appears to be unlikely that such a process could have water saturated all bentonite in the outer 250 mm annulus at that time.

An alternative explanation can be sought by modifying the retention curve in such a way that the suction is reduced almost completely at some water content between the initial content and water saturated conditions. A similar type of behavior was observed in the TBT_3 mock-up, and in the modelling of this experiment it was found that this type of curve was required in order to reproduce the experimental results as closely as possible (Åkesson 2008), see Figure 6-6 and Figure 6-7. This was also the approach for the models presented by the UPC CODE_BRIGHT team in section 2.2 of this report.

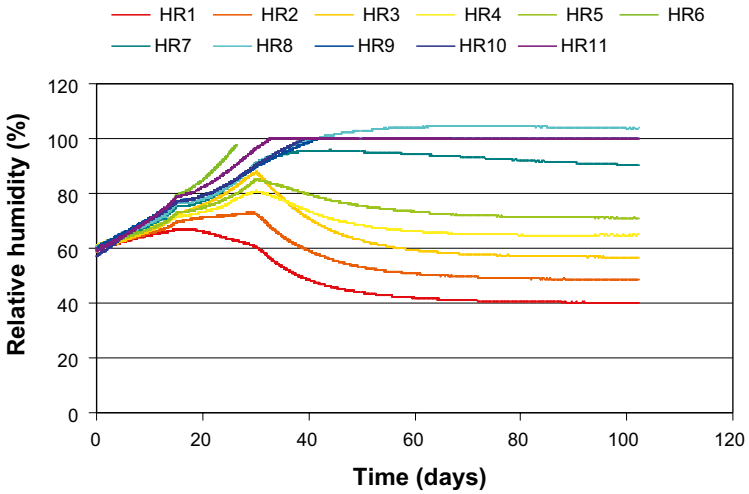

Figure 6-6. *Evolution of relative humidity in TBT_3 (from Åkesson 2008).*

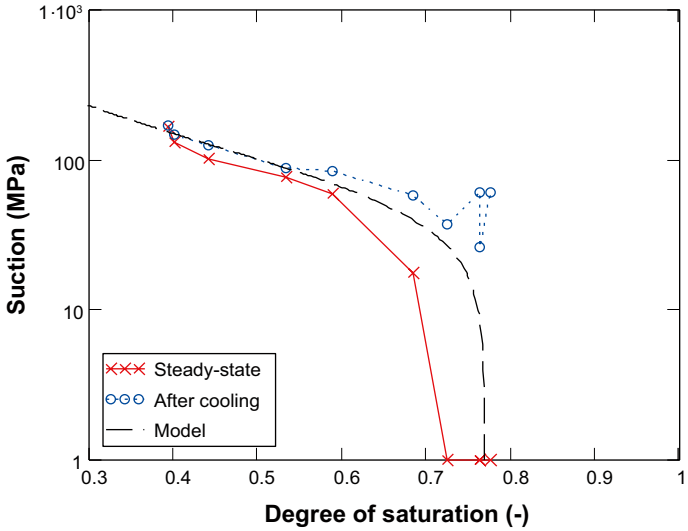

Figure 6-7. *Evaluated in situ retention curve of TBT_3 (from Åkesson 2008).*

Results from simple analytical calculations of moisture redistribution are shown in Figure 6-8. These are based on the following assumptions:

i) Radial heat flow with constant thermal conductivity. This implies a logarithmic temperature distribution:

$$T(r) = 135 + 71.6 \cdot \ln\left(\frac{0.305}{r}\right) \quad (^{\circ}C) \tag{6-3}$$

ii) Equilibration of a homogenous vapor pressure (p_v), not exceeding the local saturated vapor pressure, which implies a relative humidity (RH) distribution. This condition corresponds to a case with no advective liquid flow. This is an efficient simplification for illustrating the effect of the retention curve, although it is not consistent with the material models:

$$\mathrm{RH}(r, p_v) = \min\left[\frac{p_v}{p_{sat}(T(r))}, 1\right] \tag{6-4}$$

p_{sat}(T) is the saturated vapor pressure and follows the implemented function in CODE_BRIGHT.

iii) The porosity and the total water volume are assumed to be constant:

$$\int_{r_i}^{r_o} r \cdot \theta(s(r, p_v)) \cdot dr = \int_{r_i}^{r_o} r \cdot \theta_{init} \cdot dr \tag{6-5}$$

$\theta(s)$ is a retention curve i.e. degree of water saturation (θ) as a function of suction (s). The latter is calculated with Kelvin's law. θ_{init} is the initial saturation (= 0.755). r_i and r_o is 0.305 and 0.820, respectively. An equilibrated vapor pressure can thus be derived for a specified retention curve.

Two cases are shown in Figure 6-8: one with a conventional retention curve (θ_1 in Equation (6-6 which is of a Fredlund type), and one composite curve (θ_3 below) with identical properties below θ_{init}, but with extensive suction reduction above θ_{init} and with zero suction for $\theta \geq 0.84$.

$$\begin{cases} \theta_1(s) = \left(1 - \dfrac{\ln\left(1+\dfrac{s}{6.7}\right)}{\ln\left(1+\dfrac{10^6}{6.7}\right)}\right) \cdot \left(\ln\left(e + \left(\dfrac{s}{139.44}\right)^{1.97}\right)\right)^{-2.28} \\ \theta_2(s) = 0.2 \cdot \exp(-2 \cdot s) + 0.8 \cdot \exp(-s/794) \\ \theta_3(s) = \min\left[0.84, \dfrac{\theta_1(s)}{1+\exp(46-s)} + \dfrac{\theta_2(s)}{1+\exp(s-46)}\right] \end{cases} \quad (6\text{-}6)$$

The effect of this modification is illustrated by the saturation profiles. The limitation of the saturation to 0.84, implies a higher equilibrated vapor pressure (1.0 bar instead of 0.6 bar) and a less extensive dehydration in the hot part. The comparison of RH profiles with experimental data illustrates the consistency of the results.

Pore pressures

The sensor function control, see Goudarzi et al. (2010), showed that the investigated Geocon pore pressure sensors in general showed correct output signals after the dismantling operation and therefore appeared to be quite reliable. The data from the pore pressure sensors (Figure 6-4 and Figure 6-5) should therefore be regarded as basically correct.

Significant measured pore pressures were first observed around day 700–800, a period which coincided with relatively high filter pressures. The outermost sensors (at 785 mm radii) in Ring 9 as well as in Ring 3 responded at that time. In Ring 9, the registered pore pressure was highly correlated with the filter pressure. In contrast, the pore pressure in Ring 3 was lower and displayed a more stable trend.

A second event with beginning responses from the pore pressure sensors occurred concurrently with the general increase of the power output (1,500 → 1,600 W), at day 1,171. At this time the two additional sensors in Ring 9 (at 635 and 710 mm radii) began to display trends correlated with the filter pressure, although at a higher level.

A third response occurred at the same time as the major increase in power output (1,600→ 2,000 W), at around day 1,700. At that time the three additional sensors in Ring 3 (at 420, 535 and 635 mm radii) began to display significant levels, although with different trends.

The sensors data thus clearly shows that pore pressures have occurred at various times during the test period. It is however unclear if this pore pressure, especially in Ring 3, has been caused by water or gas. For instance, the buildup of pore pressure in Ring 3 around day 700–800 coincides with increasing vapor pressures evaluated from RH-sensor readings in the inner part of Ring 4 (see Figure 6-21, right graph). This vapor pressure buildup indicates that the lower package was gas tight at that time.

The bentonite around the upper heater was however not gas tight at that time, as was shown by the subsequent shield hydration operation. The pore pressure readings from Ring 9 thus appear to be caused by water. The high correlation between pore pressures and filter pressures supports this notion.

Some of the pore pressure responses coincide with increasing temperatures, and this could very well be caused by water that expands and thus fills up the local remaining pore space. An alternative explanation could be that increasing temperature leads to increasing vapor pressures. This is however not a likely explanation for the conditions in Ring 9 in which the temperature never exceeded 100°C, and where the vapor pressure thereby never could yield any positive relative pressure.

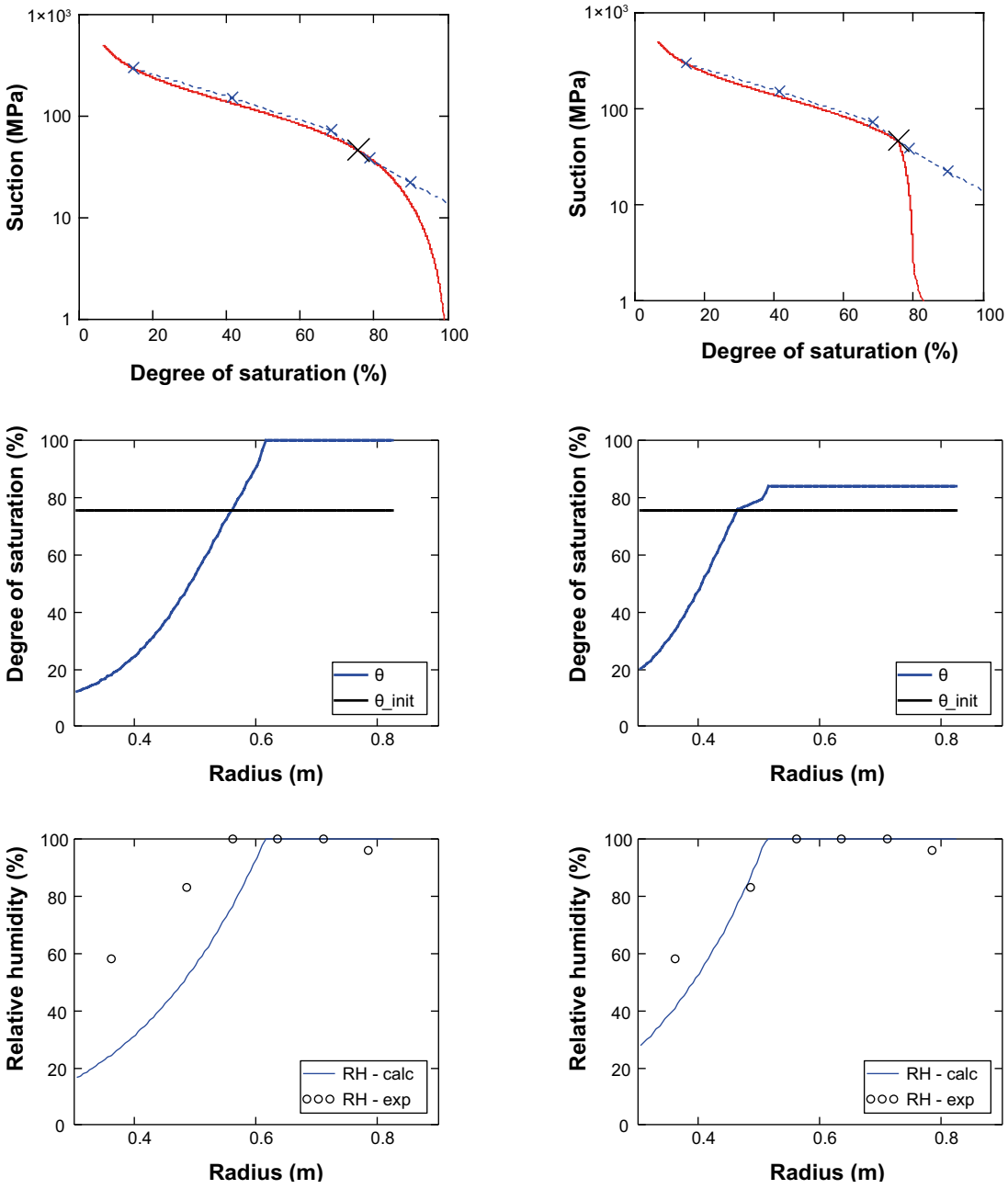

Figure 6-8. *Axisymmetric 1D analytical calculation for a thermal condition with constant conductivity resulting in a temperature profile with 135 and 64°C at inner and outer radius, respectively. Left graphs show steady-state conditions with conventional retention curve and homogenous vapor pressure of 0.6 bar. Right graph shows results for a retention curve with maximum saturation at 0.84, in which the homogenous vapor pressure is 1.0 bar.*

For the conditions in Ring 3 however, some results indicate that the vapor pressure explanation can be plausible. Figure 6-9 shows the temperature profile in Ring 4 just before the termination of the heaters at day 2,335 and the corresponding saturation vapor pressure profile. It should be noted that the pressure are shown as relative pressure and the zero value thus corresponds with 100°C at a radius of 0.62 m. Pore pressure profiles as registered by the pore pressure sensors and in the sand filter are marked for day 1,700, i.e. just subsequent to the major power increase, and for day 2,300. The filter pressures were approx. 3 bar during period, and 0.6 bar has been added to this value due to the height difference between Ring 3 and the pressure sensors in the tunnel. The pore pressure level at the three innermost sensors in the first profile (1.3 bar) coincides approximately with the local saturation vapor pressure at the innermost sensor position at 420 mm radius. It therefore appears to be probable that the pore pressure level was governed by the hydration condition at the innermost

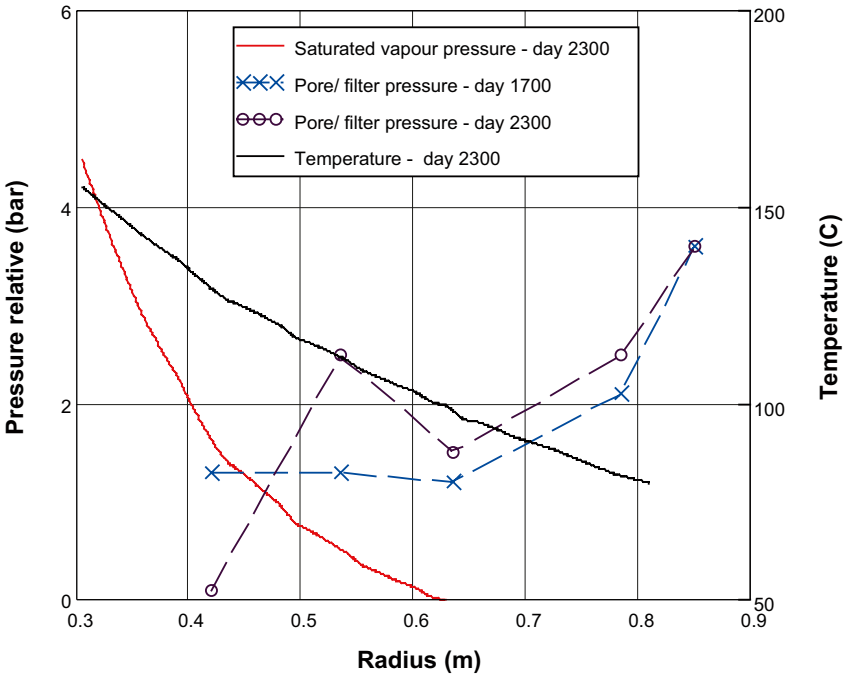

Figure 6-9. *Profiles of temperature (solid black line) and saturated vapor pressure (solid red line) for day 2,300. Pore pressure and filter pressure measurements at day 1,700 (blue symbols) and day 2,300 (black symbols).*

sensor position at that time. The rapid equilibration and quite even pressure profile could suggest that gas transport was possible at that time, which would indicated that the bentonite at far out as a radius of 635 mm was not water saturated. Still, this would also mean that the vapor was supersaturated outside the 420 mm radius. From the time of the power increase (day 1,700) until the termination of the heaters (day 2,300) the pore pressure at the innermost sensor position decreased, which indicates that the bentonite dehydrated during that period. In contrast, the pore pressure at the two other sensor positions (535 and 635 mm radius) increased and thereby exceeded the local saturated vapor pressure significantly, which suggest that the bentonite reached water saturation during that period. This would suggest the presence of a *water saturation front* at some position between 420 and 535 mm radius.

The notion of a stable water saturation front appears to have one lesson for the adoption of water retention curves. The problem is illustrated in Figure 6-10 in which a saturation front is schematically outlined. Two moisture fluxes are usually present in two-phase flow models (e.g. CODE_BRIGHT) of unsaturated conditions: suction gradient driven liquid flux (q_w); and vapor mass fraction gradient driven vapor diffusion (j_g^w). And these two fluxes should also be present on the unsaturated side of a saturation front. The material model states that the vapor flux is proportional to the degree of gas saturation ($1–S_l$), which implies that the vapor flux is reduced to zero at the position of the saturation front:

$$j_g^w \propto (1-S_l)\cdot\nabla\varpi_g^w \rightarrow 0 \qquad (6\text{-}7)$$

If the saturation front is stable, then the total moisture flux ($j_g^w + q_w$) is zero, which means that the liquid flux as well as the pressure gradient is zero:

$$q_w \propto S_l^3\cdot\nabla P_l \propto \frac{dP_l}{dS_l}\cdot\nabla S_l \rightarrow 0 \qquad (6\text{-}8)$$

A saturation front implies however that the saturation gradient (∇S_l) is non-zero, and this in turn implies that the derivative of the retention curve (dP_l/dS_l) is zero close to the point of saturation ($S_l=1$). Such a slope is usually not implemented in the standard material models.

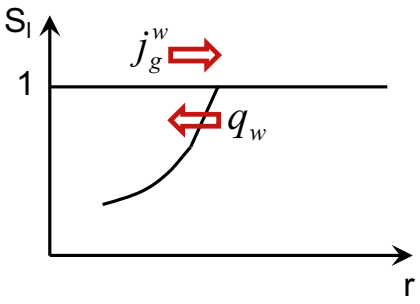

Figure 6-10. *Schematic saturation profile for a stable water saturation front and associated moisture fluxes.*

Final remarks on the thermo-hydraulic models

Some of the experimental results from TBT display behaviours that are usually not captured by the standard material models. The evaluation above gives some indications how the model possible could be improved, in this case through modification of the water retention curve. The relevance of the flow coefficients (the relative permeability and the vapour diffusivity) and their dependence of the water saturation were previously discussed in the TBT_3 modelling report (Åkesson 2008).

It has however been outside the scope of TBT to pursue any tests of these indications by trying to formulate new functions for the different constitutive law. The value of such attempts is probably of limited value, since this would basically mean that the material models would be tailored to the experiment in question. Instead it is suggested that the fundamental mechanisms behind the thermo-hydraulic processes are investigated in the future, in order to have a foundation for supporting or possibly refining the different constitutive laws and parameters values.

6.4 Mechanical model

General

The mechanical model has in general not reached the same level of development and consensus as the thermo-hydraulic model discussed in the previous sections. In the modelling of TBT, at least four quite different models have been used:

i. ABAQUS, with porous-elastic model, Drucker-Prager and moisture-swelling.
ii. CODE_BRIGHT, with standard BBM.
iii. CODE_BRIGHT, with BBM with void ratio dependent kappa_s-function.
iv. CODE_BRIGHT, with BExM.

General evolution of stresses has been fairly well mimicked by the ABAQUS contribution (Figure 4-26). The void ratios around upper heater (Figure 4-22), as well as the cable forces (Figure 4-29) and the lid displacements (Figure 4-28) were also well reproduced.

The CODE_BRIGHT models presented by UPC (using standard BBM or BExM) showed that the general evolution of stresses could be fairly well mimicked (Figure 2-9 and Figure 2-39), although the deviatoric stresses around the upper heater were under-predicted (Figure 2-28). The final dry-density distribution around the lower heater could also be fairly well reproduced (Figure 2-10).

The third model, presented by the ClayTech CODE_BRIGHT team also showed that the general evolution of stresses could be fairly well mimicked (Figure 3-18 to Figure 3-20, Figure 3-26, Figure 3-27 and Figure 3-31), and that the final void ratio distributions could be fairly well reproduced (Figure 3-22 and Figure 3-32). This model is in this section chosen for an in-depth evaluation, basically since the main author has largely been responsible for the adoption of this material model and therefore has the most insight into the capabilities of it. Still, it should also be mentioned that this approach constitutes the only attempt to develop a general and clear-cut strategy to quantify the mechanical parameters for all relevant dry-densities in a KBS-3 concept (Åkesson et al. 2010b). A scheme for this strategy is shown in Figure 6-11, and the approach for the determination of the parameters which defines the yield surface is illustrated in Figure 6-12.

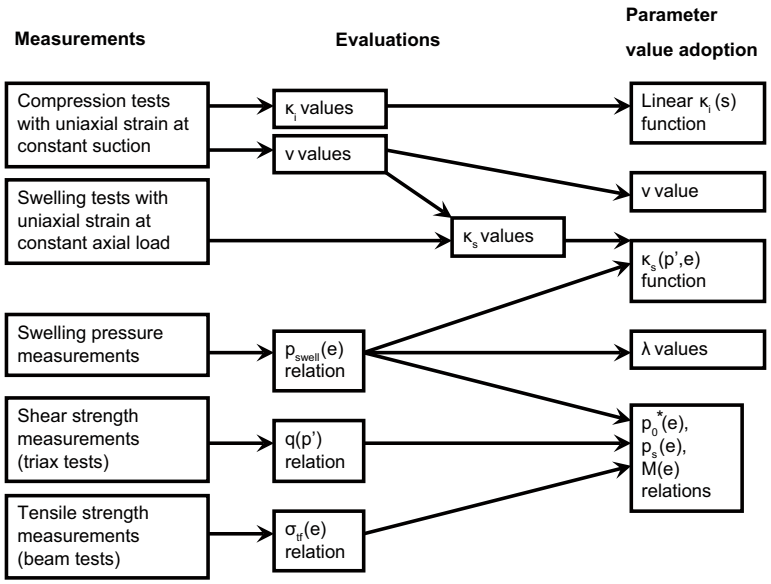

Figure 6-11. *Strategy for adoption of mechanical parameter values (from Åkesson et al. 2010b).*

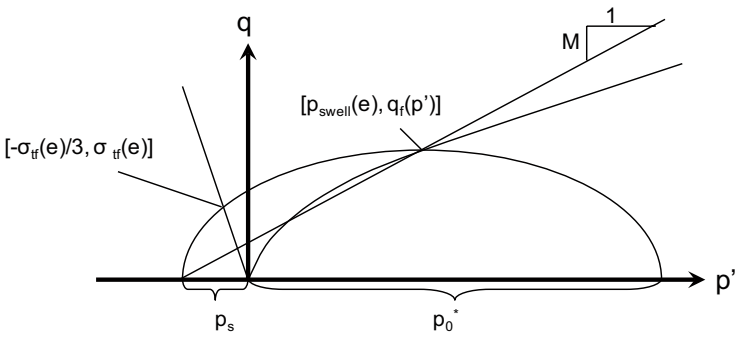

Figure 6-12. *Determination of plastic parameters p_s, p_0^* and M from shear strength relation and void ratio dependences of swelling pressure and tensile strength (from Åkesson et al. 2010b).*

Swelling pressure

The chosen swelling pressure curve, $p_{swell}(e)$, is central for the model, and in the original formulation it was adopted to a swelling pressure curve fitted to experimental data from SKB TR-06-30 (blue line in Figure 6-13, left). During the course of the first applications of the model (Åkesson et al. 2010a) it was however noticed that this swelling pressure curve is slightly too high and that it would be more accurate to use an alternative curve which is based on retention data (green line in Figure 6-13, left). This second curve was therefore used for the modelling of the TBT experiment.

Since the swelling pressure curve is central for the mechanical model, a direct indication of the validity of the model can be obtained by comparing the used swelling pressure curve with the experimental data. A compilation of experimental data was presented in section 5.3 and is shown in Figure 6-13 (right). It can be noted that the experimental data in general follows the swelling pressure curve quite well.

The most noticeable exception is the condition for Ring 3 for which the swelling pressures are lower than the used curve. This could be caused by the possibly water unsaturated conditions close to the heater. An alternative explanation could be that the properties of the bentonite changed due to the thermal heat load.

A confirmation that the model adheres to the swelling pressure curve is illustrated by Figure 6-14. The stress paths display the characteristic behaviour by which bentonite that only swells (or remain constant volume) ends up exactly on the swelling pressure curve, whereas material that undergoes consolidation is forced beyond the curve, which means that the local net mean stress is higher than

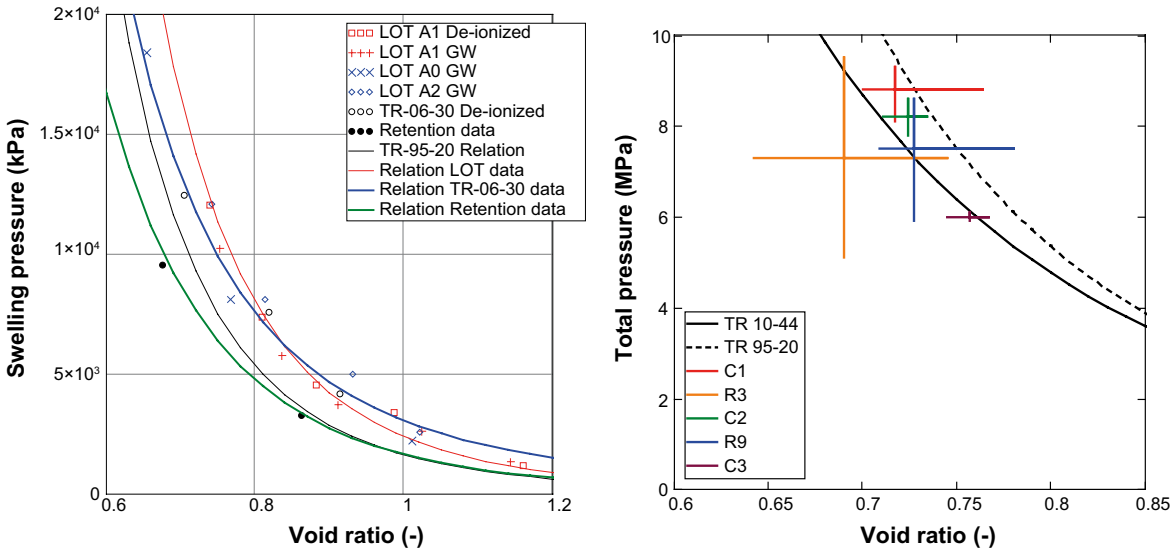

Figure 6-13. *Swelling pressure versus void ratio. Left graph show independent measurements and adopted relations (from Åkesson et al. 2010b). Right graphs shows two adopted relations and compilations of final swelling pressures and void ratios at dismantling for each instrumented block in TBT (from section 5.3).*

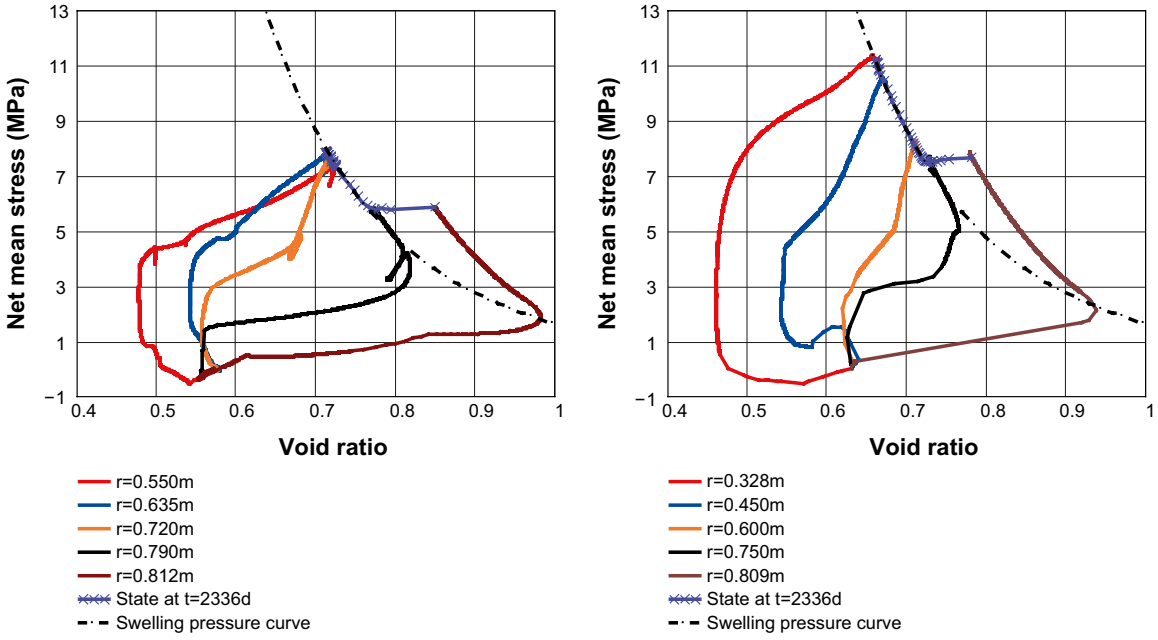

Figure 6-14. *Stress paths for different radii and final state in numerical models together with adopted swelling pressure curve. Left graph shows results for model of the upper package (TBTR10A2). Right graph shows results for model of the lower package (TBTR4_THMg_A1).*

the swelling pressure for the void ratio in question. A question mark can possibly be raised for the innermost points, for which the initial shrinkage appears to be slightly exaggerated.

Shear strength

The shear strength of compacted bentonite is basically determined through tri-axial compression tests, and the deviatoric stress at failure is the main result from such tests for the determination of yield surface parameters. Results from several compressions tests have been evaluated as a function of the mean effective stress, i.e. $q_f(p')$, see Åkesson et al. (2010b).

The shear strength is in the model represented by the modified Cam-Clay envelope. The plastic parameters for this (p_0^*, p_s and M) is set in such a way that the net mean stress for the critical state point is equal to the swelling pressure for the void ratio in question. The deviatoric stress for the same point is in turn given by the empirical $q_f(p')$-relation. A third condition necessary to

determine the plastic parameters is a value of the tensile strength, and in the original strategy (see Figure 6-12) this was given by a void-ratio dependent function. But this function cannot be used in combination with the swelling pressure curve derived from retention data, and instead is the value of the parameter p_s derived directly from the original parameter value evaluation.

A central notion behind the mechanical model is that the shear strength is a property which is basically determined by the void ratio, and not by the degree of saturation or the suction value. This means that the modified Cam Clay envelope is considered to be dependent of the void ratio, but independent of the suction value so that p_0 is equal to p_0^* . In turn, this means that the plastic stress-strain module, λ, is independent of the suction value. The void ratio dependence implies a narrowing of the envelope when the material undergoes swelling (see Figure 6-15), but there is no mechanism for this type of behaviour in the BBM model. So in the original strategy for the adoption of parameters values, the envelope parameters for compacted bentonite blocks were set for a homogenised target void ratio.

This approach was however found to underestimate the von Mises stresses measured in TBT (see Chapter 3). And instead a suction dependence was adopted for λ module in such a way that a suction dependent yield surface would mimic the narrowing of the modified Cam Clay envelope caused by the increase in void ratio. However, even with such a refined approach the model still underestimated the measured maximum von Mises stress (see Figure 6-16).

This underestimation may be a reflection of the uncertainties and possible limitations of the strategy for parameter value determinations. Still, it could reflect a true behavior which cannot be captured by the model, for instance due to another shape of the yield surface than the modified Cam-Clay envelope. A compilation of results from triaxial test on one hand, and unconfined compression test on the other is shown in Figure 6-17. The p'-values for the unconfined compression tests results are simply calculated as $q_f/3$. This graph indicates that the maximum deviatoric stress is approximately the same for a given void ratio, regardless of the type of test. This suggests that the actual yield surface is horizontal or perhaps sloping with decreasing q_f-values for increasing p'-value at the maximum von Mises stress, rather than the elliptical shape implied by the modified Cam-Clay envelope.

Elastic properties

The plastic model is the most complex part of the mechanical model, which requires the largest number of parameter value adoptions specific for the problem in question. The complexity of the elastic part is on the other hand intentionally limited to a minimum (Figure 6-11). The main reason for this is the porous-elastic description for which the validity is limited. For instance, a specified κ_i-value implies per definition a zero bulk modulus for unloaded conditions. This has been handled by the adoption of a linear suction dependence by which the κ_i-value is zero for the initial suction value, while for water saturated conditions (zero suction) a general κ_{i0}-value of 0.12–0.15 has been adopted. Moreover, the specification of a minimum bulk modulus (K_{min}) replaces the κ_i-value at low stress levels. This modulus is however set low (e.g. ≤ 20 MPa) in order to adhere to the BBM model as far as possible (Åkesson et al. 2010b).

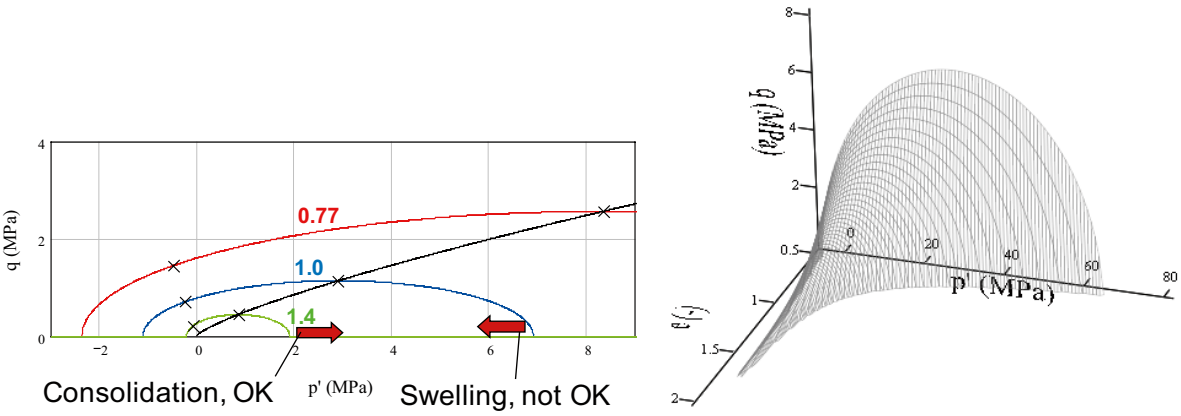

Figure 6-15. *Examples of yield surfaces in p-q plane for different void ratios (left), and continuous yield surface in p-q-e space (swelling pressure curve based on TR-06-30 data).*

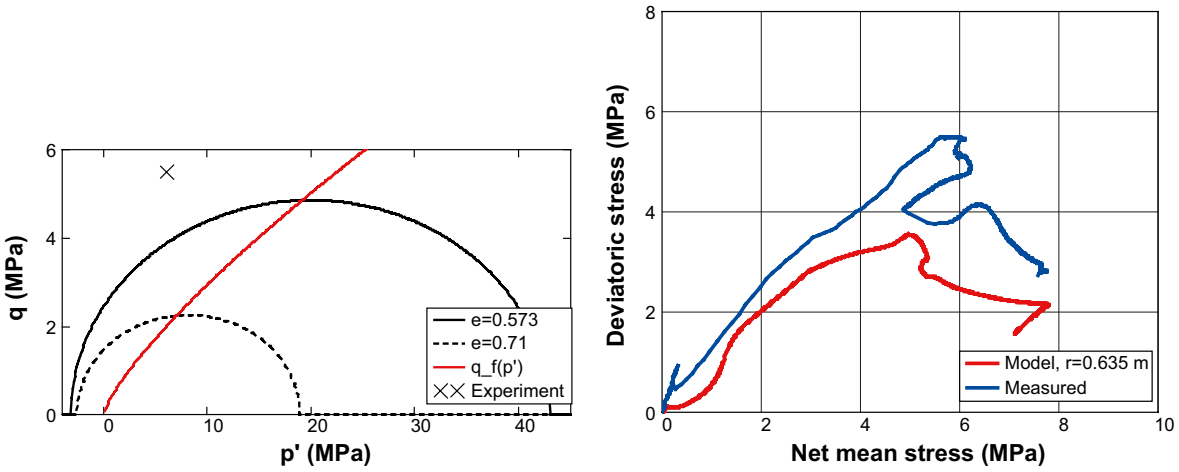

Figure 6-16. *Left graph shows empirical relation for von Mises stress at failure vs. mean effective stress (red line), adopted modified Cam Clay envelopes for two different void ratios (black lines), and condition in Ring 9 at day ~200 (cross). Right graph shows stress paths, measured and model (TBTR10A4), in p-q plane at 635 mm radius in Ring 9.*

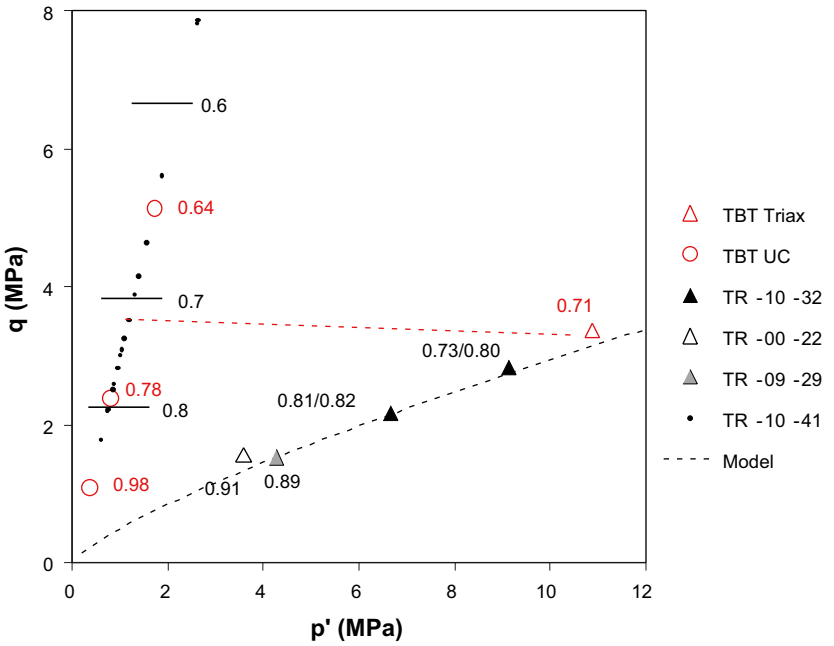

Figure 6-17. *Compilation of results from triaxial test (triangles) and unconfined compression tests (circles). Data from TBT reference material marked red (Åkesson et al. 2012). Void ratios are marked for every point, except for the TR-10-41 data (Dueck 2010) for which the approx. q levels for void ratios 0.6, 0.7 and 0.8 are marked. Black dotted line is the used $q_f(p')$ function. Red dotted line joins the data from both tests types for a void ratio of 0.71. Additional data from triaxial test: TR-10-32: (Dueck et al. 2010); TR-00-22: (Karnland et al. 2000); TR-09-29: (Karnland et al. 2009).*

This approach is apparently quite relevant for the reproduction of the build-up of stresses (see Chapter 3). However, some results suggest that this will underestimate the stiffness of the bentonite blocks. For example, the stress paths for the inner nodes shown in Figure 6-14 indicate that the adopted parameter values overestimate the elastic compression of these parts. It may therefore be valuable if the linear elastic properties of bentonite blocks could be more directly addressed in the mechanical model.

The swelling/shrinkage modulus of the elastic model (κ_s) can in the original CODE_BRIGHT code be assigned dependencies of suction as well as the net mean stress. This was further developed for the SR-Site modelling (Åkesson et al. 2010a, b) to also include a void ratio dependence. This modification adjusts the pressure dependence in such a way that the swelling modulus is zero if the net mean stress is equal to a pre-defined swelling pressure for the current void ratio. This is an efficient way to mimic a swelling pressure curve (see Figure 6-14). Still, this cancelation of the modulus is only relevant for negative suction increments (i.e. swelling), and this is the most common direction at high stress levels. One major exception appears however to occur during cooling at high stress levels. At such events, the thermal contraction of water leads to a reduction in liquid saturation and an increase in suction (see section 6.5). The shrinkage strain will apparently be underestimated due to the high stress levels. There is currently no obvious path how to overcome this inconsistency.

Final remarks

The overall capabilities of the mechanical model are generally encouraging considering the ability to implement a swelling pressure curve and to mimic the hysteretic behaviour. It should nevertheless be stressed that with the inclusion of mechanical processes in a numerical model follows some significant numerical difficulties which in many cases are insoluble.

6.5 Thermal expansion of water

The thermal expansion of water (α) is currently specified as a constant in both CODE_BRIGHT and ABAQUS. In CODE_BRIGHT, a default value of $3.4 \cdot 10^{-4}°C^{-1}$ is used. Attempts have been made to adapt an α-value that represents the density change for the temperature step between 20 and 150°C ($6 \cdot 10^{-4}°C^{-1}$). With such a modification it should be possible to mimic the final water volume reduction after the termination of the heaters (see Figure 6-18).

Still, this adaption appears to be insufficient to reproduce the temporary pressure drops that have been observed subsequent to occasional power failures, and especially after the termination of the heaters. This may to some extent be due to the employed value is too low in the high temperature range. But more notably, the reproduction of a pressure drop with the used conceptual models requires that a number of processes are well represented.

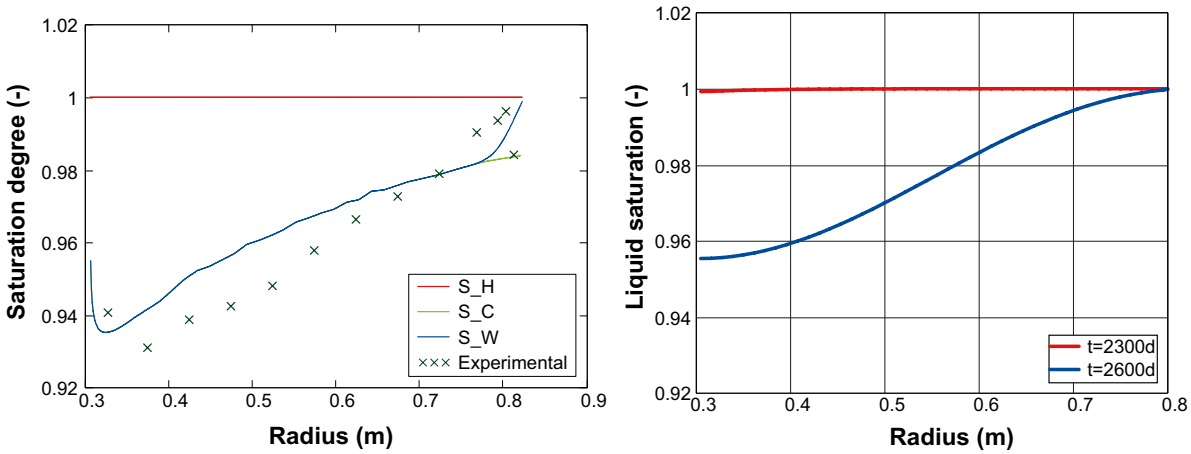

Figure 6-18. *Calculated saturation profiles for Ring 4 before and after cooling. Left graphs shows results from analytical calculations (from section 5.4). Right graphs shows results from numerical model with increased α-value for water (TBTR4_THg_A6).*

In the models, a temperature decrement leads to a suction increment, and this relation is given by three derivatives: i) the thermal "contraction" of water, which is described by the α-value; ii) the reduced degree of saturation; and iii) the increase of suction, which is given by the derivative of the retention curve:

$$\frac{d\rho_l}{dT} \approx \alpha \cdot \rho_l \qquad \frac{dS_l}{d\rho_l} = -\frac{S_l}{\rho_l} \qquad \frac{ds}{dS_l} = \frac{1}{S_l'(s)} \tag{6-9}$$

A suction increment leads to an elastic volume decrement (shrinkage), which in turn leads to a stress decrement under constant volume conditions:

$$de_h + de_m = -\frac{\kappa_s}{s+0.1} ds - \frac{\kappa_i}{p'} dp' = 0 \qquad \frac{dp'}{ds} = -\frac{\kappa_s}{\kappa_i} \frac{p'}{s+0.1} \tag{6-10}$$

In total the stress reduction following a temperature reduction is given by the following expression:

$$\frac{dp'}{dT} = \frac{dp'}{ds}\frac{ds}{dS_l}\frac{dS_l}{d\rho_l}\frac{d\rho_l}{dT} \approx \frac{\kappa_s}{\kappa_i}\frac{p'}{s+0.1}\frac{S_l}{\rho_l}\frac{1}{S_l'(s)}\alpha \tag{6-11}$$

A number of parameters therefore have to be finely tuned. It should be noted that both α and $S_l'(s)$ have negative values. The currently used pressure dependence of the swelling modulus (κ_s) may imply that the shrinkage is underestimated.

A more relevant description would perhaps be to relate the pressure drop to the compressibility of water (β). For a constant density, this would imply the following expression:

$$d\rho_l^{\,T} + d\rho_l^{\,P_l} \approx \alpha \cdot \rho_l \cdot dT + \beta \cdot \rho_l \cdot dP_l \approx 0 \quad \Rightarrow \quad \frac{dP_l}{dT} \approx -\frac{\alpha}{\beta} \tag{6-12}$$

With the default values of α and β used in CODE_BRIGHT ($-3.4 \cdot 10^{-4}$ C°$^{-1}$ and $4.5 \cdot 10^{-4}$ MPa^{-1}, respectively) this derivative has the value of 0.76 MPa/C°. Slightly higher values can be expected for the temperatures in TBT. An indication of the relevance of this approach is given by the evolution of the pressures and temperatures immediately after the beginning of the termination of the heaters on day 2,336 (see Figure 6-19). The highest slopes were recorded by the sensors in Cylinder 2 and 1, and these were approx. in the same order as the estimated derivative.

6.6 Gas transport

The CODE_BRIGHT tool has an option to include a gas phase which enables the explicit representation of water in both liquid and vapor form. For conditions with moderate temperatures below 100°C, it is usually relevant to prescribe a constant atmospheric gas pressure as long as the gas can escape

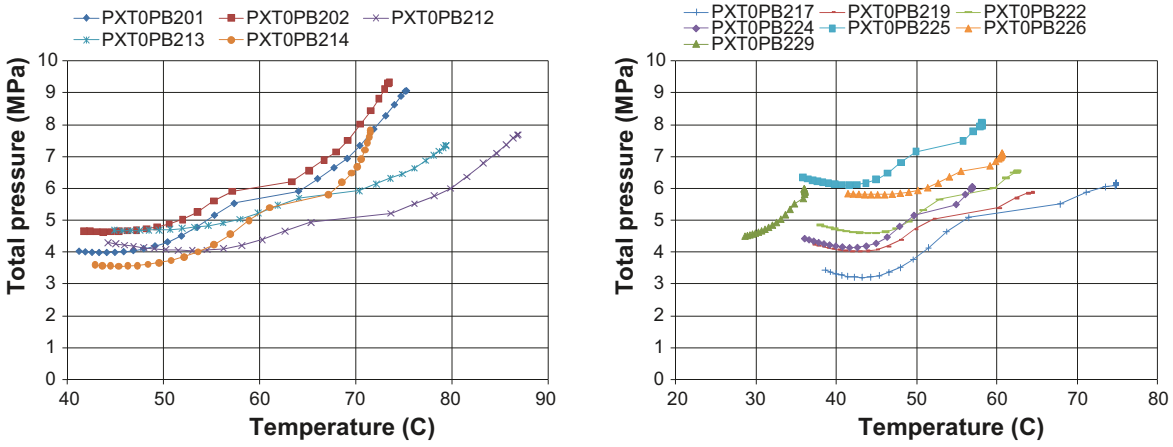

Figure 6-19. *Relations between total pressures and temperatures in functional sensors during the period from day 2,335 to day 2,362 (data for days 2,346 and 2,347 not shown due to irregular temperatures). Left graph shows data from C1, R3 and C2; Right graph shows data from R9 and C3 (sensor PB226 outside R7).*

from the modeled problem in question. For conditions above 100°C however, such an approach will imply that the material cannot reach water saturation. This was the case in the predictive modelling presented by Fälth et al. (2005). This can possibly be handled by prescribing a constant gas pressure higher than atmospheric, but a more relevant approach is to solve the equations for the mass balance of gas. This is then a true two phase flow problem, which implies that the parameter values for the gas transport have to be adopted, and that boundary conditions for the gas transport have to be defined.

Assessment of overall gas movements

The main problem is that the air in the void space at the installation, has to be able to escape (or dissolve in water) in order to allow for the water saturation of the bentonite. There is no obvious approach for how to define gas boundaries in different model geometries of the TBT experiment, except that the tunnel floor should be kept at a constant atmospheric gas pressure. More specific, the main route for gas escape at the level of the tunnel floor should be the slot between concrete plug and the rock wall.

Below the concrete plug, there are a number of permeable paths in which the gas pressure could in effect be kept at low levels. One such path is the outer slot with the sand filter and the pellets filling. There is no record of any water pressures in the filter during the first 562 days, and the outer slot could therefore have acted as a path for gas escape during this period, especially during the first 377 days when water only was injected through the lower injection points. The water pressures that were registered later on reflect the condition that the sand filter was sealed off, presumably due to the hydration of the pellets filling.

The hydration of the pellets filling (or more specific the sealing ability of this) appears however to be limited to the lower part of this filling. This is evident from the leakage detected at the end of the shield hydration operation at around day 1,750. Water could at that time flow from the sand shield, around the upper heater, to the tunnel floor through the cable-filled slots in the rock wall. This water flow must have passed the pellets filling and the upper bentonite blocks as well, and the fractures observed in Cylinder 3 appear to be the most likely route for this escape. In effect, it is likely that there was a permeable path from the tunnel floor down the sand shield, at least until the filling of the shield with water, which could maintain atmospheric gas pressures in the shield. This view is supported by the data from the pore pressures sensor in the sand shield.

The water injection through the sand filter and the water uptake in the outer parts of the bentonite blocks implies that the sand filter was sealed off from the inner parts of the bentonite blocks (see Figure 6-20). The maintained atmospheric gas pressure in the sand shield should however effectively minimize the gas pressure in the entire upper package. In the lower package, on the other hand, one would expect a noticeable increase in gas pressure, since the temperature increased, the gas-filled pore-space is reduced and there was no permeable route for gas escape, except for the slot around the heater and possibly the inner part of Cylinder 2, which should have remained unsaturated for a significant time period.

The relative humidity sensors in Ring 4 can give some information of this evolution. Figure 6-21 shows evaluated vapor pressures from these sensors, both as radial distributions for a few early points in time, and as evolutions during the first 1,200 days. These results indicate that the vapor pressure did not exceed one bar until around day 600.

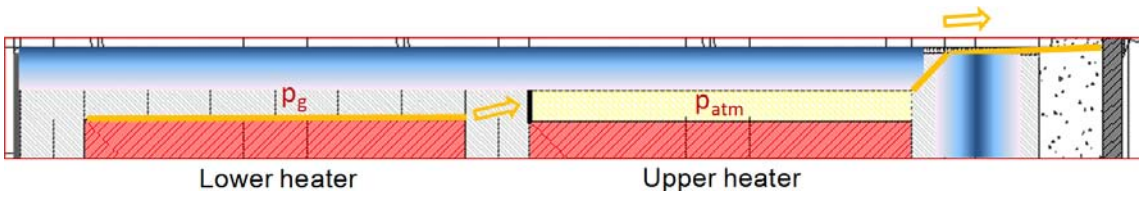

Figure 6-20. *Schematic illustration of the escape of gas. Shaded blue areas denote hydrated part of the bentonite, and yellow lines and arrows denote tentative routes for gas escape.*

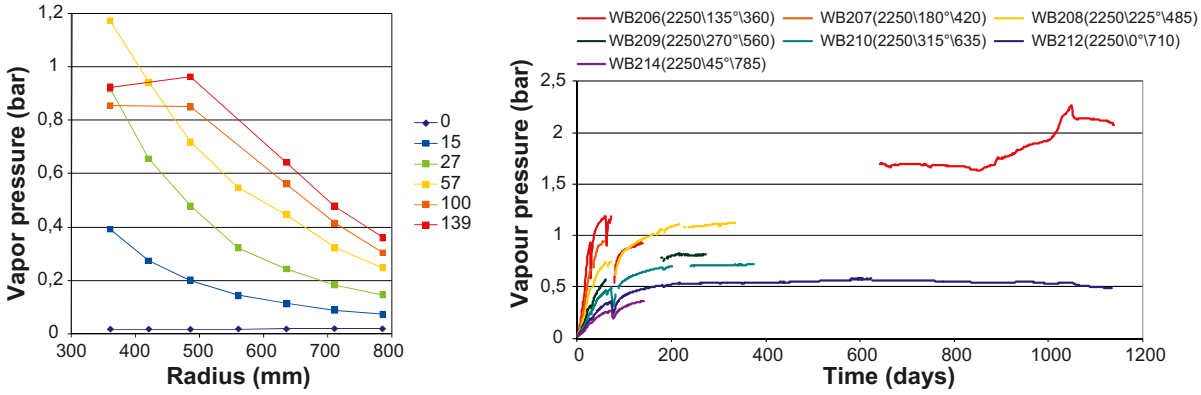

Figure 6-21. *Vapor pressures profiles for different days (left) and evolutions (right) in Ring 4. Calculated from RH-sensor readings (both RH and temperature) and the CODE_BRIGHT function for the saturated vapor pressure.*

Influence of gas transport on the thermo-hydraulic problem

The inclusion of the gas mass balance equation in the numerical model can influence the thermo-hydraulic problem in general and the transport of water vapour in particular. One such obvious point of influence is the gas pressure dependence of the vapour diffusivity:

$$D_m^w = \tau \cdot 5.9 \cdot 10^{-6} \frac{(273.15+T)^{2.3}}{p_g} \qquad \left(m^2/s\right) \qquad (6\text{-}13)$$

This means that the vapour diffusivity will be lower if a high gas pressure is allowed to develop than if the gas pressure is kept constant at an atmospheric level.

Another point of influence, which probably is more important, is that the inclusion of the gas mass balance equation will introduce an advective vapour transport. This will enhance the dehydration of the bentonite and is therefore of importance for conditions with a dry rock.

It is difficult to quantify this enhancement without performing the numerical modelling. A simple assessment of the ratio between the advective and diffusive fluxes can however be made for a steady-state condition. The situation is illustrated in Figure 6-22. It should be noted that the air dissolved in water is neglected in this evaluation.

The sum of the fluxes of air is zero:

$$j_g^a + \theta_g^a q_g = 0 \qquad (6\text{-}14)$$

The sum of the diffusive flux is zero:

$$j_g^a + j_g^w = 0 \qquad (6\text{-}15)$$

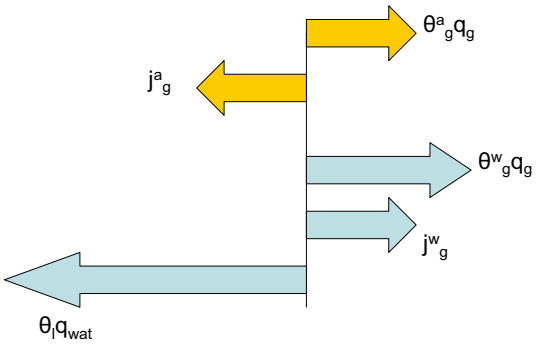

Figure 6-22. *Advective (θq) and diffusive fluxes (j) of dry gas (yellow) and moisture (blue) in a steady-state condition with a thermal gradient (left is hot and right is cold).*

The following relations between masses per unit volumes (θ) and mass fractions (ω) can be derived:

$$\varpi_g^w = \frac{\theta_g^w}{\theta_g^a + \theta_g^w} \quad \Leftrightarrow \quad 1 - \varpi_g^w = \frac{\theta_g^a}{\theta_g^a + \theta_g^w} \quad \Leftrightarrow \quad \frac{\varpi_g^w}{1 - \varpi_g^w} = \frac{\theta_g^w}{\theta_g^a} \tag{6-16}$$

From these equations a relation between the convective and the diffusive vapor flux can be derived as:

$$\theta_g^w q_g = \frac{\theta_g^w}{\theta_g^a} \theta_g^a q_g = -\frac{\varpi_g^w}{1 - \varpi_g^w} j_g^a = \frac{\varpi_g^w}{1 - \varpi_g^w} \cdot j_g^w \tag{6-17}$$

It should be noted that this relation is valid regardless of the values of the flow coefficients.

Inherent gas pressure profiles along thermal gradients

The situation in Figure 6-22 illustrates that a thermal gradient give rise to a liquid flux towards higher temperatures and diffusive vapor flux towards lower temperatures. Since the total diffusive flux is zero, this means that there is a diffusive flux of air toward higher temperature. This leads to a buildup of a gas pressure profile, with high pressures at the hot side and low pressures at the cold side. An example of a gas profile for a case with an atmospheric gas pressure boundary at the outer radius is shown in Figure 6-23. If a similar boundary would have been defined at the inner radius instead, this would lead to pressures below atmospheric at the outer boundary.

This behavior, with parallel gradients of the gas pressure profile and the temperature profiles, is quite counterintuitive, but a consequence of the two counter-directed water fluxes and the condition for zero total diffusive flux (6-14). The effect can be reduced by increasing the gas permeability.

A consequence of a high gas pressure at the hot end is that this can sustain a vapor pressure which exceeds the boundary liquid pressure (see Figure 6-23). It is therefore possible to get virtually saturated conditions even if the liquid pressure doesn't exceed the saturated vapor pressure, since the suction value at the hot end will be set by the gas pressure in this point and the liquid boundary pressure. The model thus implies that a boundary condition with an atmospheric gas and liquid pressure is sufficient to reach essentially saturated conditions, even at temperatures above 100°C.

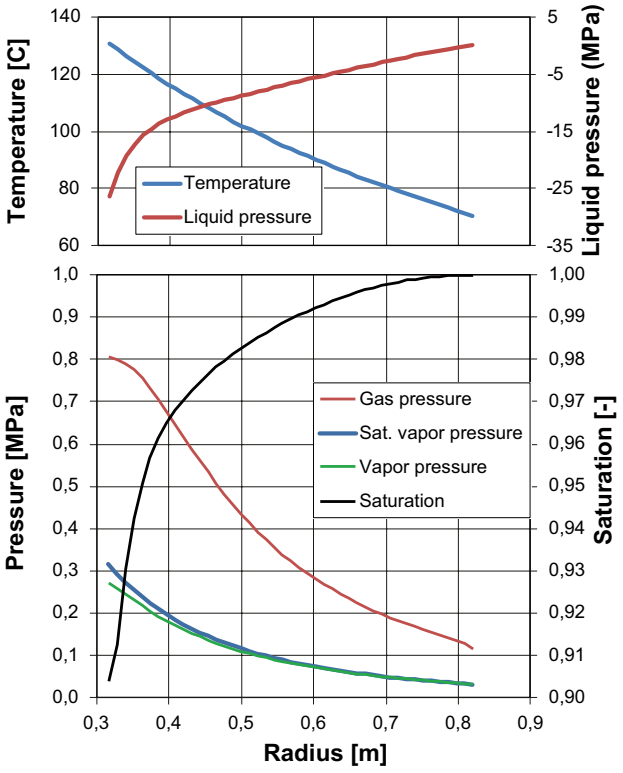

Figure 6-23. *Typical pressure profiles in numerical models (TBTR4_TMHgA1 at day 1,100).*

6.7 Sand compressibility

Independent oedometer tests

The sand-filled slots in TBT have had a major influence on the mechanical processes, and the mechanical properties have determined the extent of the radial swelling of the bentonite.

Independent measurements have been made through oedometer tests. Figure 6-24 shows a test curve that has been available throughout the test period. The evaluation of the oedometer modulus for the sand in the filter and the shield was based on this curve and the initial density of the fillings. For the filter the density was 1,729 kg/m^3 and for the shield the density was 1,820 kg/m^3. It should be noted that the density value for the filter is very sensitive on the diameter value for the deposition hole. The density value used here was based on diameter value of 1,757 mm (stated by Andersson and Johansson (2002)). For a target density of approx. 1,970 kg/m^3 at 8 MPa axial stress this leads to the oedometer modulii of 67 and 106 MPa for the filter and shield, respectively. With the assumption that the Poisson's ratio for the sands was 0.2, these values correspond to Young modulus values of 60 and 95 MPa for the filter and shield, respectively.

During the course of the modelling task it was noticed that the models tended to overestimate the stresses in the bentonite, and it was therefore suspected that the evaluated modulus values were too high. New oedometer tests were therefore performed and the results from these are shown in Figure 6-25. It can readily be noted that the densities at 8 MPa was lower than the 1,970 kg/m^3 found in the original measurement, which shows that the new measurements indicated even higher modulus values.

Still, in these evaluations it was assumed that the friction could be neglected. This may however lead to an overestimation of the oedometer modulus. Guidelines for compression properties of coarse soils ("friktionsjord" in Swedish) (Sällfors and Andréasson 1986) indicate that the ring friction may almost be as high as 30% of the vertical load for a sample height – diameter ratio of 0.6, as was used in the independent tests. This would imply that the evaluated oedometer modulus may be overestimated with 30%.

Plastic behaviour

The measured void ratio profile in the bentonite displays a very steep gradient close to the sand filter. The reason for this appears to be that the bentonite contracted as a result of the cooling at the end of the experiment, and that the outer part of the bentonite subsequently could swell outwards since water was available in the filter (see section 5.4). Still, this would require that the sand could remain compressed against the rock wall, and in order to reproduce such behaviour it is probably necessary to use an elastoplastic model for the sand.

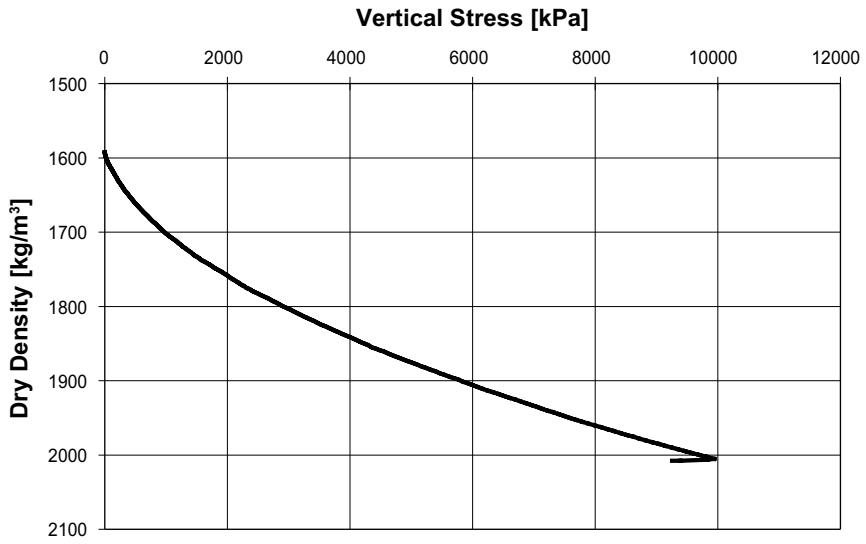

Figure 6-24. *Results from compression tests performed on Dalby sand (from Johannesson et al. 2010).*

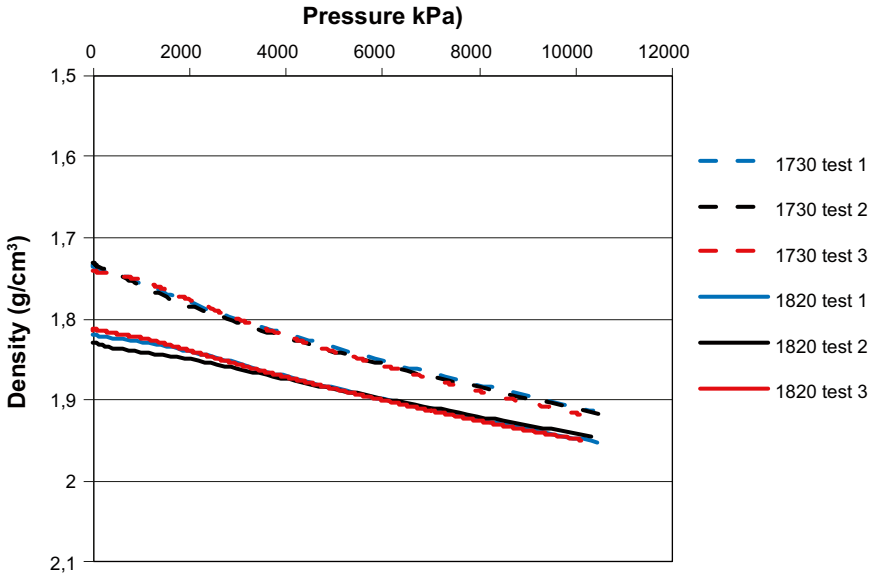

Figure 6-25. *Results from new compression tests performed on Dalby sand.*

Analytical sensitivity analyses

An analytical tool has been formulated in order make simple assessments of the equilibration of radial stresses and how different factors can influence the stress levels. The problem geometry is illustrated in Figure 6-26. The problem is simplified as a 1D plane strain problem, and the different stress components are the same throughout the bentonite: σ_a, σ_r and σ_t denote axial, radial and tangential stresses, respectively.

The problem is further simplified with the assumption that the axial and tangential stresses are equal (i.e. $\sigma_a = \sigma_t$). This implies that the mean stress (p) can be calculated as $(2\sigma_a + \sigma_r)/3$. In addition, the deviatoric stress (q) can be calculated as $\sigma_a - \sigma_r$.

A swelling pressure curve defines a relation between the void ratio and the mean stress:

$$p = f_1(e) \tag{6-18}$$

For this the swelling pressure curve which is based on retention data was used (green line in Figure 6-13, left). In order to minimize the radial stress, the stress state is assumed to fall on the empirical relation between the maxim deviatoric stress and the mean stress (see section 6.4).

$$q = f_2(p) \tag{6-19}$$

For a given set of initial values of the void ratio (e), as well as the inner and outer boundary positions (r_i and r_o) of the bentonite, and by assuming a homogenous final void ratio, a relation can be derived by which the radial stress in the bentonite is a function of the inner and outer boundary positions:

$$\sigma_r^{bentonite} = f_3(r_i, r_o) \tag{6-20}$$

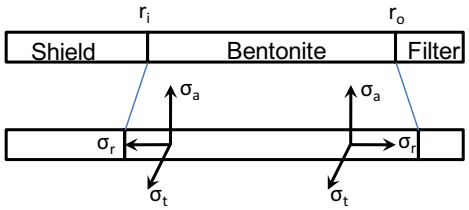

Figure 6-26. *Scheme for analytical calculation of stress equilibrium.*

Corresponding relations can be derived for the sand-filled slots. These are directly based on the test curve for the sand compaction shown in Figure 6-24 and the initial values of the density and the boundary position towards the bentonite:

$$\begin{cases} \sigma_r^{shield} = f_4(r_i) \\ \sigma_r^{filter} = f_5(r_o) \end{cases} \tag{6-21}$$

These functions are illustrated with black and brown lines in Figure 6-27. The solution is sought for the condition that all three radial stresses equilibrate for common values of r_i and r_o, respectively. This radial stress, as given by (6-20), is illustrated with red lines in Figure 6-27. Corresponding axial and tangential stresses are shown with blue lines.

It should be noted that the geometry of the lower package only includes the sand filter and a minor air-filled slot towards the heater. This problem is therefore simpler so that the inner boundary position (r_o) is specified, and that only the function for the filter in Equation (6-21) is taken into account.

Results from four different calculations are shown in Figure 6-27.

The two graphs to the left show results for the upper package. The upper graph is a base case (e_{init} of 0.573) which clearly exaggerates the stress levels, while the lower graph is calibrated for an initial void ratio of 0.628, which could be interpreted as an axial strain of 3.5%. This is in agreement with the sum of the relative changes in block heights for Ring 10 in Table 5-2 ($\varepsilon_{CI}+\varepsilon_{ID}$ = 3.3%), but not for Ring 9 ($\varepsilon_{CI}+\varepsilon_{ID}$= 0%). This discrepancy appears to be caused by the large inwards displacements in Ring 9 (see Figure 6-28), for which there is no obvious explanation. The radial displacements

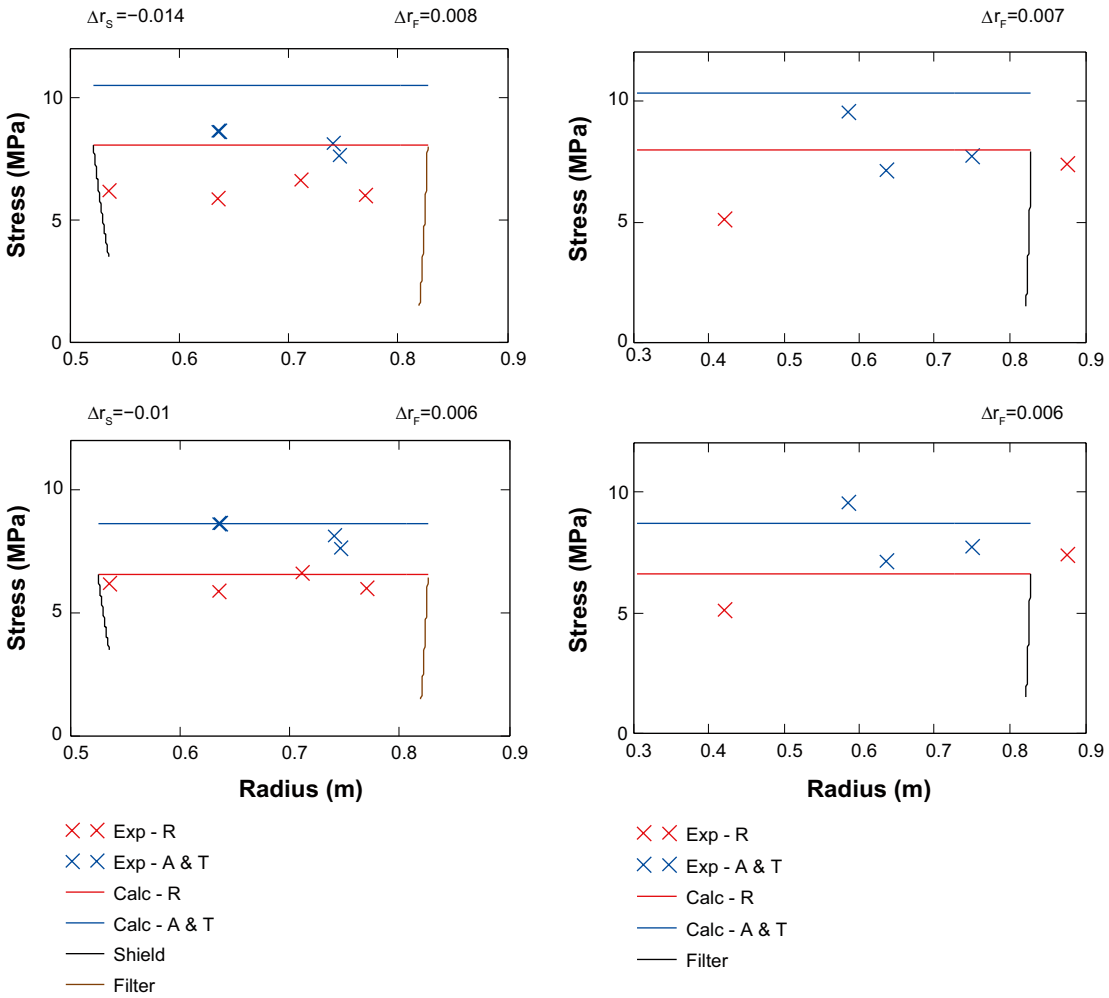

Figure 6-27. *Results from stress equilibrium calculations. Left graphs shows results for Ring 9/10: base case (upper) and with 3.5% axial strain (lower). Right graphs shows results for Ring 3/4: base case (upper) and with 2% axial strain (lower).*

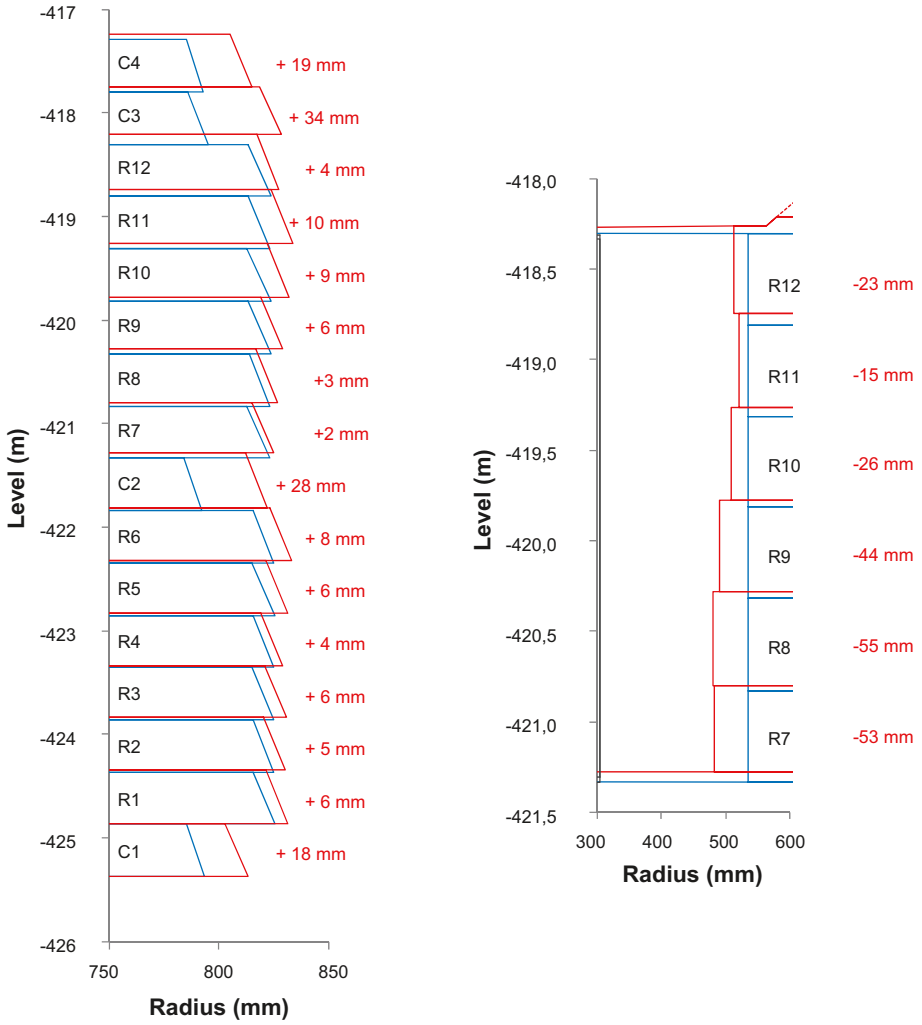

Figure 6-28. *Changes in outer radius for each block (left), and inner radius for rings in upper package (right). (From Åkesson 2010).*

are given as Δr_S and Δr_F values for each case. For the calibrated case these are –10 and +6 mm, respectively. While the value for the outer displacement is in agreement with the experimental data, the value for the inner displacement is clearly lower than what was measured (see Figure 6-28).

The two graphs to the right show results for the lower package. The upper graph is a base case (e_{init} of 0.631) which clearly exaggerates the stress levels, while the lower graph is calibrated for an initial void ratio of 0.664, which could be interpreted as an axial strain of 2%. This is in fairly good agreement with the sum of the relative changes in block heights for Ring 3 and 4, if the ε_{CI} value stated in Table 5-2 (0.9%) is added with the estimated axial strain for all blocks in the lower package (0.8%), see section 5.2. The radial displacements are given as a Δr_F values for each case. For the calibrated case this is +6 mm, which corresponds fairly well with the experimental data (see Figure 6-28).

Final remarks

The general observation that the models tends to overestimate the stresses in the bentonite appears to be caused by axial strains, rather than a high compressibility of the sand. Such an explanation requires however that the lower part of the upper rings (R7–R9) expanded significantly inwards. The reason for this type of deformation (Figure 6-28) is not understood. The large radial displacements inwards should also lead to very high densities of the sand in the shield (see Figure 6-2). There may therefore be an inconsistency between the initial sand densities and the observed radial displacements, possibly caused by the conditions during the retrieval test. An alternative explanation could be that the evaluated oedometer modulus values from the independent tests are overestimated.

6.8 Friction along rock wall

The friction along the rock wall can have a significant contribution to the overall force balance of the experiment. An assessment of the downward directed force component was presented in Goudarzi et al. (2006) and is shown in Figure 6-29. In this, the development of vertical forces acting on the upper package is shown: from below on Ring 10, and from above on the lid. The lower force is given by two functional axial transducers at the top of Ring 9 and under the assumption that these pressures are representative for a horizontal surface of 1.24 m^2. The force on the lid is simply given as the sum of the cable forces. The gravity force of the package resting on Ring 9, i.e. the six bentonite blocks, the plug and the lid, is only approx. 0.2 MN and can therefore be ignored in this balance.

The cable forces appear to have surpassed the force on Ring 10 at around day 1,000, coinciding with the activation of the filter mat. Prior to this event the results implied an upward directed net force, which should be balanced by a downward directed shear force at the rock wall. After day 1,000, the balancing force appeared to be directed upwards which reasonably has to involve the heater-shield package. The same situation seems to have occurred during the first two months. It should not be excluded that both types of balancing forces may have acted simultaneous. For instance, an upward directed force may also have acted on the heater prior to day 1,000, but the balancing shear force would on the same time have to be increased with the same magnitude. The marked forces in Figure 6-29 is thus the *minimum* net balancing forces.

If the force balance would be clear-cut, with negligible forces through heater during the period marked red in Figure 6-29, then the maximum shear force would be approx 3 MN. A schematic illustration of the mobilization of such a friction force is shown in Figure 6-30 (left). If this force (F) is assumed to be homogenously localised to a certain height (h), then it should be given by the following expression:

$$F = 2\pi rh \cdot p \cdot \tan(\phi) \qquad (6\text{-}22)$$

where p is the normal pressure, r is the radius of the deposition hole and ϕ is the friction angle. An evaluation of the height of friction as a function of the normal pressure is shown for two different friction angles in Figure 6-30 (right). It can be noted that the height of friction is quite small (< 2 m) according to this evaluation.

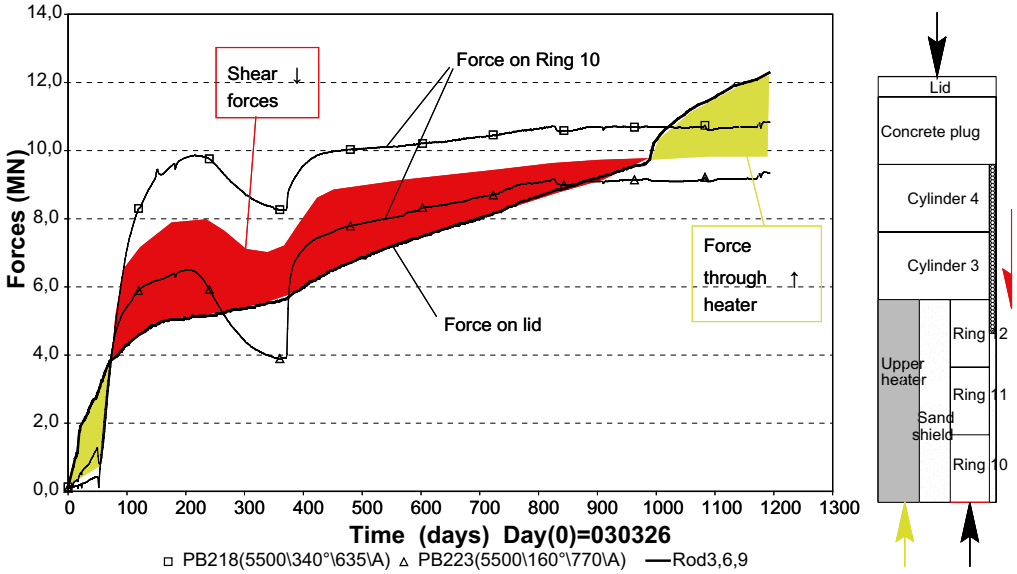

Figure 6-29. *Axial forces on the lid and on Ring 10 (two values given for the latter). Minimum net balancing forces are marked: shear forces (red) and through heater (green). From Goudarzi et al. 2006.*

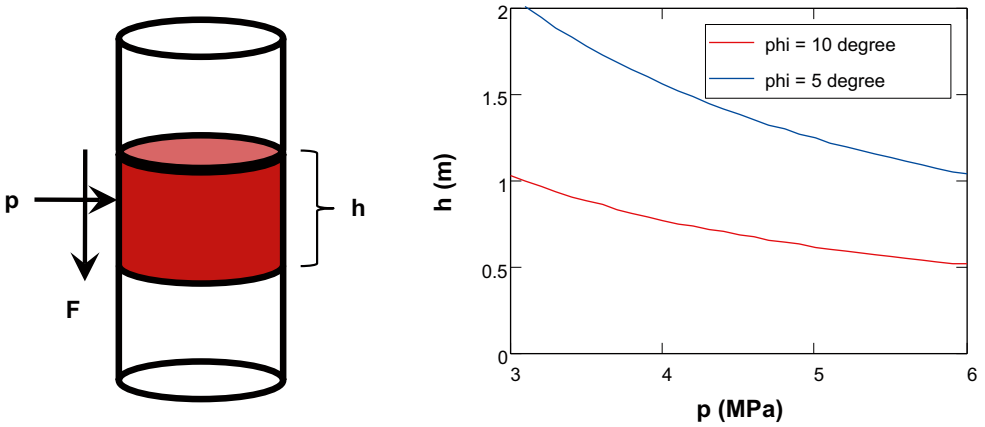

Figure 6-30. *Left picture shows a friction force (F) and normal pressure (p) localized to a certain height h. Right graph shows an evaluation of the height of friction as a function of the normal pressure for two different friction angles and a friction force (F) of 3 MN.*

Results from ABAQUS model

The abovementioned force balance is to some extent supported by the results from the ABAQUS model. A series of boundary graphs of the shear stress along the rock wall is shown in Figure 6-31. According to the model, a friction force directed downwards has acted on the two upper cylinders. After one year this force was approx. 4 MN, and at the end of the test it was 5–6 MN. Still, in the final state there was also a significant upward directed force at the level of the interface between Ring 12 and Cylinder 3.

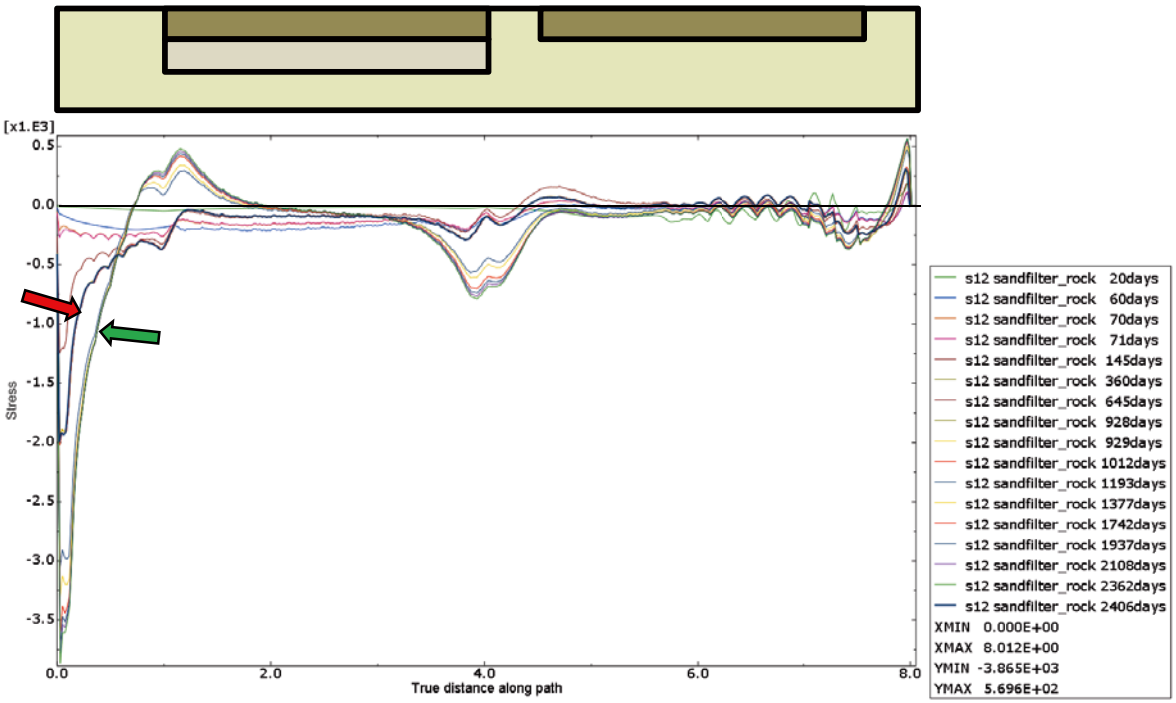

Figure 6-31. *Boundary graphs of shear stress along the rock wall; distance defined from concrete plug and negative stress values are directed downwards. Red arrow marks the graphs for 360 to 1,012 days; green arrow marks subsequent graphs.*

6.9 Conclusions

The following conclusions can be made from the presented assessments.

The results from the *thermal model* are generally in good agreement with experimental data. However, the ABAQUS model under-predicted the temperatures, especially in the inner parts, while some of the UPC CODE_BRIGHT models over-predicted the temperatures in the peripheral parts of the lower package. Still, these deviations appear to be caused by the geometry and boundary conditions, rather than by limitations in the material model.

For the *TH-model* the following observations can be made:

- Experimental data can be reproduced to a limited extent, if uncertainties are addressed and the flow coefficients as well as the retention properties are varied within relevant bounds.
- The hydration process around the upper heater, with moderate temperatures, can be fairly well reproduced with the material model adopted for CODE_BRIGHT (see section 3.3), whereas the corresponding process around the lower heater, with very high temperatures, tends to exaggerate the dehydration and delay the re-saturation process. This is essentially the result from both teams using CODE_BRIGHT. The ABAQUS model did not display any exaggerated dehydration, but in order to achieve this it was necessary to effectively halve the vapor diffusivity function.
- Early RH-evolution and pore-pressures (if accurate) in the lower package cannot be reproduced with current constitutive laws.
- Investigations of fundamental mechanism for supporting different constitutive laws and parameters values would be valuable. For instance, the early RH-evolution and the pore-pressures evaluated in section 6.3 appear to have lessons for the adoption of water retention curves.

For the *mechanical model,* the following observations can be made:

- Swelling pressures, i.e. the relation between the void ratio and net mean stress during the final state, can be well reproduced with the material model developed for the SR-Site (see the Clay Tech CODE_BRIGHT contribution in sections 6.4, 3.3.6, 3.4.3 and 3.5.4).This is facilitated by the inbuilt swelling pressure relation in the kappa_s function.
- The plastic parameters describing the yield surface is highly related to the void ratio. The yield surface is however (according to the BBM) unaffected during swelling at fairly isotropic stress states. The current approach (for the ClayTech CODE_BRIGHT contribution) to adopt plastic parameters for swelling materials (i.e. highly compacted blocks) has therefore been to set the parameter values for a target void ratio representing totally homogenized conditions. This approach was improved in this modelling task, through the adoption of a LC-curve included in the BBM. The void ratio dependence of the yield surface can in this way be mimicked by a suction dependence of the yield surface.
- Calculated von Mises stresses are in some cases significantly lower than the experimental data. This suggests that the shape of the actual yield surface is different than the shape implied by the modified Cam-Clay surface included in the BBM.
- General evolution of stresses has been fairly well mimicked by the ABAQUS contribution, using a porous elastic model with moisture swelling and Drucker Prager. The void ratios around upper heater, as well as the cable forces and the lid displacements were also well reproduced.
- The CODE_BRIGHT models presented by UPC (using BBM or BExM) showed that the general evolution of stresses could be fairly well mimicked, although the deviatoric stresses around the upper heater were under-predicted. The final dry-density distribution around both heaters could also be fairly well reproduced.

The *thermal expansion of water* is treated as a constant in the used codes.

- The default values are representative for temperatures at around 30°C and are therefore inadequate for TBT conditions. The ClayTechnology contribution using CODE_BRIGHT demonstrated however that this can to some extent be compensated by adopting a higher parameter value. This approach was not pursued by the other modelling teams.
- One phenomenon which should be influenced by the thermal expansion is the occurrence of pressure drops at occasions with decreasing temperatures. This process is however not really captured with the current constitutive laws, and the prospects is therefore currently small for reproduction of such pressure drops in a consistent way.

The inclusion of *gas transport* is necessary for conditions with temperatures exceeding 100°C for codes with explicit representation of water vapor. In addition, the inclusion of gas generally enhances the vapor transport. Both modelling teams using CODE_BRIGHT have included the gas transport in all models with temperatures exceeding 100 C. Gas transport is however not considered in the ABAQUS model.

- The experimental data suggest that TBT has been influenced by a gas escape route, which has limited the gas pressure in the sand shield to an atmospheric level. This condition could be sustained until the shield was filled with water. In addition, this gas escape route may also have limited the gas pressure in the lower package. This notion is to some extent supported by results from numerical models.
- Then inherent model behavior, with parallel gradients of the gas pressure profile and the temperature profiles, is quite counterintuitive. It would therefore be valuable to investigate the fundamental mechanism behind this process together with the general TH model.

The employment *of sand compressibility* values from independent oedometer tests result in overestimated stress levels. This is essentially the conclusion for all the modelling teams. This could be a consequence of the 1D geometry, by which no axial strains is allowed. The experimental results suggest that axial strains were significant in Ring 3, Ring 4 as well as in Ring 10, but not in Ring 9. An alternative explanation could be that the independent oedometer tests tend to underestimate the compressibility of the sand.

The *friction along rock wall* is of importance for reproducing the balance between the cable forces and the swelling pressures. The magnitude of this force component can to some extent be evaluated from the experimental data, and this is supported by the results from the ABAQUS model which also could reproduce the evolution of the cable forces. It has however not been possible to reproduce this force balance with the CODE_BRIGHT models.

References

SKB's (Svensk Kärnbränslehantering AB) publications can be found at www.skb.se/publications.

Alonso E E, Gens A, Josa A, 1990. A constitutive model for partially saturated soils. Géotechnique 40, 405–430.

Alonso E E, Vaunat J, Gens A, 1999. Modelling the mechanical behaviour of expansive clays. Engineering Geology 54, 173–183.

Andersson C, Johansson Å, 2002. Boring of full scale deposition holes at the Äspö Hard Rock Laboratory. Operational experiences including boring performance and a work time analysis. SKB TR-02-26, Svensk Kärnbränslehantering AB.

Autio J, Hjerpe T, Siitari-Kauppi M, 2003. Porosity, diffusivity and permeability of EDZ in crystalline rock and effect on the migration in a KBS-3 type Repository. Proceeding of the a European Commission CLUSTER Conference and Workshop on EDZ in Radioactive Waste Geological Repositories, Luxembourg, 3–5 November 2003.

Baldi G, Hueckel T, Pellegrini R, 1988. Thermal volume changes of the mineral–water system in low-porosity clay soils. Canadian Geotechnical Journal 25, 807–825.

Bear J, 1972. Dynamics of fluids in porous media. Dover Publications, New York.

Börgesson L, 2001. Äspö Hard Rock Laboratory. Compilation of laboratory data for buffer and backfill materials in the Prototype Repository. SKB IPR-01-34, Svensk Kärnbränslehantering AB.

Börgesson L, Hernelind J, 1999. Coupled thermo-hydro-mechanical calculations of the water saturation phase of a KBS-3 deposition hole. Influence of hydraulic rock properties on the water saturation phase. SKB TR-99-41, Svensk Kärnbränslehantering AB.

Börgesson L, Fredrikson A, Johannesson L-E, 1994. Heat conductivity of buffer materials. SKB TR 94-29, Svensk Kärnbränslehantering AB.

Börgesson L, Johannesson L-E, Sandén T, Hernelind J, 1995. Modelling of the physical behaviour of water saturated clay barriers. Laboratory tests, material models and finite element application. SKB TR 95-20, Svensk Kärnbränslehantering AB.

Börgesson L, Fälth B, Hernelind J, 2006. Water saturation phase of the buffer and backfill in the KBS-3V concept. Special emphasis given to the influence of the backfill on the wetting of the buffer. SKB TR-06-14, Svensk Kärnbränslehantering AB.

Cekerevac C, Laloui L, 2004. Experimental study of thermal effects on mechanical behaviour of a clay. International Journal for Numerical and Analytical Methods in Geomechanics 28, 209–228.

Chen G J, Ledesma A, 2009. Coupled thermohydromechanical modelling of the full-scale *in situ* test "Prototype repository". Journal of Geotechnical & Geoenvironmental Engineering 135, 121–132.

Chen N H, Othmer D F, 1962. New generalized equation for the gas diffusion coefficient. Journal of Chemical Engineering Data 7, 37–41.

Dueck A, 2004. Hydro-mechanical properties of a water unsaturated sodium bentonite: laboratory study and theoretical interpretation. PhD thesis. Lund Institute of Technology, Sweden.

Dueck A, 2010. Thermo-mechanical cementation effects in bentonite investigated by unconfined compression tests. SKB TR-10-41, Svensk Kärnbränslehantering AB.

Dueck A, Börgesson L, 2007. Model suggested for an important part of the hydro-mechanical behaviour of a water unsaturated bentonite. Engineering Geology 92, 160–169.

Dueck A, Börgesson L, Johannesson L-E, 2010. Stress-strain relation of bentonite at undrained shear. Laboratory tests to investigate the influence of material composition and test technique. SKB TR-10-32, Svensk Kärnbränslehantering AB.

ENRESA, 2000. FEBEX project. Full-scale engineered barriers experiment for a deep geological repository for high level radioactive waste in crystalline host rock. Final report, ENRESA. Madrid.

Fredlund D G, Xing A, 1994. Equations of the soil-water characteristic curve. Canadian Geotechnical Journal 31, 521–532.

Fälth B, Börgesson L, Hökmark H, Hernelind J, 2005. THM predictive modelling of the Temperature Buffer Test – Clay Technology's contribution. In Alonso E E, Ledesma A (eds). Advances in Understanding Engineered Clay Barriers: proceedings of the International Symposium on Large Scale Field Tests in Granite, Sitges, Barcelona, Spain, 12–14 November 2003. London: Taylor & Francis, 461–482.

Gens A, 1995. Constitutive laws. In Gens A, Jouanna P, Schrefler B A (eds). Modern issues in non-saturated soils. Wien: Springer, 129–158.

Gens A, Alonso E E, 1992. A framework for the behaviour of unsaturated expansive clays. Canadian Geotechnical Journal 29, 1013–1032.

Gens A, Garcia-Molina A J, Olivella S, Alonso E E, Huertas F, 1998. Analysis of a full scale *in situ* test simulating repository conditions. International Journal for Numerical and Analytical Methods in Geomechanics 22, 515–548.

Gens A, Sánchez M, Do N Guimarães L, Alonso E E, Lloret A, Olivella S, Villar M V, Huertas F, 2009. A full-scale *in situ* heating test for high-level nuclear waste disposal: observations, analysis and interpretation. Géotechnique 59, 377–399.

Goudarzi R, Åkesson M, Hökmark H, 2005. Temperature Buffer Test. Sensors data report (Period: 030326-060101) Report No: 7. SKB IPR-06-04, Svensk Kärnbränslehantering AB.

Goudarzi R, Åkesson M, Hökmark H, 2006. Äspö Hard Rock Laboratory. Temperature Buffer Test. Sensors data report (Period 030326–060701) Report No:8. SKB IPR-06-27, Svensk Kärnbränslehantering AB.

Goudarzi R, Åkesson M, Nilsson U, 2010. Temperature Buffer Test. Sensors data report (Period 030326–100301) Report No: 13. SKB P-12-03, Svensk Kärnbränslehantering AB.

Hoffmann C, Alonso E E, Romero E, 2007. Hydro-mechanical behaviour of bentonite pellet mixtures. Physics and Chemistry of the Earth 32, 832–849.

Hueckel T, Baldi G, 1990. Thermoplasticity of saturated clay: experimental constitutive study. Journal of Geotechnical Engineering 116, 1778–1796.

Hueckel T, Borsetto M, 1990. Thermoplasticity of saturated soils and shales: constitutive equations. Journal of Geotechnical Engineering 116, 1765–1777.

Hökmark H, 2004. Hydration of the bentonite buffer in a KBS-3 repository. Applied Clay Science 26, 219–233.

Ikonen K, 2003. Thermal analyses of spent nuclear fuel repository. Posiva 2003–04, Posiva Oy, Finland.

Jacinto A C, 2010. Thermo-Hydromechanical behaviour of expansive clays under high temperatures. Application to the Temperature Buffer Test Project. PhD thesis. UPC – Technical University of Catalonia, Barcelona, Spain.

Johansson H, Siitari-Kauppi M, Skålberg M, Tullborg E L, 1998. Diffusion pathways in crystalline rock – examples from Äspö-diorite and fine-grained granite. J. Contaminant Hydrology, 35, 41–53.

Johannesson L-E, Sandén T, Åkesson M, Bárcena I, García-Siñeriz JL, 2010. Temperature Buffer Test. Installation of buffer, heaters and instruments in the deposition hole. SKB P-12-02, Svensk Kärnbränslehantering AB.

Johannesson L-E, Sandén T, Åkesson M, 2010. Temperature Buffer Test. Installation of buffer, heaters and instruments in the deposition holes. SKB P-12-02, Svensk Kärnbränslehantering AB.

Karnland O, Sandén T, Johannesson L-E, Eriksen T, Jansson M, Wold S, Pedersen K, Motamedi M, Rosborg B, 2000. Long term test of buffer material. Final report on the pilot parcels. SKB TR-00-22, Svensk Kärnbränslehantering AB.

Karnland O, Olsson S, Dueck A, Birgersson M, Nilsson U, Hernan-Håkansson T, Pedersen K, Nilsson S, Eriksen T E, Rosborg B, 2009. Long term test of buffer material at the Äspö Hard Rock Laboratory, LOT project. Final report on the A2 test parcel. SKB TR-09-29, Svensk Kärnbränslehantering AB.

Knutsson S, 1983. On the thermal conductivity and thermal diffusivity of highly compacted bentonite. SKBF/KBS TR 83-72, Svensk Kärnbränsleförsörjning AB.

Lloret A, Villar M V, Sánchez M, Gens A, Pintado X, Alonso E E, 2003. Mechanical behaviour of heavily compacted bentonite under high suction changes. Géotechnique 53, 27–40.

Massman W J, 1998. A review of the molecular diffusivities of H_2O, CO_2, CH_4, CO, O_3, SO_2, NH_3, N_2O, NO, and NO_2 in air, O_2 and N_2 near STP. Atmospheric Environment 32, 1111–1127.

Olivella S, Gens A, 2000. Vapour transport in low permeability unsaturated soil with capillary effects. Transport in Porous Media 40, 219–241.

Olivella S, Carrera J, Gens A, Alonso E E, 1994. Nonisothermal multiphase flow of brine and gas through saline media. Transport in Porous Media 15, 271–293.

Olivella S, Gens A, Carrera J, Alonso E E, 1996. Numerical formulation for a simulator (CODE_ BRIGHT) for the coupled analysis of saline media. Engineering Computations 13, 87–112.

Philip J R, de Vries D A, 1957. Moisture movement in porous materials under temperature gradients. Transactions, American Geophysical Union 38, 222–232.

Pollock D W, 1986. Simulation of fluid flow and energy transport processes associated with high-level radioactive waste disposal in unsaturated alluvium. Water Resources Research 22, 765–775.

Pusch R, 1980. Swelling pressure of highly compacted bentonite. Technical Report 80-13, SKBF/KBS. Stockholm.

Pusch R, Liedtke L, 2003. EDZ formation in crystalline rock by TBM drilling and related alteration of hydraulic conductivity. In proceedings of the A European Commission CLUSTER Conference and Workshop on EDZ in Radioactive Waste Geological Repositories, Luxembourg, 3–5 November 2003.

Pusch R, Bluemling P, Johnson L, 2003. Performance of strongly compressed MX-80 pellets under repository-like conditions. Applied Clay Science 23, 239–244.

Sánchez M, 2004. Thermo-hydro-mechanical coupled analysis in low permeability media. PhD thesis. Geotechnical Engineering Department, Technical University of Catalonia, Barcelona.

Sánchez M, Gens A, Guimarães L D N, Olivella S, 2005. A double structure generalized plasticity model for expansive materials. International Journal for Numerical and Analytical Methods in Geomechanics 29, 751–787.

Schmidt E, Grigull U, 1982. Properties of water and steam in SI-units. 3rd ed. Berlin: Springer-Verlag.

Seager S L, Geertson L R, Giddings J C, 1963. Temperature dependence of gas and vapour diffusion coefficients. Journal of Chemical & Engineering Data 8, 168–169.

Sällfors G, Andréasson L, 1986. Geotekniska laboratorieanvisningar. Del 10, Kompressionsegenskaper. Stockholm: Statens råd för byggnadsforskning. (In Swedish.)

Tang A-M, 2005. Effet de la température sur le comportement des barrières de confinement. PhD thesis. École Nationale des Ponts et Chaussées, Paris.

Tang A-M, Cui Y J, Barnel N, 2008. Thermo-mechanical behaviour of a compacted swelling clay. Géotechnique 58, 45–54.

Villar M V, 2005. MX-80 bentonite. Thermo-hydro-mechanical characterisation performed at CIEMAT in the context of the Prototype Project. Technical Report 1053, CIEMAT, Spain.

Villar M V, Gómez-Espina R, 2007. Retention curves of two bentonites at high temperature. In Schanz (ed). Experimental Unsaturated Soil Mechanics. Berlin: Springer. (Springer Proceedings in Physics 112), 267–274.

Villar M V, Martín P L, Lloret A, 2005. Determination of water retention curves of two bentonites at high temperature. In Tarantino A, Romero E, Cui Y J (eds). Advanced experimental unsaturated soil mechanics: Experus 2005. Leiden: Balkema, 77–82.

Villar M V, Gómez-Espina R, Martín P L, 2006. Behaviour of MX-80 bentonite at unsaturated conditions and under thermo-hydraulic gradient. Technical Report 1081, CIEMAT, Spain.

Åkesson M (ed), 2006. Äspö Hard Rock Laboratory. Temperature Buffer Test. Evaluation modelling – Field Test. SKB IPR-06-10, Svensk Kärnbränslehantering AB.

Åkesson M (ed), 2008. Äspö Hard Rock Laboratory. Temperature Buffer Test. Evaluation modelling. TBT_3 Mock-up test. SKB IPR-08-09, Svensk Kärnbränslehantering AB.

Åkesson M, 2010. Äspö Hard Rock Laboratory. Temperature Buffer Test. Dismantling operation. SKB P-12-04, Svensk Kärnbränslehantering AB.

Åkesson M, Jacinto A C, Gatabin C, Sánchez M, Ledesma A, 2009. Bentonite THM behaviour at high temperatures: experimental and numerical analysis. Géotechnique 59, 307–318.

Åkesson M, Kristensson O, Börgesson L, Dueck A, Hernelind J, 2010a. THM modelling of buffer, backfill and other system components. Critical processes and scenarios. SKB TR-10-11, Svensk Kärnbränslehantering AB.

Åkesson M, Börgesson L, Kristensson O, 2010b. SR-Site Data report. THM modelling of buffer, backfill and other system components SKB TR-10-44, Svensk Kärnbränslehantering AB.

Åkesson M, Olsson S, Dueck A, Nilsson U, Karnland O, Kiviranta L, Kumpulainen S, Lindén J, 2012. Temperature Buffer Test. Hydro-mechanical and chemical/mineralogical characterizations. SKB P-12-06, Svensk Kärnbränslehantering AB.